Development and characterization of co-substituted hydroxyapatites for biomedical applications via advanced electrohydrodynamic processing

Yu Jiang

A thesis submitted for the degree of

Doctor of Philosophy

Department of Mechanical Engineering

University College London

Sep 2021

Declaration

I, Yu Jiang, confirm that the work presented in this thesis is my own. Where information has been derived from other sources, I confirm that this has been indicated in the thesis.

Acknowledgement

I would like to express my sincere gratitude to my supervisor Dr Jie Huang. I am very fortunate to have such a wise and enthusiastic supervisor, without whom my PhD study could never be accomplished.

I would like to thank Dr Lena Ciric for her instruction on the use of flow cytometer, thank Dr Tom Gregory for his instruction on the use of scanning electron microscope, thank Mr Martin Vickers for his instruction on the use of X-ray diffraction and thank Dr Zhiyu Yuan for her help in the cell proliferation assay.

I would like to thank Prof Anthony Harker and Prof Chaozong Liu for their massive valuable advice on the development of my research in my upgrade viva.

I also want to thank the family of Prof. Tao Chen for her invaluable help in my life when I first came London.

I appreciate the family of Dr Wei Cui for their inspiring guidance in my life when I feel lost in this PhD research.

It is a great honor for me to get the China Scholarship Council-UCL Joint Research Scholarship that strongly aided me in my research activities.

Special thanks are given to my wife Dr Huihan Zhi for her wholehearted, day and night support for my work and life over the past eight years.

My special thanks also give to my parents, Mr Hua Jiang and Mrs Ju Zhang, for their love and support in my life, to my parents-in-law, Mr Hongfa Zhi and Mrs Hua Wang, for their wise and valuable advice.

Publications and Conference Presentations

Journal Publications

Jiang, Y., Yuan, Z., & Huang, J. (2020). Substituted hydroxyapatite: a recent development. *Materials Technology*, 35(11-12), 785-796.

Jiang, Y., Jiang, X., Luo, K., & Huang, J. Triethylamine (TEA) as a dispersant in the formation of hydroxyapatite (HA) oligomers. 2021. *Biomaterialia*, Under reviewing.

Jiang, Y., Yuan, Z., Matharu, R., Ciric, L., & Huang, J. Co-substitution of Copper and Zinc into Hydroxyapatite for a Multi-functional Implant Coating Material. 2021. In preparation.

Jiang, Y., and Huang, J. Ball-tip-Nozzle – a Novel System producing a Stable Cone-jet in Electrohydrodynamic Atomization. 2021. In preparation.

Jiang, Y., and Huang, J. Using Magnetic Hydroxyapatite in Patterning Process Through a Novel EHD Coating Method Combining TAEA and Magnetic Fields. 2021. In preparation.

Conference Publications and Presentations

Jiang, Y., & Huang, J. (2017). Multi-functional Coating with Novel Bio-mimic Nanostructures for Medical Implants. Oral and poster presentation at, in University College London, U.K.

Jiang, Y., & Huang, J. (2018). Synthesis and characterization of Cu/Zn Co-substituted hydroxyapatite for antimicrobial applications. Oral and poster presentation, MechEng Research Conference, University College London, U.K.

Jiang, Y., Yuan, Z., Matharu, R., Ciric, L., & Huang, J. (2019). Cu and Zn Co-substituted Hydroxyapatite for Enhancing Antibacterial Ability and Biocompatibility. Conference Abstract and oral presentation: 7th China-Europe Symposium on Biomaterials in Regenerative Medicine, in Guangzhou, China.

Chen, H., Jiang, Y., & Huang, J. (2020). Investigation of filler reinforcements and printing patterns on mechanical properties of 3D printed PCL composites for bone implants. Poster presentation, 11th World Biomaterials Congress Virtual.

Abstract

Hydroxyapatite (HA) is a well-known bioactive material for biomedical applications, particularly for bone graft and implant coatings. Substitutions with metal ions in HA can provide add-on functions, such as magnetic property by adding Fe^{3+} and Mn^{2+} and antimicrobial property by adding Cu^{2+} and Zn^{2+}.

Electrohydrodynamic atomization (EHDA) has been developed for coating using nanosuspensions. The stability of Taylor cone in EHD jetting was improved by a modification of nozzle geometry. Spherical-nozzles introduced were able to overcome the instability caused by frequent spray-mode switches, which interferes coating processing. As a result, the uniformity of the deposition was improved and 10-fold increase in the through-put of processing of HA nanosuspensions was achieved. Importantly, a stable cone-jet could be achieved with a water-ethanol ratio up to 4:1, which was significantly improved from 5% aqueous solution with conventional nozzle and extended the range of processable materials.

Iron and manganese co-substituted HA (Fe-MnHA) has been synthesized to combine magnetic property with bioactivity. An analysis of the deposition of nanoparticles (NPs) using template-assisted electrohydrodynamic atomization (TAEA) under magnetic field showed that Fe-MnHA NPs was highly responsive in comparison with mono-

substituted HAs, magnetic iron oxide nanoparticles (IONPs) and IONPs-HA mixture (50/50wt%). The in vitro bioactivity of Fe-MnHA was in the same level as HA but higher than IONPs and their mixture in simulated body fluid (SBF) testing. Therefore, Fe-MnHA balanced the magnetic property and bioactivity, and may have a great potential in biomedical applications, from cell guidance, contrast agents for medical imaging to cancer therapy.

Multifunctional copper and zinc co-substituted HA (Cu-ZnHA) has been formulated to combine bioactivity with antimicrobial ability. Flow cytometry and crystal violet assays indicated its effective antibacterial and antibiofilm ability against *E. coli* and *S. aureus*. At the lowest metallic content (0.005mol%), Cu-ZnHA was not only antibacterial, but also showed a high biocompatibility by supporting the growth of human osteoblast-like MG63 cells. Therefore, Cu-ZnHA is a promising material for developing multifunctional implant coatings.

Impact statement

This study provides a comprehensive investigation on the designed multifunctional nanomaterials for biomedical applications. Biocompatible and antibacterial nanomaterials are widely needed in medical, industrial, environmental and cosmetic fields, such as wound dressing, surgical devices, drug delivery system, antibacterial packaging, water disinfection and antibacterial drugs. Biocompatible materials with magnetic property are important in biological applications such as drug delivery, contract agent for medical imaging, hyperthermia purposes and magnetic field-controlled patterning processing.

This project innovatively brought the benefits of different metallic ions to HA via co-substitution, to confer anti-infection ability and magnetic property. The co-substitution of Cu and Zn in HA successfully introduced the antibacterial and anti-biofilm formation abilities of HA with a very low metallic content level. It guides a new direction for designing biomaterials that require well-balanced anti-infection ability and biocompatibility. The co-substitution of Fe and Mn into HA provided a relatively high magnetic property. With the incorporation of Fe-MnHA with the MTAEA process, finer coating patterns were achieved with the co-existence of good bioactivity.

To the best of my knowledge, it is the first time systematically investigated a ball-tip nozzle assisted electrospray system, which could maintain a high stability of the cone-jet mode in EHD atomization and increase the coating efficiency. Meanwhile, this study created a magnetic and template assisted EHDA (MTAEA) technology and investigated the influence of magnetic field on the distribution and bioactivity of magnetic HA in patterned coatings. For the first time, magnetic fields were combined with TAEA technology in nanoparticle patterning process. This system provided a flexible platform for the deposition of 2D patterns, as well as a potential to fabricate complex structure in 3D architectures. It is an innovative platform that produce biomimetic nano-topographies and can be considered as a new and high-efficiency 3D printing/coating technology.

Consequently, different types of HA based materials synthesized in this project provided multiple functions that well filled the requirements in the implant coating industry with anti-infection ability and biocompatibility. Moreover, well designed devices and technologies in this project further enhanced the production efficiency and pattern flexibility of implant coating. With the modified systems, this project successfully achieved the mass production of nanoparticles' deposition and improved the patterning quality in the MTAEA processing. This work provided an insight into the next generation implant and medical devices coating technology.

Contents

LIST OF FIGURES **14**
LIST OF TABLES **17**
NOMENCLATURE **18**
CHAPTER I **21**
1 INTRODUCTION AND LITERATURE REVIEW **21**
1.1 Introduction 21
1.2 Bone 25
1.3 Biomaterials 28
1.3.1 Calcium Phosphate Bioceramics 30
1.3.2 Hydroxyapatite 31
1.3.3 Current Studies and Applications of HA 33
1.3.3.1 Drug Delivery and Drug Release Monitoring 34
1.3.3.2 Gene Delivery 35
1.3.3.3 Implant Coatings 36
1.4 Implant Coating Characteristics 37
1.4.1 Biocompatibility 38
1.4.2 Osseointegration 39
1.4.3 Anti-infection Abilities 41
1.4.4 Anti-biofilm Formation Abilities 43
1.5 Ionic Substituted HA 44
1.5.1 Antimicrobial Ionic Substituted HA 47
1.5.2 Magnetic Ionic Substituted HA 55
1.5.3 Multi-ionic substituted HA 60
1.6 The Synthesis Methods of HA 64
1.7 Implant Surface Topography 75
1.7.1 Implant Coating Technologies 76
1.7.1.1 Electrohydrodynamic Atomization 77
1.7.1.2 Electrospray Modes 82
1.7.1.3 Cone-jet Mode 85
1.7.1.4 Nozzle Geometry Determines the Stability of Cone-jet 88
1.7.1.5 Nozzle Geometry Affects the Solvent Incompatibility of EHDA 93
1.7.1.6 Template-assisted Electrohydrodynamic Atomization for Patterning Process 95
1.8 Research Questions 100
CHAPTER II **103**
2 METHODOLOGY **103**
2.1 Materials 103

2.2 Sample Preparation 105
2.2.1 Synthesis of HA and Metallic Ions Substituted HA Nanoparticles..... 105
2.2.2 Synthesis of Fe_2O_3 Nanoparticles..... 109
2.2.3 Fabrication and Analysis Ball-tip Nozzles and Flat-tip Nozzle 110
2.2.4 Electrospraying 113
2.2.5 Magnetic Field and Templates Assisted EHDA 117
2.2.6 Heat Treatment..... 123
2.3 Characterization of subHA 123
2.3.1 Powder X-Ray Diffraction (XRD) 123
2.3.2 Fourier-Transform Infrared Spectroscopy (FTIR)..... 126
2.3.3 Scanning Electron Microscopy (SEM) and X-ray Analysis Spectroscopy (EDS) 127
2.4 In vitro Biological Tests 127
2.4.1 In vitro Bioactivity Test..... 128
2.4.2 Bacteria Culture 131
2.4.3 Antibacterial and Anti-biofilm Formation Tests 132
2.4.4 Biocompatibility Test..... 139
CHAPTER III 141
3 BALL-TIP-NOZZLE – A NOVEL SYSTEM PRODUCING A STABLE CONE-JET IN ELECTROHYDRODYNAMIC ATOMIZATION 141
3.1 Introduction..... 141
3.2 The Effect of Ball-tip Size on the Stability of Electrospray Cone-jet..... 143
3.3 Stability of Ball-tip Nozzles Equipped Cone-jetting..... 147
3.4 Effect of Ball-tip Nozzles to the Coating Topographies 150
3.5 The Solvent Compatibility of Different Nozzles 152
3.6 Discussion 158
3.6.1 Unstable Cone-jet in Straight Nozzle 158
3.6.2 Strong Stability and High Throughput of Cone-jet in Ball-tip Nozzles... 160
3.6.3 6mm is the Most Suitable Size for Ball-tip Nozzles in Stabilizing the Cone-jet 162
3.6.4 Strong Water Compatibility of Ball-tip Nozzle 163
3.6.5 Ball-tip Nozzle would not Disturb the EHD Process 164
3.7 Conclusions..... 165
CHAPTER IV 166
4 MAGNETIC HA IN MAGNETIC FIELD AND TEMPLATE ASSISTED ELECTROHYDRODYNAMIC ATOMIZATION PATTERNING PROCESS 166
4.1 Introduction..... 166
4.2 Structural Characterization of HA, FeHA, MnHA and Fe-MnHA..... 169
4.2.1 XRD Characterization 169
4.2.2 FTIR Characterization..... 172
4.2.3 Investigating the Morphologies of Nanoparticles via SEM 176

4.3 In vitro Bioactivity Studies with SBF Soaking Test 177
4.4 Effect of Magnetic Fields 182
4.5 The Influence of Magnetic Fields on the Patterns of Electrospray with Different Materials 185
4.6 The Influence of Magnetic Field on the TAEA Patterns 187
4.7 The Magnetic Sensitivity of MHA with Different Metallic Content Substitution Level 192
4.8 Discussion 193
4.8.1 Fe and Mn Substituted into HA 193
4.8.2 Bioactivity of Fe-MnHA 194
4.8.3 Magnetic Properties of Fe-MnHA 195
4.8.4 Magnetic Field Affects the Distribution of Magnetic Nanoparticles 198
4.8.5 The Spontaneously Reduced Width of IONPs and MHA TAEA Patterns 199
4.9 Conclusions 202
CHAPTER V 204
5 MULTI-FUNCTIONAL CU AND ZN CO-SUBSTITUTION OF HA FOR IMPLANT COATING 204
5.1 Introduction 204
5.2 Characterization of HA, CuHA, ZnHA and Cu-ZnHA 206
5.2.1 XRD Characterization 206
5.2.2 FTIR Characterization 212
5.2.3 EDS Analysis 216
5.2.4 Investigating the Morphologies of Nanoparticles via SEM 218
5.3 Antibacterial Test of HA, CuHA, ZnHA and Cu-ZnHA 220
5.4 Antibiofilm Formation Abilities of HA, CuHA, ZnHA and Cu-ZnHA 223
5.5 *In vitro* Biocompatibility Studies with MG63 Cells 225
5.6 Discussion 228
5.6.1 Metallic Content Affected the Crystallinity and Unit Cell Parameter of MHA 228
5.6.2 Co-substitution of Cu and Zn into HA May Result in High Releasing Rate and Enhance Antibacterial Ability 229
5.6.3 The Enhanced Antibiofilm Formation Ability of Cu-ZnHA 232
5.6.4 The High Biocompatibility of Cu-ZnHA 233
5.7 Conclusions 235
CHAPTER VI 237
6 GENERAL DISCUSSION AND FURTHER STUDIES 237
6.1 General Findings of This Study 237
6.1.1 Ball-tip Nozzle Assisted MTAEA Process Achieved Stable and Flexible Patterning Process 239
6.1.2 Metallic Ions Substituted HA has Multi-functions 241
6.1.3 Fe-MnHA Well Matched the Designed Magnetic Property and

Maintained a Good Bioactivity 242
6.1.4 Co-substitution of Cu and Zn Achieved the Antibacterial and Anti-biofilm Formation Abilities..... 243
6.2 Further Studies 244
6.2.1 Ball-tip Nozzle can Serve as a Liquid Fuel Injector in a Microcombustor 244
6.2.2 Using MTAEA in Fabricating Biomimicking Antibacterial Nanostructures 245
6.2.3 Evaluation of the potential application of Fe-MnHA in Hyperthermia Treatment 246
6.2.4 Cu-ZnHA has Great Potential as Antibacterial Drugs 247
7 REFERENCE 249

List of Figures

Figure 1-1 Hierarchical structure of the bone 27
Figure 1-2 HA structure 32
Figure 1-3 Antibacterial mechanism of antimicrobial metal nanocomposites 49
Figure 1-4 Previous studies based on the biological properties of CuHA and ZnHA 55
Figure 1-5 Synthesis methods of HA 65
Figure 1-6 Schematic diagram illustrating the dry methods (Solid state method and mechanochemical method) and high-temperature methods (Combustion method and pyrolysis method) in HA synthesis 67
Figure 1-7 Schematic diagram illustrating the chemical precipitation methods in HA synthesis 73
Figure 1-8 Schematic diagram of EHDA system and Taylor cone 81
Figure 1-9 Schematic showing various possible jet modes during electrospraying process 83
Figure 1-10 The impact on EHD performance 88
Figure 1-11 EHD nozzle with guard plate (A) and extend cap (B). 92
Figure 1-12 Normal electrospray needle and co-axial needles. 93
Figure 1-13 Template assisted electrohydrodynamic atomization set-up 97
Figure 1-14 The nanostructure and the antibacterial mechanism of cicada wings 99
Figure 1-15 Project Development and Perspectives 102
Figure 2-1 Ball-tip nozzles Structure 112
Figure 2-2 EHD set up 114
Figure 2-3 Diagram of device setting up of TAEA (A), MAEA (B) and MTAEA (C). 119
Figure 2-4 Measuring the TAEA template and TAEA patterns. 122
Figure 2-5 A unit cell is the smallest repeating portion of a crystal lattice 125
Figure 2-6 Diagram of sample placing in the in vitro bioactivity testing 131
Figure 2-7 Schematic of flow cytometry cell counting. 134
Figure 2-8 The live/dead gating analysis of flow cytometry patterns of a Live/Dead sample. 136
Figure 3-1 Hanging drops and corresponding average volume on different nozzles 144
Figure 3-2 The processing map of straight nozzle and ball-tip nozzle with different extended cap size 146
Figure 3-3 EHD performance of a straight nozzle and a 6 mm ball-tip equipped nozzle. 148
Figure 3-4 Comparison of EHD Modes Variation between straight and ball-tip nozzles. 149
Figure 3-5 HA coatings collected by different nozzles under different voltages. 151
Figure 3-6 Droplet size of straight nozzles and ball-tip nozzles with different voltages

..... 152
Figure 3-7 The processing zone of ball-tip nozzles with different water: ethanol ratios. 154
Figure 3-8 Average Voltage Range (V_{RG}) with Different Water Ratio. 156
Figure 3-9 Average Voltage Ratios (V_{RT}) with Different Water Ratio. 157
Figure 3-10 Forces involved in a cone-jet formation with a ball-tip nozzle. 162
Figure 4-1 XRD patterns of MHA and HA powders. 170
Figure 4-2 FTIR spectra of mono- and multi-ionic substituted HA with variety Fe and Mn content. 174
Figure 4-3 Unit cell parameters, crystal size, crystallinity measured in XRD results and FTIR Peak intensity (PI) of PO_4^{3-} stretching peak at 1027cm^{-1}. 175
Figure 4-4 The morphologies of FeHA, MnHA and Fe-MnHA with variety metallic content. 177
Figure 4-5 SEM images of 50FeHA, 50MnHA, 50(Fe-Mn)HA, samples and the formed apatite in SBF after 2 days. 180
Figure 4-6 SEM images of 50FeHA, 50MnHA and 50(Fe-Mn)HA samples soaked in SBF for 4 and 7 days. 181
Figure 4-7 Coverage percentage of formed apatite in 7-day SBF soaking test. 182
Figure 4-8 Magnet simulation by ANSYS MAXWELL 184
Figure 4-9 EHD coated patterns of different materials with or without the appliance of magnets. 186
Figure 4-10 MTAEA patterns of 50 MHA, HA, IONPs and IONPs-HA mixture samples. 189
Figure 4-11 Average width of lines of 50(Fe-Mn)HA MTAEA patterns under different magnetic field. 190
Figure 4-12 The relative line width reduction of different materials in response to different magnetic flux density 191
Figure 4-13 Average width of lines of different MHA MTAEA patterns in M4 region. 193
Figure 4-14 Magnetic susceptibility of Fe^{3+}HA and MnHA. 197
Figure 4-15 Schematic diagram of TAEA setting up 201
Figure 4-16 Schematic diagram of hypothetical mechanism that may lead to the accumulation of IONPs in a TAEA system. 202
Figure 5-1 XRD patterns of as-synthesized Cu-ZnHA, ZnHA, CuHA and HA powders. 208
Figure 5-2 XRD patterns of heat-treated Cu-ZnHA, ZnHA, CuHA and HA powders... 210
Figure 5-3 FTIR spectra of mono- and multi-ionic substituted HA with variety Cu and Zn content. 214
Figure 5-4 Unit cell parameters, crystal size, crystallinity measured in XRD results and Peak intensity (PI) of PO_4^{3-} stretching peak at 1027cm^{-1}. 215
Figure 5-5 Measured XC based on EDS results of both mono-ionic and multi- ionic

substituted HA. 217
Figure 5-6 The morphologies of ZnHA, CuHA and (Cu-Zn)HA with variety metallic content. 219
Figure 5-7 The live/dead gating analysis of flow cytometry patterns of Cu-ZnHA samples. 221
Figure 5-8 Antibacterial abilities of CuHA, ZnHA and Cu-ZnHA against E. coli and S. aureus. 222
Figure 5-9 Anti-biofilm formation abilities of CuHA, ZnHA and Cu-ZnHA relative to that of HA. 224
Figure 5-10 In vitro biocompatibility test based on alamarBlue cell proliferation assay. 226
Figure 5-11 SEM images of Osteoblast-like cell MG63 cultured on HA and Cu-ZnHA surface 227

List of Tables

Table 1-1 Calcium phosphates and chemical formula 31
Table 1-2 Chemical composition of HA, bone, dentin and enamel..... 46
Table 1-3 Antimicrobial abilities of metal ions substituted HA..... 51
Table 1-4 Biological tests of multi metallic ions co-substituted HA 62
Table 1-5 Effective ionic radii in picometre (pm) of elements in function of ionic charge 63
Table 1-6 The HA morphologies and reaction parameters in commonly used wet methods for synthesis of HA. 74
Table 1-7 Different coating techniques for HA..... 78
Table 1-8 Electrohydrodynamic modes..... 84
Table 1-9 Surface tension of commonly used solvents for EHDA processing 95
Table 2-1 Sample list of HA and MHA with various metal fraction that substituted into HA lattice structure. 109
Table 2-2 Ion concentration of human plasma and synthetic solution, mM 128
Table 2-3 Material list in SBF synthesis 130
Table 4-1 Lattice parameters, crystal size and crystallinity of MHA with different metallic content. 172
Table 5-1 Lattice parameters, crystal size and degree of crystallinity (X_C) of MHA with different metallic content. 212
Table 5-2 MHA concentration and metallic ions concentrations in vitro tests 235

Nomenclature

2D	Two-dimensional
3D	Three-dimensional
A. pleuropneumoniae	Actinobacillus pleuropneumoniae
AA	Antibacterial ability
ABS	Acrylonitrile Butadiene Styrene
AgHA	Ag substituted hydroxyapatite
Agr	Accessory gene regulator
ALP	Alkaline Phosphate
ATR	Attenuated total reflection
Ca/P	Calcium to phosphate ratios
CaP	Calcium phosphate
CD14+	Cluster of differentiation 14
CeHA	Ce substituted hydroxyapatite
CHA	Carbonate substituted hydroxyapatite
CMC	Carboxymethyl cellulose
CoHA	Co substituted hydroxyapatite
COL	Type I collagen expression
COVID-19	Novel coronavirus disease 2019
Cu-ZnHA	Cu and Zn co-substituted hydroxyapatite
CuHA	Cu substituted hydroxyapatite
DCPA	Dicalcium phosphate anhydrous
DCPD	Dicalcium hydrogen phosphate dihydrate
DMF	N-N dimethylformamide
DNA	Deoxyribonucleic acid
E. coli	Escherichia coli
Eap	Extracellular adherence protein
Emp	Extracellular matrix protein
eDNA	Extracellular DNA
EDS	Energy-dispersive X-ray analysis spectroscopy
EHD	Electrohydrodynamic
EHDA	Electrohydrodynamic atomization
EPS	Extracellular polymeric substances
EuHA	Eu substituted hydroxyapatite
F/MgHA	F and Mg co-substituted hydroxyapatite
F/SrHA	F and Sr co-substituted hydroxyapatite
FBCs	Ferrimagnetic bioglass ceramics

FeHA	Fe substituted hydroxyapatite
Fe-MnHA	Fe and Mn co-substituted hydroxyapatite
FHA	Fluoridated HA
FWHM	Full width at half maximum
GaHA	Ga substituted hydroxyapatite
GO	Grapheme oxide
GSH	Glutathione
HA	Hydroxyapatite
HEPES	(4-(2-hydroxyethyl)-1-piperazineethanesulfonic acid)
HIV/AIDS	Human immunodeficiency virus infection and acquired immunodeficiency syndrome
hMSCs	Human mesenchymal stem cells
HOBC	Human osteoblast cell
HOCC	Human osteoclast cell
HPW	Half peak width
ICDD	International Centre for Diffraction Data
IONPs	Iron oxide nanoparticles
L/W	Length to width ratios
LPS	Lipopolysaccharide
M/P	Metal ions to phosphate ratios
MAEA	Magnetic field-assisted electrohydrodynamic atomization
Mg/AgHA	Mg and Ag co-substituted hydroxyapatite
Mg/CHA	Mg and carbonate co-substituted hydroxyapatite
Mg/SrHA	Mg and Sr co-substituted hydroxyapatite
MgHA	Mg substituted hydroxyapatite
MHA	Metallic Substituted HA
mM	Millimolar
MnHA	Mn substituted hydroxyapatite
MRI	Magnetic resonance imaging
MTAEA	Magnetic field and template-assisted electrohydrodynamic atomization
NaHA	Na substituted hydroxyapatite
NMP	N-methyl-2-pyrrolidone
OCN	Osteocalcin secretion
OCP	Octacalcium phosphate
OD	Optical density
OLED	Organic light emitting diodes
P. aeruginosa	Pseudomonas aeruginosa
PCL	Poly (e-caprolactone)
PC	Phosphorylcholine

PDF	Powder diffraction file
PEG	Poly (ethylene glycol)
PEO	Poly (ethylene oxide)
PGA	Poly-N-acetylglucosamine
PI	Peak intensity
PLGA	Poly(lactic-co-glycolic acid)
pm	Picometre
PMMA	Poly(methyl methacrylate)
PU	Polyurethanes
RNA	Ribonucleic acid
ROS	Reactive oxygen species
S. aureus	Staphylococcus aureus
S. epidermidis	Staphylococcus epidermidis
S. suis	Streptococcus suis
SARS-CoV-2	severe acute respiratory syndrome coronavirus 2
SA/V	Surface area to volume ratio
SeHA	Se substituted hydroxyapatite
SEM	Scanning Electron Microscopy
SiHA	Si substituted hydroxyapatite
Sr/CeHA	Sr and Ce co-substituted hydroxyapatite
Sr/CHA	Sr and carbonate co-substituted hydroxyapatite
Sr-CuHA	Sr and Cu co-substituted hydroxyapatite
SrHA	Sr substituted hydroxyapatite
sub-HAs	Substituted hydroxyapatite
TAEA	Template-assisted electrohydrodynamic atomization
tas-SBF	Simulated body fluid
TCP	Tricalcium phosphate
TEM	Transmission Electron Microscopy
THF	Tetrahydrofuran
TiHA	Ti substituted hydroxyapatite
TRIS	Tris(hydroxymethyl)aminomethane
V_{MAX}	Maximum voltages
V_{MIN}	Minimum voltages
VRC	Vaccine Research Center
V_{RG}	Voltage range
V_{RT}	Voltage ratios
XRD	X-Ray Diffraction
ZnHA	Zn substituted hydroxyapatite

Chapter I

1 Introduction and Literature Review

1.1 Introduction

Hydroxyapatite (HA) is the main mineral composition in bone and teeth (Fihri et al., 2017). Due to their favorable bioactivity and biocompatibility HA nanoparticles have been widely used in the biomedical field, such as drug delivery, gene delivery and bioactive coatings on metallic osseous implants (Tram Do et al., 2012, Šupová, 2015, Mondal et al., 2018). However, medical demands in practice are complicated. Ideally, a good biomaterial should not only resemble the host tissue, but also provide add-on functions, such as anti-infection ability and magnetic property to extend the biomedical applications (Boanini et al., 2010). HA is an ideal platform because the charged species can be replaced by different elements, which plays a vital role in providing different physical, chemical and biological functions that can fit into different medical applications (Šupová, 2015).

Bacterial infection and biofilm formation on health care medical device surfaces, especially the implantable devices, such as sutures, catheters, orthopedics implants,

etc., may lead to bleak prognosis and high healthcare cost. Medical statistics showed around 2% to 5% infections occurred in spinal surgeries, which is highly possible to cause morbidity and mortality (Hickok and Shapiro, 2012). Therefore, a prophylactic anti-infection regimen is required to minimize infections after the surgical intervention, especially when large foreign materials are inserted (Hickok and Shapiro, 2012). In order to introduce the anti-infection ability into biocompatible materials such as HA to combine biocompatibility and antimicrobial ability, Cu and Zn have been considered as good candidate (Huang et al., 2015). With a high metallic content substitution level, such as X_{Cu} or X_{Zn} = 0.1 (X represents the mole fraction, which is the amount of moles of a content divided by the total amount of moles of all contents in a mixture, X_{Metal}=Metal(mol)/(Metal(mol) + Ca(mol))), ZnHA has exhibited a good antibacterial ability and CuHA has a higher bactericidal effect than ZnHA (Hidalgo-Robatto, 2018). However, the lowest observed cytotoxicity level of CuHA is at molar ratio as X_{Cu} = 0.01 (Li et al., 2010b), and the antibacterial ability of CuHA with low metallic content level (X_{Cu} < 0.01) is even lower than ZnHA (Stanić et al., 2010). Therefore, a strategy that may improve or maintain their antibacterial abilities and meanwhile avoid the potential cytotoxicity is co-substituting Cu and Zn into HA to overcome their limitations (Huang et al., 2015).

Magnetic nanoparticles have attracted great attentions in biomedical applications.

Different types of magnetite ferrite-based iron oxide nanoparticles (IONPs) have been widely studied for drug delivery, cancer treatment and medical imaging. However, there is a safety concern on these ferrite-based magnetic nanoparticles due to their relatively low biocompatibility and unstable structures (Gupta and Gupta, 2005, Ito et al., 2006, Thorek et al., 2006). As biomedical applications, the biocompatibility was required. Conferring magnetic property into HA has great potential to meet this requirement. Therefore, FeHA and MnHA are considered as alternative magnetic biomaterials without cytotoxicity (Wu et al., 2007a, Li et al., 2012). FeHA and MnHA were known to have high magnetic properties and many studies have indicated the increased biocompatibilities when Fe^{3+} or Mn^{2+} were co-substituted with different elements into HA (Li et al., 2009b, Huang et al., 2016a, Huang et al., 2018, Ullah et al., 2018, Pasandideh et al., 2020). Both Fe and Mn co-substituted with other elements have exhibited benefits such as increased bioactivities. Therefore, co-substitution of Fe and Mn into HA has a good prospect to achieve high level bioactivity as well as maintain the strong magnetic property.

One of the applications of metallic substituted HA is acting as a coating material to achieve specifically designed surface topographies to improve the biological performance of implants. The surface topography of implant coatings can directly affect the cellular behavior and further regulate the tissue regeneration (Rahmany and

Van Dyke, 2013). Bioactive materials coated on the surface of implants with a well-designed pattern can gain more biological benefits than a continuous deposited coating (Zhao et al., 2008). The well-designed patterns can be produced by a widely studied implant coating patterning technology known as template-assisted electrohydrodynamic atomization (TAEA). It is realized by putting templates above the collecting substrates to restrict the coating area of nanoparticles (Li et al., 2008). Therefore, via combining magnetic fields with TAEA process, it is possible to precisely control the distribution of magnetic nanoparticles and achieve high-resolution patterning process. Consequently, a very attractive application of the magnetic Fe-MnHA may function as a feed material in the magnetic and template assisted EHDA (MTAEA) patterning process to achieve high-resolution patterned deposition.

Apart from the materials, coating technology also plays an important role in influencing the quality of implant coating. Two challenges of electrohydrodynamic atomization (EHDA) are the processing instability and solvent incompatibility of cone-jet mode in electrospraying (Lastow and Balachandran, 2007, Dastourani et al., 2018). According to current understanding of EHDA, the nozzle geometry is an important parameter that determines the stability coating efficiency and quality of EHDA process.

1.2 Bone

The term of bone refers to the rigid tissue of the vertebrate skeletal system. The skeleton supports the structure of body, enables mobility and protects the organs. From the material perspective, bone is a bioceramic composite with a unique organic-inorganic architecture, which provides a great mechanical property with high strength and fracture toughness. The composition of bone contains 10 wt% water, 25 wt% organic material and 65 wt% mineral phase (Chen et al., 2011b).

The skeletal system is very complex. Different bone structure varies between different species and even between different bone types in a single organism. In general, the bone formation system can be divided into two main types, primary and secondary bones formation (Little et al., 2011). The primary bone formation occurs at epiphysial cartilage, also known as endochondral ossification, is an unorganized mineralization with very loose, small fibril bundles of collagen. This is due to the collagen fibril in cartilage is too narrow for mineral deposition, which results in extrafibrillar mineralization. The collagen cannot direct the mineralization process. Therefore, the mineral crystals form clusters within the proteoglycan matrix, which leads to spherulitic arrangement (Little et al., 2011).

The mineralization process in the secondary bone formation is more optimal to

achieve extraordinary structures of bone, such as parallel-fibered or lamellar bones that formed the hierarchical structure of bones, where the collagen fibrils are highly organized in close-packed lamellar structures (Little et al., 2011). The hierarchical structure of bones has been well studied. In general, different levels of hierarchy, that composed of HA nano-platelets aligned within collagen fibrils, which form layers in parallel to construct the lamellae structures. The lamellae structures are then distributed around blood vessel and formed osteons, which can further form compact bone or woven as a trabecular network of microporous bone (Olszta et al., 2007).

Besides the complex structures of bones, the basic nanostructure of bone is arrays of HA crystals fixed within the collagen matrix, which is created via the intrafibrillar mineralization of collagen. This structure functions as the key to the mechanical properties of bones (Figure 1-1) (Olszta et al., 2007). In the collagen matrix of bone, the collagen was assembled as a triple helical structure composed of tropocollagen molecules (Figure 1-1) (Hamed and Jasiuk, 2013, Farokhi et al., 2018). Further interaction between this tropocollagen units form a fibrillar structure called 'quarter-staggered array', which created the hole and overlap zones in the collagen matrix. Such structure leaves gaps around 40 nm between each periodic unit, where crystal nuclei can be observed (Figure 1-1) (Hamed et al., 2010).

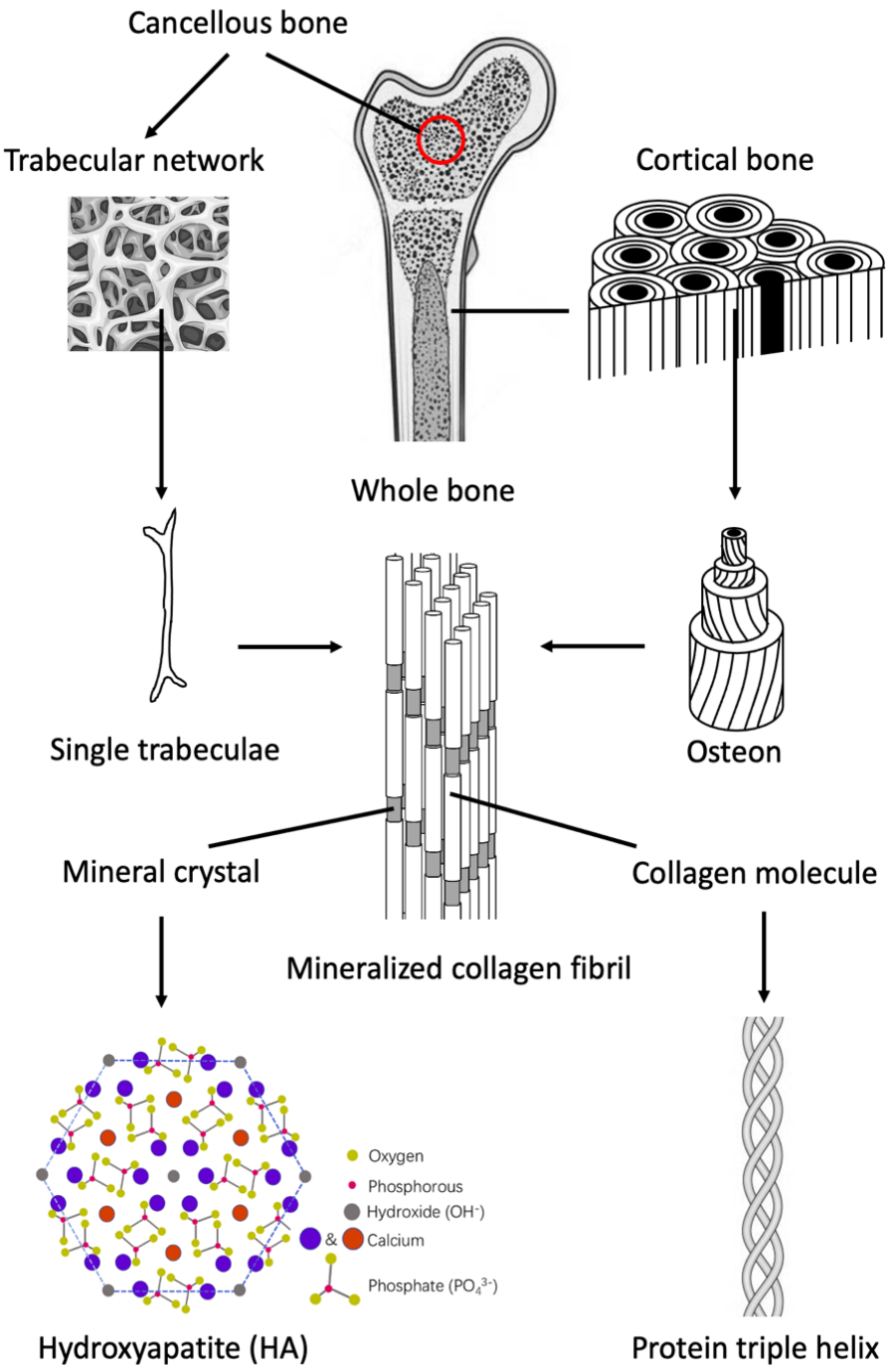

Figure 1-1 Hierarchical structure of the bone

In the macroscale, two bone types, trabecular and cortical, composed the whole structure of bone. In the microscale, the osteons and Haversian canals are primary feature. In the nanoscale, type I collagen fibrils reinforced with HA mineral forms the lamellar or woven bone. Figure re-drawn with permission from Elsevier (Rho et al., 1998, Hamed et al., 2010, Tadano and Giri, 2012, Hamed and Jasiuk, 2013, Farokhi et al., 2018)

The based composition of bones from nano- to micro- scales provides an excellent mechanical property that can bear the mechanical stress it faces every day. However, bone defects can still develop due to different reasons such as infection, tumor, trauma and surgery. For centuries, scientists were trying to find or produce materials that can replace missing bone tissues. In 17th century, the first transplantation of a piece of cranial bone from a dog to human was reported (Fernandez de Grado et al., 2018). Afterwards, different non osseous materials from wood to marble were used as bone graft. However, until 1892, the implantation of a calcium sulfate-based material finally resulted in a convincing success (Peltier et al., 1957).

Nowadays, more than 2 million cases of bone grafting were reported around the world every year (Fernandez de Grado et al., 2018). Many different materials have been investigated in repairing bone defects, such as allogenic bone, xenogeneic bone, or different types of biomaterials including the synthetically inorganic or biologically organic combinations (Pryor et al., 2009).

1.3 Biomaterials

The term of biomaterial represents any natural or artificial materials that were designed for inserting into human body to replace the fractured, lost and diseased host

tissues, or replace natural functions, in order to improve the quality of life (Geetha et al., 2009, Tathe et al., 2010). Biomaterials can be derived from nature (e.g. reprocessed collagen and cellulose) or synthesized in the lab by using metallic components (e.g. stainless steel, titanium and alumina), polymers (e.g. Poly(methyl methacrylate) (PMMA), polyurethanes (PU) and hydrogels), ceramics (e.g. HA) or composite materials (e.g. silicone rubber and Dacron) (Tathe et al., 2010). The required characteristics of biomaterials could be very complex according to the targeted functions. Ideally, a biomaterial should be biocompatible and contains properties like osteointegration, superior corrosion and wear-resistance, or other required therapeutic effects in order to sustain intended functions in the body for a long time (Navarro et al., 2008, Mahajan and Sidhu, 2018, Winkler et al., 2018). For example, Polyurethane, Teflon and Dacron have been used as vascular grafts owing to their abilities in maintaining the mechanical integrity and long-term blood compatibility without causing blood clotting. PMMA and silicone have been used for contact lenses due to their long-term biocompatibility and good optical properties (Tathe et al., 2010). Anti-infective biomaterials such as Graphene oxide (GO), Silicon nitride (Si_3N_4), Poly (ethylene glycol) (PEG), Poly (ethylene oxide) (PEO), Phosphorylcholine (PC)-based polymers, etc. have been widely studied owing to their bioinert surfaces and low bacterial adhesion properties (Kingshott et al., 2003, Roosjen et al., 2003, Hirota et al., 2005, Liu et al., 2011, Webster et al., 2012).

1.3.1 Calcium Phosphate Bioceramics

Biomaterials have been used every day in surgery, drug delivery and dental applications to regulate interactions with living systems (Tathe et al., 2010, Chen and Thouas, 2015). The most widely used biomaterial in orthopedics and dentistry is calcium phosphate (CaP) bioceramics. CaP was found in bones since the last quarter of 17^{th} century (Eliaz and Metoki, 2017). In 1920, CaP was first introduced as an implant to treat rabbit bone fractures. In 1950, HA was first distinguished from octacalcium phosphate (OCP) due to its chemical stability and excellent biocompatibility. It was first applied as implant coatings of hip prosthesis in human in 1985 (Epinette and Manley, 2003).

CaP has incomparable advantages in the field of bone regeneration due to their good biocompatibility, osteoconduction and osseointegration (Eliaz and Metoki, 2017). CaP represents a family of minerals composed of Ca cations (Ca^{2+}) and phosphate groups, such as orthophosphate (PO_4^{3-}), metaphosphate (PO^-), or pyrophosphate ($P_2O_7^{4-}$). Sometimes hydroxide (OH^-) or hydrogen (H^+) ions may also be involved (Table 1-1) (Eliaz and Metoki, 2017).

Table 1-1 Calcium phosphates and chemical formula

Ca/P ionic ratio	Orthophosphates, di- and monohydrogen phosphates	Ca^{2+} combined with PO_4^{3-},$H_2PO_4^-$, and/or HPO_4^{2-}
0.5	Monocalcium phosphate (MCPM)	$Ca(H_2PO_4)_2 \cdot H_2O$
0.5	Monocalcium phosphate (MCPA)	$Ca(H_2PO_4)_2$
1.0	Dicalcium phosphate dihydrate (DCPD), mineral brushite	$CaHPO_4 \cdot 2H_2O$
1.0	Dicalcium phosphate anhydrous (DCPA), mineral monetite	$CaHPO_4$
1.33	Octacalcium phosphate	$Ca_8H_2(PO_4)_6 \cdot 5H_2O$
1.5	α-Tricalcium phosphate (α-TCP)	α-$Ca_3(PO_4)_2$
1.5	β-Tricalcium phosphate (β-TCP)	β-$Ca_3(PO_4)_2$
1.2-2.2	Amorphous calcium phosphate (ACP)	$Ca_xH_y(PO_4)_z \cdot nH_2O$, n=3-4.5; 15-20% H_2O
	Di- and polyphosphates	Ca^{2+} combined with the polyphosphates
1.0	Dicalcium diphosphate	$Ca_2P_2O_7$
0.83	Calcium triphosphate	$Ca_5(P_3O_{10})_2$
	Hydroxy- and oxo-phosphates	CaP contain other anions
1.67	Hydroxyapatite	$Ca_5(PO_4)_3(OH)$
1.67	Apatite	$Ca_{10}(PO_4)_6(OH, F, Cl, Br)_2$
2.0	Tetracalcium phosphate	$Ca_4(PO_4)_2O$

This table is adapted with permission from Elsevier (Dorozhkin, 2009, Szcześ et al., 2017).

1.3.2 Hydroxyapatite

Hydroxyapatite is named due to the hydroxide deficiency in bone apatite (Pu'ad et al., 2020). HA is the most widely used CaP ceramic (Posner, 1969, Jiang et al., 2020). It can promote the bone and implant integration due to the similar crystal structure and chemical composition as human skeletal apatite (Kim, 1998, Reyes et al., 2007, Stanić et al., 2010, Fihri et al., 2017). It was indicated that 65% of bone, 70% of dentin and 97% of enamel were made up by HA (Dorozhkin and Epple, 2002, Nudelman and Sommerdijk, 2012, Szcześ et al., 2017, Pu'ad et al., 2020). HA possesses a hexagonal

lattice structure, with cell dimension of a = b = 0.9418 nm and c = 0.6884 nm (Yao et al., 2003, Zhang et al., 2014b, Kebiroglu et al., 2017). HA is commonly represented as $Ca_{10}(PO_4)_6(OH)_2$, rather than $Ca_5(PO_4)_3(OH)$, because it has two formula units in one unit cell, which contains Ca (I) and Ca (II) sites. Ca(I) is synchronized by nine oxygen atoms, while Ca (II) is synchronized by one hydroxyl group and five oxygen atoms (Figure 1-2) (Basirun et al., 2018).

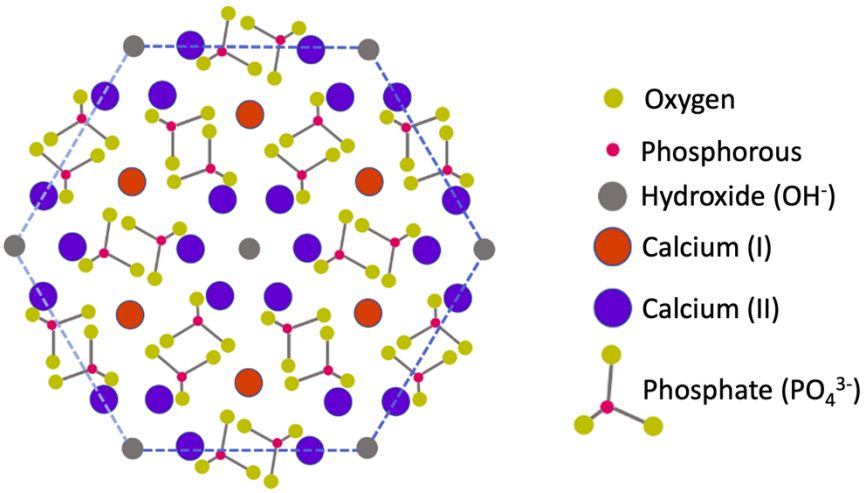

Figure 1-2 HA structure
HA: $Ca_{10}(PO_4)_6(OH)_2$, has a hexagonal lattice structure and is composed by 39.6wt% Ca, 18.5wt% P; and Ca/P molar ratio of 1.667. Figure re-drawn with permission from Elsevier (Šupová, 2015).

HA has porous structure, which is suitable for bone substitution and reconstruction (Yoshikawa et al., 1996, Anselme et al., 1999, Mohseni et al., 2014). HA has been commonly used in various biomedical applications such as bioactive coatings on metallic implants, bone grafting materials, dental materials, middle ear implant and

tissue engineering system due to its high bioactivity and intrinsic osteoconductive activity that could induce regenerative responses in human body (Sadat-Shojai et al., 2013, Raghavendra et al., 2017). For example, HA coatings could significantly improve the cytocompatibility of various materials such as ceramics and titanium (Ti) (Sachse et al., 2005, Xu et al., 2012). Moreover, HA was able to enhance the human mesenchymal stem cells (hMSCs) osteogenic differentiation towards human primary osteoblasts and prompt the formation of film on mineralized foci (Sima et al., 2010).

1.3.3 Current Studies and Applications of HA

Many studies have contributed great efforts in investigating different applications of HA based materials. The current understanding of HA indicates it can form different structure, size and mineral phases that varies the biological properties. A common strategy to extend the physical-chemical or biological functions of HA is substituting different functional ions into HA (Šupová, 2015).

HA-based materials were perfect carriers for a range of materials such as amino acids, antibiotics, antigens, drugs and genes (Syamchand and Sony, 2015). The antibacterial ions substituted HA have been widely applied in public hygiene and medical field such as medical devices, body insert materials and implant coatings (Lim et al., 2013).

Magnetic ions can also be substituted into HA lattice structure and function as a magnetic hyperthermia therapy agent in cancer treatment or contrast agent in medical imaging or drug delivery monitoring (Chen et al., 2011a, Ribeiro et al., 2020). Many other extended properties of ions substituted HA have been developed for different purposes, including the controllable delivery and release of drugs as well as in vitro and in vivo gene transfection.

1.3.3.1 Drug Delivery and Drug Release Monitoring

The lack of bioactive drug delivery system is a big challenge in the treatment of many diseases. Lots of researches were aiming at developing drug-delivery systems with site-specific, controllable distribution and selective delivery abilities (Mondal et al., 2018). Due to the excellent bioactivity and physical-chemical properties, HA-based materials have been widely used as delivery systems, as it can facilitate specific targeting and minimize the side effect. There are different types of HA-based drug-delivery systems, including porous HA nanoparticles, polymer-coated HA particles and drugs conjugated HA scaffolds. Different functional ions can be substituted into HA due to their ability in introducing different biofunctions (Mondal et al., 2018). HA-based theranostic system has been developed to combine a diagnostics response with a controllable drug delivery system. Such theranostic system can be achieved via coating or encapsulating

the diagnostic and therapeutic materials together to trigger the drug delivery function (Blanco et al., 2009). For instance, a designed HA drug delivery carrier has been developed for cancer treatment, which has a higher dissolution rate in low pH environment that normally appears at the vicinity of tumors (Uskoković and Uskoković, 2011).

Apart from using HA as a drug carrier, many studies were interested in luminescent HA as a drug-releasing monitoring system. Different types of lanthanide groups ions substituted HA were employed as contrast agents in monitoring the releasing rate and distribution of drugs. For example, a Eu and Gd co-substituted HA has been used to track the ibuprofen (IBU) in vitro releasing and in vivo distribution of nude mice (Chen et al., 2011a). In the meantime, the lanthanide ions substituted HA still exhibited good biological function such as bone remodeling (Mondal et al., 2018).

1.3.3.2 Gene Delivery

The HA nanoparticles are also known as ideal materials for gene delivery, therefore, the HA based gene vaccine is a hot topic to be studied. Commonly, vaccines contain purified products derived from pathogens, such as toxoid vaccines, protein subunit vaccines and other experimental vaccines, such as RNA and DNA vaccines. The gene

vaccines have many advantages comparing to conventional vaccines, including manufacturing, accessibility and economic advantages as well as wider range of immune responses and the gene vaccine has been widely applied from laboratory to veterinary field (Liu, 2011). Since 2020, due to the outbreak of the novel coronavirus disease 2019 (COVID-19) the United States Food and Drug Administration (FDA) has approved the emergency use authorization on the first two mRNA vaccines against the severe acute respiratory syndrome coronavirus 2 (SARS-CoV-2) developed by Pfizer/BioNTech and Moderna in the U.S. (Anand and Stahel, 2021). As a good gene carrier, HA could be a good candidate for non-viral vector (Tram Do et al., 2012). HA as non-viral vectors have several advantages over viral vectors, such as easy to prepare and scale-up, more flexible with DNA or RNA size and not likely to elicit specific unexpected immune response (Schmidt-Wolf and Schmidt-Wolf, 2003).

1.3.3.3 Implant Coatings

Another application of HA is to coat a thin layer over orthopedic implants (Reyes et al., 2007). Due to the distinct biocompatibility of HA, orthopedic implants with HA coatings can be inserted into body without worrying about immune response, which can provide long time bone alignment (Goodman et al., 2013). Meanwhile, many studies have investigated different types of ionic substituted HA in order to better

mimic the human bone mineral composite and stabilize implants inside the body. Moreover, by modifying the types and amount of substituted ions, it is possible to modify the biological properties of HA, such as biocompatibility, osseointegration and anti-infection functions, which can accelerate the bone healing process as well as provide different therapeutic functions (Goodman et al., 2013).

1.4 Implant Coating Characteristics

Since the bone and cartilage are vulnerable to injury and their recovery could be very long and difficult, replacing or regenerating functions of these tissues by biomaterials have been studied for centuries. The basic physiological requirement for implants that used for hard tissue replacement is the mechanical property that can support the function as load bearing or lubrication in joints. Hence, most of orthopedic implants were composed of pure and/or alloy form of metals such as steel, cobalt-chrome and titanium. However, the bioinert property of metallic implants normally generate slow osseointegration process, which can delay or impair the healing progress and result in a non-union of the bone. This problem is even more serious in elder population due to the much slower proliferation and differentiation rates of bone cells (Li et al., 2009b).

Therefore, in order to promote the bone healing process and prolong the anchoring

time of implants inside human body, a complex series of biological functions are required, such as bioactivity, biocompatibility, biostability, osseointegration, osteoconduction, osteoinduction and therapeutic capability (Al-Amin et al., 2020). Research to improve the biological functions of implants is an ongoing topic. Various factors of biomaterials such as surface topography, heterogeneity, chemical and physical properties directly affect the outcome biological functions (Raghavendra et al., 2017).

1.4.1 Biocompatibility

In clinical field, a big challenge involved in implantation is foreign body reaction, which severely restricts the implants clinical performance (Reyes et al., 2007). After insertion into human body, the surface properties of implants directly affect the cellular and host responses. Thus, an important research target is to enhance the surface compatibility of implants with bones, which could reduce the fibrous encapsulation and inflammatory response to implants (Moura et al., 2010). Biocompatibility is a very important property of implants, which guarantees their prolonged usage in the human body. Biocompatibility is the most commonly used term to describe the ability of a material to perform its desired function without eliciting detrimental local or systemic responses in the body (Manam et al., 2017).

Since the human immune response is very complicated, a large number of in vitro tests and clinical trials were needed to verify their biocompatibility. A general requirement for biocompatible materials is capacity to coexist with human tissue without triggering damages to the body system. More specifically saying, it can not cause any negative effect on the human body system, including all adverse effects of biomaterials on all involved host surroundings, such as ionic composition of body fluids and plasma, bones and soft tissues (Navarro et al., 2008, Geetha et al., 2009, Patel and Gohil, 2012). However, no material is completely inert in human body considering the long insertion period. Thus, the development of biomaterials in practice are more focused on non-toxic or almost-inert materials as well as those are found as trace elements in human body (Manam et al., 2017). This raises another direction of biomaterial development that materials can release therapeutic ions or drugs to promote bone healing or other compounds without triggering unwanted reactions also can be considered as biocompatible materials, so called bioactive materials. Bioactive materials have been widely accepted by modern medicine due to their ability to promote high osteointegration with adjacent tissues (Manam et al., 2017).

1.4.2 Osseointegration

A biocompatible implant coating should be able to provide high osteoconductivity

(Reyes et al., 2007). Osteoconductivity is a prerequisite for osseointegration. Osteoconductivity refers to the ability in promoting the osteoblast growth on implant surfaces and forms implant-to-bone contact, which further contributes to the implant osseointegration and stability for long-term anchoring of implants (Reyes et al., 2007). Nowadays, the term osseointegration is applied to all biomaterials such as polymers, bioactive glass, bioceramics and other materials that have the ability to integrate to living bone tissues (Guglielmotti et al., 2019). It is a standard requirement for designing biomaterials aiming to incorporate into living system and facilitate the regeneration of tissues or tissue functions (Albrektsson and Wennerberg, 2019, Guglielmotti et al., 2019).

Since 1950's, Brånemark first tried the direct anchorage of metallic implants to bones at the resolution level of the light microscope and coined the term osseointegration as a direct connection between implants and living bones (Brånemark et al., 1977, Albrektsson and Wennerberg, 2019). Over the next 40 years, titanium was considered as a bioinert, high-corrosion-resistant and osteoconductive element suitable for fabricating orthopaedic implants. However, in 1990's, Donath first demonstrated that the osseointegration of such widely utilized metallic implants could actually cause a foreign body reaction (Donath et al., 1992). Afterwards, many researches have also indicated titanium was actually not totally bioinert but can induce immune responses

and further protect nearby tissues by forming a dense layer of bone tissue (Albrektsson et al., 2014). Therefore, the term of osseointegration also involves the foreign body reaction that forms interfacial bone that isolate the implant from the host tissues (Jacobsson et al., 2017).

Currently, the orthopedic implant surface treatment is focusing on employing bioceramics as implant coating to provide osteointegration. The most common artificial implant coating bioceramics is CaP, which normally applied as a thin layer on the implant surfaces providing good biocompatibility and osteoconductivity. After the insertion of implants into the human body, the body fluid could directly contact the implant surface and the pH value at the surrounding area of implant surface would decrease subsequently, which leads to the partial dissolution of the coating materials and consequently induce the calcium and phosphate ions releasing. These free ions would reprecipitate afterwards and absorbed by the collagen matrix and further stimulate chemotaxis to guide the adhesion of cells to the surface (von der Mark and Park, 2013).

1.4.3 Anti-infection Abilities

Orthopedic implants may also suffer from infections after the implantation, which can

easily cause medical implant failures (Bishop et al., 2012). A prophylactic antibacterial regimen is required to minimize infections after the implantation surgery (Edmiston et al., 2006). Moreover, in the clinical field, revision or second surgery sometimes are required, which makes the long-term release of antibacterial agents in implant coating became a decisive property (Page et al., 2009). Therefore, many studies have put their efforts into the development of robust and stable antibacterial coatings. Different types of antibacterial implant coatings have been designed to inhibit the bacterial colonization on the surface and further restrict the spreading of infections (Zhao et al., 2009, Bishop et al., 2012, Salwiczek et al., 2014).

Current release profiles of antibacterial coatings that simply anchor antibacterial agents in porous structure of coating layers or between different coating layers would produce a first burst release followed by a declining release. However, as an implanted device, the coating material should sustain their antibacterial ability until fully integration with the surrounding tissues (Šupová, 2015). To overcome this limitation, many alternative strategies have been introduced to enhance the performance of composited antibacterial agents in coating layers. Several nontraditional antibacterial agents, such as carbon nanotubes, metal and metal oxide nanoparticles and metal ions releasing nanomaterials, have been explored. It was demonstrated that the metal ion-releasing nanomaterials can inhibit many of gram-positive and gram-negative bacteria

due to their excellent physicochemical and inherent antibacterial properties (Kadiyala, 2018). Moreover, the antibacterial metal ions can be constituted as an integral part of the HA coatings by substituting one of the charged species (Šupová, 2015).

1.4.4 Anti-biofilm Formation Abilities

Naturally, microorganism including pathogenic bacteria does not exist freely in bulk solution. Instead, most of time bacteria prefer to exist as a unit attached to a surface, which is known as biofilm (Berlanga et al., 2014, Souza, 2014). Biofilm is a sessile community of bacteria that attach to each other or to a substrate and embedded in adhesive extracellular polymeric substances (EPS) produced by themselves (Nicolau Korres et al., 2013, Aggarwal et al., 2015). With a suitable condition, nearly all bacteria species can adhere to both biotic and abiotic surfaces (Marinho et al., 2013, Zameer, 2016). The microstructure of biofilm can be a simple structure with a single layer of microcolonies or can be complex structures with vertical and horizontal channels support the nutrient uptake and waste dispersion (Wilking et al., 2013).

Many chronic bacterial infections were caused by bacterial biofilm (Donlan and Costerton, 2002). The biofilm on the surface of an indwelling medical device by human pathogens can cause serious damages via triggering human immune response.

Bacterial cells inside the biofilm are fundamentally different from the suspended cells. Biofilm can provide greater resistance to antimicrobial agents due to the specific structure of biofilm that prohibit the penetration of antibacterial agents through the biofilm, which makes bacteria cells inside the biofilms become less sensitive to antibiotics (Costerton, 2005, Nan et al., 2016).

Therefore, it is desirable to develop a coating material for indwelling medical devices that could kill bacteria and inhibit the biofilm formation. Many approaches have been developed to prevent and treat the biofilm related infections. Chemistry methods have been used to treat bacterial infections for a long time, but the bacterial biofilm could protect against these chemical materials and mask the underlying chemical functionality by secreting surfactants. Moreover, chemistry-based methods have their own demerits such as antibiotics resistance and chemical based complications (Mah, 2001). Hence, it is important to create persistently bacteria-resistant materials that can disrupt the formation of bacterial biofilms. The anti-biofilm formation abilities of many metal materials have been confirmed. For example, silver nanoparticles have shown more than 95% inhibition in biofilm formation when treating *P. aeruginosa* and *S. epidermidis* for 24h (Kalishwaralal et al., 2010).

1.5 Ionic Substituted HA

Currently, it is hard to find a material that naturally match all required characteristics of implant coatings. A strategy with great potential is employ HA as a platform and substitute different ions into its lattice structure for different biological functions such as enhancing the biocompatibility and osseointegration or introducing antibacterial and anti-biofilm formation abilities.

The natural mineral phase of human bones is not stoichiometric HA but substituted by a variety of cations and anions (Table 1-2). According to the basic biomimetic principle, a fabricated biomaterial should be as close as possible to the host tissue (Boanini et al., 2010). The formula of substituted HA is $Ca_{10-x}\alpha_x(PO_4)_{6-y}\beta_y(OH)_2\theta_z$, which can form three groups of substitution, including group (1) that Ca^{2+} can be replaced by cations (α) such as Na^+, Mg^{2+}, Zn^{2+}, Sr^{2+}, Cu^{2+}, $Fe^{2/3+}$ and Mn^{2+}, group (2) that PO_4^{3-} can be replaced by anion groups (β) such as CO_3^{2-}, $SiO_4^{4-}$and SeO_3^{2-}, and group (3) that OH^- can be replaced by anion groups (θ) such as CO_3^{2-}, F^- and Cl^-. Substitution of (Ca^{2+}), (PO_4^{3-}) or (OH^-) groups in the HA structure can change their morphologies, lattice parameters and solubilities without altering the hexagonal symmetry.

Table 1-2 Chemical composition of HA, bone, dentin and enamel

Composition (wt%)	HA	Bone	Dentin	Enamel
Calcium (Ca)	39.6	34.8	35.1	36.5
Phosphorus (P)	18.5	15.2	16.9	17.7
Carbonate (CO_3)	0	7.4	5.6	3.5
Magnesium (Mg)	0	0.72	1.23	0.44
Chloride (Cl)	0	0.13	0.01	0.3
Sodium (Na)	0	0.9	0.6	0.5
Potassium (P)	0	0.03	0.05	0.08
Fluoride (F)	0	0.03	0.06	0.01

This table is adapted with permission from Elsevier (Dorozhkin and Epple, 2002).

Promoting the osteogenesis via enhancing the osteoconductivity is one of the aims in substituted HA studies. For instance, many studies have introduced the mineral ions in human bones, such as CO_3^{2-} and SiO_4^{4-}, into HA and increased the degradation rates and bioactivity of HA (Spence et al., 2009). The substitution of silicate groups into the HA has enhanced both in vitro and in vivo bioactivities (Patel, 2002, Patel, 2005, Henstock et al., 2015). Silicate substituted HA (SiHA) has a more negative surface charge than pure HA, which contributes to higher bone formation (Botelho, 2002). Mg substituted HA (MgHA) has enhanced the osteoconductivity of HA by promoting the differentiation and proliferation of osteoblast cells (Zhao et al., 2013). Both Sr and Zn substituted HA (SrHA and ZnHA) can stimulate cellular proliferation and differentiation of human osteoblast cells (Lin et al., 2013, Ratnayake et al., 2017).

Recently, another direction of substituted HA study has moved to the incorporation of

therapeutic functions for medical purposes, such as introducing magnetic properties to HA as a drug delivery agent, magnetic resonance imaging (MRI) contrast agent and hyperthermia therapy heat mediator as well as anti-infection properties to avoid implant failure (Wu et al., 2007a, Getzlaf et al., 2016). For example, iron substituted HA (FeHA) and manganese substituted HA (MnHA) have been well studied for their magnetic properties and good biocompatibilities (Li et al., 2012). Copper substituted HA (CuHA) and zinc substituted HA (ZnHA) have attracted more attentions due to their antibacterial abilities. The released Cu^{2+} and Zn^{2+} ions can bind to bacterial cell membrane and destroy their cellular structures, which may significantly inhibit the adhesion and surface growth of bacteria and make them good candidates for antibacterial implant coating materials (Radovanović et al., 2014, Yang et al., 2017).

1.5.1 Antimicrobial Ionic Substituted HA

The microbial infection has become the biggest threat to public health. From a historical perspective, many researchers have devoted their efforts to develop either bactericidal or bacteriostatic antimicrobial materials. Antimicrobial materials are widely used in medical, industrial, environmental and cosmetic fields, such as wound dressing, surgical devices, drug delivery system, antibacterial packaging and water disinfection (Ji et al., 2016).

Antimicrobial agents are group of materials that fight against pathogenic microorganisms and can be classified into organic antimicrobial materials, inorganic antimicrobial materials, metal and metal oxide nanoparticles, chemicals, antibiotic drugs and other different substrate materials contain antimicrobial substances. Organic antimicrobial materials include quaternary ammonium salt, the halide amine and the chitosan (Mo et al., 2014), while inorganic antimicrobial materials often refer to metal ions such as Ag^{+}, Cu^{2+} and Zn^{2+}. Metal and metal oxide nanoparticles include Ag, Al_2O_3, Au, CeO_2, Cu2O, CuO, MgO, Fe_3O_4/Fe_2O_3, MgO, MnO_2, TiO_2 and ZnO (Vargas-Reus et al., 2012, Slavin et al., 2017, Naseem and Durrani, 2021). The chemical antimicrobial agents are often irritating and toxic and can only be operative for short-term. The usage of traditional antibiotics can lead to the issue of antibiotic resistance and makes it extremely difficult to treat the infection (Buffet-Bataillon et al., 2012, Cheong et al., 2017). Evidence has indicated that more than 70% of bacterial infections are resistant to one or more antibiotics that are generally used (Allahverdiyev, 2011). It is very important to develop new and effective antimicrobial agents to overcome the antibiotic resistance and improve the current antimicrobial therapies. Hence, the recent investigations are targeted toward safe and long-term biocidal materials (Yadav et al., 2016). The antimicrobial metal/metal-oxide nanoparticles have been widely investigated due to their excellent anti-infection ability and long-term inhibition against microorganisms (Ren et al., 2009b, Vargas-Reus et al., 2012), although the

mechanism of antimicrobial metallic materials is not completely clear. A common agreement on the mechanism of positively charged antimicrobial nanoparticles is based on the disruption and destructive to the bacterial cell membrane, which can lead the cell content leakage and finally cause the cell death (Figure 1-3)(Altun et al., 2019). Moreover, antimicrobial metallic materials are known to be able to inactivate DNA or RNA replication and denature proteins by binding to functional groups of proteins, which could cause structural changes or degradation of cellular proteins and finally lead to the cell death (Li et al., 2011).

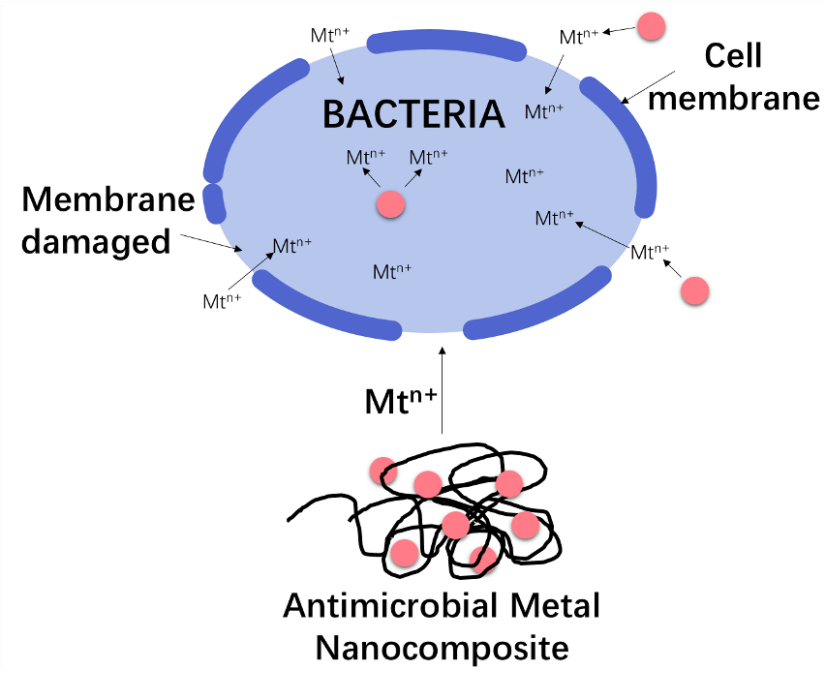

Figure 1-3 Antibacterial mechanism of antimicrobial metal nanocomposites
'Mt' represents 'metal'. Figure re-drawn with permission from Elsevier (Dizaj et al., 2014)

A promising strategy to balance the good antimicrobial ability of metallic materials and high biocompatibility is introducing these antimicrobial metal ions into HA nanoparticles (Gopi et al., 2014a, Gopi et al., 2014b, Mocanu et al., 2014). The antimicrobial abilities of metallic ions substituted HA (MHA) are mainly caused by the continuous release of metallic ions. After the insertion of implants coated with the antimicrobial MHA into the human body, the physiological fluid can directly contact the implant surface, where the pH value would decrease subsequently leading to partial dissolution of the MHA coatings and release of the antimicrobial metallic ions (von der Mark and Park, 2013).

The antimicrobial abilities of different MHA have been well studied (Table 1-3). Among these metal ions, the three most effective metal ions are Ag^{+}, Cu^{2+} and Zn^{2+} (Stanić et al., 2010, Stanić et al., 2011, Thian et al., 2013, Morad et al., 2016). The AgHA has been confirmed as the strongest antimicrobial MHA, while CuHA and ZnHA also produce strong antimicrobial abilities. The great antimicrobial and anti-inflammatory properties of silver and silver-based nanoparticles make them excellent candidates for many applications in medical fields (Yang et al., 2010), but they still have drawbacks due to nanotoxicity (Prabhu and Poulose, 2012). It has been indicated that silver nanoparticles can promote the reactive oxygen species (ROS), cause DNA damage and trigger apoptosis in human cells, which can further lead to adverse effects on human,

such as skin, liver, lung, brain kidney and vascular system damages and untoward changes in blood cells (Panyala, 2008, Ahamed et al., 2010, Yang et al., 2010, Prabhu and Poulose, 2012). Another problem is Ag has the potential to accumulate in human body and cannot be metabolized. Ag accumulation was reported in rat organs including kidney, liver, spleen, brain and lung (Ahamed et al., 2010). To solve this problem, alternative metal ions such as Cu^{2+} and Zn^{2+} have been considered as good candidates in antimicrobial medical field.

Table 1-3 Antimicrobial abilities of metal ions substituted HA

Substitution	Empirical formula	Substitution level	Duration	The percentage of microorganism reduction (R)		
				E. coli (G-)	*S. aureus* (G+)	*C. Albicans* (Fungi)
AgHA [1]	$Ca_{10-x}Ag_x(PO_4)_6(OH)_2$	X_{Ag}=0.004	2h	100%	99.7%	99.8%
		X_{Ag}=0.0004		99.9%	99.3%	99.1%
CuHA [2]	$Ca_{10-x}Cu_x(PO_4)_6(OH)_2$	X_{Cu}=0.004	2h	98.5%	97.7%	98.9%
		X_{Cu}=0.0004		97.2%	97.2%	92.4%
ZnHA [3]	$Ca_{10-x}Zn_x(PO_4)_6(OH)_2$	X_{Zn}=0.004	2h	98.6%	97.7%	87.9%
		X_{Zn}=0.0004		97.6%	97.5%	79.8%
CoHA [4]	$Ca_{10-x}Co_x(PO_4)_6(OH)_2$	X_{Co}=0.091	24h	N/A	93.6%	N/A
		X_{Co}=0.018			70.9%	
TiHA [5]	$Ca_{10-x}Ti_x(PO_4)_6(OH)_2$	X_{Ti}=0.28	24h	78.9%	N/A	N/A
		X_{Ti}=0.028		65.6%		

- The MHA nanoparticles concentration in antimicrobial tests was 10mg/mL.
- $X_{(Metal)}$=Metal(mol)/[Metal(mol) + Ca(mol)];
- "N/A": no test has been done.

[1]:(Stanić et al., 2011, Morad et al., 2016), [2]: (Stanić et al., 2010), [3]: (Thian et al., 2013), [4]: (Tank et al., 2013), [5]: (Kim, 1998, Li et al., 2010b, Stanić et al., 2010, Thian et al., 2013, Shanmugam and Gopal, 2014, Hidalgo-Robatto, 2018, Sergi et al., 2018).

Although the bactericidal mechanism of CuHA and ZnHA are still not well understood,

both of them are considered to be highly reactive on bacteria. The antibacterial mechanisms of Cu^{2+} and Zn^{2+} are mostly considered as binding to proteins on the bacterial cell wall by reacting with the sulfur- or phosphorus-containing proteins to destroy the cell membrane and further cause the release of cell content (Li et al., 2010b, El-Sherif and Eldebss, 2011, Thian et al., 2013, Mocanu et al., 2014, Shanmugam and Gopal, 2014, Huang et al., 2015). Another explanation is Cu^{2+} and Zn^{2+} can bind to bacterial DNA and RNA, and thus further prohibiting the bacterial replication (Heinlaan et al., 2008, Bondarenko et al., 2012). Cu^{2+} and Zn^{2+} have also been indicated to be able to attack the respiratory chain, which could lead to cell distortion and finally result in cell death (Culotta et al., 2006).

Cu is an essential trace element for human, which could stimulate several enzyme activities and contribute to the cross-linking of collage and elastin of bones (Gür et al., 2002). CuHA has been indicated as a safe material for implant coating. Huang et al. has claimed the CuHA has no cytotoxicity at a low substitution level (X_{Cu}=0.0127), where a strong antimicrobial effect could be achieved (Huang et al., 2014). CuHA can inhibit gram-positive, gram-negative bacteria and yeast, mainly via undermining outer cell membrane of pathogens, changing the cell permeability and releasing the cell contents (Huang et al., 2014, Huang et al., 2015).

The antibacterial ability of CuHA corresponding to X_{Cu} values can be plotted out according to many previous antibacterial studies (Figure 1-4). Li et al. have indicated antibacterial properties of CuHA with different metallic contents (X_{Cu}= 0.0099, 0.0476, 0.09 and 0.13), but they also indicated the cytotoxicity of all tested CuHA against human fetal osteoblast cells (Li et al., 2010b). Later on, Huang et al. have indicated a 76.9 % killing ratio of CuHA (X_{Cu}=0.056) against *E. coli* when coated on a titanium substrate (Huang et al., 2014). They have suggested CuHA at X_{Cu}=0.056 has no cytotoxicity in the MTT test based on osteoblast-like MC3T3-E1 cells, which is contradictory to Li et al.'s results. Most recently, Hidalgo et al. synthesized CuHA with Cu content ranging from X_{Cu}=0.025 to X_{Cu}=0.1 and tested their anti-biofilm formation abilities and cytotoxicity. They found CuHA significantly reduced the biofilm of *E. coli* and *S. aureus* and claimed there was no cytotoxicity against pre-osteoblast cell (MC3T3-E1) (Hidalgo-Robatto, 2018).

Zn is another important essential trace element in human body, which could stimulate the osteoblastic cells proliferation and is involved in many hormones and enzymes activities (Chen et al., 2014). ZnHA is well known for its ability in stimulating the osteoblast activity and inhibiting the osteoclast differentiation that finally promote the growth and development of skeletal system (Ito, 2000, Thian et al., 2013). Several studies have confirmed the good antibacterial abilities of ZnHA against gram-positive,

gram-negative bacteria and fungi (Chung et al., 2006, Stanić et al., 2010, Anwar, 2016). The released Zn^{2+} from ZnHA can generate ROS and bind to membrane proteins of bacteria to destroy their cellular structures (Szuster-Ciesielska et al., 2000, Song et al., 2010). Kim et al. was the first group that compared the antibacterial abilities of ZnHA and CuHA. They tested three different levels of metallic contents ranges from X_M=0.0005 to X_M=0.05 and indicated the ZnHA has a stronger antibacterial ability than CuHA (Kim, 1998). Stanić et al. also indicated ZnHA exhibited a stronger killing ability against *E. coli* and *S. aureus* compared to CuHA at a very low metallic content (X_M=0.0004 and 0.004) (Stanić et al., 2010). However, with a higher metallic content, ZnHA starts to show a lower antibacterial ability than CuHA. For example, Hidalgo et al. indicated the antibacterial and anti-biofilm formation abilities of ZnHA is lower than CuHA at the range of X_{Cu}=0.025 to 0.1 (Figure 1-4) (Hidalgo-Robatto, 2018).

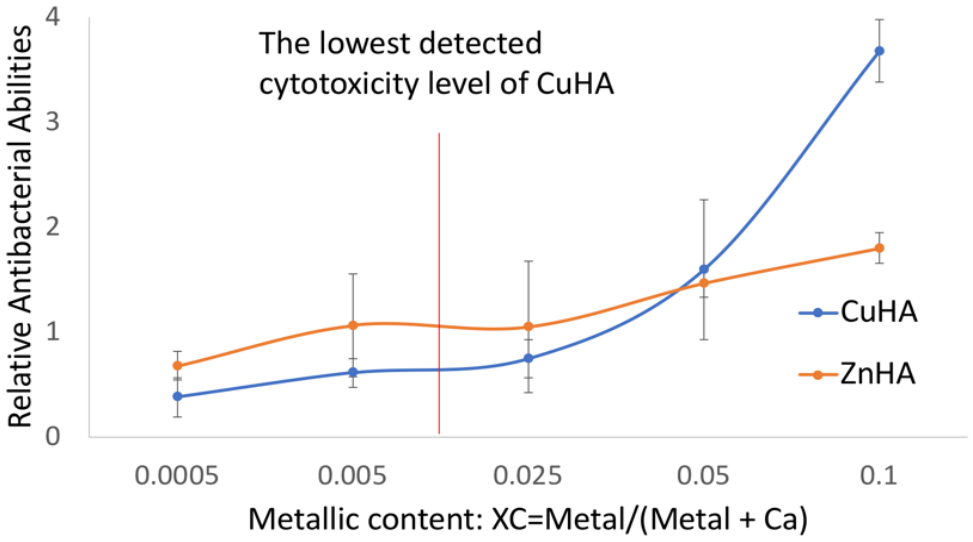

Figure 1-4 Previous studies based on the biological properties of CuHA and ZnHA. With a higher metallic content, CuHA normally has a higher antibacterial ability than ZnHA, while with a low metallic content, ZnHA has shown a stronger antibacterial ability than CuHA (Kim, 1998, Li et al., 2010b, Stanić et al., 2010, Thian et al., 2013, Shanmugam and Gopal, 2014, Hidalgo-Robatto, 2018, Sergi et al., 2018).

1.5.2 Magnetic Ionic Substituted HA

Many magnetic nanoparticles have been well developed for biological applications that act as drug delivery agent, magnetic hyperthermia therapy agent and medical imaging contrast agent (Hussain et al., 2006, Ito et al., 2006, Thorek et al., 2006). For instance, magnetic nanoparticles have the potential to precisely deliver anti-inflammatory drugs to the exact area of inflammation, which could reduce the drug dosage, eliminate side effect and increase therapeutic effect (Gupta and Gupta, 2005).

Magnetite ferrite-based IONPs (γ-Fe_2O_3 or Fe_3O_4) is the most widely studied magnetic nanoparticle due to their high magnetic susceptibility (Jordan et al., 2001). The low biocompatibility of IONPs restricted their biological applications. The uptake of IONPs leads to the intracellular unbound iron and result in cell death (Smaniotto et al., 2005). Many strategies were delivered to enhance the biocompatibility of IONPs. For example, a previous study has constructed IONPs with a biocompatible shell of poly (lactic-co-glycolic acid) (PLGA) that successfully increased the biocompatibility of IONPs. However, such a core-shell like structure is relatively unstable, the break of outside polymeric materials will expose the central IONPs (Hajikarimi et al., 2014). Although an alternative strategy such as ferrimagnetic bioglass ceramics (FBCs) for MRI and hyperthermia purposes has been developed, the ultra-high preparing temperature (800 ℃) and complex quenching process can cause crystal growth that prevent the formation of nano-sized particles and restricted their applications (Takegami et al., 1998, Arcos et al., 2003, Leventouri et al., 2005). Another alternative method is to substitute magnetic ions into biocompatible biomaterial, such as HA, to combine the magnetic property and biocompatibility. For example, FeHA nanoparticles with ferromagnetic or superparamagnetic properties have been synthesized and confirmed to have a good biocompatibility in enhancing the osteoblast adhesion (Wu et al., 2007a, Li et al., 2012).

To understand the magnetic property of Fe and Mn, the first is to understand the interactions of materials in magnetic fields, which were classified as diamagnetism and paramagnetism (Carlin, 2012). Diamagnetism is a quantum mechanical effect that occurs in all materials. It only makes negligible response to a magnetic field. Compounds such as HA that have all the electrons were paired up only have diamagnetism to magnetism. The response of the other forms of magnetism such as ferromagnetism or paramagnetism are much stronger to a magnetic field. A material at least one electron is not paired with another is paramagnetism (Martín‐Hernández and Ferré, 2007). When placing this material into a magnetic field, the interaction tends to attract the materials into the field. Ferromagnetism happens when all individual atoms in a crystalline material are paramagnetic and the spin vector are aligned parallel to each other to maintain a lowered-energy state, which spontaneously parallelly line up the magnetic moments of the electrons even in the absence of an applied field (Martín‐Hernández and Ferré, 2007). The magnetic properties of Fe and Mn were related to the spin and orbital angular momentum of the contained electrons. Both Fe and Mn belong to the group of transition metals, which can be simply defined as elements with partially filled d sub-shell, which leads to the paramagnetism (Figgis and Lewis, 1960). The magnitude of the paramagnetism is reflected as the magnetic susceptibilities. Magnetic susceptibility represents the strength of an interaction when a substance is placed into a magnetic field. The

magnetic susceptibilities of different transition metal ions were well-studied. Fe^{2+} has 4 unpaired electrons, and the observed magnetic moment is 5.1-5.7 μ_B. Both Mn^{2+} and Fe^{3+} have 5 unpaired electrons, their observed magnetic moments are 5.65-6.10 μ_B and 5.7-6.0 μ_B respectively (Figgis and Lewis, 1960).

Many studies have investigated the magnetic susceptibilities of FeHA and MnHA. The magnetic susceptibilities of Both Fe-HA and MnHA nanoparticles were increased with the increase of Fe and Mn content (Li et al., 2009b, Li et al., 2012, Zilm et al., 2018). A study compared the magnetic susceptibilities of Mn^{2+} and Fe^{2+} substituted HA and indicated the magnetic moment of MnHA (X_M=0.062) was 5.51 μB, while the magnetic moment of the Fe^{2+}HA (X_M=0.062) sample was 3.44 μB (Zilm et al., 2018). Therefore, in order to achieve a higher magnetic property, Fe^{3+} is more suitable to be substitution into HA than Fe^{2+}.

Besides the magnetic property, FeHA also has a good biocompatibility. It has a great potential to be incorporated to specific sites and targeting nidus such as tumor owing to the good magnetic-induced thermal property that can rapidly raise the temperature from 25℃ to 40℃ in 60 s, which makes it a good candidate as a heating mediator in hyperthermia therapy for cancer treatment (Tampieri et al., 2012). For example, a mouse in vivo test has successfully achieved a dramatic reduction of tumor size for

48.5% after the injection of FeHA nanoparticles into the tumor sites after 3 days (Hou et al., 2009). Previous studies have indicated the cell proliferation in a Fe^{3+}HA (X_{Fe}=0.052) was even twice more than pure HA (Li et al., 2009b, Li et al., 2012). The addition of Fe^{3+} ions increased the negative charge of nanoparticles and lead to a higher osteoblast cells adhesion than HA (Li et al., 2012). Manganese is also a key trace element in human body, which is crucial for protein synthesis and nucleic acid synthesis (Bellof et al., 2007, Aaseth et al., 2012, Parker-Esquivel et al., 2012). It was indicated that both cartilage and subchondral bone regeneration were induced by Mn^{2+} in Mn-TCP tissue engineering scaffolds (Zilm et al., 2018). MnHA has shown good potential in promoting the cell adhesion via enhancing the ligand binding affinity (Mayer et al., 2003). A 7-day cell proliferation test confirmed the MnHA (X_{Mn}=0.04) has 27% more cells than MnHA (X_{Mn}=0.01), which reveals the addition of Mn ions has positive effects to the biocompatibilities (Li et al., 2012).

Alternative magnetic substituted HAs such as selenium (Se) HA and cobalt (Co) HA have also been investigated. Co can replace Ca sites in HA and Se can replace the phosphate site. The CoHA has been investigated on their potential to act as a contrast agent in MRI, while SeHA nanoparticles have been well studied for their anti-cancer ability (Yanhua et al., 2016, Lin et al., 2019). However, both CoHA and SeHA have the safety concerns due to their relatively lower biocompatibility (Jiang et al., 2020).

Therefore, FeHA and MnHA were considered to have a greater potential in implantable medical applications.

1.5.3 Multi-ionic substituted HA

Based on the knowledge of mono-ionic substitutions, recent studies are more interested in developing multi-ionic co-substituted HA, which provides add-on or enhanced biological functions of HA to extend their applications. Co-substitution of different ions into HA has the potential to gain both benefits of different elements and improve their biological performance such as antibacterial abilities and biocompatibilities (Table 1-4) (Gopi et al., 2014a, Kaygili and Keser, 2015). It has been confirmed that the biological properties of many multi-ionic substituted HA can better mimic the native bioapatites compare to mono-ionic substituted HA (Zhang et al., 2014a, Chen et al., 2016, Geng et al., 2016). For example, the co-substitution of Mg^{2+} and CO_3^{2-} into HA (Mg-CHA) has enhanced the adhesion, proliferation and metabolic activations of both mesenchymal stem cells (MSCs) and human osteoblast like cells (MG-63) (Landi et al., 2006).

Another advantage of co-substitution in HA is the potential in producing relatively high phase purity without secondary phases or metal oxide, so that it can enhance the

biocompatibility as well as additional biological functions. According to many studies on the CuHA and ZnHA, there is a common phenomenon that the total amount of metallic content that could be substituted into HA lattice structure is limited. For example, Li et al. observed a second phase of CuO in XRD pattern when Cu ions reached X_{Cu}=0.1 (Li et al., 2010b). Shanmugam and Gopal noticed the formation of the secondary phase as β-tri calcium phosphate (β-TCP) with the increase of Cu content from X_{Cu}=0.5 to 2.0 in CuHA (Shanmugam and Gopal, 2014). In ZnHA, similar results were observed. Shepherd and Best have synthesized ZnHA with metallic contents range from X_{Zn}=0.003 to X_{Zn}=0.012 and a secondary phase (TCP) appeared in X_{Zn}=0.012 ZnHA samples (Shepherd and Best, 2013). Similarly, Sergi et al. indicated that when the substituted Zn increased to X_{Zn}= 0.1, a secondary phase of α-TCP appeared (Sergi et al., 2018).

Table 1-4 Biological tests of multi metallic ions co-substituted HA

	Empirical formula	Biological test (Control: HA)
Mg/CHA [1]	$Ca_{10-x}Mg^{2+}_x(PO_4)_6(OH)_{2-y}(CO_3)^{2-}_y$	MG63: **P**↑/**D**↓(ALP); MSCs: **P**↑/**D**↓(ALP)
Sr/CHA [2]	$Ca_{10-x}Sr^{2+}_x(PO_4)_6(OH)_{2-y}(CO_3)^{2-}_y$	MC3T3-E1: **P**↑; Cell membrane integrity: ↑
Mg/AgHA [3]	$Ca_{10-x-y}Mg^{2+}_xAg^{+}_y(PO_4)_6(OH)_2$	MG63: **P**↑; **AA**: ↑(Control: HA, *E. coli*)
Mg/SrHA [4]	$Ca_{10-x-y}Mg^{2+}_xSr^{2+}_y(PO_4)_6(OH)_2$	MG63: **A**↑/**P**↑/**D**↑(ALP)
F/MgHA [5]	$Ca_{10-x}Mg^{2+}_x(PO_4)_6(OH)_{2-y}F^{-}_y$	MG63; **P**↑/**D**↑(ALP)
F/SrHA [6]	$Ca_{10-x}Sr^{2+}_x(PO_4)_6(OH)_{2-y}F^{-}_y$	MC3T3-E1: **P**↑
Sr/CeHA [7]	$Ca_{10-x-y}Sr^{2+}_xCe^{3+}_y(PO_4)_6(OH)_2$	**AA**: ↓(Control: CeHA, *E. coli* & *S. aureus*)
Sr/CuHA [8]	$Ca_{10-x-y}Sr^{2+}_xCu^{2+}_y(PO_4)_6(OH)_2$	MG63: **P**↑/**D** ↑ (ALP)
		AA: ↑ (Control: HA, *E. coli*)
Cu/ZnHA [9]	$Ca_{10-x-y}Cu^{2+}_xZn^{2+}_y(PO_4)_6(OH)_2$	MC3T3-E1: **P**Ø
		AA: ↑(Control: HA, *E. coli* & *S. aureus*)

Biocompatibility tests: "**A**": cell adhesion; "**P**": cell proliferation "**D**": Cell differentiation; **ALP**: Alkaline.
Antibacterial ability tests: **AA**: Antibacterial ability.
"↑": positive effects; "↓": negative effects, "Ø" no effect
[1]: (Landi et al., 2006), [2]: (Valiense et al., 2016), [3]: (Gopi et al., 2014b), [4]: (Jaworek and Sobczyk, 2008, Geng et al., 2016, Morad et al., 2016), [5]: (Jaworek and Sobczyk, 2008, Cai, 2010), [6]: (Huang et al., 2013b), [7]:(Gopi et al., 2014a),

Moreover, the co-substitution of specific metallic ions can enhance the releasing rate of metallic ions, which may improve their biological performance (Lim et al., 2012, Huang et al., 2016a). For example, when Mn^{2+} ions were co-substituted with Ag^{+} or Sr^{2+} into HA, a relatively higher ion exchange rate was observed, which significantly contributed to their biocompatibility (Huang et al., 2016a, Huang et al., 2018). When Fe^{3+} co-substituted with Co^{2+} and Sr^{2+}, a higher ionic activity and increased apatite formation rate were observed in in vitro bioactive tests (Ullah et al., 2018, Pasandideh et al., 2020).

The lattice structure of HA has two kinds of Ca^{2+} sites (I and II) that can be replaced by different cations (Kaygili and Keser, 2015, Geng et al., 2016). Both experimental and computational studies have investigated the potential substitution sites of different cations, including Cd^{2+}, Cu^{2+}, Pb^{2+}, Sr^{2+} and Zn^{2+}. It has been shown that a high dopant concentration is energetically favorable to substitute Ca^{2+} at the Ca(II) site, while at a low dopant concentration, the Ca(I) site is energetically preferred, which can affect the releasing rate of doped metallic ions (Badraoui et al., 2002, Ellis et al., 2006, Tamm and Peld, 2006, Bigi et al., 2007). For example, Radovanović et al. indicated that due to the different ionic radii of Cu^{2+} and Ag^{+}, although both Ag^{+} and Cu^{2+} prefer to substitute Ca(I) sites at a low metallic concentration (X_M=0.002 & 0.004), while Cu^{2+} is more likely to retain in HA lattice structure than Ag^{+}. Table 1-5 indicate the ionic radii of different metallic ions comparing to Ca^{2+}. Due to the larger ionic radii, Ag^{+} is relatively harder to be hosted in HA.

Table 1-5 Effective ionic radii in picometre (pm) of elements in function of ionic

Ionic	Ag^{+}	Ca^{2+}	Ce^{3+}	Co^{2+}	Cu^{+}	Fe^{2+}	Fe^{3+}	Mg^{2+}	Mn^{2+}	Sr^{2+}	Ti^{3+}	Zn^{2+}
r(pm)	115	100	102	70	77	70	60	72	70	118	67	74

(Shannon, 1976)

In CuHA, the Ca(II) site is favorable to be substituted by Cu^{2+} at high dopant

concentration (e.g. X_{Cu}=0.1) but Ca(I) site and surface phase of nanoparticles were more preferred with a lower concentration (e.g. X_{Cu}=0.05) (Qu et al., 2014), which reduced the releasing rate of Cu^{2+} (Huang et al., 2014, Radovanović et al., 2014). In ZnHA, atomistic simulations showed the preferred Ca site for Zn^{2+} substitution in HA is Ca(II) site , which could facilitate the uptake and release rate of Zn^{2+} without disrupting the framework of HA (Terra et al., 2002, Tang et al., 2009). The same preference also appeared when Zn^{2+} co-substituted with other cations in HA. Tamm and Peld studied the preferred substitution sites of Cd^{2+} and Zn^{2+} in both mono-substituted HA and Cd-Zn co-substituted HA (Tamm and Peld, 2006). According to the calculated energy differences, both Ca(I) and Ca(II) can be replaced by Cd^{2+} and Zn^{2+} in mono-ionic substitution, but only Ca(II) sites can be replaced in Cd-Zn co-substituted HA. They have suggested that the occupation of Cd^{2+} in a Ca(I) site would create an area that requires much higher energy for Zn^{2+} to replace, which can inhibit the uptake of Zn^{2+}.

1.6 The Synthesis Methods of HA

The resulting biological function of HA is not only affected by the different ions substituted into HA, but also affected by different synthesis methods. Various synthesis methods of HA have been studied in detail during the past decades. In order to modify the desired characteristic of HA, such as crystallinity, particle size, morphology, phase

purity and stoichiometry, many different synthesis methods were designed, which can be classified into dry, wet and high-temperature methods (Figure 1-5) (Sadat-Shojai et al., 2013). Different synthesis methods result in the altering of characteristics of HA, which consequently affect the bioactivity, mechanical and biological properties of HA and finally determine the biomedical applications of HA (Cox et al., 2015).

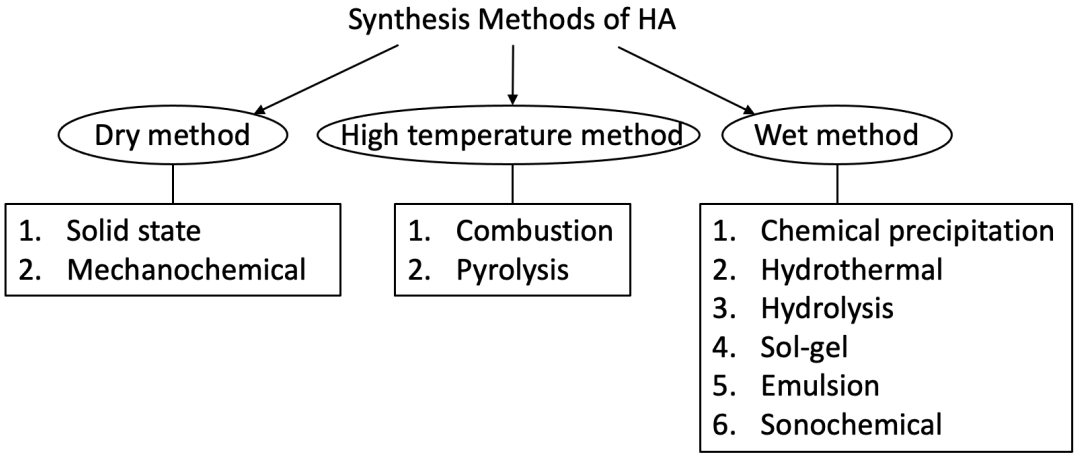

Figure 1-5 Synthesis methods of HA
The major methods in HA synthesis including dry method, high temperature method and wet method.

The dry methods are ideal for the mass production of powders. It can be achieved by mixing the precursor chemicals in a dry form, such as previously prepared CaP salt. There are two different dry methods, including solid-state and mechanochemical methods. The solid-state method is a kind of decomposition reaction that the solid

reactants are heated to produce new solids (Figure 1-6) (Sadat-Shojai et al., 2013). However, due to the requirement of a high temperature (more than 1000 ℃) during the synthesis process and relatively lower phase purity of products, it is unpreferable both scientifically and technologically (Pu'ad et al., 2020). The chemical transformation in a mechanochemical method is achieved via compression, shear or friction (Figure 1-6) (Achar et al., 2017). It utilizes ball- or planetary-milling as well as high speed to compress the precursor chemicals to boost the chemical reaction and transformation (Yeong et al., 2001). However, the mechanochemical method also has problems such as contamination, no control on particle morphology and agglomerates, which makes it not ideal for small amount lab synthesis (Pu'ad et al., 2020).

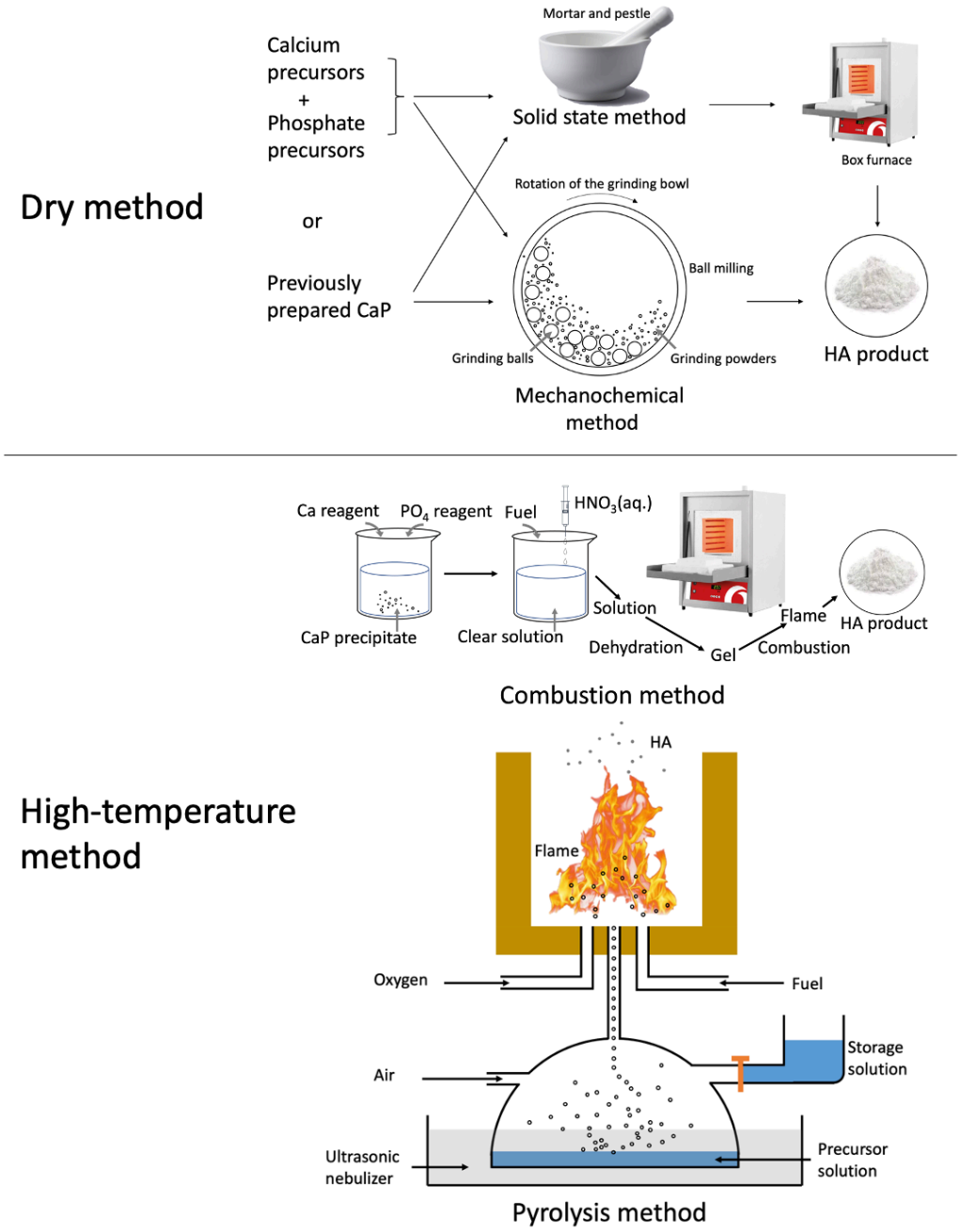

Figure 1-6 Schematic diagram illustrating the dry methods (Solid state method and mechanochemical method) and high-temperature methods (Combustion method and pyrolysis method) in HA synthesis.

Figure re-drawn with permission from Elsevier (Sadat-Shojai et al., 2013).

Another HA synthesis method is the high-temperature method, which utilizes high temperature to decompose the materials. The high-temperature processes, including the combustion and pyrolysis, can avoid unwanted CaP phases and produce HA with good chemical homogeneity and high crystallinity (Nguyen and Byun, 2009). The combustion method is based on self-sustaining redox reaction to achieve very rapid exothermicity followed by a rapid cooling process (Figure 1-6) (Sadat-Shojai et al., 2013). Although the combustion method can produce high crystalline HA, the byproducts make it not suitable for HA synthesis when a high purity was required (Pu'ad et al., 2020).

The other high-temperature method named pyrolysis is a kind of aerosol method, which normally used in gas-to-particle or liquid-to-particle conversions (Figure 1-6) (Itatani et al., 2010). Although pyrolysis method is effective in HA production, it is also restricted by the low purity of produced HA. For example, at a high temperature (usually above 2000 ℃), small amount of HA may decompose into α-TCP. The pyrolysis always forms secondary aggregates and it has poor control over the processing variables (Sadat-Shojai et al., 2013).

The wet methods of HA synthesis, including chemical precipitation, hydrolysis, hydrothermal, sol-gel, emulsion and sonochemical methods, are methods that use

aqueous solutions during the synthesis process. In general, the morphology and size of HA synthesized via wet methods can be easily and precisely controlled, thus they are widely utilized in scientific research. Due to the low processing temperature, the crystallinity of HA produced by wet methods were relatively low and other CaP phases may appear (Sadat-Shojai et al., 2013).

The hydrothermal method mainly utilizes elevated temperature and pressure to stimulate the reaction via employing an autoclave or pressure vessel (Fihri et al., 2017). However, the hydrothermal method requires expensive equipment and has poor capability in controlling the morphology and size of HA nanoparticles (Sadat-Shojai et al., 2013).

The sol-gel method starts with mixing the calcium and phosphorous precursors and then removing the organic residues via using post-heat treatment. The synthesized HA via sol-gel method has stoichiometric structure close to biological apatite with a large surface area, small cluster size and high bioresorbability (Fathi et al., 2008). However, the sol-gel method also produces secondary phase, usually calcium oxide, which is harmful to the biocompatibility of produced HA (Eshtiagh-Hosseini et al., 2007).

Another wet method is hydrolysis, which is least used in the HA synthesis. It is a water

ionization process that diffuse the hydrogen and hydroxide ions, which can transform the CaP precursors such as dicalcium phosphate anhydrous (DCPA), tricalcium phosphate (TCP) and dicalcium hydrogen phosphate dihydrate (DCPD) to a high purity HA (Nakahira et al., 1999, Winkler et al., 2018). In order to complete the transformation of HA, most of hydrolysis methods require very long processing time. Table 1-6 shows the reaction conditions of several studies that utilized hydrolysis method.

Sonochemical method is based on the chemical reactions triggered by ultrasound radiation (Jevtic et al., 2008, Han et al., 2009). The sonochemical method can produce uniform, small and pure crystals with minimal agglomeration (Kuznetsov et al., 2008, Rouhani et al., 2010). The HA can be synthesized after 15-60 min sonication, but the phase purity of HA is very sensitive to the sonication time. It was indicated that a shorter treating time was not sufficient for complete HA formation while longer time resulted in the generation of calcium phosphate phases other than HA (Kuznetsov et al., 2008, Rouhani et al., 2010).

The chemical precipitation method has been selected in this project due to it has the advantages as high-yield, low cost, low manipulation difficulty and high phase purity of the product (Santos et al., 2004). Chemical precipitation is perhaps the most widely

used method for laboratorial synthesis of HA or MHA due to its advantage of high-yield and low cost (Santos et al., 2004). Several crucial processing parameters are needed in the chemical precipitation method (Figure 1-7). As the first stage, the mixing rate of calcium and phosphate containing reagents must be set according to the amount of reagents. The synthesis process requires an accurate molar ratio of the chemical precursor, otherwise it would reduce the phase purity. In the situation of HA synthesis, the molar ratio of elements (Ca/P) must be kept at 1.67 and the chemical reaction is shown in equation (Eq. *(1-1)*):

$$10Ca^{2+} + 6PO_4^{3-} + 2OH^- \rightarrow Ca_{10}(PO_4)_6(OH)_2 \qquad (1\text{-}1)$$

HA morphologies could be directly affected by reaction parameters. For example, a typical mixing procedure is the dropwise addition of one reagent into another with continuous stirring. A faster mixing rate would reduce phase purity. The mixture should then be adjusted to a specific pH, which usually is at alkaline pH. The pH is an important factor in determining the phase purity of the synthesized HA nanocrystal. Many studies have examined the optimal pH for HA synthesis. It was indicated that at a low pH level, Ca content would decrease accordingly, while the increase of pH would lead to smaller particle sizes, which is ideal for increasing the surface area to volume ratio (SA/V) and benefits biological functions of HA nanoparticles (Pu'ad et al., 2020). In addition, the

temperature and ageing process also affects the morphology of HA. A previous experiment that precipitated HA from $Ca(OH)_2$ and H_3PO_4 indicated the increase of precipitation temperature from 22 °C to 95 °C could lead to different morphologies of HA changing from tiny needles to well-rounded crystals (Lazić et al., 2001). It was also indicated that the higher precipitation temperature can improve the dissolution of precursors and enhance the reaction kinetics of HA, reduce the crystallite size of HA and lead to consistent particle shape and size (Bouyer et al., 2000, Nayak, 2010, Yelten-Yilmaz and Yilmaz, 2018). A direct comparison of HA morphologies under different conditions is presented in Table 1-6.

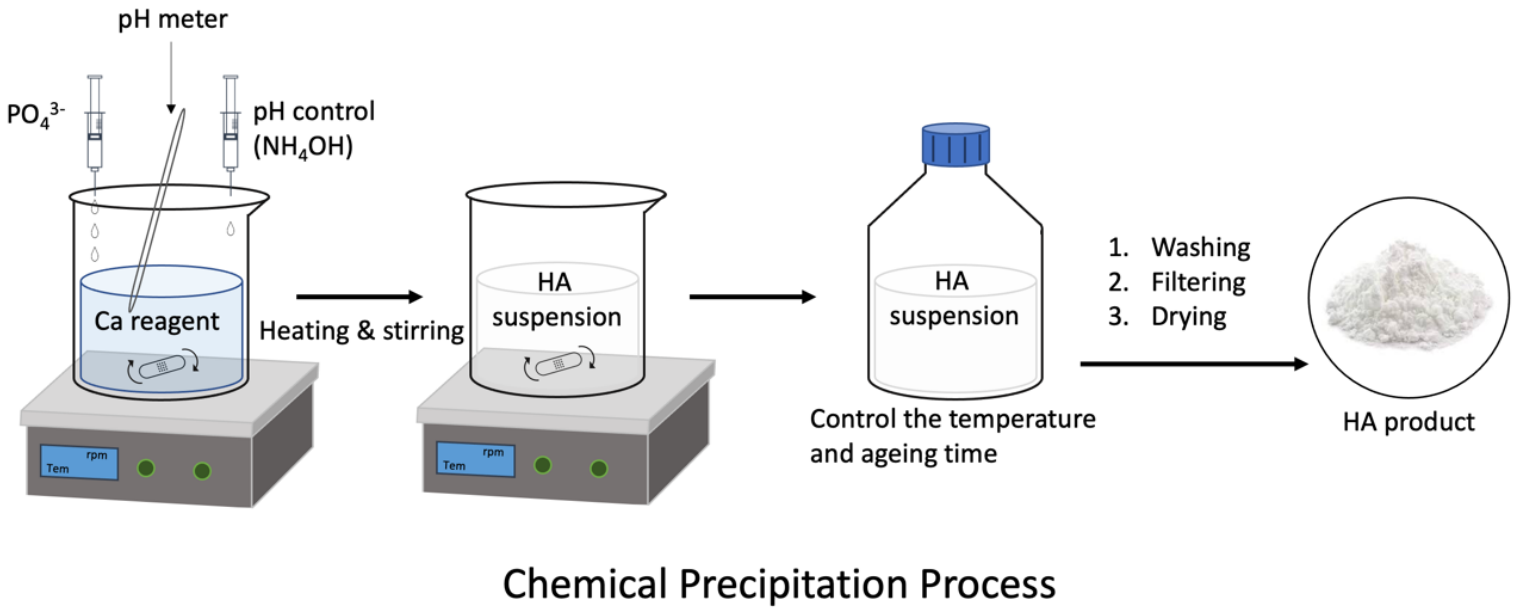

Figure 1-7 Schematic diagram illustrating the chemical precipitation methods in HA synthesis
Figure re-drawn with permission from Elsevier (Sadat-Shojai et al., 2013).

Table 1-6 The HA morphologies and reaction parameters in commonly used wet methods for synthesis of HA.

Methods	Ca/P source	Reaction parameters			HA morphology	Ref
		pH	Temperature	Stirring/aging		
Chemical precipitation	$Ca(OH)_2$, H_3PO_4	>9	30, 50 and 85 °C	7 days maturation and sintered at 950and 1250 °C	Spherical 0.2-1.6 um	[1]
	$Ca(OH)_2$, H_3PO_4	7.5, 8.5, 9.0	40±2 °C	Stirred vigorously for 1 h	Rod-like, 200nm in length, 50 nm in diameter	[2]
	$Ca(NO_3)_2{\cdot}4H_2O$, $(NH_4)_2HPO_4$	11	25 °C	Calcined at 100, 450, 900 and 1200 °C for 1 h.	Spherical 8-20 nm	[3]
	$Ca(NO_3)_2{\cdot}4H_2O$, Na_3PO_4	High-gravity level of 1098 m/s2 with a rotating speed of 800-2000 rpm		Aged at room temperature overnight	Short nano-rod, diameter 1.9-14.2 nm length 4.0-36.9 nm	[4]
Hydrothermal	$CaCl_2$, H_3PO_4	10	100 °C	10h	Rod-like, 80nm in length, 15 nm in diameter	[5]
	$CaCl_2$, K_2HPO_4	12	60-150 °C	12–24 h	Rod-like, 60-75nm in length, 15-20 nm in diameter	[6]
	$Ca(NO_3)_2{\cdot}4H_20$, $(NH_4)_2HPO_4$	10	25-180 °C	N/A	Granule-like shape, 30, 50, and 75 nm	[7]
Hydrolysis	α-TCP	11	70 °C	24-72h	Whisker-like, 0.5-1.0 um in length, 100-200 nm in diameter	[8]
	$Ca(NO_3)_2$, $(NH_4)_2HPO_4$	10	136 °C	24 h	Needle-like, 140-180nm in length, 60-80 nm in diameter	[9]
	DCPD	N/A	75 °C	N/A	Rod-like, 30 nm in length, 25 nm in diameter	[10]

[1]: (Yelten-Yilmaz and Yilmaz, 2018), [2]: (Afshar et al., 2003, Morad et al., 2016), [3]: (Mobasherpour et al., 2007), [4]:(Peng et al., 2015), [5]: (Zhang et al., 2011), [6]: (Wang et al., 2006), [7]: (Nagata et al., 2013), [8]: (Nakahira et al., 1999), [9]: (Mechay et al., 2012), [10]: (Wang et al., 2015).

1.7 Implant Surface Topography

Besides the chemical composition, many other factors could affect the outcome cellular response to an implant coating, such as material porosity, dissolution behaviour and surface micro- and nano- structures (Rahmany and Van Dyke, 2013). The surface topography is very important in affecting the the initial cellular response and bone tissue regeneration, mainly via affecting the protein absorption rate of cells from the surrounding environment (Curtis and Wilkinson, 1997, Li et al., 2010a). Nowadays it still lacks a standard assessment on the influence of surface topography on the cellular behaviour due to the difficulty to quantitatively measure the protein absorption rate from the surrounding body fluids (Rahmany and Van Dyke, 2013). However, specifically designed implant surface topographies have been shown that can directly affect the cellular behaviours such as cell adhesion, migration, proliferation, spreading and differentiation and can finally modify the cell morphology and orientation (Deligianni et al., 2000, Zhu et al., 2004a, Zhu et al., 2004b, Zhu et al., 2005). A study indicated a well-designed nanogroove structure (nanoscale groove ridge patterns) on the surface of polystyrene can guide the alignment of osteoblast cells and collagen fibres (Zhu et al., 2005). Another study also indicated a grooved nanostructure on implant surface successfully increased the bone formation rate compared with a smooth surface both in vitro and in vivo (Zhao et al., 2008). Such

nano grooved structures are considered to be able to induce 'contact guidance' due to their ability in promoting cell migration and proliferation rate. The alignment of cells can enhance the production of cellular growth factors that contribute to the differentiation of osteogenic cells and further increase the synthesis of osteocalcin and ALP activity (Zhao et al., 2008).

1.7.1 Implant Coating Technologies

It was known a well-defined patterned deposition provides more biological benefits than a continuous coating (Huang et al., 2004). Many coating technologies have been developed to fabricate implant coatings with complex topographies, such as photolithography and ink-jet writing. However, their applications were restricted by the high operation difficulty, high production cost and low yield. It is important to develop the next generation coating technologies to reduce the cost and increase the production capacity.

The current coating technologies used for HA deposition including dip coating, thermal spray, plasma spraying, sputter coating, pulsed laser deposition and so on. They were all limited by certain disadvantages (Table1-7). For example, a common drawback of pulsed laser deposition and sputter coating is the requirement of high vacuum, which

dramatically increases the production cost (Ahmed et al., 2015). Only plasma spraying process has been approved by the FDA (Yang et al., 2005). Different kinds of HA-based coatings have been produced by plasma spraying, such as antibacterial AgHA coatings, fluoridated HA (FHA) and HA–carbon nanotube composite coatings. However, this technique requires a very high temperature and cannot incorporate bioactive agents such as organic components in coating layers, which restricts their performance in bone healing process. Currently, many biomaterial researches are interested in an wet-chemical implant coating technology namely EHDA for the preparation of CaP coatings (Bosco et al., 2012).

1.7.1.1 Electrohydrodynamic Atomization

EHDA is a technology that uses electrical filed to break up fluid jet into fine droplets (Dastourani et al., 2018). The common set-up of EHDA is composed of a needle with high voltage and a collection substrate connected to a ground electrode (Figure 1-8 A) (Nguyen et al., 2014). During the coating process, a suspension containing the functional materials is pumped to the nozzle with a controlled flow rate. Due to the high electric charge on the meniscus of liquid surface, under the combined hydrostatic, electrostatic, and capillary forces, it can develop a liquid micro-jet and produces charged droplets. The pointed menisci was known as Taylor cone (Figure 1-8) (Taylor,

1964, Zhakin, 2012, Pan and Zeng, 2019). EHDA has attracted great attentions due to its features of high-resolution printing and thin film deposition (Huang et al., 2013a). This leads to two main techniques including electrospraying and electrospinning, which can produce nano- to micro- scale monodisperse droplets and fibres respectively through adjusting the processing parameters (Figure 1-8 C) (Reneker and Yarin, 2008, Wu and Clark, 2008, Kien Nguyen et al., 2014, Buga et al., 2019).

Table 1-7 Different coating techniques for HA

Technique	Advantages	Disadvantages
Dip coating	Inexpensive; coatings applied quickly, can coating complex substrates	Requires high sintering temperatures, thermal expansion mismatch
Sputter coating	Uniform coating thickness on flat substrates	Line of sight technique, expensive, time consuming; produces amorphous coatings
Pulsed laser deposition	Uniform coating thickness on flat substrates	Line of sight technique
Hot isostatic pressing	Produces dense coatings	Cannot coat complex substrates
Electrophoretic deposition	Uniform coating thickness, rapid deposition rates, can coat complex substrates	Difficult to produce crack-free coatings, requires high sintering temperatures
Thermal spraying	High deposition rates	Line of sight technique, high temperatures induce decomposition, rapid cooling produces amorphous coatings
Sol-gel	Can coat complex shapes, low processing temperature, relatively cheap as coating are very thin	Some processes require controlled atmosphere, expensive raw materials
Dynamic mixing method	High adhesive strength	Line of sight technique; expensive; produces amorphous coatings
Electro spraying	Uniform and small particles generation, flexible process, self-dispersing particles	Low throughput, high control requirement, sensitive to liquid physical property

(Yang et al., 2005, Choudhury and Agrawal, 2012, Ahmed et al., 2015)

Electrospray has low processing temperature, low cost, simple controlling processes and can achieve very fine particle sizes and uniform particle distribution (Xie et al., 2015). Therefore, it has been applied in different fields to extend its application. The electrospray drying process was used to produce materials for food, cosmetics or pharmaceutical industry due to the ability in fabricating fine powders from solutions or suspensions of a materials dissolved in solvent (Singh and Van den Mooter, 2016). Another application of electrospray is the surface coating. During the surface coating process, materials are supplied from solutions or suspensions and formed droplets during deposition process, while solvent has been evaporated before landing onto the substrate to form the coating (Jaworek et al., 2018). The quality of the coatings can be affected by the size and morphology of nanoparticles, the evaporating rate of the solvent, the adhesion of coatings to the substrate and the thickness of the coating layers (Krella et al., 2017, Jaworek et al., 2018). Moreover, owing to the low processing temperature, organic substances in electrospraying process can remain active, which makes it a suitable tool to achieve coatings with organic contents (Oyane et al., 2012, Rahmany and Van Dyke, 2013, Townsend-Nicholson and Jayasinghe, 2018). For example, a DNA immobilized CaP composite layers that contains both osteoconductive bioceramics and transfection reagents has achieved a high biocompatibility and affected the cell behaviour on their surfaces (Oyane et al., 2012).

Due to the relatively high stability and low environmental requirement, the deposition process of electrospray thus has more flexibility. For example, it was found that by modifying the processing parameters of electrospray, it is possible to control the geometries of the jet. They are known as different electrospray modes, including micro-dripping mode that emits droplets, cone-jet mode that emits fine continuous conical jets and multi-jet mode that forms multiple cone-jet at the same nozzle (Nguyen and Byun, 2009, Kien Nguyen et al., 2014).

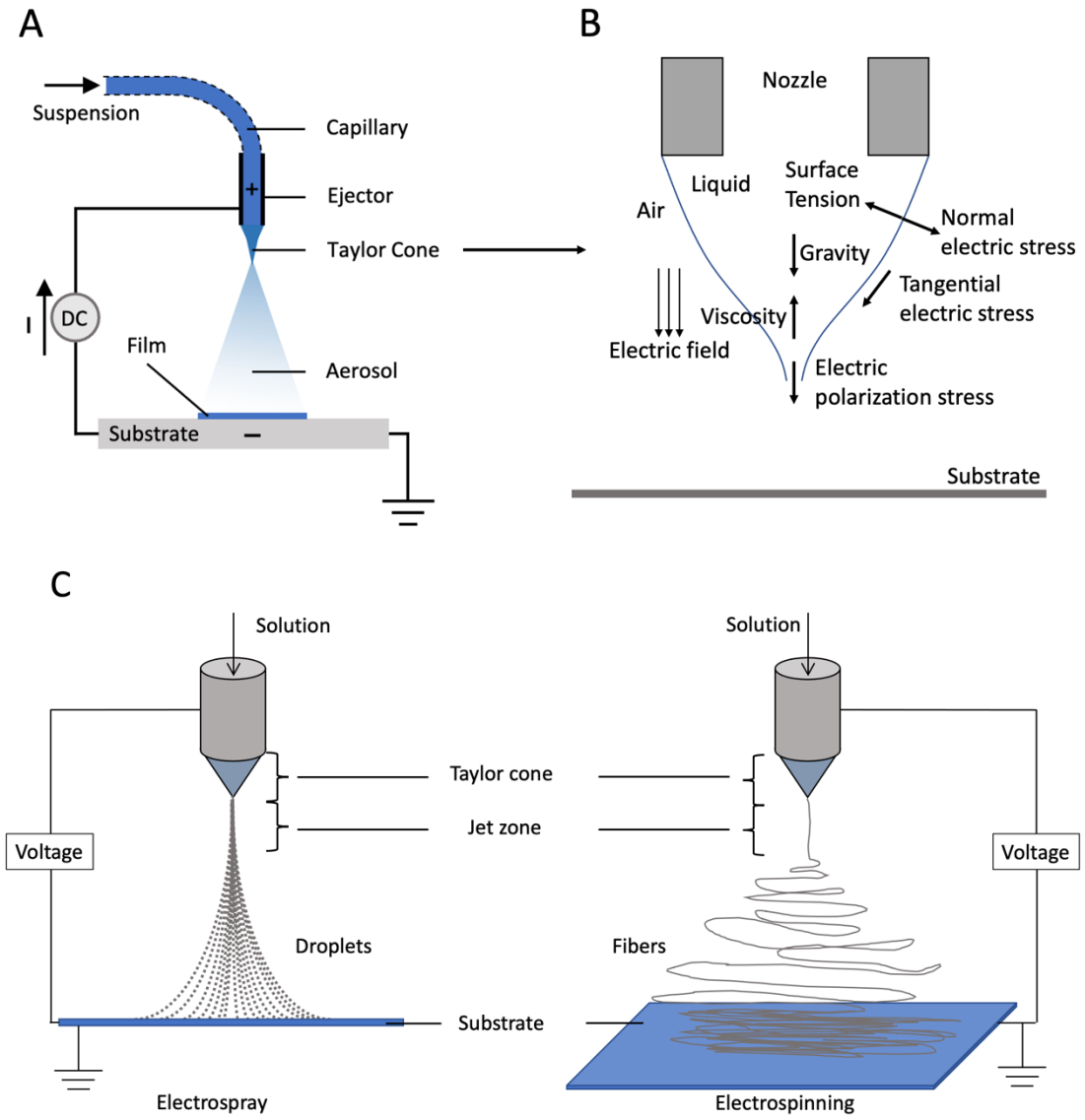

Figure 1-8 Schematic diagram of EHDA system and Taylor cone

EHDA setting up (A); Distribution of active forces on the liquid cone-jet (B). Demonstration of the electrospray and electrospinning processes (C).

Figure re-drawn with permission from MDPI (Pan and Zeng, 2019, Morais et al., 2020).

1.7.1.2 Electrospray Modes

During the electrospray process, a range of behaviors could happen when a drop emerged from a nozzle with the balance between accelerating forces and surface tension, including the dripping and jetting modes (Verdoold et al., 2014). More specifically saying, many factors can affect electrospray process, such as surrounding conditions, geometrical features and operating parameters (Dastourani et al., 2018). Depending on these factors, different electrospray modes can be achieved (Figure 1-9) (Table 1-8) (Cloupeau and Prunet-Foch, 1990, Jaworek and Krupa, 1999a, Jaworek and Krupa, 1999b). It is still an ongoing challenge to understand the underlying physics of all possible modes (Verdoold et al., 2014).

The formation of cone-jet structure starts by applying an adequate level of voltage- 'minimum voltage' (V_{MIN}) that can provide a normal electrical stress on the liquid surface to counterbalance the surface tension (Figure 3-10). At a fixed flow rate, increasing the voltage can reduce the cone height and increase the cone angles, which is due to the increased normal electric stress to accelerate the consumption of the liquid cone (Park et al., 2007). When the applied voltage is high enough that achieve the 'maximum voltage' (V_{MAX}) to make liquid amount reduced to a certain level that the surface tension can no longer bear such a high overall electric field intensity, the

drop will break up into a multi-jet structure.

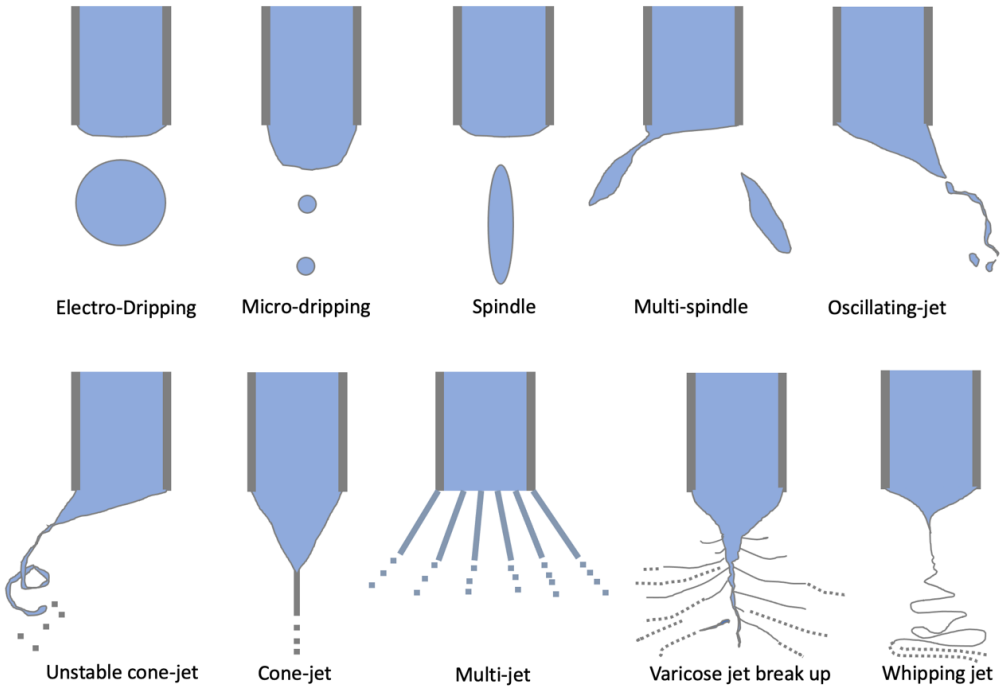

Figure 1-9 Schematic showing various possible jet modes during electrospraying process

The modes are listed mainly in the order as the applied voltage increased, except spindle mode, which appear due to the increase of flow rate.

Figure adapted from (Cloupeau and Prunet-Foch, 1989).

Table 1-8 Electrohydrodynamic modes.

Mode	Formation conditions, motion and fragmentation pattern of jetting modes
Periodic EHD modes	Periodic axial emission of liquid fragments
Electro-dripping [1]	It happens commonly at low voltage and similar to electrically neutral condition. The growing of drop falls when the gravitational force overcomes the surface tension force and the process repeat itself. The diameter of droplet is larger than capillary
Micro-dripping [1]	When the voltage is sufficiently to keep a stable hemispherical meniscus, micro-dripping happens due to the meniscus cannot contract back after the droplet detachment. Droplet is much smaller than capillary diameter.
Spindle [2]	Spindle mode happens when both voltage and flow rate was higher than dripping mode. High electric field detaches a fragment of liquid rather than regular droplets before the formation of continuous jet.
Multi-spindle [2]	It happens when spindle-like jet became multiple due to increase of voltage. Because the liquid velocity is higher than the velocity of jets, no continuous jetting can be formed. The shape of droplet was controlled by the electric field and space charge of detaching droplets, due to the gathering of liquid, a sufficiently high excitation field can accelerate the elongating of liquid.
Oscillating-jet [3]	A further increase in the flow rate can cause a continuous and steady jet connected to the capillary, which oscillates or rotates due to the space charge of formerly emitted droplets.
Unstable cone-jet [4]	It is also known as precession mode due to the regularly rotating of both cone and jet around the capillary axis
Steady EHD modes	Continuous emission of jets
Cone-jet [1]	Further increase the voltage, a steady cone-jet can be formed from unstable cone-jet. The jet issues from the capillary through an axisymmetric cone, which apex stretching along the capillary axis.
Multi-jet [3]	Multi-jet can be achieved from cone-jet by increasing the voltage. Due to the higher voltage, the extra charge build-up on the surface of Taylor cone, result in multiple jets.
Corona discharge [5]	The corona discharge occurs when the electric field between the needle and the ground electrode becomes larger than the electrical breakdown threshold of the surface energy of liquid surrounding air interface. The phenomenon is likely to occur especially when the liquid has a high surface tension and require a high electric field to offset the capillary pressure
Cone-jet sub-modes	
Varicose jet break up [6]	The jet was composed by an inner spray of main droplets surrounded by an outer shroud spray of satellite droplets. This is due to the undispersed main droplet caused by the growth of axisymmetric undulations on the jet surface
Whipping jet [7]	It happens when the jet has a 'whipping' patterns due to the lateral displacement and get amplified in the liquid flow.

The modes are listed mainly in the order as the applied voltage increased, except spindle mode, which appear due to the increase of flow rate.
[1]:(Hijano et al., 2015); [2]:(Verdoold et al., 2014, Pu'ad et al., 2020); [3]:(Jaworek and Krupa, 1999b); [4]:(Jayasinghe and Edirisinghe, 2002, Buga et al., 2019); [5]:(Cloupeau and Prunet-Foch, 1989, Yoshikawa et al., 1996); [6]:(López-Herrera et al., 2005); [7]:(Sachse et al., 2005, Rosell-Llompart et al., 2018).

1.7.1.3 Cone-jet Mode

Cone-jet is the most widely used mode among different electrospray modes, (Chen et al., 1995, Cloupeau and Prunet-Foch, 1989, , Gamero-Castaño, 2008, Rosell-Llompart et al., 2018). The cone-jet mode is considered as the steadiest mode, which has an advantage in producing evenly distributed droplets with more consistent size compared with multi-jet mode, which makes the cone-jet mode irreplaceable during the implant coating process (Suh et al., 2005). Many studies were focused on the precise control of electrospray processes that highly relied on the cone-jet mode, it has been employed in the deposition of biomaterials into patterns with micro- or nano- scales (Kim et al., 2007). However, the major limitation of cone-jet is the limited operable voltage and flow rate range (Dastourani et al., 2018). For an industry application, it is very important to provide a stable jetting process with a sufficient high flow rate and fine droplet size.

The stability of cone-jet was demonstrated based on three stages of cone-jet build up, including acceleration of liquid, jet break-up and spray evolution after droplet production (Hartman et al., 1999a). During the liquid acceleration phase, the forces involved in the cone structure contain the applied electric stress balanced by the outward stresses such as gravity and liquid surface tension (Taylor, 1964). The second

stage is the droplet production process, where the liquid is ejected and broken into droplets (Hartman et al., 1999a, Rulison and Flagan, 1994,).

The formation of a cone-jet requires the electric potential and liquid flow rate to achieve the minimum magnitudes. At a certain flow rate, a cone-jet can be formed when the applied voltage was within V_{MIN} and V_{MAX}. Likewise, at a certain voltage every liquid has a flow rate range to achieve the cone-jet. The V_{MIN} can be estimated as given by Morris et al. (Morris et al., 2013): (Eq. *(1-2)*):

$$\Phi_{on} = \sqrt{\frac{\gamma d_e}{2\varepsilon_0}}\, ln(\frac{4L}{d_e}) \qquad (1\text{-}2)$$

where γ is the surface tension coefficient, d_e is the emitter diameter, L is the distance from emitter to ground electrode and ε_0 denotes vacuum permittivity.

The required minimum flow rate for a cone-jet can be calculated by the following equation (Rosell-Llompart and De La Mora, 1994): (Eq. *(1-3)*):

$$Q_{min} = \frac{\gamma \varepsilon_r \varepsilon_0}{\rho K} \qquad (1\text{-}3)$$

where ρ is the liquid density, ε_r represents the relative permittivity of liquid and K is the electrical conductivity of liquid.

The axisymmetric instability was considered as the main reason of the jet breaks up at this minimum flow rate (Gañan-Calvo et al., 1996). After the ejection of droplets from the cone surface, different sized droplets can be formed due to different electric interaction between droplets. Smaller droplets or satellite droplets normally appear at the edge of the spray, while the larger sized droplets appear in the center (Gañán-Calvo et al., 1994, Hartman et al., 1999b, Hartman et al., 1999a). The initial radial positions of droplets remain consistent during the spraying process and smaller droplets would have a higher acceleration rate and gain a higher radial velocity, therefore produce a circular shape with a higher growth rate of coating in the center (Hartman et al., 2000).

The liquid properties such as surface tension, electrical conductivity and liquid viscosity can also regulate the stability of cone-jet and the droplet size (Figure 1-10). The liquid electrical conductivity is the key to the formation of conical shape of Taylor cone (Hartman et al., 2000, Cloupeau and Prunet-Foch, 1989). A suitable surface tension is also important in maintaining a stable cone-jet. Liquid with a higher surface tension normally requires higher electric field, which may make the electric field to be too high and exceed the V_{MAX} for a cone-jet, thus producing a multi-jet directly (Tang and Gomez, 1995). Moreover, the liquid viscosity is important in determining the relic size of electrospray. A high liquid viscosity normally leads to a bigger relics (Jayasinghe

and Edirisinghe, 2002).

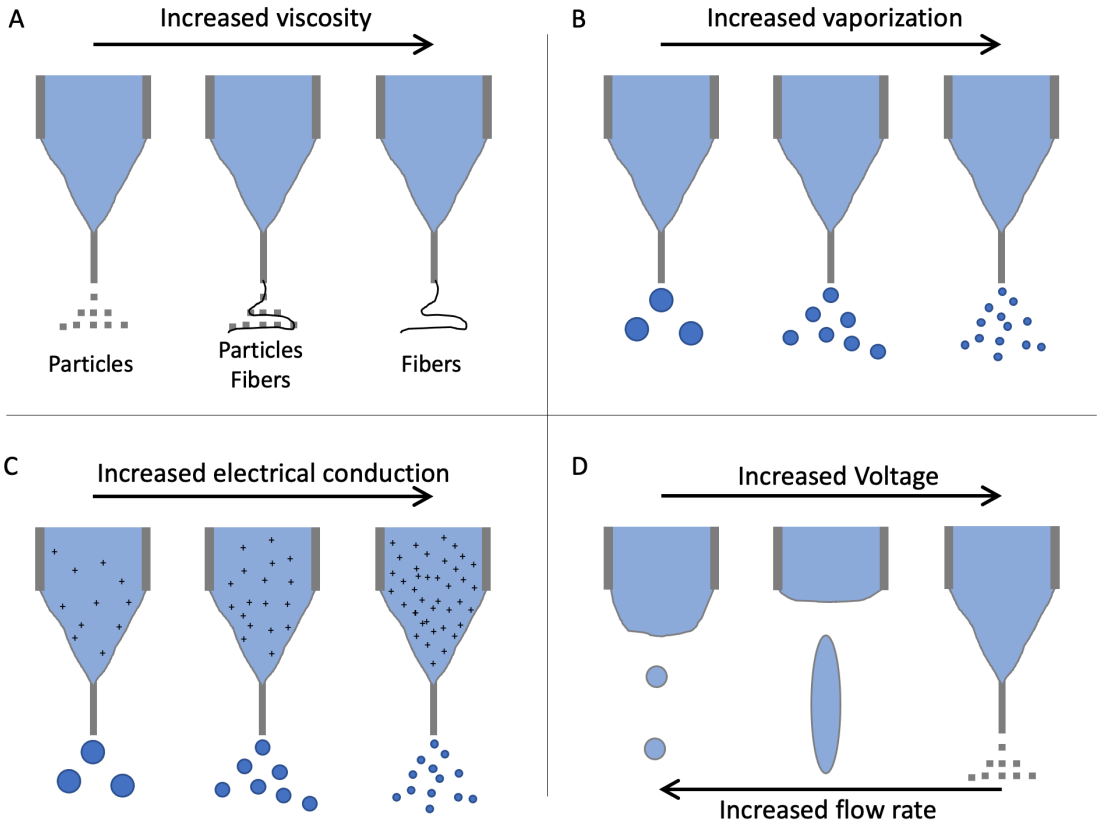

Figure 1-10 The impact on EHD performance
(A) Higher polymer concentrations tend to change electrospray into electrospinning; (B) and (C) the increase of solvent volatility and electrical conduction decrease the droplet size respectively; (d) effect of flow rate and voltage on electrospray.
Figure re-drawn with permission from MDPI (Morais et al., 2020).

1.7.1.4 Nozzle Geometry Determines the Stability of Cone-jet

The geometry of nozzle could also affect the EHDA performance. To promote the

coating efficiency and quality as well as extend the range of applicable solvents in electrospray cone-jet, the key is to extend the cone-jet processing zone. The cone-jet processing zone is determined by the convert voltages (voltage range) at different flow rates that can stabilize the cone-jet in an electrospray process. A wider cone-jet processing zone can dramatically reduce the operation difficulty and enhance the stability and precision. It can be achieved via modifying the involved coating parameters such as solvent property and nozzle geometry.

A strategy was enhancing the attach area of the nozzle tip to stabilize the cone-jet mode. The mechanism was explained by a one-dimensional form of Navier-Stokes equation that demonstrated the forces involved in a cone-jet, including the velocity pressure (p_{Ekin}), liquid pressure (p_{liq}), normal viscous stresses (σ_μ), polarization stress (σ_ε), hydrostatic pressure (p_g), tangential viscous stresses (τ_μ) and tangential electric stress (τ_{Er}) (Hartman et al., 1999b). They function together to determine the structure of Taylor cone. Their relation was stated as: (Eq. *(1-4)*):

$$\frac{\partial(p_{Ekin}+p_{liq}-\sigma_\mu-\sigma_\varepsilon-p_g)}{\partial z}=\frac{2}{r_s}(\tau_\mu+\tau_{Er}) \qquad (1\text{-}4)$$

Among all of these forces, liquid pressure can be further affected by several parameters: surrounding air pressure (p_{out}), stress on the liquid-gas interface due to

viscous effects ($\Delta p_{n,\mu}$), electrical normal stress on the interface (Δp_{En}) and surface tension stress (Δp_s). Their relation was stated as: (Eq. *(1-5)*):

$$p_{liq} = p_{out} + \Delta p_{n,\mu} + \Delta p_{En} + \Delta p_s \qquad (1\text{-}5)$$

These two equations contain all forces involved and can be used to predict the phenomenon of a cone-jet. The cone-jet is mainly dominated by the electrical normal and tangential stresses, the surface tension stress and the velocity pressure (Ganan-Calvo et al., 1997, Hartman et al., 1999b). According to these studies, attenuating the electric field intensity at the tip of nozzle is a potential strategy to broaden the voltage range of cone-jet and consequently reduced the manipulation difficulty in maintaining a stable cone-jet (Saez and Carbonell, 1987, Or and Ghezzehei, 2000, Saif, 2002).

The first attempt based on this theory was via adding a circular conducting guard plate near the capillary nozzle tip (Figure 1-11 A). The conducting guard plate was able to reduce the electric field near the cone-tip and can prevent the electric disturbances. It successfully maintained a stable cone-jet with an extended the voltage range (Park et al., 2004). More recently, similar studies based on this theory have been widely investigated. Another strategy is enhancing the attached liquid volume that serves as a high potential electrode to reduce the electric field intensity on the liquid-air interface (Morad et al., 2016). Lastow and Balachandran indicated blunting the edges

of nozzles to enhance the area of liquid attachment has successfully removed the discharge effect of sharp apex of liquid cone structure (Lastow and Balachandran, 2007). However, no obvious improvement has been achieved due to the inherently sharp geometries of liquid cone apex, but such explorations inspired many researchers to investigate the performance of nozzles with different geometries. A recent study introduced an extender cap equipped nozzle to increase the attaching area for the hanging drop of alcoholic solvents (Figure 1-11 B) (Morad et al., 2016). Owing to the large volume of the attached drop that reduced the electric field intensity, a higher potential difference was required to balance the electric normal stress and surface tension. The results showed an extension in the voltage-flow rate margin of cone-jet and a sturdier spray axis (Morad et al., 2016). However, the influence of the size of spherical caps on the cone-jet mode remains unclear and the influence of such extension structure on the coating topography and solvent compatibility of this type of nozzle has not been systemically studied.

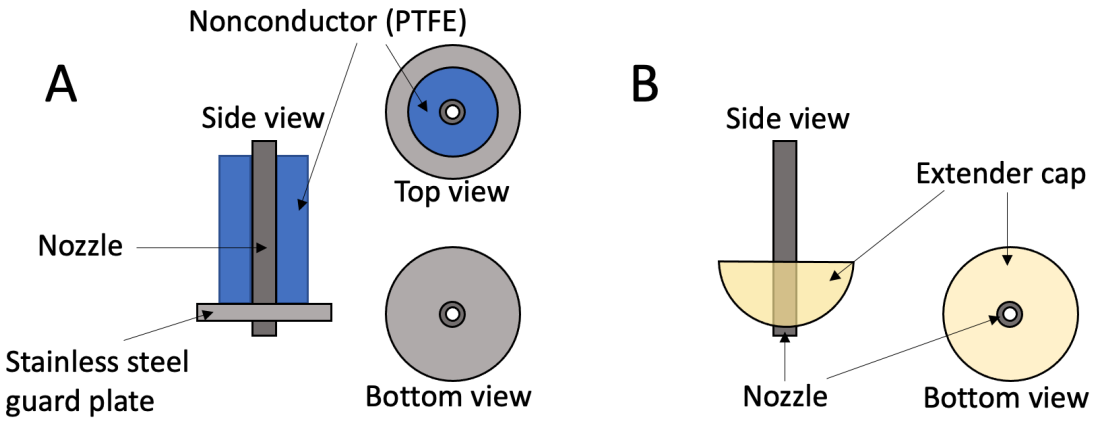

Figure 1-11 EHD nozzle with guard plate (A) and extend cap (B).
Figure re-drawn with permission from Elsevier (Park et al., 2004, Morad et al., 2016)

Another type of method used to enhance the atomization stability was based on a technique called 'co-axial nozzles' (Figure 1-12). There were two methods employed inert gas to achieve the electrospray of water. The first method used co-axial sheath to insert inert gas flowing around the spray (Karas et al., 2000). The second way fulfilled the whole surrounding spaces of the EHDA set-up with inert gas (Lastow and Balachandran, 2007). In another study, co-axial nozzle was used to mix water and methanol at the point atomization, which achieved a higher stability than aqueous solution, but inhibited the dissolution of solutes and had less stability than pure organic solvent (Li et al., 2014). Moreover, the co-axial needle is a complex system, which increased the operation difficulty and the improvement on electrospray performance was not sufficient.

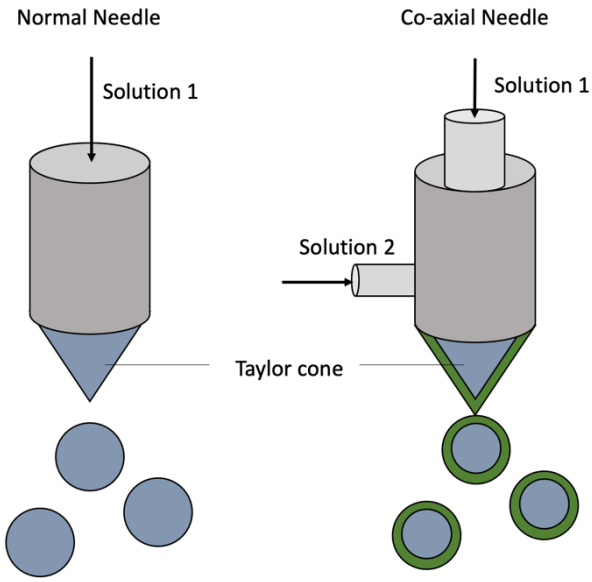

Figure 1-12 Normal electrospray needle and co-axial needles.
Figure re-drawn with permission from MDPI (Morais et al., 2020)

1.7.1.5 Nozzle Geometry Affects the Solvent Incompatibility of EHDA

Another limitation of electrospray cone-jet mode is the solvent incompatibility. The solvents that can be used in the cone-jet mode were limited by many physical or chemical properties, such as volatility, electrical conductivity, electrolytic concentrations (Cunha et al., 2002, Hogan et al., 2007). Many studies employed different kinds of alcohols or ketones, such as ethanol, methanol, 1-propanol, 1-butanol and acetone, as solvents to do electrospray due to their high volatility, low

electrical conductivity and ability in dissolving many substances or forming stable suspensions. However, there are many materials could not be dissolved or even form dispersions in these solvents. An example is graphene oxide (GO) nanomaterial. GO has attracted many attentions in biomedical applications such as drug delivery, gene transfection and biosensing. Moreover, GO has good antibacterial ability due to the synergy of oxidization capacity and membrane stress on bacterial cells (Liu et al., 2011). GO nanoparticles could only form a dispersion in a few liquids, such as water, N, Ndimethylformamide (DMF), N-methyl-2-pyrrolidone (NMP), poly (methyl methacrylate), Tetrahydrofuran (THF), and ethylene glycol. As water is nontoxic, it is the most suitable solvent to do electrospray of GO in the medical devices or implant coating (Johnson et al., 2015).

Water is a good solvent that can attract a variety of substances. However, the high surface tension, high conductivity, relatively low evaporation rate and many other physical properties of water make it not suitable for electrospray cone jet (Table 1-9). Electrospray of water-based suspensions requires a high electric voltage to break the meniscus of liquid surface into conical jets, but a high-level voltage can easily destabilize the liquid cone structure to form multiple jets directly (Lastow and Balachandran, 2007). The uncontrollability of water jet was also related to the high electrical conductivity. Although the pure water does not have a high electrical

conductivity, the solutions used in experiments always contain different kinds of solutes that could make the conductivity to be very high. The high electrical conductivity can switch the applied voltage into relaxation at the surface in a few milliseconds, which can lead to uncontrollable disruption to the liquid jet (Lastow and Balachandran, 2007).

Table 1-9 Surface tension of commonly used solvents for EHDA processing

Solvent	**Surface Tension** @20 °C (mN/m)
Acetonitrile	29.04
Acetone (2-Propanone)	25.20
Benzene, Annulene	28.88
Chloroform	27.10
Dichloroethane	26.50
Ethanol, Ethyl alcohol	22.10
Methanol, Methyl alcohol	22.70
Nitromethane, Nitrocarbol	36.80
Propanol, Propyl alcohol	23.70
Tetrahydrofuran	26.40
Water	72.86

Date acquired from several data bank: (Engineering ToolBox, DataPhysics Instruments GmbH, European Chemicals Agency (ECHA) Databases, Dortmund Data Bank)

1.7.1.6 Template-assisted Electrohydrodynamic Atomization for Patterning Process

The coating topography plays a significant role in influencing cell responses, such as

cell adhesion, orientation, migration, proliferation and differentiation (Munir et al., 2011b). The initial cellular responses and orientation of cell attachment on the implant surface have considerable impacts on tissue regeneration and the structure of resultant tissue respectively (Monsees et al., 2005). In recent years, many different techniques were introduced to manufacture 3D structures of biomaterials on substrate surfaces, such as photolithography or chemical etching process (Kim and Han, 2010). Although the etching process can easily create precise surface structures, but only on ductile materials such as metallic and polymeric materials (Le Guéhennec et al., 2007). It is not applicable in brittle bioceramics materials such as HA coatings. A direct patterning process based on EHDA is direct writing technique (Kim and Han, 2010). The advantage of direct writing comparing to subtractive top-down technologies such as chemical etching or photolithography is the formation of patterns does not need the lithography step (Wu et al., 2008). However, the application of direct writing is restricted in the laboratory scale due to the relatively low stability, fabricating rate and pattern resolution (Jaworek et al., 2018).

An alternative way to produce patterned coatings was focused on employing assisting masks during deposition process, which has developed into many branches such as photo-immobilization process, pulsed-laser deposition, mask-assisted electrochemical micromachining and template-assisted ion beam sputtering (Barbucci et al., 2003, Peruzzi et al., 2004, Kern et al., 2007, Puckett et al., 2008). Nevertheless, the common drawbacks of above-mentioned techniques are low production yield, high processing cost and complex procedure, which restrict their application in implant coating industries. Therefore, an alternative technology combining the benefits of EHDA (low process temperature, low-cost and simple control processes) and masks assisted deposition process named TAEA is a considerable method to offer a low cost, high resolution and high efficiency patterning process (Figure 1-13) (Li et al., 2010a, Munir et al., 2011a, Munir et al., 2011b).

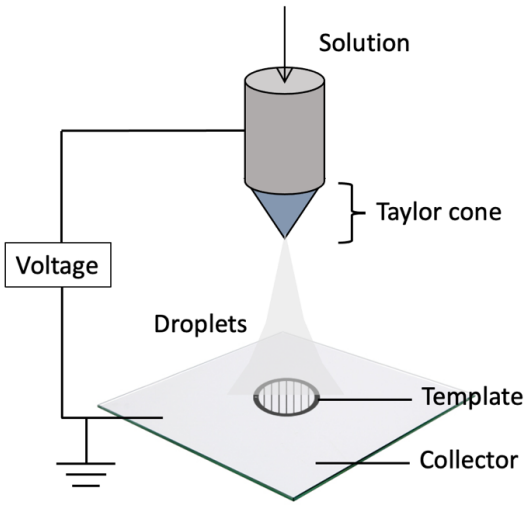

Figure 1-13 Template assisted electrohydrodynamic atomization set-up

TAEA employs templates above the collection plate to deposit well-defined microscale features of nanoparticles on a substrate (Li et al., 2010a). TAEA has a low energy requirement and simple setting up (Ahmad et al., 2006). During TAEA process, the droplets break-up from the EHDA jet and are driven by the electrical force to cover the whole area of collection region including the templates and substrate. After removing the templates, a well-defined pattern of deposited materials can be achieved on the substrate surface (Li et al., 2008). TAEA has the potential in fabricating well aliened nanostructures that can mimic the nanostructures of natural antibacterial surfaces such as cicada wings, which was composed of many nano-conical structures (R=30 nm) and achieved contact killing ability against both G+ and G- bacterium (Figure 1-14) (Pogodin et al., 2013).

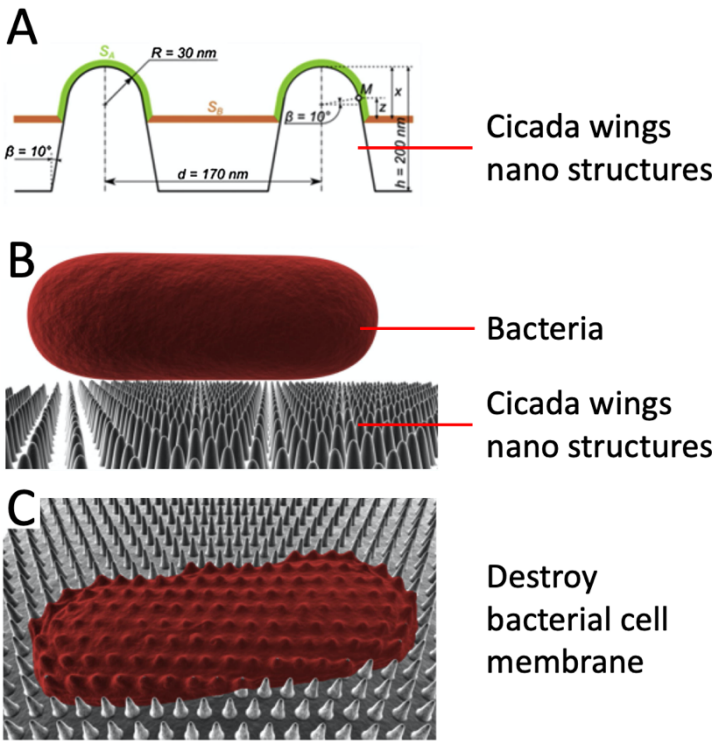

Figure 1-14 The nanostructure and the antibacterial mechanism of cicada wings
Figure re-drawn with permission from Elsevier (Pogodin et al., 2013).

The precision of templates directly restricted the precision of TAEA fabricated patterns. Since the designed patterns in implant coatings are mainly aiming to guide the cellular response, it requires very high resolution that is compatible with the size of bone cells (approx. 40 µm (osteoblasts)) (Ahmad et al., 2006). To improve the TAEA coating resolution, a conventional method is changing templates with a smaller spacing size, while in a micro- or nano- scaled level, decreasing the template size will increase the manipulation difficulty and raise the cost of production exponentially. Thus, alternative methods that can alter the shape or size of patterns with large-scaled template is

desirable.

Besides the electric field, previous studies have employed different methods to induce the jetting process. For example, a pressure assisted jetting system with co-axial nozzle was created to generating fine micro scaled droplets and a range of 2D and 3D architectures (Arumuganathar and Jayasinghe, 2008). An aerodynamically assisted jets technology has used a pressure field through air flow for drawing liquids to produce microbubbles and microfoams or disperse cells or organisms (Arumuganathar et al., 2008, Jayasinghe, 2017). Therefore, it is possible to employ a field or pressure that can provide extra attractive forces on the nanoparticles or suspension during the jetting process to control the dispersing of nanoparticles. A promising strategy is introducing magnetic fields into the TAEA system, which may be possible to guide the distribution of magnetic nanoparticles to increase the resolution of patterns.

1.8 Research Questions

The ultimate purpose of this project is to synthesize different metallic ions substituted HAs, which introduces the antibacterial ability and magnetic property to the biocompatible HA and identify their potential applications. The project development and perspectives have been shown in Figure 1-15.

1. To investigate whether modifying nozzle geometry indeed promotes the stability of EHDA, the effect of fabricated ball-tip nozzles on the coating efficiency and stability of EHDA cone-jet, solvent adaptation and their resulting depositions were studied.

2. To synthesize nanoparticles with magnetic property and good biocompatibility, HA was employed as a platform that can be substituted by different magnetic ions. The bioactivity of synthesized nanoparticles was studied and the localization ability of a MTAEA patterning process was conducted.

3. To achieve antibacterial coating with good biocompatibility, metallic co-substituted HA with good antibacterial ability was synthesized to reduce the required metallic content while maintaining or enhancing the anti-infection ability and biocompatibility.

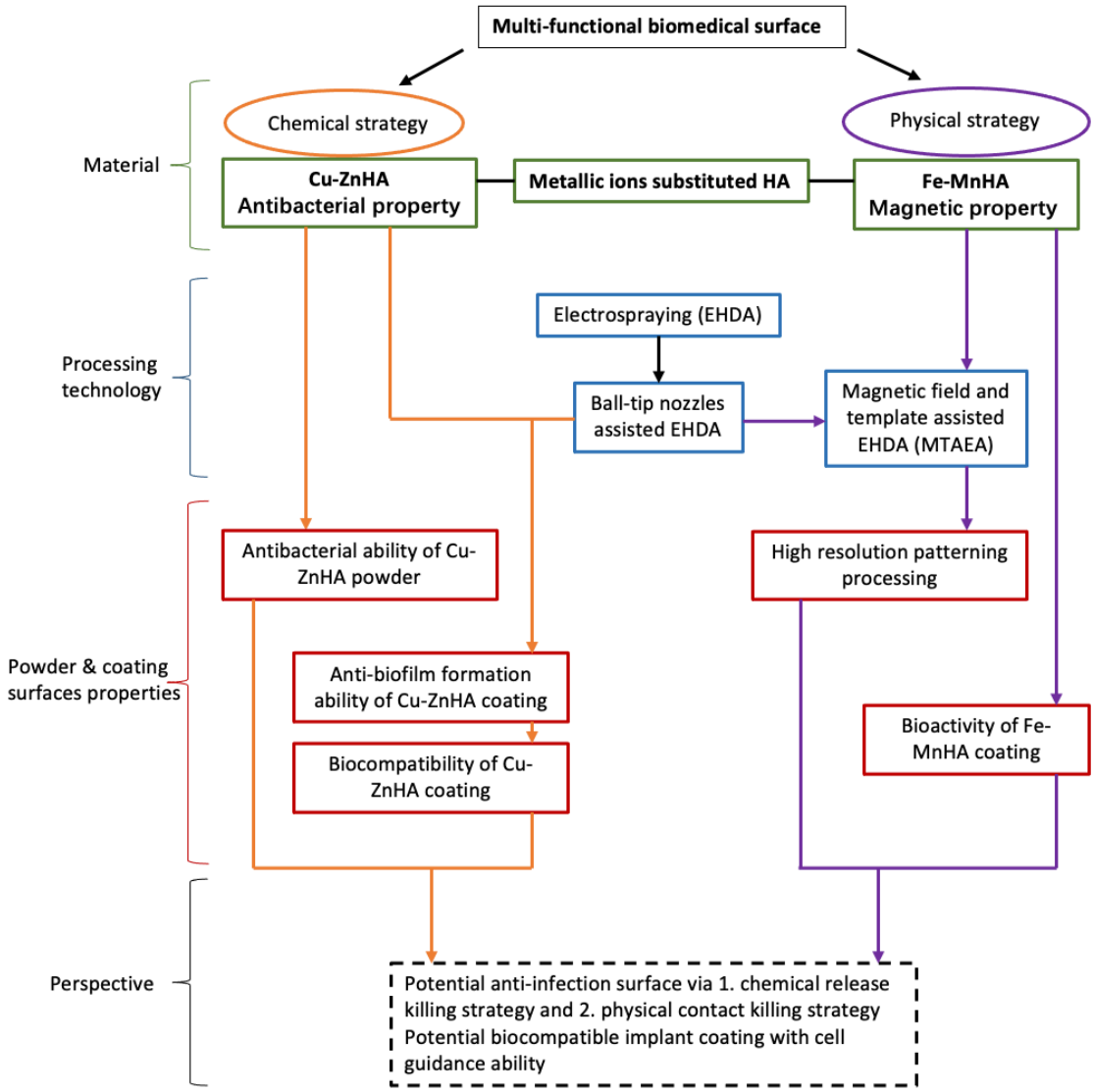

Figure 1-15 Project Development and Perspectives

Chapter II

2 Methodology

This chapter contains the details of synthesis and characterization of materials and the methods used to evaluate the designed EHDA. The characterization on the composition and morphologies of synthesized materials are based on the optical microscopy, scanning electron microscopy (SEM), X-Ray diffraction (XRD) and Fourier-transform infrared spectroscopy (FTIR). The in vitro characterization of synthesized materials contains the in vitro bioactivity test, antibacterial test (cell staining and flow cytometry assay), antibiofilm formation test against *Escherichia coli* (*E. coli*) and *Staphylococcus aureus* (*S. aureus*) bacteria, and biocompatibility test based on alamarBlue assays. To evaluate the designed EHDA, the fabrication of different sized ball-tip nozzles and the analysis on their EHDA performances are introduced. The details of analysing the performance of the MTAEA technology are also presented.

2.1 Materials

Ammonium hydroxide solution (33.5%), Ammonium phosphate dibasic (≥98%), Calcium hydroxide (≥95.0%)**,** Calcium nitrate tetrahydrate (≥99.0%), Iron (II) chloride

tetrahydrate (≥99.0%), Iron(III) chloride hexahydrate (97%), Manganese chloride tetrahydrate (≥99%), Nitric acid (70%), Phosphoric acid (85 wt. % in H_2O), Sulfuric acid (95%-98%), D-(+)-Glucose (≥99.5%), crystal violet ((Hucker Formulation) ≥99.5%), Dulbecco's Modified Eagle's Medium (DMEM), Fetal Calf Serum (FCS), penicillin-streptomycin (P/S), L- glutamine (L-G) and trypsin/EDTA, were purchased from Merck Life Science UK Ltd., Dorset, UK.

E. coli (ATCC® K12), *S. aureus* (ATCC® 6538) and MG-63 cells (Homo sapiens, osteosarcoma, ATCC® CRL-1427™), were purchased from American Type Culture Collection, Manassas USA. Both *E. coli* and *S. aureus* were employed to validate if the synthesized materials have potent and broad antibacterial efficacy against both Gram-negative and Gram-positive bacteria. The MG63 cell has been widely applied in biocompatibility test for a long time. It a good model for human osteoblast proliferations because it proliferates faster compared to normal osteoblast and can retain a differentiated phenotype under culturing conditions (Gu et al., 2011, Attik et al., 2014).

Luria broth powder (Invitrogen™ Luria Broth Base (Miller's LB Broth Base)™,Tryptone Soya Broth (TSB) and Thermo Scientific™ OXCM0129 casein soya bean digest broth were purchased from Thermo Fisher Scientific Inc., MA, USA.

Alamar blue® cell viability reagent, alamarBlue®, Bio-Rad Laboratories, Inc. California,

USA.

Ethanol (100%) was purchased from Chemistry stores, chemistry department, University college London, UK.

2.2 Sample Preparation

2.2.1 Synthesis of HA and Metallic Ions Substituted HA Nanoparticles

Fe-MnHA, FeHA and MnHA (X_M = 0.005, 0.025, 0.05), Cu-ZnHA, CuHA and ZnHA (X_M = 0.0005, 0.0025, 0.005) and HA nanoparticles were synthesized using wet chemical method.

In the synthesis of Fe-MnHA, FeHA, MnHA, calcium hydroxide ($Ca(OH)_2$), manganese chloride tetrahydrate ($MnCl_2{\cdot}4H_2O$) and iron(III) chloride hexahydrate ($FeCl_3{\cdot}6H_2O$) and phosphoric acid (H_3PO_4) were utilized as the sources for Ca, Mn, Fe, and P, respectively due to the lower toxicity of iron(III) chloride and manganese chloride than manganese nitrate and ferric nitrate (Zaidi et al., 2005) (According to material safety data sheet from Sigma-aldrich and Thermo Fisher Scientific). Pure HA was synthesized using the same precursors as a control group. The reactions involved in the synthesis processes

of HA and ionic (co-)substituted HA can be expressed as follows (Eq. *(2-1)* and *(2-2)*):

$$10Ca(OH)_2 + 6H_3PO_4 \rightarrow Ca_{10}(PO_4)_6(OH)_2 + 18H_2O \quad (2\text{-}1)$$

$$10Ca(OH)_2 + 6H_3PO_4 + xFeCl_3{\cdot}6H_2O + yMnCl_2{\cdot}4H_2O + NH_4OH \rightarrow Ca_{10-x-y}Fe_xMn_y(PO_4)_6(OH)_2 + NH_4Cl + H_2O \quad (2\text{-}2)$$

In the synthesis of CuHA, ZnHA and Cu-ZnHA, calcium nitrate tetrahydrate ($Ca(NO_3)_2{\cdot}4H_2O$), zinc nitrate hexahydrate ($Zn(NO_3)_2{\cdot}6H_2O$), cupric nitrate ($Cu(NO_3)_2{\cdot}3H_2O$), and ammonium dihydrogen phosphate ($NH_4H_2PO_4$) were utilized as the sources for Ca, Zn, Cu, and P, respectively. Synthesis HA with this group of precursors was suggested to be able to increase the phase purity (Othman et al., 2016). To minimize the effect of using different synthesis precursors, pure HA was synthesized using the same precursors. The reactions involved in the synthesis processes of HA and ionic (co-)substituted HA can be expressed as follows (Eq. *(2-3)* and *(2-4)*):

$$10Ca(NO_3)_2{\cdot}4H_2O + 6NH_4H_2PO_4 \rightarrow Ca_{10}(PO_4)_6(OH)_2 + 6NH_4NO_3 + 14HNO_3 + 38H_2O \quad (2\text{-}3)$$

$$10Ca(NO_3)_2{\cdot}4H_2O + 6NH_4H_2PO_4 + xCu(NO_3)_2{\cdot}3H_2O + yZn(NO_3)_2{\cdot}6H_2O + NH_4OH \rightarrow Ca_{10-x-y}Cu_x\,Zn_y(PO_4)_6\,(OH)_2 + NH_4NO_3 + H_2O \quad (2\text{-}4)$$

Besides water, the byproducts during the ionic (co-)substituted HA synthesis process were ammonium chloride (NH_4Cl), ammonium nitrate (NH_4NO_3) and nitric acid (HNO_3),

all of them were highly soluble in water, hence can be completely washed away. According to many previous studies, HA and different ionic substituted HA can be synthesized via both groups of precursors (Wu et al., 2007a, Li et al., 2009b, Li et al., 2012, Huang et al., 2015, Othman et al., 2016).

During the synthesis process, appropriate amount of calcium hydroxide and calcium nitrate tetrahydrate with $Zn(NO_3)_2 \cdot 6H_2O$ and/or $Cu(NO_3)_2 \cdot 3H_2O$ were dissolved in 250 mL deionized (DI) water and stirred at 500 rpm while sink in water bath at 98.5 ℃ for 30 mins (Magnetic hotplate stirrers, VELP Scientifica, MB, Italy) (Table 2-1). The pH of the solution was adjusted and kept at 11 by adding 28% ammonia solution (ammonium hydroxide) until the end of synthesis process.

Appropriate amount of phosphate solution was then prepared by using H_3PO_4 (For Fe-MnHA, FeHA, MnHA and HA) or $(NH_4)_2HPO_4$ (For Cu-ZnHA, CuHA, ZnHA and HA) diluted in DI water (Table 2-1). Phosphate solutions were then added into calcium solution in a dropwise manner by a peristaltic pump (Sci Q 400 Peristaltic Pump, Watson Marlow Ltd., Falmouth, UK) through a silicone pump tube (0.039 ×0.063" Platinum-cured peristaltic silicone pump tubing, Helix Medical Inc., CA, USA) with flow rate as 4 ml/min under constant stirring. After mixing the solutions, Cu-ZnHA, CuHA, ZnHA and HA precipitates were formed. Samples were continuously stirred and

maintained at 90 °C for 9 h. Differently, $FeCl_3$ and $MnCl_2$ solutions with different molar quantity were added after mixing the Ca and P solutions for the ion exchange process. The mixture was further stirred at 500 rpm at 98.5 °C for 2h. All precipitates were then aged for 2 days at room temperature, then filtered using a Whatman 542 grade filter paper of average pore size 2.7 µm (Whatman products plc, Cytiva, Little Chalfont, UK). The precipitates produced were washed with DI water for three times to remove all impurities. Afterwards, the precipitates were dried at 80℃ and ground to powder using a mortar and pestle and sieved by a 38-µm sieve (50×25mm, mesh size 0.038mm, VWR, Lutterworth, UK). Table 2-1 listed the amount of materials used in HA and ionic (co-)substituted HA synthesis in the project.

Table 2-1 Sample list of HA and MHA with various metal fraction that substituted into HA lattice structure.

Sources	Ca	Fe	Mn	P	Ca+M	(Ca+M)/P
Materials	$Ca(OH)_2$	$FeCl_3.6H_2O$	$MnCl_2.4H_2O$	H_3PO_4		
HA	0.2004 mol	-	-	0.1200 mol	0.2004	1.67
5FeHA (X_M=0.005)	0.1994 mol	0.0010 mol	-			
25FeHA (X_M=0.025)	0.1954 mol	0.0050 mol	-			
50FeHA (X_M=0.05)	0.1904 mol	0.0100 mol	-			
5MnHA (X_M=0.005)	0.1994 mol	-	0.0010 mol			
25MnHA (X_M=0.025)	0.1954 mol	-	0.0050 mol			
50MnHA (X_M=0.05)	0.1904 mol	-	0.0100 mol			
5(Fe-Mn)HA (X_M=0.005)	0.1994 mol	0.0005mol	0.0005mol			
25(Fe-Mn)HA (X_M=0.025)	0.1954 mol	0.0025 mol	0.0025 mol			
50(Fe-Mn)HA (X_M=0.05)	0.1904 mol	0.0050 mol	0.0050 mol			
Sources	Ca	Cu	Zn	P	Ca+M	(Ca+M)/P
Materials	$Ca(NO_3)_2{\cdot}4H_2O$	$Cu(NO_3)_2{\cdot}3H_2O$	$Zn(NO_3)_2{\cdot}6H_2O$	$NH_4H_2PO_4$		
HA	0.2004 mol	-	-	0.1200 mol	0.2004	1.67
0.5CuHA (X_M=0.0005)	0.2003 mol	0.0001 mol	-			
2.5CuHA (X_M=0.0025)	0.1999 mol	0.0005 mol	-			
5CuHA (X_M=0.005)	0.1994 mol	0.0010 mol	-			
0.5ZnHA (X_M=0.0005)	0.2003 mol	-	0.0001 mol			
2.5ZnHA (X_M=0.0025)	0.1999 mol	-	0.0005 mol			
5ZnHA (X_M=0.005)	0.1994 mol	-	0.0010 mol			
0.5(Cu-Zn)HA (X_M=0.0005)	0.2003 mol	0.00005 mol	0.00005 mol			
2.5(Cu-Zn)HA (X_M=0.0025)	0.1999 mol	0.00025 mol	0.00025 mol			
5(Cu-Zn)HA (X_M=0.005)	0.1994 mol	0.00050 mol	0.00050 mol			

X_M represents metallic content and it was calculated by X_M=(Metallic content)/(Metallic content +Ca).

2.2.2 Synthesis of Fe_2O_3 Nanoparticles

The IONPs were synthesized via the co-precipitation method that ammonium hydroxide was added as a stabilizing agent into ferric chloride solutions at an elevated temperature (Farahmandjou and Soflaee, 2015). 100 ml 0.5 M ammonium hydroxide (NH_4OH) solution was added into 150 ml 0.2 M iron(III) chloride hexahydrate ($FeCl_3{\cdot}6H_2O$) aqueous solution under 4kW sonication for 5 mins (Digital Sonifier 250,

Branson Ultrasonics, CT, USA) in order to precipitate colloidal $Fe(OH)_3$ from $FeCl_3 \cdot 6H_2O$. The mixture was poured into 300 ml 0.5 M NH_4OH aqueous solution and left to grow for 30 mins. Finally, the synthesized IONPs was washed with 7 times using centrifugation and DI water to remove all impurities.

2.2.3 Fabrication and Analysis Ball-tip Nozzles and Flat-tip Nozzle

To modify the nozzle geometry, ball-tip and flat-tip nozzles were fabricated by fixing extender caps at the tip of nozzles (Figure 2-1). The straight nozzle is 19 gauge (Hamilton™ 51mm 19-gauge stainless steel nozzles with luer lock, Hamilton Co., MA, USA), which has an outer diameter of 1.067 mm, an inner diameter of 0.686 mm and wall thickness as 0.191 mm. The extenders were made from acrylonitrile butadiene styrene (ABS) with a central hole that penetrated the whole structure. The diameters of the spherical structures are 2 mm, 4 mm, 6 mm, 8 mm and 10 mm. The diameter of the flat cap is 20 mm.

To compare the performance of ball-tip, flat-tip and straight nozzles, the hanging drop volumes of different nozzles were recorded. Different nozzles were vertically fixed in the nozzle stand and connected to a syringe pump via a silicone pump tube, which

supplies 0.24 wt% HA ethanol solution with a flow rate as 40 μL/min. The pumped solution was calculated by measuring the left solution in the syringe after collected 50 drops.

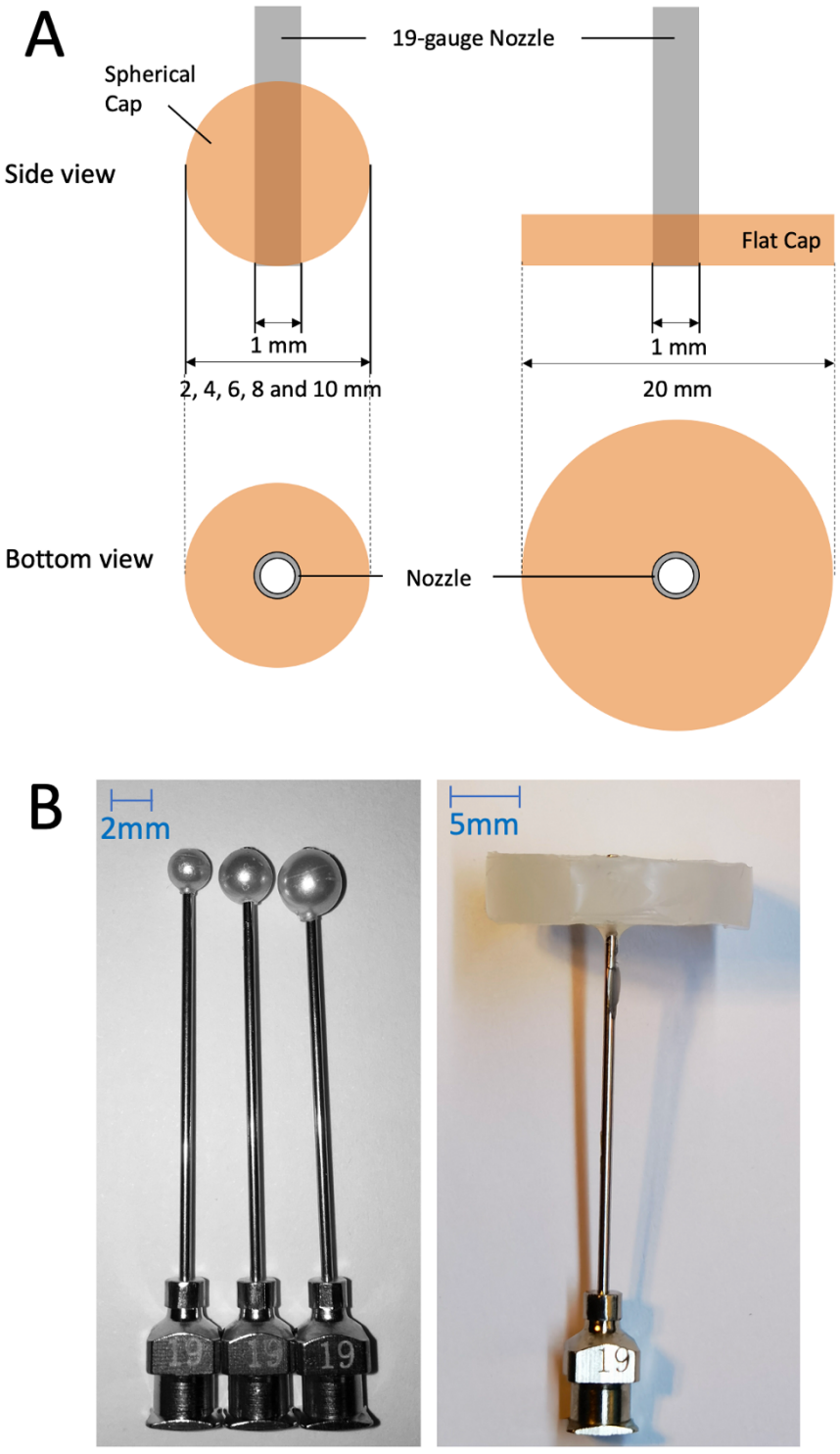

Figure 2-1 Ball-tip nozzles Structure

Image A is the diagram of the structure of ball-tip nozzles and flat cap nozzle. The size of spherical caps includes 2 mm, 4 mm, 6 mm, 8 mm and 10 mm. a flat cap equipped nozzle was also fabricated, that fabricated by penetrating holes (1 mm diameter) through ABS beads and insert the 19-gauge nozzles into the spherical structure. the size of flat cap is 20 mm in diameter.

2.2.4 Electrospraying

Before the electrospray process, all solutions were sonicated for 5 mins in 4kW power (Sonifier-BRANSON®) to break intermolecular interactions of nanoparticles in liquids. The solutions were collected by a 5 mL syringe (TERUMO® centric luer-tip syringe, 0.80x38mm/5ml, Terumo Co., Tokyo, Japan.) and pumped by a syringe pump (Infuse/Withdraw PHD 4400 Hpsi Programmable syringe Pump, Harvard Apparatus Ltd., UK. Pump calibrated by using silicone calibration oil – 500 (density 971 kg/cm3), VWR, Lutterworth, UK), which provided flow rate up to 320 ul/min. High voltages were applied by connecting the high voltage power supply (Glassman Europe Ltd., Hampshire, UK.) to the stainless-steel nozzle and connect the aluminum alloy holding plate to a ground cable (Figure 2-2). The high voltage provided an electrostatic force that elongates the solution and forms a cone-jet. The voltage applied to the needle could be up to 30 kV, and the collection distance between nozzle and collection plate was controlled by an aluminum alloy holding plate to control the deposition area (OHAUS™ Lab Lift, OHAUS Co. NJ, USA). Sample collection substrates including 10 x 10 mm and 75x50 mm glass slides (Corning® Plain Microscope Slides, Corning Life Sciences, NY, USA) and titanium plates (Provided by the department of mechanical engineering, UCL). In order to achieve consistent results, all tests involved in the EHDA performance section employed a standard solution, which contains 0.24 wt% HA

nanoparticles as solutes and ethanol as solvent so as to achieve stable suspension.

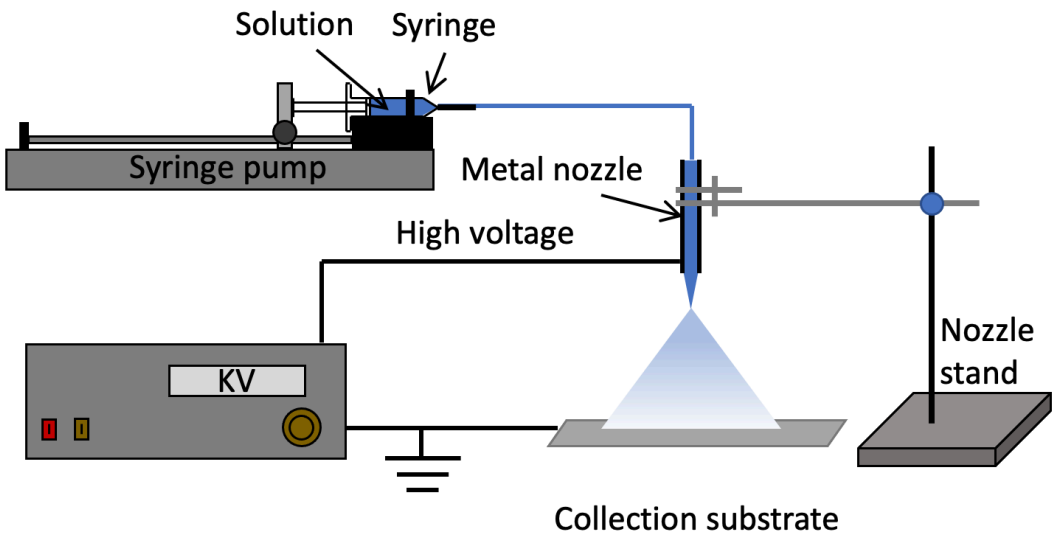

Figure 2-2 EHD set up

EHD spraying is composed of a nozzle, which connected to a high voltage and a ground electrode as the collection substrate. The liquid was pumped through the nozzle. By applying a high electric charge on the meniscus of liquid surface the small drop of liquid can be broken up into fine jets, which composed of an ionized meniscus (Taylor cone) and an aerosol plume. The ejected particles would move to the collection substrate and form a deposition.

a. Investigating Nozzle Geometry Effects on EHDA Processing

To compare the performance of ball-tip and straight nozzles, the electrospray mode perturbation of straight and ball-tip nozzles was recorded. The mode variation of both nozzles at a fixed flow rate as 15 µL/min were recorded by camera at 30 fps (frame per

second). The flow rate of 15 μL/min was chosen because the switch between 3 different spray modes can be observed for both types of nozzles within a small voltage range (6-12 kV) under this flow rate. The spray mode in each frame was identified and plotted out.

Besides the video recording, a more detailed investigation on the EHDA performance of different nozzles was based on creating a processing maps (cone-jet processing zone) via recording the voltage and flow-rate boundaries for cone-jet. The processing maps were created by recording the V_{MIN} and V_{MAX} of each fixed flow rate.

To compare the morphology of HA deposition using different nozzle, glass slides (75 mm × 50 mm for optical microscopy and 1 cm × 1 cm for SEM) were placed around 6 cm (with appropriate modification to maintain a constant coating area) underneath the nozzles and spraying for 1min at the flow rate of 15 μL/min in order to achieve samples that can distinguish the difference in their particles distribution. Then samples were analyzed by optical microscopy and SEM.

b. Investigating the solvent compatibility of different nozzles on cone-jet process

In order to investigate the influence of nozzle geometry on the solvent compatibility,

HA suspensions with different water-ethanol ratio were employed in ball-tip and flat-cap nozzles equipped EHDA systems to generate stable cone-jet. There were 7 different solvents were prepared, which varies in the water concentrations include 0% (pure ethanol), 5%, 20%, 40%, 60% and 80%. The processing maps of different solvents and different nozzles were plotted out.

c. Sample preparation for anti-biofilm formation and biocompatibility testing

HA and ionic (co-)substituted HAs were coated on titanium plates and glass slides via cone-jet electrospray with 196 ul/min flow rate for 30 mins in order to achieve the same metallic ions centration in culture medium comparing to antibacterial test. The deposition processes were performed on the fabricated 6 mm ball-tip nozzle and the round EHD deposition area was fixed to 3 cm in diameter and MHA nanoparticles were collected in 1 cm × 1 cm collection substrates. Therefore, around 14.1 wt% MHA (2 mg) that electrosprayed during the whole deposition process (5.8 ml 0.24 wt% MHA) can be collected in each collection plate.

d. Sample preparation for in vitro bioactive testing

Materials including the MHA ((5, 25, 50)Fe-MnHA), (5, 25, 50)MnHA and (5, 25,

50)FeHA), HA, IONPs and HA-IONPs mixture were coated (using 6 mm ball-tip nozzle) on glass slides (1 cm × 1 cm) for in vitro bioactive test. The deposition parameters used in this section was fixed to as 15 μL/min for 30 s to minimize their influence on deposition topography.

2.2.5 Magnetic Field and Templates Assisted EHDA

Different EHDA based coating methods including TAEA, magnetic assisted EHDA (MAEA) and MTAEA were employed to modify the distribution of magnetic nanoparticles (Figure 2-3).

The TAEA process can be considered as the EHDA process with a template placed above the collection substrate (Figure 2-3 A). The template used was Agar TEM grids 75 Parallel Bar Copper 3.05mm, Agar Scientific, Ltd., Essex, UK.

The MAEA process can be considered as a EHDA process with a magnet placed beneath the collection substrate (Figure 2-3 B). Three magnets (Magnet Expert Ltd., Nottinghamshire, UK) were used to provide a gradient of magnetic field and a control group without magnet were selected for observing the distribution of magnetic nanoparticles in the EHDA process.

The MTAEA process is based on a TAEA process that different magnetic fields were introduced to assist the distribution of nanoparticles. The MTAEA process has a template placed above the collection substrate and a magnet placed beneath the collection substrate (Figure 2-3 C). During the MTAEA and MAEA process, the collection surface was at the largest surface of these magnets. The collection distance were modified to ensure that the diameter of the sprayed particles matches the length of the magnet.

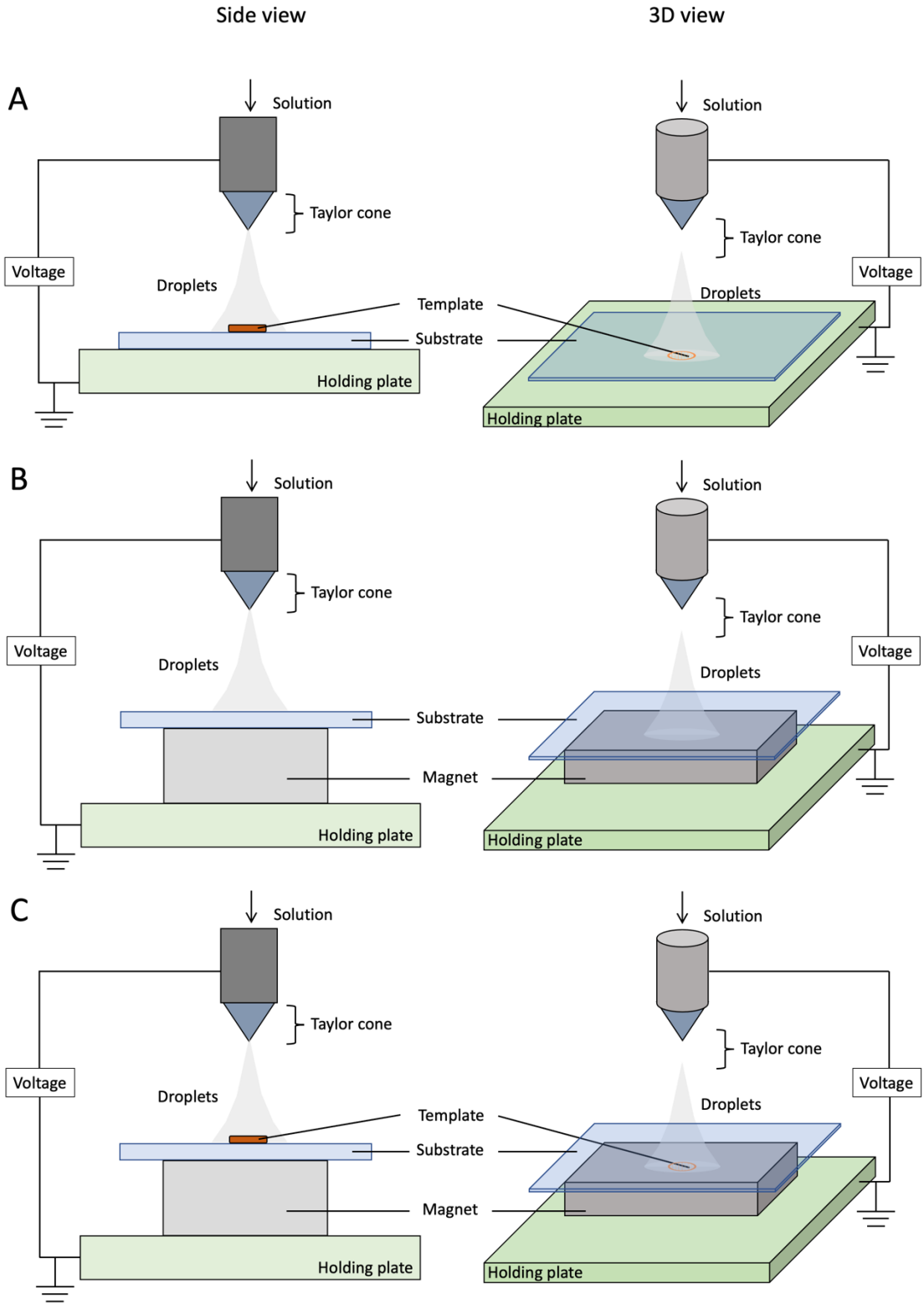

Figure 2-3 Diagram of device setting up of TAEA (A), MAEA (B) and MTAEA (C).

In order to select the regions on magnets that can form a gradient of magnetic strength, the magnetic flux density on the surface of magnets were simulated using ANAYS Maxwell, which is an electromagnetic field simulation software designed for analyzing a wide range of electromagnetic or magneto-static devices. In this study, the magneto-static solver can be applied. The magnetic field formulation was calculated through Ampere's Law and Gauss's Law shown as the following equations: (Eq. *(2-5)* and *(2-6)*):

$$\text{Ampere's Law: } \nabla \times \vec{H} = \vec{J} \qquad (2\text{-}5)$$

$$Gauss's\ Law: \nabla \times \vec{B} = 0 \qquad (2\text{-}6)$$

Where H is the magnetic field strength, J is the electric current density and B represents the magnetic flux density. The magnetization M can be calculated as below: (Eq. *(2-7)*):

$$\vec{B} = \mu_0(\vec{H} + \vec{M}) \qquad (2\text{-}7)$$

Firstly, the 3D magnetostatic solver, material, property and size of magnet was defined. The material of magnet was NdFe35, which had relative permeability as 1.0997785406, bulk conductivity as 625000 siemens/m and magnitude as -890000 A/m. The

magnetizing direction was also defined. Secondly, a sphere structure was defined to indicate the calculation domain. The radius of this sphere module was set as 100 mm, which could cover the whole magnet and give enough space for the calculation of magnetic field. The material fulfilled the sphere structure was defined as air. The surrounding parameters involved temperature and absolute pressure, which were set as 293.15 K and 1 atm. The magnetic insulation defined the boundary of magnetic fields simulation. the analysis region was assigned for all directions similarly to restrict the analysis region. Before analyzing specific properties, the boundary conditions were defined, which determined the magnetic field at the interfaces of the analysis region in order to apply the mesh on the object via the finite element method to solve the Maxwell equations. The Maxwell discretized the geometry of the problem into basic unit such as tetrahedral elements (average element quality was around 0.677 mm) by adding and building a free tetrahedral node to meet the required level of accuracy in field computation with a suitable computation time (around 2 mins). Then, the calculation was set on different points above the surface of magnets that added the thickness of applied glass slides (2mm) and considered the cover area of template (5 points were selected in the circle area of template of 8.35 mm^2), which is where the nanoparticles were collected. It can achieve the evaluations of numerical results globally or in a point. In this simulation, both global and points value evaluation were studied.

a. Investigating the MTAEA performance via optical microscopy and image analysis

Samples were analyzed under optical microscopy (Leica® DM750, Leica, Wetzlar, Germany). 4x100, 10x100 and 40x100 magnifications were used to observe the distribution and topography of nanoparticles. For analyzing the TAEA results, the width of lines in the patterns were taken as an important parameter. The gap between each line of the template was measured by image J (Figure 2-4 Left). To measure the width of lines in TAEA patterns, an aided complete circle was drawn in the image and two guidelines that indicate the horizontal and vertical directions were applied to help the measurement. Each line in the patterns were measured for five points by image J (Figure 2-4 Right).

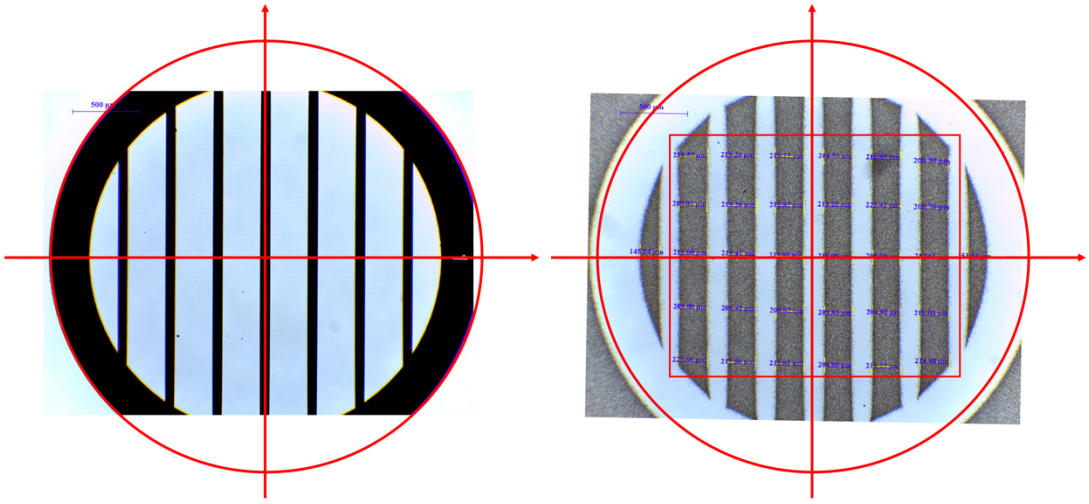

Figure 2-4 Measuring the TAEA template and TAEA patterns.
Optical microscopy photos of a TEM grid that used as a template in TAEA process (dark region) (Left) and a HA pattern collected by TAEA (Right). The red guidelines indicate the vertical and horizontal directions of the template. Each pattern has 30 fixed positions to be measured, five positions in each line (shown inside the red rectangle).

2.2.6 Heat Treatment

A heat treatment was employed to enhance the coating stability before in vitro tests. MHA nano-powders and depositions on titanium plates were placed in a nitrogen gas supplied tube furnace for 8h warming (from 20℃ to 400℃, warming rate was +47.5 ℃/h), 4 h heating at 400 °C and 8h cooling (from 400℃ to 20℃, cooling rate was -47.5 ℃/h). The warming and cooling rates were determined to prevent the potential hot tearing to coating layers.

2.3 Characterization of subHA

HA and metallic ions (co-)substituted HAs were characterized by XRD, FTIR, SEM and EDS to observe the influences of metallic content on their crystallinity, crystal size and the morphologies.

2.3.1 Powder X-Ray Diffraction (XRD)

In order to investigate the composition of synthesized materials, a powder X-Ray diffraction (PXRD) was performed. PXRD is a widely used XRD technique for characterizing materials owing to the accurate results and low manipulation difficulty.

XRD is a technique that can detect the atomic and molecular structure of crystal. XRD (STOE® STADI-P; Mo Kα1, STOE & Cie GmbH, Darmstadt, Germany) was used to analyse the crystalline phase structure of the as prepared and heat-treated materials. The XRD was operated at 50kV and 30mA. The reflection angle 2θ ranged from 2° to 40° with step size as 0.5°.

The acquired XRD patterns are normally consists of a series of peaks with different intensities, which are corresponds to the x-ray diffracted from a specific set of planes in the sample. The phase identification relies on the strongest reflections from the sample, the peak position depends on the crystal structure of the materials, the width of peaks reflects the crystallite size and the presence of lattice distortions. The acquired XRD patterns of samples were compared to ICDD (International Centre for Diffraction Data) database to identify the material compositions.

According to the direction (peak position) and intensities of x-ray beams, the atomic structure of crystals can be derived. The term of 'unit cells' (Figure 2-5) represents the periodically repeated identical structural units in space, which can be defined via three vectors, a, b and c and interaxial angles between them, α, β, and γ. The repeat distance of the unit cells determines the directions of diffracted x-rays and the arrangement of atoms in each unit cell determines the intensities of the diffracted beams.

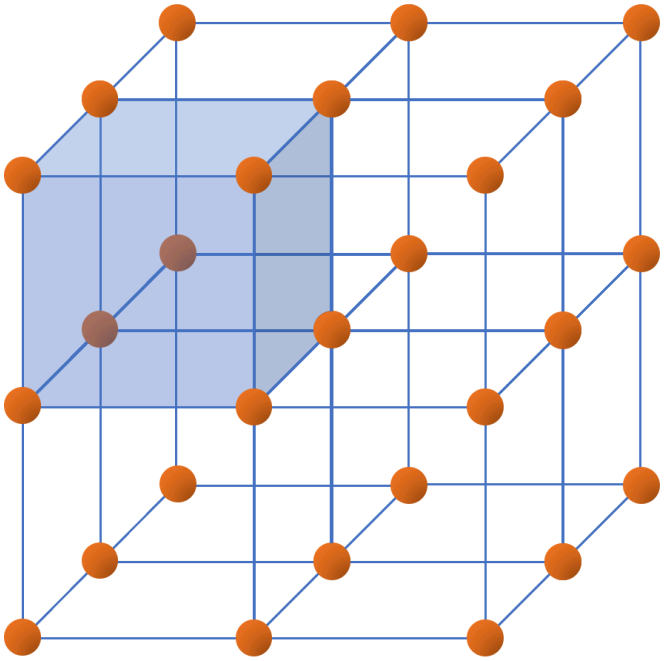

Figure 2-5 A unit cell is the smallest repeating portion of a crystal lattice

The lattice parameters were calculated by Rietveld refinement method. The hexagonal unit cell volume of (V) of the as-prepared materials were calculated using (Eq. *(2-8)*):

$$V = (a^2 \mathrm{c}) \sin 60^{\circ} \qquad (2\text{-}8)$$

The crystal size of the precipitates was calculated based on Scherrer equation: (Eq. *(2-9)*):

$$D_{hkl} = k\lambda / B_{1/2} \cos \theta_{hkl} \qquad (2\text{-}9)$$

Where, D_{hkl} is the average crystallite size, k is a constant as 0.9, which represents

crystallite shape factor, λ is the X-Ray wavelength (0.70930 Å), $B_{1/2}$ is the line broadening in radians, θ_{hkl} = Bragg angle; The crystallinity X_c was calculated based on: (Eq. *(2-10)*):

$$X_C = \left(K_A / B_{1/2}\right)^3 \quad (2\text{-}10)$$

In which K_A is a constant set at 0.24 and $B_{1/2}$ is the FWHM (Full width at half maximum) of the (002) reflection. X_c stands for the fraction of the crystalline phase in a sample volume.

2.3.2 Fourier-Transform Infrared Spectroscopy (FTIR)

The functional groups within the synthesized materials were analysed by FTIR spectrometer (FTIR spectrometer, PerkinElmer® Spectrum two FT-IR spectrometer, PerkinElmer Inc., USA), ranging from 400 to 4000 cm^{-1} with 64 number of scans and 4 cm^{-1} resolution. FTIR was conducted on pure Fe-MnHA, Cu-ZnHA, FeHA, MnHA, CuHA, ZnHA and HA powders.

2.3.3 Scanning Electron Microscopy (SEM) and X-ray Analysis Spectroscopy (EDS)

The morphologies and elemental analysis were identified using SEM (ZEISS EVO-25 SEM, Carl Zeiss, Germany), equipped with energy-dispersive X-ray analysis spectroscopy (EDS) with a field emission electron gun operated from 5 to 20 kV. In order to enhance the electrical conductivity, all samples were insulated by coating gold layer on sample surface via a sputtering machine (Quorum® Q150R Rotary-Pumped Sputter Coater, Quorum Technologies, East Sussex, UK) for 15 mins before placing into SEM chamber.

2.4 In vitro Biological Tests

The biological performance of HA and metallic ions (co-)substituted HAs were further analyzed by different in vitro biological tests, including the in vitro bioactivity test, antibacterial test, antibiofilm formation assays and biocompatibility test via cell proliferation assay.

2.4.1 In vitro Bioactivity Test

In order to test the bioactivity of synthesized subHA, an in vitro bioactivity test based on simulated body solution (SBF) was employed. SBF is made popular by Prof. Tadashi Kokubo as a tool of processing the material prior to its implantation (Kokubo, 1990). If the material immersed in the SBF solution contains Ca^{2+} ions in its crystalline structure and if Ca^{2+} ions leach into the solution, it will increase the Ca/P molar ratio of SBF solution (initially 2.50) and precipitate nanoparticles of apatitic CaP (Jalota et al., 2006, Kokubo and Takadama, 2006, Bohner and Lemaitre, 2009). Many different SBF solutions have been investigated, among which the Tas-SBF is the most related SBF mimics the composition of the electrolyte of the human blood plasma, while other SBF solutions such as c-SBF and r-SBF have significant (HCO_3^-) bicarbonate ion-deficiency (Table 2-2) (Jalota et al., 2006, Kokubo and Takadama, 2006).

Table 2-2 Ion concentration of human plasma and synthetic solution, mM

	Blood plasma	Kokubo c-SBF [1]	Tas-SBF [2]	Kokubo r-SBF [3]
Na^+	142.0	142.0	142.0	142.0
K^+	5.0	5.0	5.0	5.0
Ca^{2+}	2.5	2.5	2.5	2.5
Mg^{2+}	1.5	1.5	1.5	1.5
Cl^-	103.0	147.8	125.0	103.0
HCO^{3-}	27.0	4.2	27.0	27.0
HPO_4^{2-}	1.0	1.0	1.0	1.0
SO_4^{2-}	0.5	0.5	0.5	0.5
Ca/P	2.5	2.5	2.5	2.5
Buffer		TRIS	TRIS	HEPES
pH	7.4	7.4	7.4	7.4

[1]:(Kokubo, 1990), [2]:(Bayraktar and Tas, 1999), [3]:(Oyane et al., 2003).

The SBF synthesis was followed by the protocol provided by Kokubo (Kokubo and Takadama, 2006). In order to prepare 1000 ml of SBF, 700 ml of ion-exchanged and distilled water was first poured into 1500 ml plastic beaker. The beaker was set in water bath to 36.5±1.5 ℃ under stirring and covered. In the first stage, only the 1st to 8th reagents following the order in table 2-3 were dissolved into the solution at 36.5±1.5 ℃. In the next step, the pH was adjusted to 2.0±1.0 when the 9th (TRIS) and 10th (HCl) reagent were added. Specifically saying, before adding the TRIS, the temperature was firstly adjusted between 35 and 38℃. Then, TRIS was added into the solution little by little by monitoring the pH change. Every time, only when TRIS was completely dissolved and the pH became constant again, more TRIS could be added. This process was stopped when the pH was raised to 7.45±0.01. After that, 1M-HCl and TRIS were used alternatively to maintain the pH between 7.42–7.45 until all TRIS was dissolved. The low pH environment was required to neutralize the pH raise caused by TRIS. TRIS was added slowly and use HCl to control the pH to avoid the rapidly increase of pH. Following that, the pH of the solution was further adjusted into 7.42±0.01 by dropping 1M-HCl and adjusting the temperature to 36.5℃. Afterwards, the solution was cooled down to 20 ℃ and added distilled water to 1000 mL. Prepared SBF was preserved in a plastic bottle at 5-10℃.

Table 2-3 Material list in SBF synthesis

Order	Reagent	Weight (g/L)
1	NaCl	9.8184
2	$NaHCO_3$	3.4023
3	KCl	0.5591
4	Na_2HPO_4	0.2129
5	$MgCl_2 \cdot 6H2O$	0.4574
6	1 M HCl	15 mL
7	$CaCl_2 \cdot 2H_2O$	0.5513
8	Na_2SO_4	0.1065
9	TRIS	9.0855
10	1 M HCl	50 mL

The volume of SBF used for testing was calculated via the following (Eq. *(2-11)*):

$$V_s = S_a/10 \qquad (2\text{-}11)$$

where V_s is the volume of SBF (ml) and S_a is the apparent surface area of specimen (mm^2). Materials were coated on 100 mm^2 glass slide, the required volume of SBF for each sample was 10 mL. Therefore, for each sample, 10 mL of SBF was first poured into a plastic bottle and heated to 36.5 ℃ and tested sample was submerged in the SBF (Figure 2-6). After soaking at 36.5 ℃ for different periods including 2, 4 and 7 days in the SBF (the SBF was changed every 48 hours), the tested sample was taken out from the SBF, washed with DI water and dried. The SEM observation was applied to observe the material formation on the specimens.

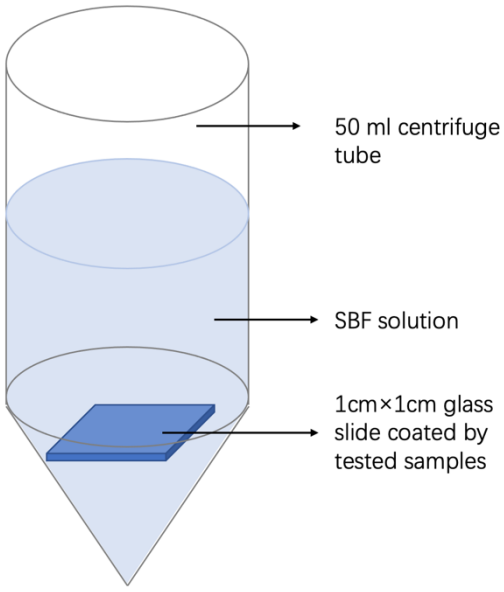

Figure 2-6 Diagram of sample placing in the in vitro bioactivity testing
Tested samples were coated on a 1cm×1cm glass slide and soaked in 10 ml SBF solution in a 50 ml centrifuge tube.

2.4.2 Bacteria Culture

Bacteria strains employed in this antibacterial and antibiofilm assays including modified strains *E. coli* ATCC K12 and *S. aureus* ATCC 6538, which can only proliferate under specific conditions and cannot survive in human gut. The LB broth used for culturing bacterial strains was prepared by adding 20g LB broth powder into 1 L DI water and sterilized at 121 ℃ for 15 mins. Afterwards, the prepared LB broth were stored in fridge at 4 ℃ for the following usage. 30 mL sterilized LB broth were added into each 50 mL sterilized culture bottle. Two bottles of *E. coli* and two bottles of *S.*

aureus were prepared by inoculating one colony of bacteria into each bottle. Then these four bottles were placed into a shaker (37 ℃, 250 rpm). The optical density (OD) of bacteria broth were measured at every one hour after the inoculation of bacteria in the first 7 hours, as well as at the 24th hour. Each time, 4 mL bacterial broth was analyzed by OD test to check the growth condition.

In the antibacterial test, 0.1 g of heat-treated MHA and HA powders were added into 9 mL LB broth respectively to achieve a stable suspension. All broths were sterilized at 121 ℃ for 15 mins. Then, the bacteria stock was diluted by LB broth to achieve OD=0.1 at 600 nm wavelength. This process guaranteed the bacterial broths that used in antibacterial test contain the same number of bacterial cells. 1 mL diluted broth was then inoculated into the 9 mL MHA containing LB broth. Afterwards, all solutions were cultured at 37 ℃ and shaking at 250 rpm for 24 hours. The control group contains a pure LB broth sample and a “live/dead” control samples prepared by heat treatment in water bath (90 ℃, 15 mins) and mixed with another half of live bacteria.

2.4.3 Antibacterial and Anti-biofilm Formation Tests

The antibacterial ability of Cu-ZnHA, CuHA, ZnHA and HA were tested according to the live/dead cell ratio by flow cytometry, a biotechnology that use laser or impedance to

count or sort cells. In this project the alive and dead cells were distinguished by detecting the different fluorescence colors in cells after staining with Invitrogen™ Live/Dead® BacLight™ Bacterial viability kit (Cell viability flow cytometry staining kit, Invitrogen™ L7012 Live/Dead® BacLight™ Bacterial viability kit, Molecular probes, Inc. OR, USA).

To prepare samples for flow cytometry analysis, bacterial broth was diluted by filtered sterilized deionized water for 1:100 by adding 10 µL bacterial broth into 990 µL filtered sterilized DI water. The stain that used to distinguish live and dead bacteria cells were prepared by adding 9 µL red-fluorescent nucleic acid stain (propidium iodide (PI)) and 9 µL green-fluorescent nucleic acid stain (SYTO9) into 6 mL filtered sterilized DI water. Then 20 µL diluted bacterial broth was added into 180 µl prepared stain and cultured in dark for 15 mins. During the measurement, each sample was inserted into the flow cytometer (Flow cytometer: Guava® easyCyte™ flow cytometer, Luminex Co. TX, USA) to measure the cell maps (Figure 2-7).

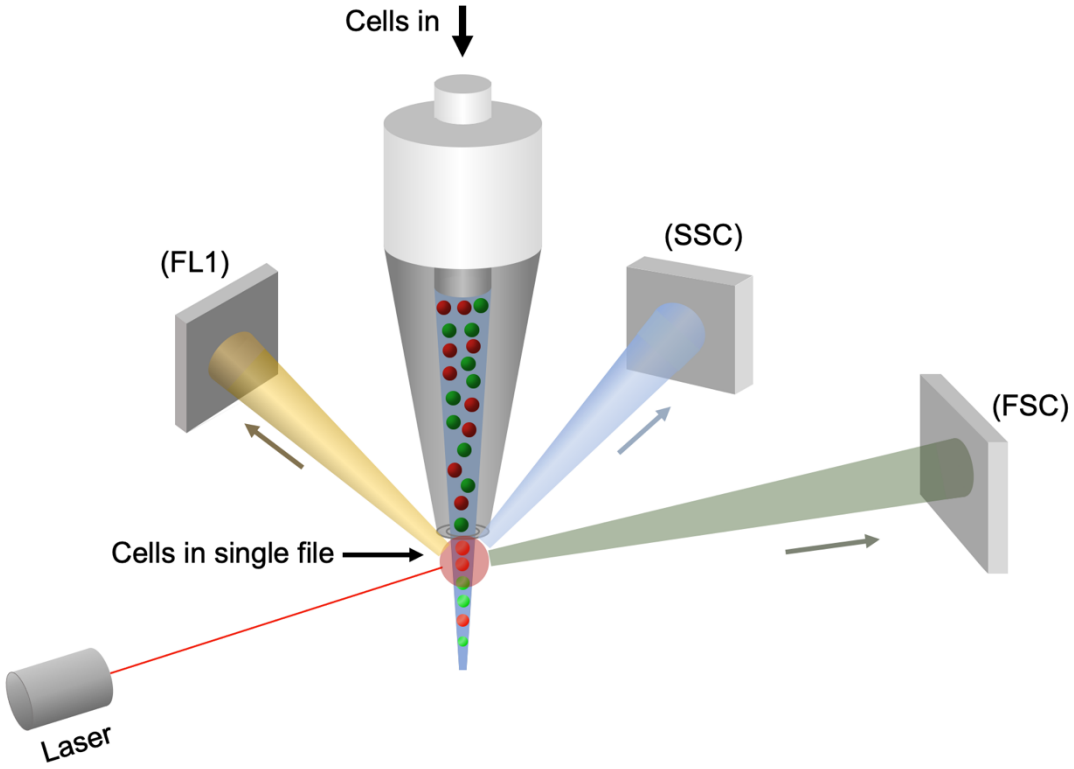

Figure 2-7 Schematic of flow cytometry cell counting.
Cells suspended in a core stream (blue) and interrogated by an excitation laser beam. Cells in the stream are detected by light scattered through the cells forward scatter (FSC) and orthogonal to the cells side scatter (SSC); fluorescently labeled cells are detected by emitted fluorescent light (FL1). Following detection of FSC, SSC, and FL1 signals, the cell numbers and different fluorescens signals of cells can be recorded. Figure re-drawn with permission from the Journal of Immunology (Jaye et al., 2012).

The determination of live and dead cells was based on the intensity of red (PI) and green (SYTO9) fluorescence that detected by flow cytometer. The analysis of the

numbers of live and dead cells was based on a flow cytometry analysis software package (FlowJo™). In the plotted analysis pattern, bacterial cells with damaged membranes that stained with less green fluorescence were appeared on the left-side, while bacterial cells with intact cell membranes that only stained by green fluorescence were appeared on the right side (Figure 2-8). Before the analysis of bacterial broth, a pure LB broth data was analyzed to set the threshold that remove all background noise. Then a heat-treated sample (bacteria live : dead =1 : 1) was used to gate the area for bacterial live and dead cells. Therefore, in the other tested samples, the cell numbers inside both live and dead gate can be counted by FlowJo™. The antibacterial abilities of MHA were marked by the killing percentage, which were calculated by the following formula: (Eq. *(12)*):

$$Killing\ percentage = \frac{Dead\ bacteria}{Alive\ bacteria + Dead\ bacteria} \qquad (2\text{-}12)$$

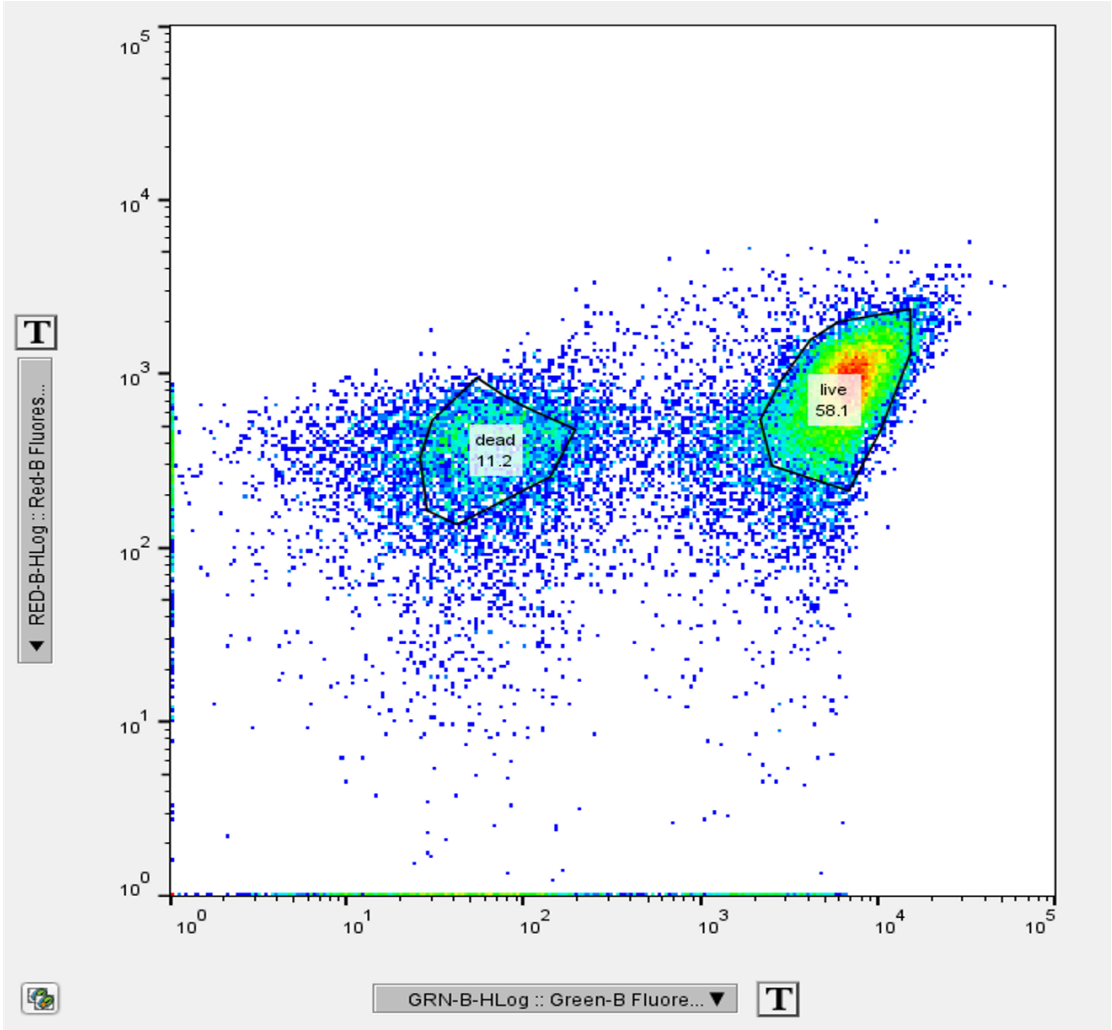

Figure 2-8 The live/dead gating analysis of flow cytometry patterns of a Live/Dead sample.

The X axis is “GreenB-H-Log”, which represents the intensity of green fluorescence and Y axis is “RedB-H-Log”, which represents intensity of red fluorescence. Red PI can enter damaged cells and stain the nucleic acid of dead bacteria, which makes another nucleic acid stain, green SYTO9, less detected, thus appear on the left-hand side of the pattern. However, bacterial cells with intact cell membranes were only stained by green SYTO9 and thereby on the right side of the pattern.

Cu-ZnHA, CuHA, ZnHA and HA deposited titanium plates were also employed in the antibiofilm formation test against *E. coli* and *S. aureus*. *E. coli* and *S. aureus* are ideal strains because they have been frequently incubated in liquid medium to distinguish the attach-preferred bacterial cells from the whole population. Tryptone Soya Broth (TSB) with the addition of 1% glucose was prepared to enhance the bacterial attach ability. 30.12 g TSB powder (CM0129 casein soya bean digest broth) and 10 g glucose (D-(+)-Glucose (≥99.5%)) were added into 1 L DI water to form the TSB culture broth. At the beginning, tested strains were transferred from the stock culture onto LB agar and then incubated overnight (37 ℃, aerobically). Then, three to four colonies were cultivated in TSB + 1% glucose broth at 37 ℃ without shaking for 18 hours. After the incubation, the aqueous-phase of the culture was removed and the stationary-phase was vortexed and diluted 1: 100 in TSB with 1% glucose. The diluted bacteria were mixed and added into a 24 well microtiter plate (10 μL per well), which contained the various MHA and HA samples coated on titanium plates. The total volume of TSB in each well was 200 μL. The inoculated plate was incubated aerobically for 24 hours at 37 ℃. After incubation, the content of the wells was removed and the bacteria was washed 3 times by 1.5 mL PBS (pH 7.2). Then the titanium plates were drained, and the remaining attached bacteria were fixed by 750 μL methanol for 20 mins. Following fixation, the titanium plates were dried overnight at room temperature.

The staining process was performed after the fixation. The adherent biofilm formed on MHA and HA samples was stained with 1 mL of crystal violet (2% Hucker's crystal violet) for 15 mins. Then, the excess stain was rinsed off by tap water. Thereafter, the microplate was air dried and the dye stained on the cell wall was resolubilized in 1 mL 95% ethanol to elute stains from attached cells. Ethanol was gently added and thereafter the plate was covered with the lid and kept at room temperature for 30 mins. The number of attached bacteria can be represented by the optical density (OD) of the eluted solution. The OD of eluted stain was measured by a microtiter-plate reader (570 nm). The inhibition of biofilm can be denoted as the reduced OD relative to non-treated control group using the following formula: (Eq. *(2-13)*):

$$I_{Biofilm} = \frac{(OD_{standard} - OD_{MHA})}{OD_{standard}} \times 100\% \qquad (2\text{-}13)$$

In which, the $I_{Biofilm}$ refers to the inhibition against bacterial biofilm formation, $OD_{standard}$ reveals the eluted stain level of the biofilm formed by bacteria on titanium plates. OD_{MHA} reveals the eluted stain level of the biofilm formed by bacteria on MHA deposited titanium plates.

2.4.4 Biocompatibility Test

The biocompatibility test based on osteoblast-like cells MG63 of the synthesized MHA were investigated via alamarBlue® cell proliferation assay, which provided a rapid, sensitive, economical and reliable way to quantitatively measure cell proliferation rate. AlamarBlue® contains a fluorescent blue indicator (resazurin). Resazurin is an oxidation-reduction (REDOX) indicator that can demonstrate the cellular metabolic reduction via colorimetric change into pink color. The intensity of fluorescence is related to the living cells respiring (O'brien, 2000).

In the cell culture step, firstly, the MG63 cells were cultured in a high-glucose DMEM contains 10% FCS, 1% penicillin, and 1% L-glutamine for 48 h at 37 °C with 5% CO_2. Afterward cells were detached using Trypsin/EDTA. Secondly, resuspended the trypsinized cells with 5 mL medium and centrifuged at 800 × *g* for 5 mins. Thirdly, remove the supernatant was removed and added fresh media to resuspend cell pellets.

In the cell proliferation assay step, the alamarBlue® reagent was diluted as 1 : 10 with normal growth medium. MG63 cells were then dispersed, suspended and seeded onto coated titanium plate samples (steam-sterilized) with a population of 1×10^4 cells in a 24-well plate. Seeded cells were left for 2 hours in the incubator (37 °C, 5% CO_2, 95%

air) to allow cell-substrate adhesion and 200 µL of complete medium was added to each well and incubated overnight. During the culturing period, the medium was replaced every 2 days. At 1, 5 and 10 days, 10% culture medium in each well was replaced with alamarBlue® medium. This cell proliferation assay was carried out by Dr. Zhiyu Yuan using MHA samples prepared in this project. Then the plate was incubated at 37 °C, 5% CO_2 for 4 hours and 100 µL of the supernatant was removed from each well and added to a 96-well plate. Fluorescence of the supernatant was measured via a fluorescence plate reader at wavelengths of 530-570 nm (excitation) and 590-600 nm (emission).

Chapter III

3 Ball-tip-Nozzle – a Novel System Producing a Stable Cone-jet in Electrohydrodynamic Atomization

3.1 Introduction

The electrospray cone-jet can only be stabilized in a limited range of voltage and flow rate, which is a bottleneck for its application. (Dastourani et al., 2018). Although a multi-jet can produce finer droplets, the cone-jet was still widely employed in implant coating process owing to its advantage in evenly distributing droplets with more consistent size (Suh et al., 2005). Therefore, it is important to increase the stability of electrospray cone-jet, thereby to promote the coating efficiency and quality.

The EHDA process can be limited by the physical and chemical properties of the solvent such as volatility, electrical conductivity and electrolytic concentrations (Hogan Jr et al., 2007). To date, many researchers use organic solvents such as alcohols, acetone or ketones as solvent in electrospray due to their high volatility and low electrical conductivity and also because many substances can be dissolved and form stable solutions in these organic solvents (Green et al., 2010). However, the most common

solvent in nature is water, which is capable of dissolving many substances. Moreover, water is an ideal solvent for biomedical applications due biocompatibility and non-toxicity. However, water-based solutions are not suitable for electrospray cone-jet due to the high surface tension, low evaporation rate and high conductivity, which make the cone-jet very unstable (Lastow and Balachandran, 2007).

To solve these problems, the key is to enhance the cone-jet stability, which may be achieved via modifying the geometry of nozzles. It is supported by previous study that increased the attaching area for alcoholic solvents, which extends the voltage and flow rate margin for a cone-jet (Morad et al., 2016). In this chapter, the effects of ball-tip nozzles on the cone-jetting of HA suspensions have been investigated via the following detailed objectives:

i. Comparing the performance of different nozzles on electrospraying.

ii. Studying the effect of modifying nozzle geometry in stabilizing the electrospray cone-jet and increasing the coating efficiency.

iii. Evaluation of processibility of electrospray cone-jet with ball-tip nozzles for aqueous suspensions.

3.2 The Effect of Ball-tip Size on the Stability of Electrospray Cone-jet

To investigate the influence of ball-tip size on the performance of electrospray cone-jet, a straight nozzle, 5 ball-tip nozzles with different cap diameters (2 mm, 4 mm, 6 mm, 8 mm and 10 mm) and a flat cap equipped nozzle were used in the following experiments.

Firstly, the hanging drops on different nozzles were evaluated, the volume of hanging drops are shown in figure 3-1. The volume increased for 5 times with increasing the ball-tip size from 2 mm to 6 mm and reached the peak at 6mm, then the volume decreased for a further increase of the nozzle size from 6 mm to 10 mm and further to a flat cap. Hence, the 6mm ball-tips supported the largest volume of hanging liquid drop among all types of nozzles.

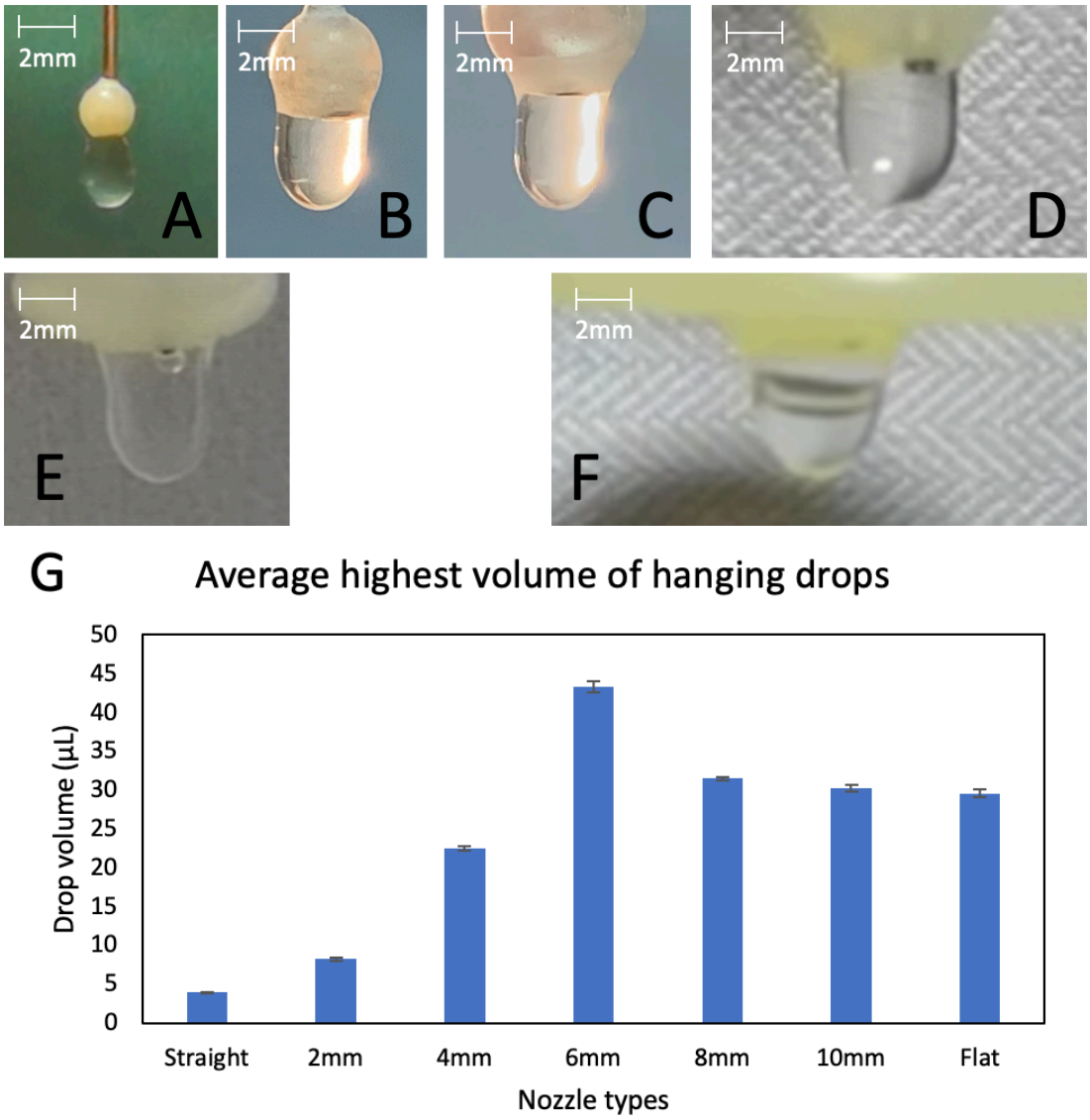

Figure 3-1 Hanging drops and corresponding average volume on different nozzles
Photos were captured by fixed camera which recorded the dripping conditions of different nozzles. The nozzle types from (A) to (F) are 2mm, 4mm, 6mm, 8mm, 10mm and flat cap equipped nozzles respectively. (G) The average hanging drop volume of different nozzles. Data are presented as mean ± SD (n=3). Error bar represents standard error.

The EHDA performance of different nozzles was evaluated according to a processing map composed by the applied voltages and flow rates (Figure 3-2). A common

phenomenon for all nozzles is both V_{MIN} and V_{MAX} for cone-jet were increased in proportion to the flow rate. However, an obvious difference between ball-tip nozzles and straight nozzle was the ball-tip nozzles have wider voltage ranges for cone-jet mode. Comparing ball-tip nozzles from 2 mm to 6 mm, no significant difference on the V_{MIN} was observed, but the V_{MAX} were increased in proportion to the cap size, which indicates the increase of cone-jet processing zone according to the extender cap size. However, the further increase in the ball-tips from 8 mm to a flat tip have shown reduced processing zone. This is due to the increase of ball-tip size from 8 mm has increased the required voltage to maintain the conical structure of liquid. Moreover, in such a high voltage, the cone-jet became very unstable and can switch into a multi-jet frequently. Besides the voltage range, the maximum flow rate for a stable cone-jet also varies between different nozzles. As shown in figure 3-2, the maximum flow rate of straight nozzle was 30 μL/min, while it increased into 320 μL/min when equipped with ball tip nozzles from 2 mm to 6 mm. Further increase the cap size reduced the maximum flow rate into 240, 200, and 60 μL/min for 8mm, 10 mm and flat-tip nozzles respectively. Therefore, increase the ball-tips larger than 6 mm have shown negative influences on the manipulation difficulty.

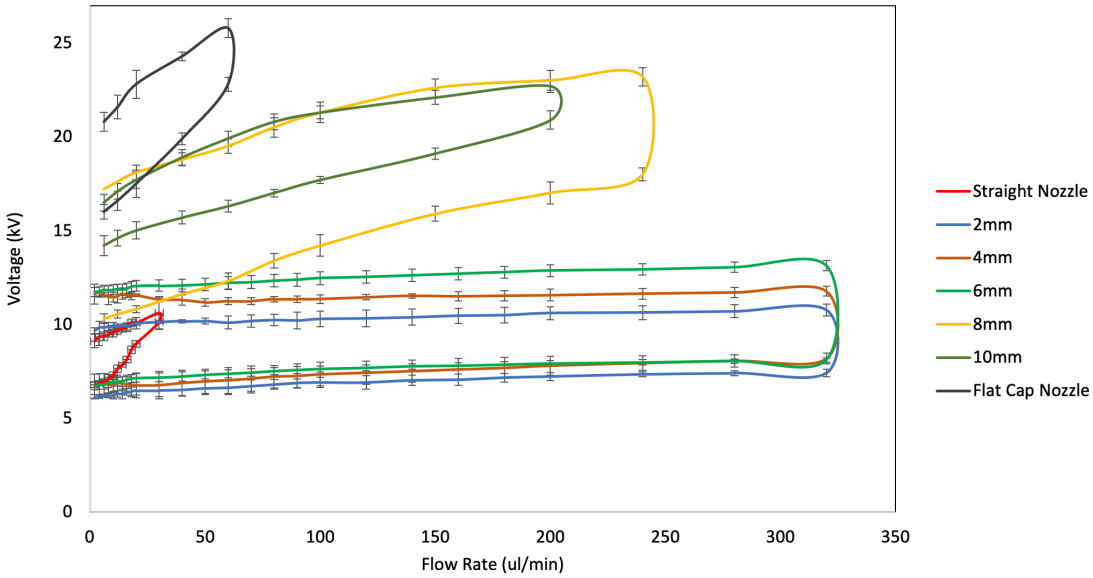

Figure 3-2 The processing map of straight nozzle and ball-tip nozzle with different extended cap size.

The characteristics of this processing (voltage-flow rate) map was based on a 0.24 wt% HA-ethanol suspension by using both straight and ball-tip nozzles. The x-axis indicated the flow rate and the applied voltage was depicted in y-axis.

Data are presented as mean ± SD (n=3). Error bar represents standard error.

The 2-, 4- and 6-mm ball-tip nozzles have stabilized the cone-jet with relatively suitable voltages comparing to larger ball-tip equipped nozzles. Especially the 6 mm nozzle, which can support the largest amount of liquid hanging drop that effectively stabilized the cone-jet when the liquid consumption in electrospray mismatches the pumping rate. It provided the widest processing zone that significantly reduced the manipulation difficulty. Therefore, the 2-, 4- and 6-mm ball-tip nozzles were employed in the following experiments to further investigate the influence of ball-tip nozzles on the coating morphologies and solvent extension.

3.3 Stability of Ball-tip Nozzles Equipped Cone-jetting

In both types of nozzles, with the increase of applied voltage, the electrospray mode switched from dripping mode to cone-jet mode and then to multi-jet mode (Figure 3-3). Under a low voltage (e.g. <6.9 kV), both straight nozzle and ball-tip nozzles exhibited dripping mode. With a high voltage (e.g. >10.2 kV for straight nozzle and >11.5 kV for ball-tip nozzles), the cone-jetting structure split and form a multi-jet mode. Only when the voltage was within a certain voltage range (e.g. 6.9 to 10.2 kV for straight nozzle and 6.9 to 11.5 kV for ball-tip nozzles), a cone-jet can be sustained.

The EHD mode switching in a straight nozzle and a 6 mm ball-tip nozzle were recorded and plotted in Figure 3-4. The electrospray using ball-tip nozzles could easily keep in one type of condition without perturbation. No perturbation was observed within 6.9 to 11.5 kV. However, the cone-jet of straight nozzle was relatively unstable. With the increase of the voltage, the intermittent switch between different modes occurred persistently in straight nozzles. Within the voltage range from 6.9 to 10.2 kV, the cone-jet mode appeared most often, but with a voltage ranges from 6.9 to 8.5 kV, the frequency of dripping mode was higher than multi-jet mode and when voltage raised from 8.5 to 10.2 kV, the frequency of multi-jet mode became higher than dripping mode (Figure 3-4 B).

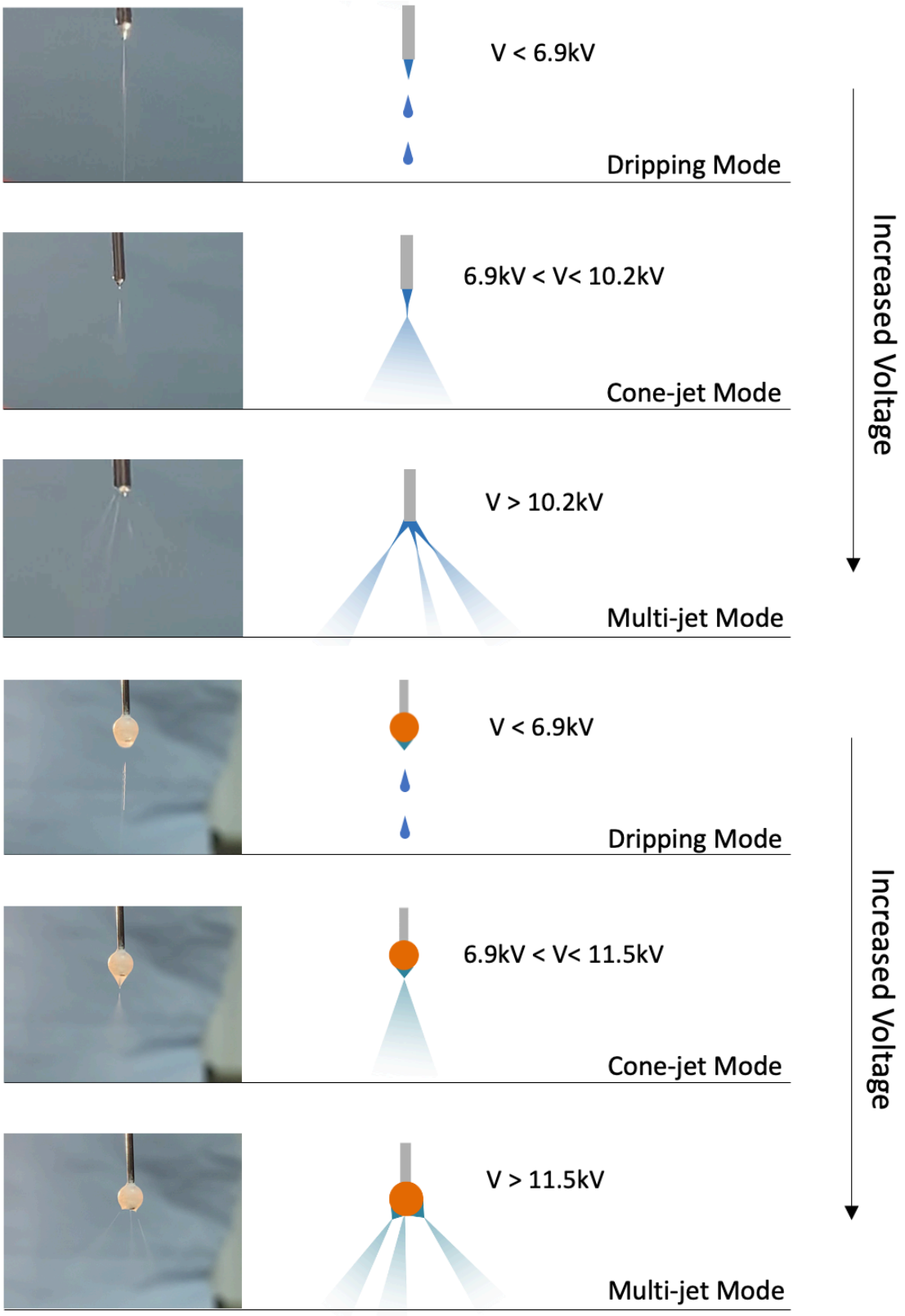

Figure 3-3 EHD performance of a straight nozzle and a 6 mm ball-tip equipped nozzle.

The images show photos with sketches of a dripping, cone-jet and multi-jet modes.

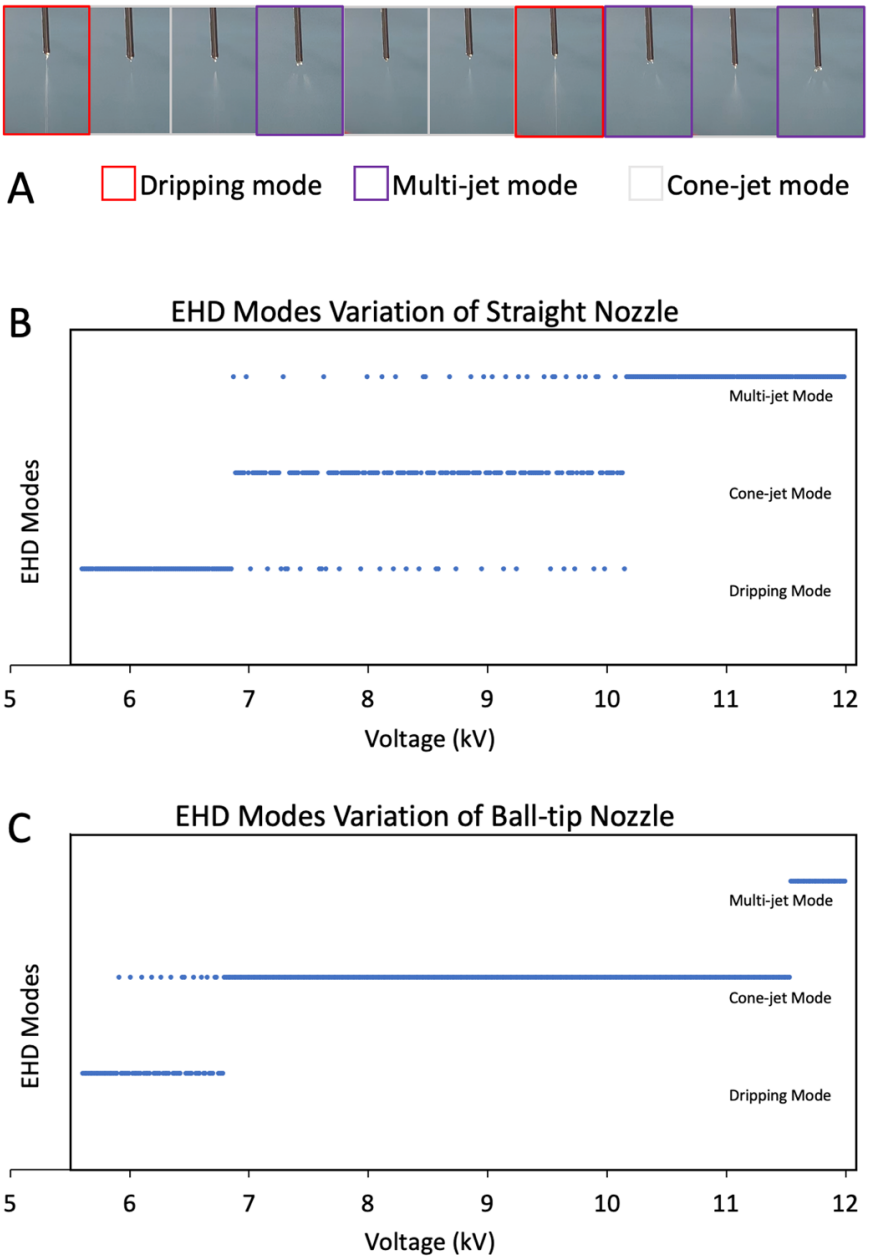

Figure 3-4 Comparison of EHD Modes Variation between straight and ball-tip nozzles.

(A) 10 frames of a high-speed video (30 fps) observed the spray mode switching of straight nozzle. (B) The switch of EHD spray modes with straight and (C) ball-tip equipped nozzles according to the increase of voltage (5.5kv-12kv) . The suspension used in this test is 0.24wt% HA; The flow rate was fixed as 15 µL/min. A 19-gauge nozzle was employed as straight nozzle. Another 19-gauge nozzle equipped with a 6mm ball-tip was used in ball-tip nozzle group. Two 30 fps videos were taken to record the mode shifting of different nozzles, while voltage was slowly increased. Each dot indicates the EHD mode in one frame.

3.4 Effect of Ball-tip Nozzles to the Coating Topographies

The advantage of the ball-tip nozzle is not only on promoting cone-jet stability, but also on the uniform coating topographies. The coating topographies of 6 mm ball-tip nozzle was further compared to the straight nozzle. HA samples collected by electrospray in different conditions were observed by SEM to compare the influence of nozzle types and coating voltage on the particle morphologies (Figure 3-5).

Results showed in the ball-tip-nozzle, the droplet size of HA decreased with the elevation of voltage (Figure 3-6). With the same deposition time, flow rate and HA concentration in suspensions, a smaller droplet size and uniform distribution of HA nanoparticles normally lead to less accumulation of nanoparticles. With the same coating condition (15 µL/min, 6 kV and 9 kV), ball-tip nozzles have produced significant smaller droplet (around 1.9 µm and 1.7 µm for 6 kV and 9 kV respectively), while the straight nozzle produced large sized droplets (around 2.5 µm and 2.4 µm for 6 kV and 9 kV respectively) were formed and lead to the large-scaled aggregations in patterns. Moreover, ball-tip nozzle can maintain the cone-jet mode at a higher voltage (11 kV), which resulted in a finer particle size (around 1.1 µm) as well as a more uniform distribution of HA nanoparticles (Figure 3-5 E and E1). As a result, ball-tip nozzle showed an advantage in achieving uniform distribution of nanoparticles.

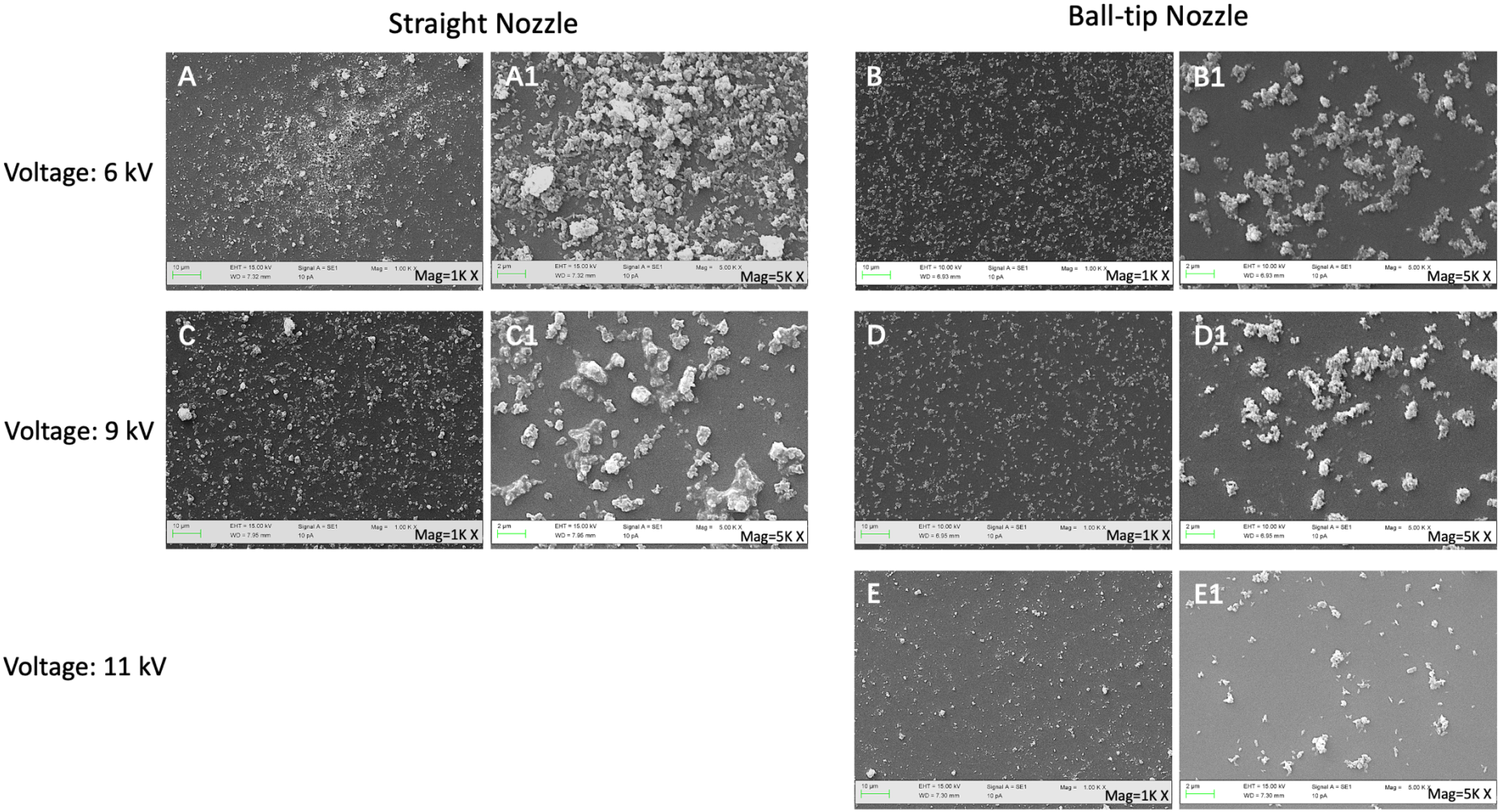

Figure 3-5 HA coatings collected by different nozzles under different voltages.

Image A and C are HA samples coated by using straight nozzle. Image B, D and E are HA samples coated by using ball-tip nozzle.

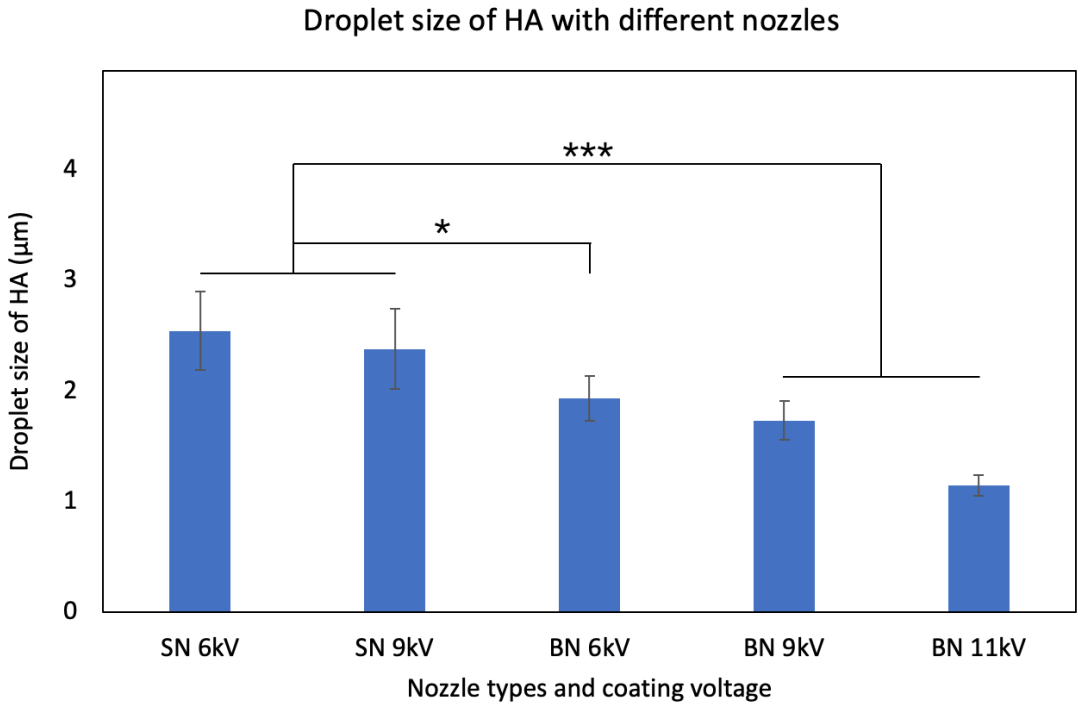

Figure 3-6 Droplet size of straight nozzles and ball-tip nozzles with different voltages

SN: Straight nozzle; BN: Ball-tip nozzle.

The droplet size was calculated by Image J. Data are presented as mean ± SD (n=3).

* represents P≤0.05; **P≤0.01; *** represents P≤0.001. Error bar represents standard error.

3.5 The Solvent Compatibility of Different Nozzles

In electrospray, solvents with low surface tension, high evaporation rate and low conductivity, such as ethanol, are preferred than those with relatively high surface tension, low evaporation rate and high conductivity, like water, even though water is a good solvent for many materials. The results have shown that the ball-tip nozzles have the advantage of maintaining cone-jet stability compared with straight nozzles, which

raises the possibility to employ alternative solvents for electrospray cone-jet, such as water. Therefore, more studies were conducted to compare the ability of different nozzles to generate stable cone-jet using solvents with increasing water ratios. Six HA suspensions were prepared to analysis the electrospray cone-jet performance of different nozzles by adding different proportion of water into ethanol as solvents from 0 to 80%. Preliminary experiment recorded the holding time of stable cone-jet in different solvents. Results has shown the ball-tip nozzles with cap size smaller than 6 mm can maintain a stable cone-jet for at least 3 mins with a water content no more than 80%. The straight nozzle and ball-tip nozzles with cap size larger than 6 mm were not able to maintain a stable cone-jet with ethanol solutions with more than 5% water. Hence the processing map of 2 mm, 4 mm and 6 mm ball-tip nozzles were plotted out to compare their performance with the increase of water content.

Adding water into solvent clearly affected the electrospray cone-jet performance of straight nozzle. The highest water concentration that straight nozzle can withstand a cone-jet for 30 s was 5%. The highest flow rate that a straight nozzle can sustain a stable cone-jet for 30 s decreased from 30 µL/min to 12 µL/min with the increase of water content from 0 to 5%. In the meantime, tests with ball-tip nozzles have shown the highest flow rate were as high as 320 µL/min and all tests can sustain the cone-jet for at least 3 mins (Figure 3-7 A-E). Only when water concentration was 80%, the 2 mm

and 4 mm ball-tip nozzle have reached the highest flow rate at a 240 µL/min (Figure 3-7 F).

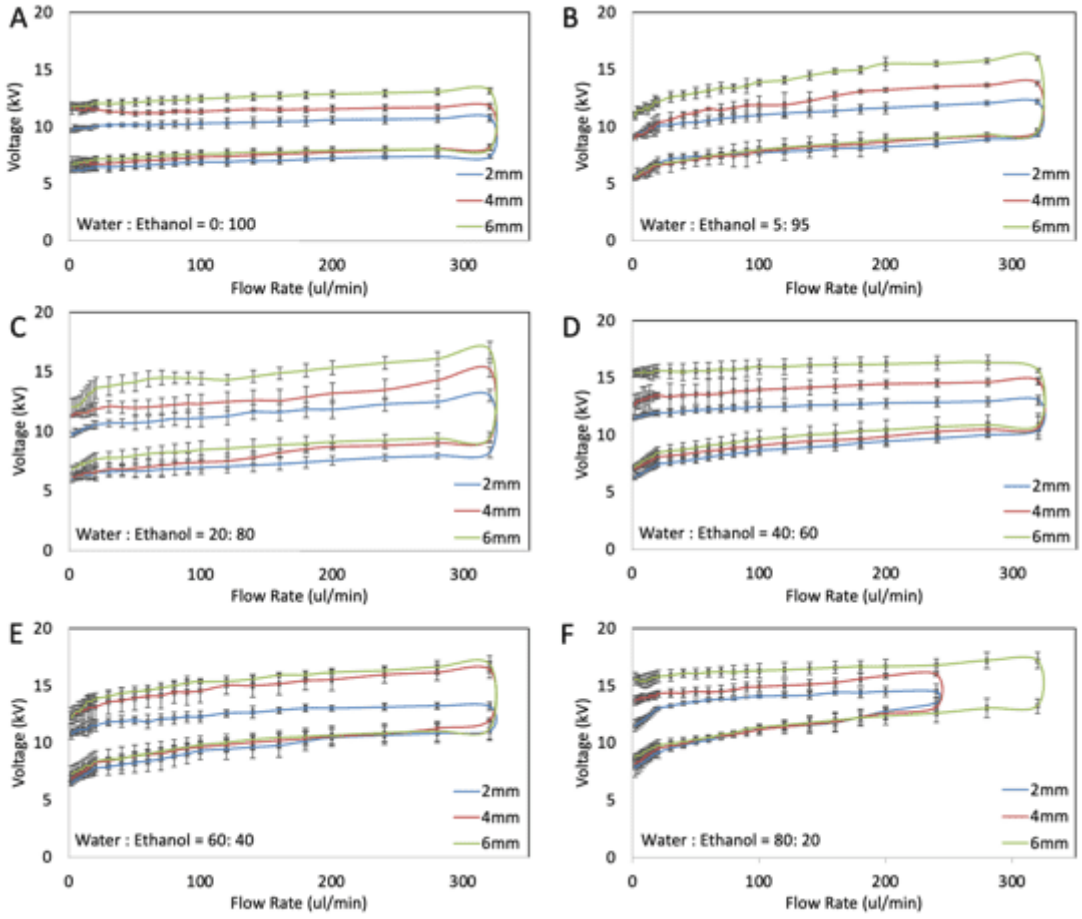

Figure 3-7 The processing zone of ball-tip nozzles with different water: ethanol ratios.
Data are presented as mean ± SD (n=3).

According to the processing maps of 2 mm, 4 mm and 6 mm ball-tip nozzles with different water concentrations, the increase of water concentrations enlarged the processing zone of cone-jet from 0 to 40%. Further increase of water concentration

restricted the processing zone, mainly due to the increase in the slopes of V_{MIN}. The increase of slopes of minimum convert voltages corresponding to the water concentrations indicates a higher voltage was required to outcompete the increased surface tension in order to form a cone-jet. In contract, the slopes of V_{MAX} have a less correlation to the water concentration but more related to the ball-tip sizes.

The increase of water concentration was expected to increase the difficulty of maintaining a stable cone-jet. However, comparing the figure 3-7 A to D, the voltage-flow rate map even covers larger area, which reveals the addition of small amount of water even has a positive effect on the manipulation of electrospray cone-jet due to the wider operating range of voltage. In order to compare the cone-jet manipulation difficulty of suspensions with different water content, two parameters including the voltage difference between upper and below voltage boundaries (V_{RG} = Avg (V_{MAX}- V_{MIN}) and the average voltage ratios (V_{RT} = Avg (V_{MAX}/V_{MIN})) were employed (Fernández de La Mora, 2007) (Figure 3-8 and 3-9).

In the average voltage ranges (V_{RG}) results, for a certain water concentration, the observed V_{RG} increased in proportion to the size of ball-tips from 2 mm to 6 mm, which means the 6 mm is the most optimal size for the ball-tip nozzles. All three ball-tip nozzles exhibited increased V_{RG} according to the water concentration from 0 to 40%

and decreased V_{RG} from 40 to 80% (Figure 3-8). This result revealed the solvent with 40% water had the widest voltage operation range for cone-jet in ball-tip nozzle. This may be due to the enhanced surface tension allowed the attachment of larger drops. The straight nozzle showed a decreased V_{RG} from 1.96 kV to 1.88 kV with the increase of water concentrations from 0 to 5%, which indicates a weak water compatibility of straight nozzle.

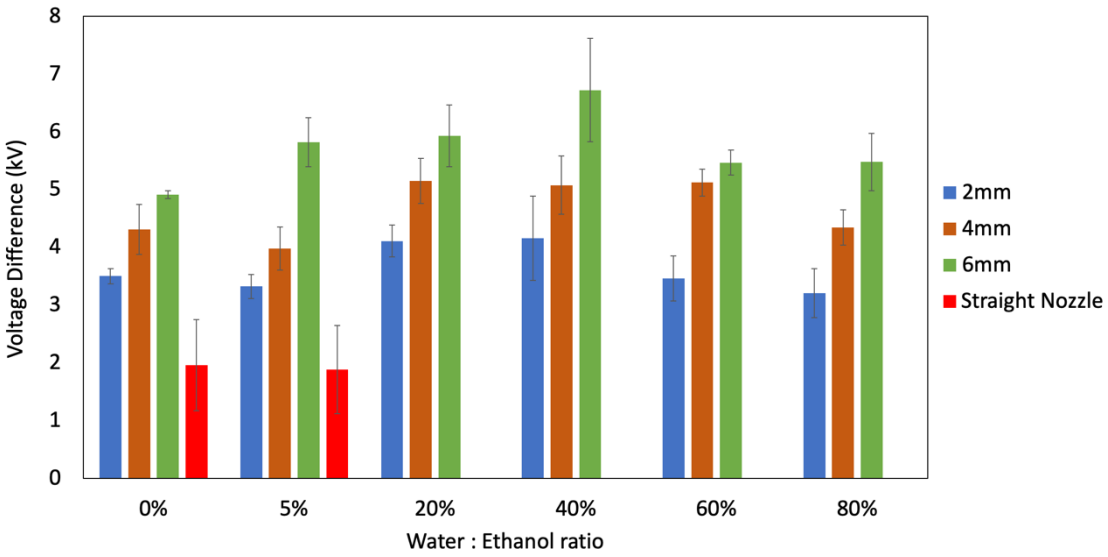

Figure 3-8 Average Voltage Range (V_{RG}) with Different Water Ratio.
The voltage range was calculated by V_{RG}=Avg (V_{MAX}-V_{MIN})
Data are presented as mean ± SD (n=3). Error bar represents standard error.

The average voltage ratios (V_{RT}) results were similar to the V_{RG} results. With a certain water concentration, higher V_{RT} were achieved with larger cap size. The increase of water concentration also increased V_{RT} firstly and the further addition of water (from

20% for 6 mm and 40% for 2- and 4-mm ball-tip nozzles), decreased the V_{RT}, which is consistent to the hypothesis that the addition of water disturbed the cone-jet (Figure 3-9). In contrast, the V_{RT} of straight nozzle reduced more rapidly comparing the ball-tip nozzles and collapsed from 20% water-ethanol ratio, which also represents the straight nozzle is unstable in water-containing solvent (Figure 3-9).

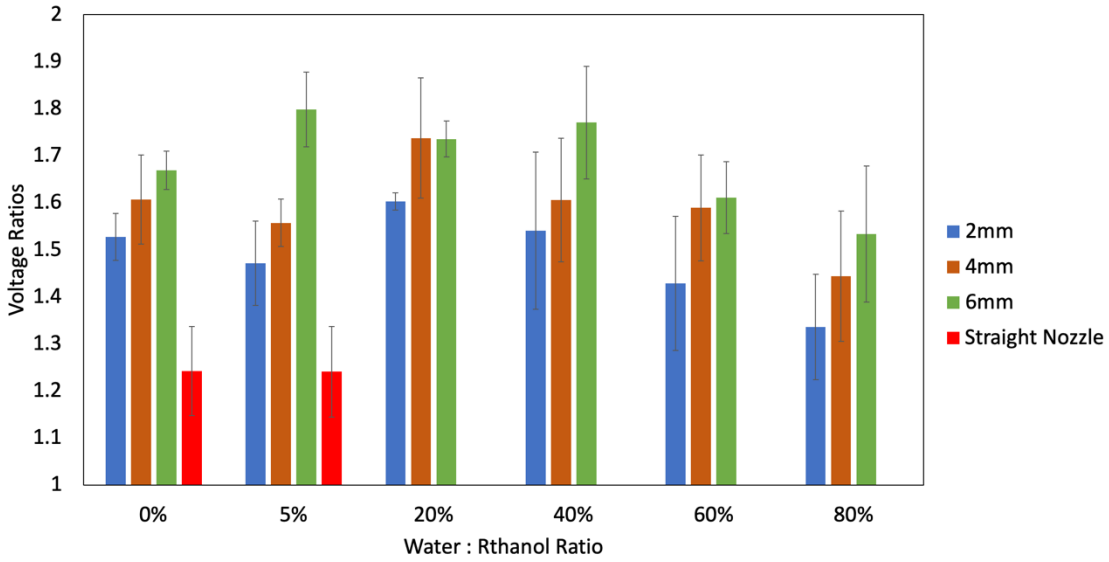

Figure 3-9 Average Voltage Ratios (V_{RT}) with Different Water Ratio.
The voltage ratios represent the ratio of maximum convert voltage and minimum voltages V_{RT} = Avg (V_{MAX}/V_{MIN})
Data are presented as mean ± SD (n=3). Error bar represents standard error.

3.6 Discussion

3.6.1 Unstable Cone-jet in Straight Nozzle

In practice, the cone-jet mode in straight nozzles can be perturbated easily, which leads to the regular switch between different spray modes (Figure 3-4 B). The frequent change of spray mode of straight nozzle is directly related to the dynamic change of liquid amount attached to the nozzle. There are three different situations involved in the electrospray process.

The ideal situation is when the liquid supply is exactly equals to the consumption of electrosprayed solution that the amount of liquid in the drop at the tip of nozzle remain constant. Therefore, a cone-jet mode can be sustained constantly. In reality, it is very hard to fix the flow rate and voltage to make sure the solution supply exactly matches the consumption of sprayed solution. Once the liquid consumption rate of spray is divergent from the input flow rate, the other two situations will happen.

One unstable situation is when the voltage is not high enough to take away sufficient liquid from the drop, such as the situation as described in Figure 3-4 B (Voltage around 6.9-8.5 kV), it can cause the gathering of liquid at nozzle head. The surface area of drop

will then increase and scatter the surface tension, which no longer bears the gravity force, and finally the drop will fall from the tip of nozzle, which contributes to the switch from cone-jet into a dripping mode. After that, the suddenly reduced amount of liquid caused the increase of electric field intensity, which can break up the liquid drop into multi-jet. Afterwards, the gathering of liquid will continue, and multi-jet switch back to a cone-jet and then a dripping will happen again. Moreover, due to the low voltage and continuous gathering of liquid, the dripping mode has a higher frequency than multi-jet mode (Figure 3-4 B (6.9-8.5 kV)).

Another situation is when the voltage is in a relatively high level, the solution supply would be lower than the consumption of sprayed solution, as described in Figure 3-4 B (8.5-10.2 kV). The liquid amount in the cone-jet will reduce, which will reduce the surface area of drop, and increase the electric field intensity and break the balance between surface tension and electric stress and finally switch the cone-jet into a multi-jet. At this situation, if the voltage is not high enough to maintain a multi-jet afterwards, the separated multi-jet can attenuate the potential and due to the low liquid consumption, the hanging liquid amount will gather and cause the appearance of cone-jet or dripping, determined by the liquid gathering rate. Therefore, in the long term, due to the higher consumption rate of liquid, the multi-jet mode has a higher frequency than dripping mode at 8.5-10.2 kV (Figure 3-4 B).

3.6.2 Strong Stability and High Throughput of Cone-jet in Ball-tip Nozzles

The cone-jet mode in ball-tip nozzles is apparently more stable than straight nozzle, with no relapse within three spray modes was observed (Figure 3-4). The attached ball-tip reduces the curve at the contact point between nozzle head and liquid drop, which reduces the surrounding air pressure and further reduce the liquid pressure. Therefore, it can support a wider range of other pressure such as velocity pressure, liquid pressure, viscous stresses and tangential electric stress, which leads to a higher flexibility of flow rate, voltage and liquid viscosity (Figure 3-10). Moreover, ball-tip nozzles have larger area for liquid to attach, which results in the formation of larger droplet. Therefore, ball-tip nozzle is more resistant to fluctuation of liquid amount of the hanging drop. Once any fluctuation of hanging drop volume happens, with a same level of gathering or consumption of liquid drop, the ball-tip nozzle can sustain the attachment of drops for a longer time than straight nozzle, which finally reflected in the stability of electrospray cone-jet.

High throughput is another advantage of ball-tip nozzles compared with straight nozzle. In the straight nozzle processing map, the V_{MIN} and V_{MAX} boundaries have shown significant differences on their correlation to flow rate. The V_{MIN} has shown a much

higher slope than the V_{MAX} according to the increase of flow rate. This is due to the different force balance involved in V_{MIN} and V_{MAX}. The V_{MIN} required for a stable cone-jet is reached by the balance among electric normal stress, velocity pressure and the surface tension (Morad et al., 2016). Increase in the flow rate can cause a higher shear stress, which requires higher V_{MIN}, while the V_{MAX} board is less related to the flow rate because the V_{MAX} is less affected by the velocity pressure, but more dependent on the balance between the surface tension and electrical normal stress (Morad et al., 2016). Therefore, increase the flow rate will increase the required V_{MIN} but less affect the V_{MAX}, and finally reduced the V_{RG}.

In the ball-tip nozzles, the larger hanging drop can lead to higher V_{MAX}, and lower slopes of V_{MIN}. Both increased the maximum flow rate for a stable cone-jet. Moreover, the ball-tip structure reduced curve at the contact point between nozzle head and hanging drop, so the tangential electric stress was able to support more fluid acceleration and prevent the excessive growth of normal electric stress (Figure 3-10). It attenuated the normal electric field balancing the surface tension and consequently postponed the multi-jet mode and broaden the voltage band of cone-jet (Morad et al., 2016).

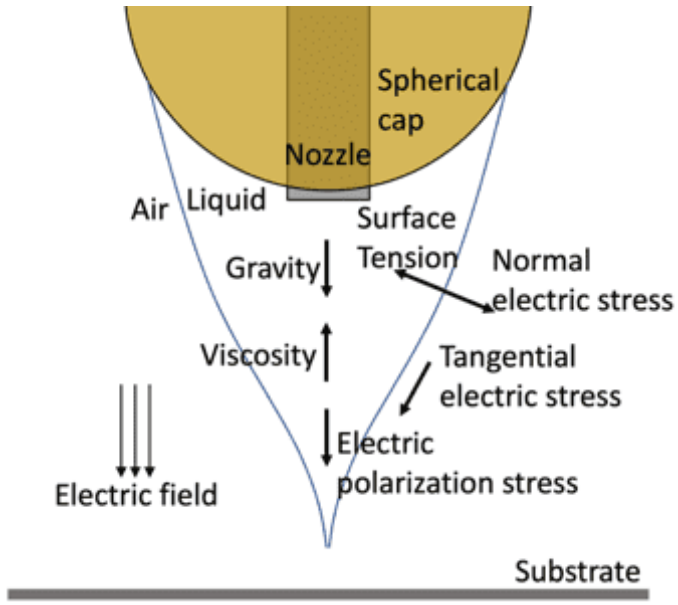

Figure 3-10 Forces involved in a cone-jet formation with a ball-tip nozzle.
The cone-jet shape is mainly controlled by the velocity pressure, the surface tension stress, the normal electrical stress and the tangential electrical stress.

3.6.3 6mm is the Most Suitable Size for Ball-tip Nozzles in Stabilizing the Cone-jet

The processing maps have shown the 6 mm ball-tip nozzle was the most suitable nozzle in maintaining the cone-jet mode. It is due to the ability in supporting large amount of hanging drop that attenuate the potential intensity and consequently broaden the voltage band and reduced the manipulation difficulty. Smaller sized ball-tips (2- and 4-mm ball-tip nozzles) and straight nozzle can support limited amount of liquid in the hanging drop, which limited the surface area of a drop and limited their ability in

attenuating the potential intensity. Therefore, smaller sized ball-tips have limited advantaged in stabilizing the cone-jet. Ball-tips from 8mm to flat caps also supported smaller volume of hanging drops and the smaller curvature that enlarged the surface area via deform the drop from ball-tip structures into flatten structure. Therefore, the required voltages for maintaining the conical structure of liquid became too high that multi-jet can be formed directly before a stable cone-jet could appear.

3.6.4 Strong Water Compatibility of Ball-tip Nozzle

Experimental results have shown that the solution contains higher water percentage has a negative effect on the stability of cone-jet mode, where cone-jet is only formed within a small range of voltage (Figure 3-7). This is due to the high electrical conductivity and high surface tension of water (72.86 ± 0.05), that requires a high voltage for the formation of cone-jet. With a high electrical conductivity, the applied voltage would switch into relaxation at the surface in a few mS, which attenuated the electric stress (Lastow and Balachandran, 2007). With a high surface tension, larger hanging drop are preferred, which also requires higher voltage to curve the liquid drop into a Taylor-cone (normally more than 10kV). However, a high voltage could destabilize the liquid cone structure and sometimes only multi-jet mode can be achieved in a straight nozzle. In a ball-tip nozzle, the increased drop surface

distinctively increased the required V_{MIN} and V_{MAX}, which increased the V_{RG} and V_{RT} accordingly compared with the straight nozzle. Therefore, it would be much easier to fix a suitable voltage between the upper and lower voltage boundaries of cone-jet using ball-tip nozzles.

3.6.5 Ball-tip Nozzle would not Disturb the EHD Process

Acrylonitrile Butadiene Styrene (ABS) was used to fabricate ball-tip, it does not react with the solvents used in this project (ethanol and water) because ABS has butyl molecules in its chain and has resistance to alcohol. Therefore, the coating process would not cause any melt or soften of this ABS ball-tip part and the attachment of liquid drop on the surface of ABS has very low probability to contaminate the solution or suspension. ABS has been known to have high rigidity, good impact resistance and low dielectric strength. Therefore, the penetrating process when making the ball-tip nozzles and the usage of ball-tip nozzles during EHD process would not cause any deformation of the spherical surface and the applying of high voltage to the nozzle would not disturb the EHD process.

3.7 Conclusions

The ball-tip nozzle is an ideal system to operate the electrospray in a cone-jet mode due to the wider processing zone and stable jetting process. The ability of ball-tip nozzles in stabilizing the cone-jet is related to the size of ball-tips. The increase of ball-tip size from 2 mm to 6 mm has shown positive effect in stabilizing the cone-jet and further increase of the cap size has negative effect in stabilizing the cone-jet. It was also observed that the ball-tip nozzle could sustain a stable cone-jet with high water content solvent, which significantly enhanced the application range of cone-jet mode in producing fine depositions with different materials. The advantage of ball-tip nozzle is not only in the stability of cone-jet, but also in the uniform droplet sizes and uniform distribution of nanoparticles in the coated films. The results also demonstrated the ball-tip nozzles are able to improve the stability of cone-jetting and achieve high throughput. This novel EHDA system was therefore applied to this project for the deposition processes of nanoparticles in the following two chapters.

Chapter IV

4 Magnetic HA in Magnetic Field and Template Assisted Electrohydrodynamic Atomization Patterning Process

4.1 Introduction

HA substituted with different metal ions provides different functions for biomedical applications, such as magnetic properties for biomagnetic agents. By adjusting the types and amount of substituted metal ions can specially tailor the magnetic properties for biological applications such as contrast agent for medical imaging, hyperthermia mediator for cancer treatment, drug delivery and cell separation (Wu et al., 2007b). Magnetic HA can be produced by substituting 3d transition metals, such as Co, Mn and Fe, for Ca in the HA structure (Zilm et al., 2018). However, there are concerns over toxicity of CoHA that inhibit the osteoblasts proliferation and the expression of osteogenic genes in vitro (Jiang et al., 2020), while both FeHA and MnHA are confirmed as non-cytotoxicity (Li et al., 2009b, Li et al., 2012, Zilm et al., 2018). Several studies indicated the co-substitution of Fe^{3+} and other ions such as Co^{2+} and Sr^{2+} into HA benefits the materials bioactivity by inducing the ionic activity of apatite

in the encircling medium and contributed to the calcium phosphate precipitations in the SBF soaking tests (Ullah et al., 2018, Pasandideh et al., 2020). Therefore, it is worthy to investigate if the co-substitution of Fe^{3+} and Mn^{2+} into HA could have the effect in enhancing the bioactivity while maintaining or enhancing magnetic property.

Surface topography with well osteoinductive and osteoconductive properties is very important to ensure the long-lasting anchorage of the implants to tissues (Rahmany and Van Dyke, 2013). Many studies have indicated that providing appropriate surface topographical patterns can guide tissue regeneration, thereby promoting the clinical performance (Zhao et al., 2008). Current methods that can produce such microgroove structures are mainly based on the photolithography or etching lithography on substrates such as silicon or fused silica, eventually also on titanium (Zhu et al., 2019). However, these techniques are highly dependent on the surface flatness of that substrate and require extremely clean operating conditions (del Barrio and Sánchez‐Somolinos, 2019). An alternative method is TAEA, which is an EHDA process that places templates above the collection substrate to deposit well-defined patterns of nanoparticles (Ahmad et al., 2006, Nithyanandan et al., 2013). However, the precision of TAEA is completely limited by the templates and increase the precision of templates on micro- or nano- scales will increase the cost of production exponentially (Gohil and Choudhury, 2019). To meet the raising demand of developing a high precision, high

efficiency and low-cost coating technology that can produce high biocompatible implant surface with microstructure to guide tissue formation, a MTAEA to deposit biocompatible magnetic nanomaterials in coating layers was introduced in this project. Therefore, this project is aiming at exploring the applications of Fe-MnHA in fabricating high-resolution patterned implant coatings. This chapter is going to focus on the following detailed objectives:

i. Synthesizing and characterizing Fe^{3+} and Mn^{2+} co-substituted and mono-substituted HA with variety metallic contents.

ii. Analysis on the bioactivities of different synthesized MHA in comparison with HA and magnetic nanoparticles including IONPs and HA-IONPs mixed powders.

iii. Design and analysis the MTAEA

iv. Investigating the influence of MTAEA processes on the distribution of MHA patterned coatings

4.2 Structural Characterization of HA, FeHA, MnHA and Fe-MnHA

Fe-Mn co-substituted HA and Fe and Mn substituted HA, with various X_M values (0.005, 0.025, 0.05) were synthesized using the co-precipitation method and characterized by SEM, XRD and FTIR to confirm the substitution of Fe and/or Mn into HA.

4.2.1 XRD Characterization

The phase purity of synthesized Fe-MnHA, FeHA, MnHA and HA was evaluated using XRD. Figure 4-1 contains the XRD patterns obtained from the MHA (MHA represents Fe-MnHA, FeHA and MnHA in this chapter) powders and pure HA powder. The XRD patterns for all samples well matches the hydroxyapatite (JCPDS No. 09–0432) without any second phase extraneous peaks, which suggests the ion exchange process has no effect on the structure of HA.

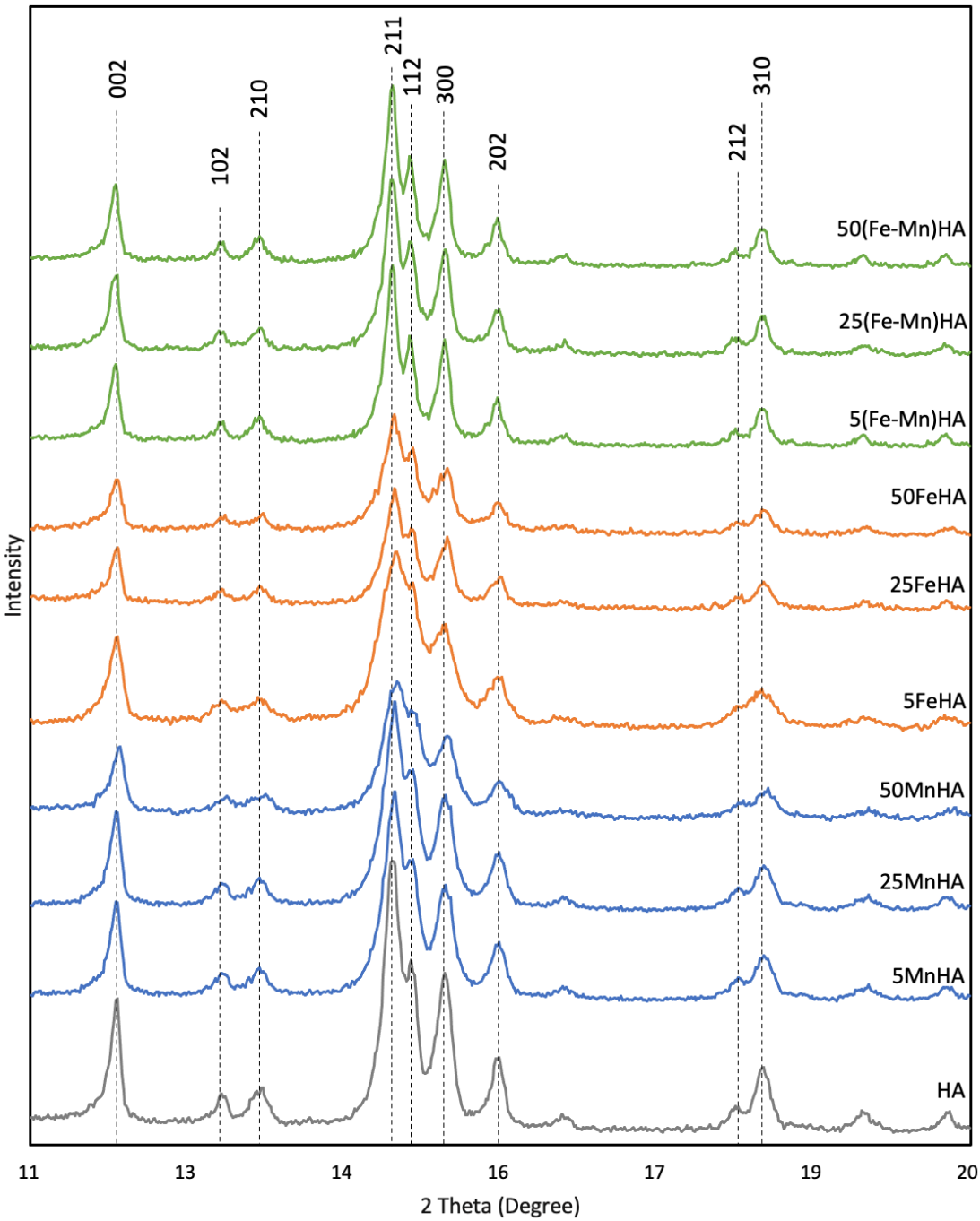

Figure 4-1 XRD patterns of MHA and HA powders.

MHA and HA XRD patterns matched the peak position and intensity of standard HA (ICDD 00-009-0432) with no indication of any second phase extraneous peaks.

In the Fe-MnHA samples, three samples exhibited similar peak structure, inconspicuous reduction of peak intensity can be observed. In FeHA nanoparticles, more obvious reduction of peak intensity was observed with the increase of substitution concentration, which reveals the substitution of Fe reduced the crystallinity. This finding agreed well with previous studies, which also observed the reduced crystallinity when substituted more Fe^{3+} into HA (Li et al., 2009b). In MnHA group, similar phenomena were observed, with the increase of Mn content, the peak intensity decreased, which represents a decrease of crystallinity. This finding reveals the co-substitution has not changed the lattice structure of Fe-MnHA and improved the crystallization comparing to mono-ions substituted HA.

The lattice parameters, crystallinity and crystal size of MHA and HA are summarized in table 4-1 and figure 4-3. Both Fe and Mn were proved to be successfully substituted into HA and with the increase of metallic contents, all MHA samples have shown decreased crystallinity. With the increase of metallic contents in MHA, the lattice parameter (*c)* of three MHA and lattice parameter (*a*) of Fe-MnHA and MnHA all decreased gradually. Although the lattice content (*a*) of FeHA increased on 50FeHA, the crystal size still decreased comparing to 5FeHA and HA. In Fe-MnHA, FeHA and MnHA, the crystal size decreased as the amount of Fe and/or Mn increased. The reduction of crystal size owing to the substitution of Fe^{3+} and Mn^{2+} ions was because

of the mismatch in the ion size between Fe^{3+} (60 pm), Mn^{2+} (70 pm) and Ca^{2+} (100 pm), which was previously shown in table 1-5 in section 1.5.3. Moreover, the results imply that Fe^{3+} and Mn^{2+} inhibited the crystallization and crystal growth of HA.

Table 4-1 Lattice parameters, crystal size and crystallinity of MHA with different metallic content.

Sample	Unit cell parameters			Crystal Size (nm)	Crystallinity (X_C)
	a (Å)	c (Å)	V ($Å^3$)		
HA	9.421	6.869	528.00	319.9	83.45±5.71%
5FeHA	9.433	6.887	531.01	319.9	84.75±3.92%
25FeHA	9.415	6.884	528.46	319.9	83.29±4.73%
50FeHA	9.418	6.882	528.66	255.9	77.86±5.94%
5MnHA	9.429	6.891	530.65	319.9	85.34±3.66%
25MnHA	9.415	6.875	527.72	255.9	83.78±3.25%
50MnHA	9.413	6.849	525.53	232.7	73.55±7.82%
5(Fe-Mn)HA	9.427	6.893	530.45	319.9	81.54±5.04%
25(Fe-Mn)HA	9.428	6.893	530.67	284.4	80.74±3.55%
50(Fe-Mn)HA	9.423	6.872	528.46	255.9	74.37±4.72%

HA has hexagonal crystal structures, so the unit cell parameter a and b constants are equal, here only unit cell parameter a (Å) and unit cell parameter c (Å) constants are displayed.

4.2.2 FTIR Characterization

The FTIR spectra acquired from the MHA and pure HA powders exhibited the typical

vibrational modes of HA. The results indicated the substitution of Fe and Mn into HA did not affect the vibrational modes of pure HA (Figure 4-2). The vibrational modes of phosphate (PO_4^{3-}) observed in all samples in the FTIR patterns are typical characteristics of HA. The weak bands around 470 cm^{-1} were assigned to the phosphate bending vibration. The bands between 560 and 602 cm^{-1} appearing as a doublet are two of the components associated with the triplet $\mathbf{v}_4$ OPO bending mode. The band at 961 cm^{-1} corresponds to the $\mathbf{v}_1$ nondegenerate PO symmetric stretching mode. The bands at approximately 1022 cm^{-1} and 1089 cm^{-1} represent the triplet $\mathbf{v}_3$ antisymmetric PO stretching mode. The weak bands around 632 cm^{-1} are OH^- vibrational mode represent hydroxyl peaks.

The peak intensity (PI) reflects the crystallinity changes of MHA according to the changes in metallic contents. The PI of the main P–O stretching bands around 961–1096 cm^{-1} were plotted in figure 4-3. The Fe-MnHA and FeHA have shown reduced PI according to the increase of metallic content, which represents the decrease of crystallinity and matches the crystallinity results measured in XRD patterns. Although the substituted Mn content has shown an increased PI from 5MnHA to 25MnHA, the 50MnHA has shown the lowest PI of P–O stretching band among the three MHA.

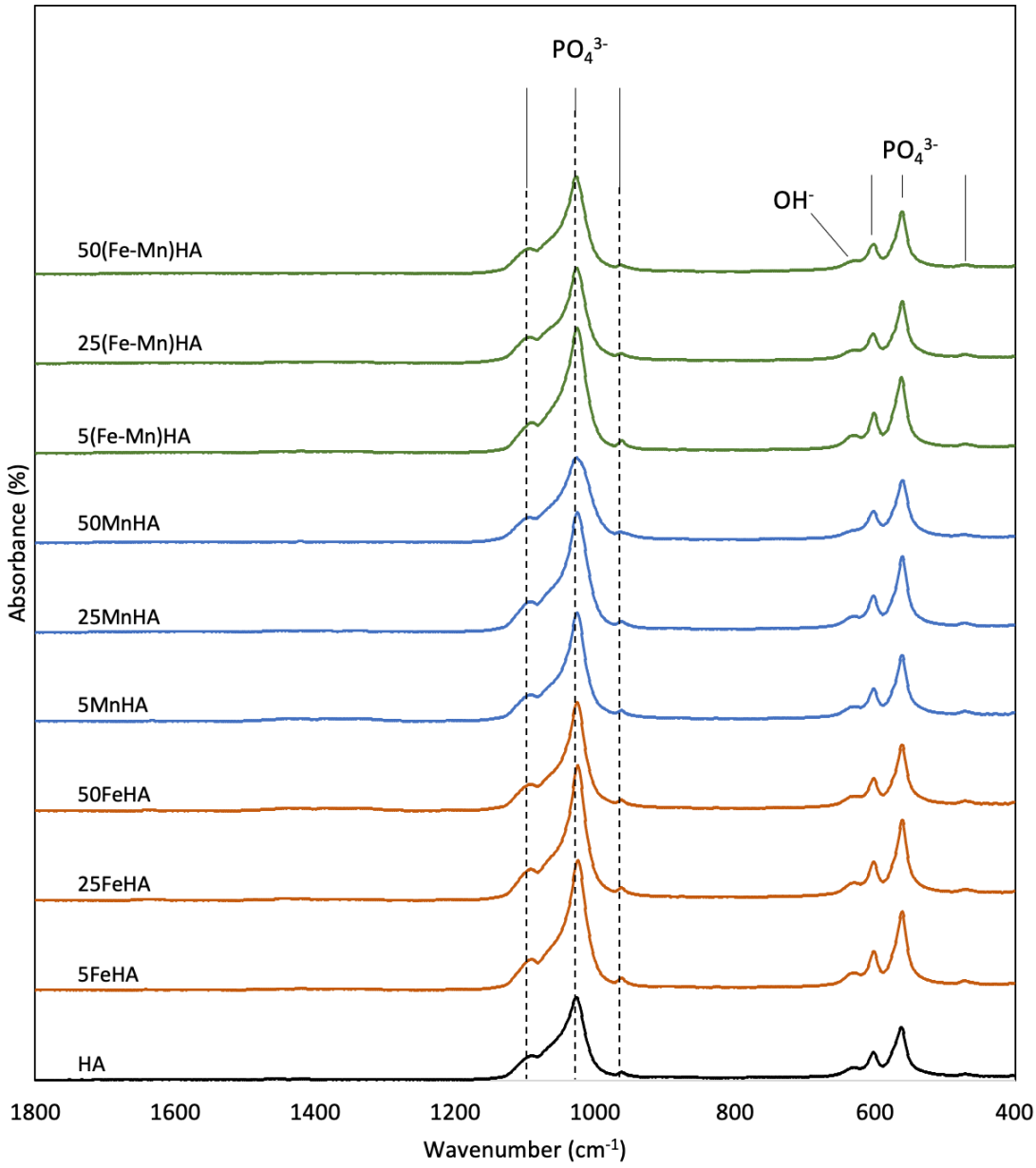

Figure 4-2 FTIR spectra of mono- and multi-ionic substituted HA with variety Fe and Mn content.

The chemical groups of the main peaks are labeled in this figure and the peaks' positions of three phosphate peaks around 961-1096 cm^{-1} are marked.

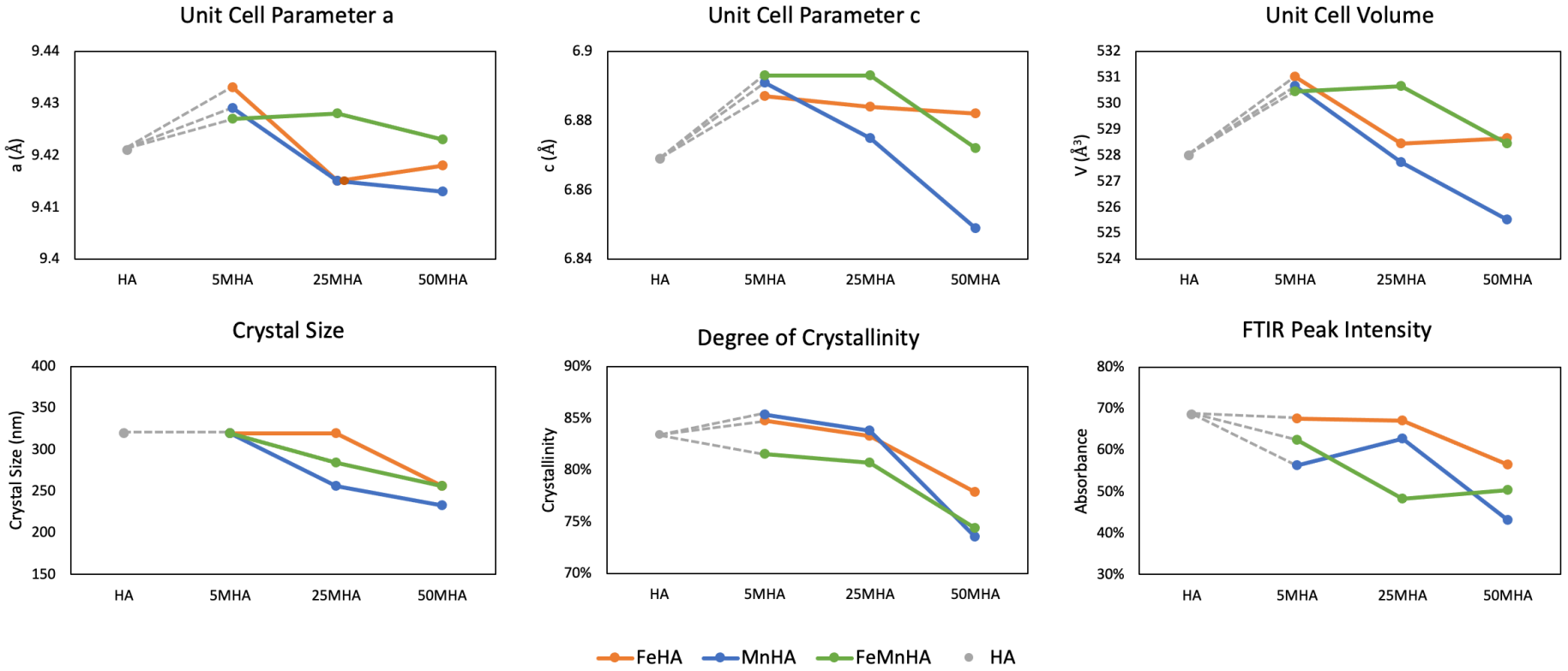

Figure 4-3 Unit cell parameters, crystal size, crystallinity measured in XRD results and FTIR Peak intensity (PI) of PO_4^{3-} stretching peak at 1027cm^{-1}.

4.2.3 Investigating the Morphologies of Nanoparticles via SEM

The SEM morphologies of Fe-MnHA, FeHA, MnHA and pure HA were depicted in figure 4-4. It was observed that both the shapes and sizes of the synthesized nanoparticles were associated to the amount of metallic content in MHA. The 5MHA and 25MHA nanoparticles have nearly spherical structure without sharp face angles (Figure 4-4 A, B, D, E). With the increase of metallic contents, all three types of 50MHA were elongated from spherical structures into rod-like structures (Figure 4-4).

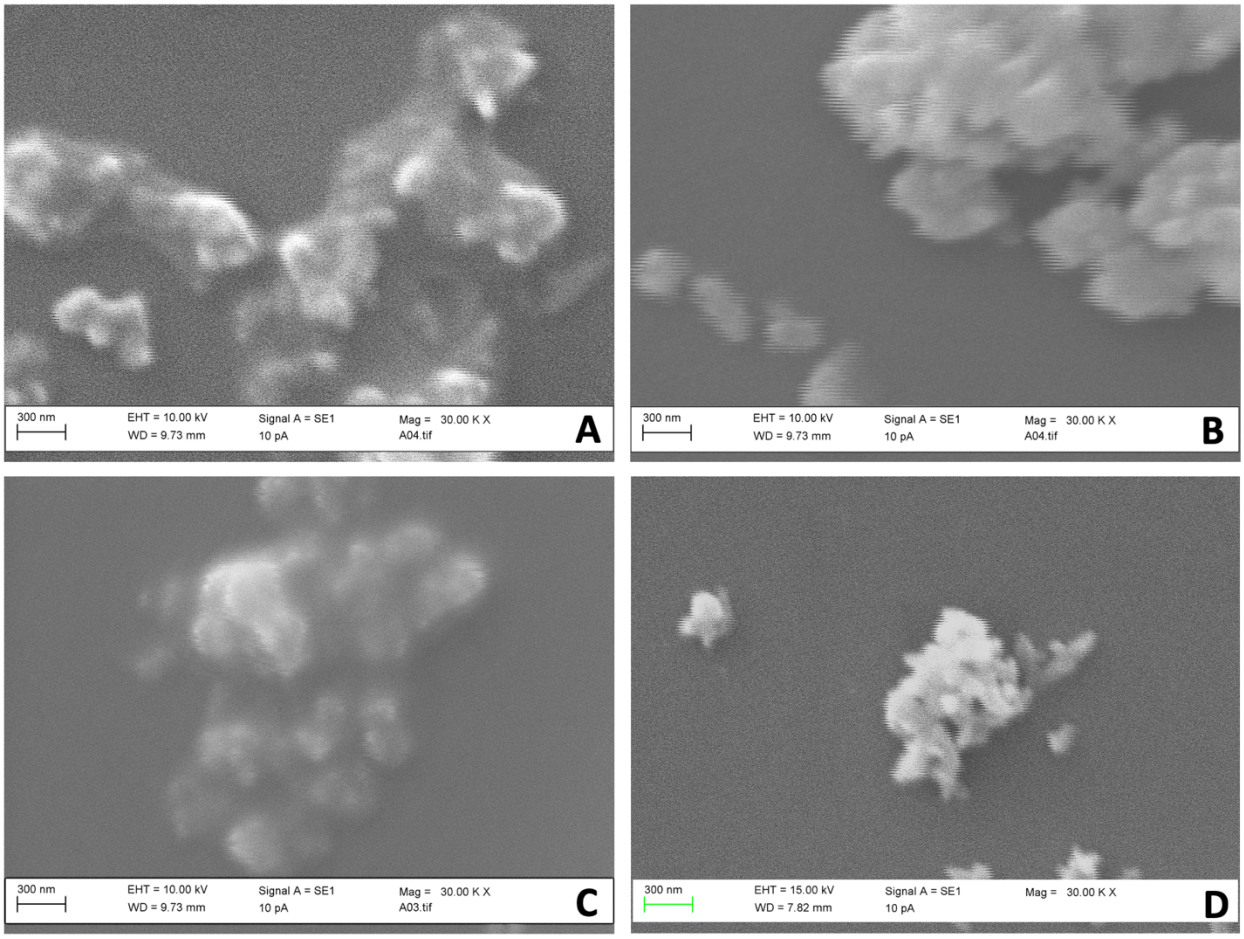

Figure 4-4 The morphologies of FeHA, MnHA and Fe-MnHA with variety metallic content.

SEM images showing the morphologies of MHA with 30 K X magnification. (A) 50FeHA, (B) 50MnHA, (C) 5Fe-MnHA, (D) 50Fe-MnHA

4.3 In vitro Bioactivity Studies with SBF Soaking Test

The bioactivities of synthesized materials were studied via SBF soaking test, through detecting the formation of CaP on the coating surface, the relative bioactivities of each material can be compared.

In order to distinguish the formed CaP globules from the electrosprayed nanoparticles, the deposition of Fe-MnHA, FeHA, MnHA, HA, IONPs and HA-IONPs mixture without soaking in SBF has been observed in SEM as control group (Figure 4-5). The CaP formation rate of three types of MHA was studied via observing the CaP formation in a 2-day, 4-day and 7-day-soaked samples (Figure 4-5, 4-6). It can be seen in images that the CaP globules was constructed by many branch-like structures. In the 2-day-soaked results, all MHA samples have facilitated the CaP globules formation, while the concentration of CaP globules in Fe-MnHA and MnHA were slightly higher than FeHA (Figure 4-5). The relatively higher apatite formation of Fe-MnHA and MnHA also reflected in the 4-day and 7-day samples. In the 4-day samples, no obvious difference on the formed CaP layers in the Fe-MnHA and MnHA samples was observed, both Fe-MnHA and MnHA samples showed the branch-like structures of apatite, while only separated CaP globules can be found in FeHA samples. The branch-like structures of apatite reveal the formed CaP achieved a relatively high concentration that can interconnect to each other (Figure 4-6). In the 7-day samples, all MHA exhibited the branch-like structures of apatite, but the concentration of formed CaP globules was obviously lower in FeHA samples (Figure 4-6). As compare, the bioactivity of pure HA, IONPs and IONPs-HA mixed deposition were also investigated. Both pure HA and IONPs-HA mixture depositions have induced the formation of CaP and formed thin layers of CaP globules. Few small sized CaP globules were observed in IONPs deposition,

while neither the amount nor the size of CaP globules was compatible to the other samples. This result suggests the HA nanoparticles were more favorable to the formation of CaP in SBF testing than IONPs nanoparticles.

Since the formed apatite has typical morphology that significantly different to the morphology of deposited nanoparticles, it is possible to be distinguished. To compare the apatite formation rate of different MHA. The formed apatite was distinguished manually from the MHA nanoparticles and export the coverage percentage of CaP globules. The coverage percentage of formed apatite were calculated by image J (Figure 4-7). The apatite coverage percentage results reveal that in the 2-day bioactive test, MnHA has a higher bioactivity than Fe-MnHA. But in the 4 and 7-day results, no significant difference between Fe-MnHA and MnHA was observed but both Fe-MnHA and MnHA have shown significant higher apatite formation rate than FeHA. In the 7-day results, the apatite formation rate of HA, IONPs and HA-IONPs mixture were added to compare. The result has indicated no significant difference in the CaP globules cover percent among Fe-MnHA, MnHA and HA, and they have shown a significant higher apatite coverage percentage than FeHA, HA-IONPs mixture and IONPs. This finding indicates both Fe-MnHA and MnHA have good bioactivities, which were similar to HA, while FeHA, HA-IONPs mixture and IONPs have relatively lower bioactivities.

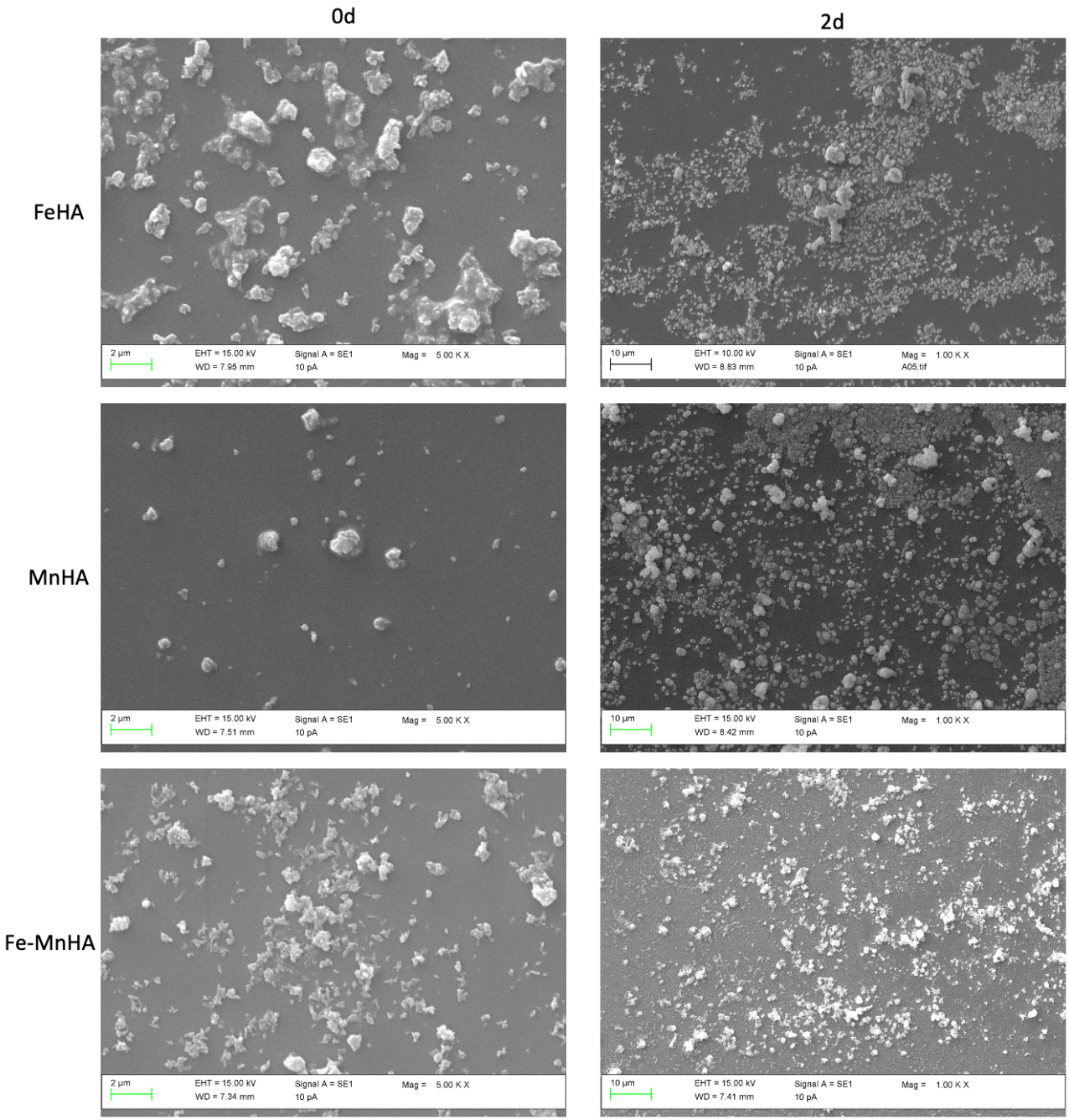

Figure 4-5 SEM images of 50FeHA, 50MnHA, 50(Fe-Mn)HA, samples and the formed apatite in SBF after 2 days.

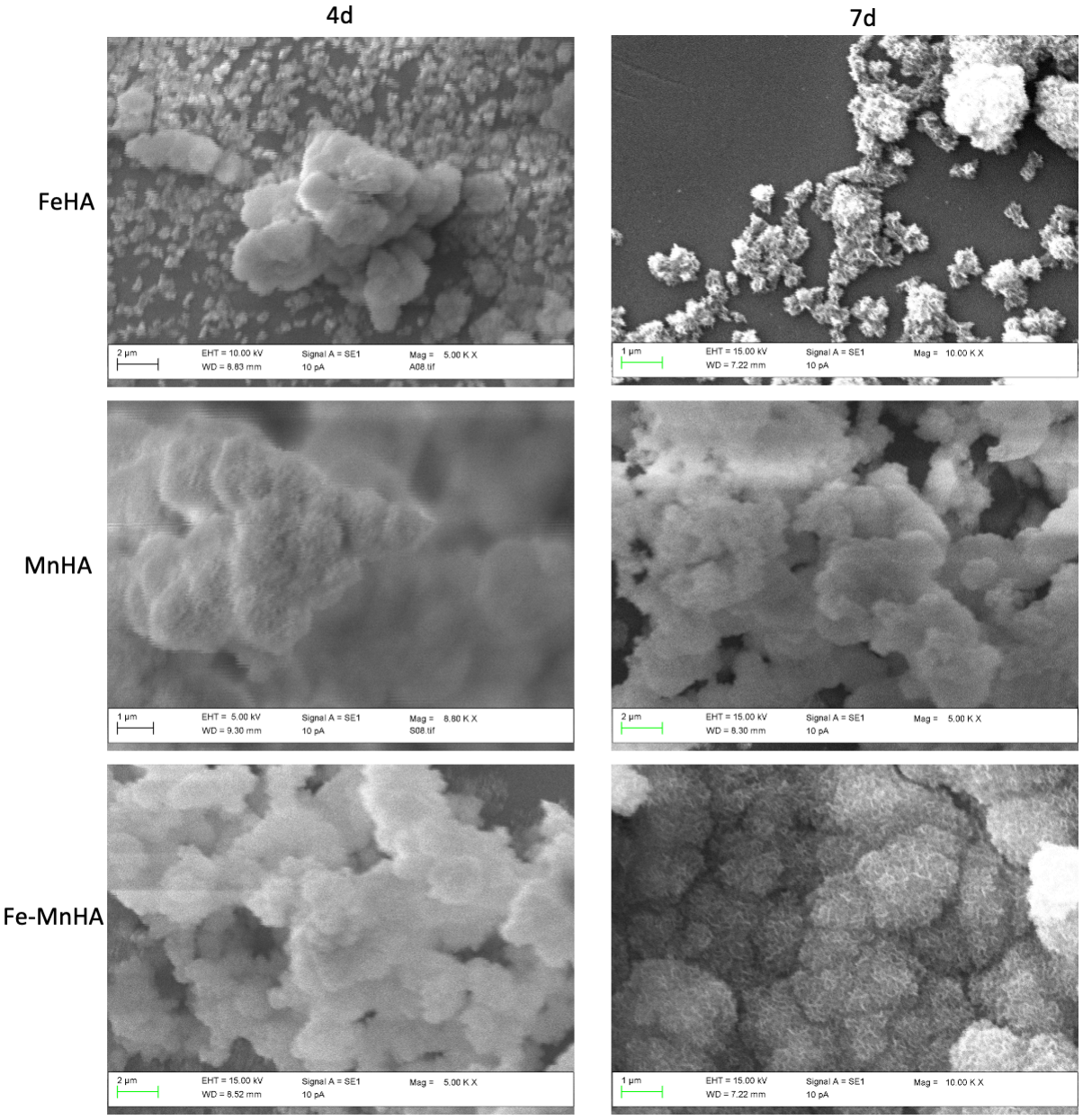

Figure 4-6 SEM images of 50FeHA, 50MnHA and 50(Fe-Mn)HA samples soaked in SBF for 4 and 7 days.

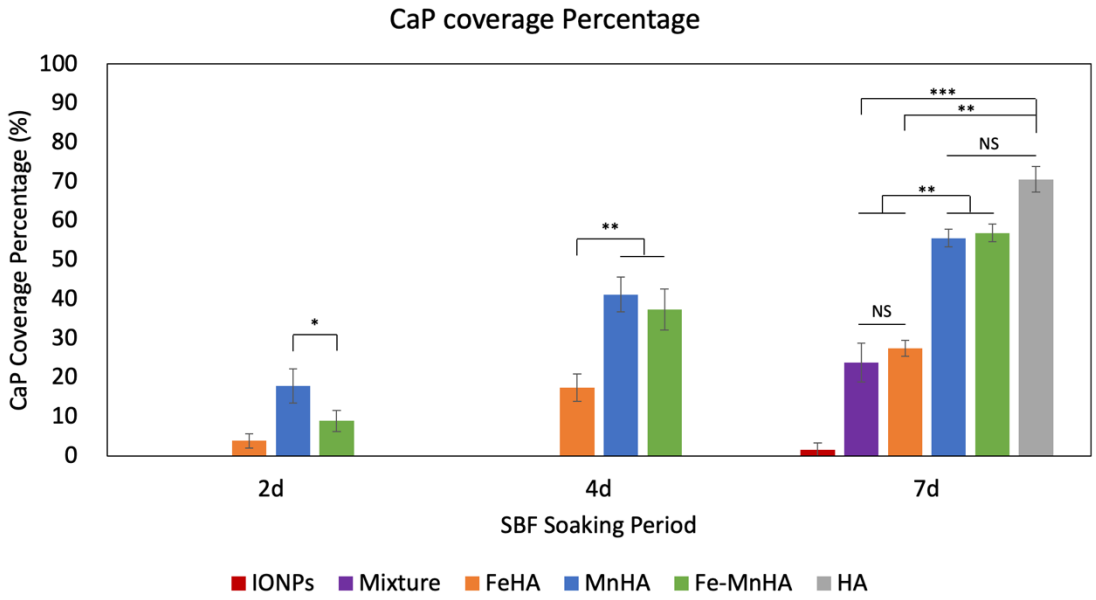

Figure 4-7 Coverage percentage of formed apatite in 7-day SBF soaking test.
The coverage percentages of formed apatite were calculated by image J via manually select the formed apatite from the deposited nanoparticles. Data is presented as mean ± SD (n=3).

4.4 Effect of Magnetic Fields

The influence of magnetic field in EHDA process was further investigated in the study. Firstly, the magnetic field strength on three selected magnets were simulated using ANSYS MAXWELL, the distribution magnetic flux density is shown in Figure 4-8. Simulation results showed that the magnetic flux density varies among different magnets and different regions of each magnet. 11.2 kg magnet has two poles along the long edge (y-axis) and 21.7 kg and 32.2 kg magnets have two poles along the z-axis (refer to x, y, z axis in Figure 4-8 A). In these magnets, the two short edges have the

highest magnetic flux density, the center region has a medium density and the long edges has the lowest density. It is consistent to a previous test of magnetic field distribution in a magnet (Oka et al., 2012). Based on the calculated results, a gradient of magnetic fields was selected to elucidate the effect of different magnetic fields on the distribution of nanoparticles, including a control group without magnet (M0) and four magnetic regions, M1 (medium strength region in 11.2 kg pull magnet), M2 (low strength region in 21.7 kg pull magnet), M3 (high strength region in 21.7 kg pull magnet) and M4 (high strength region in 32.2 kg pull magnet) (Figure 4-8 B).

A

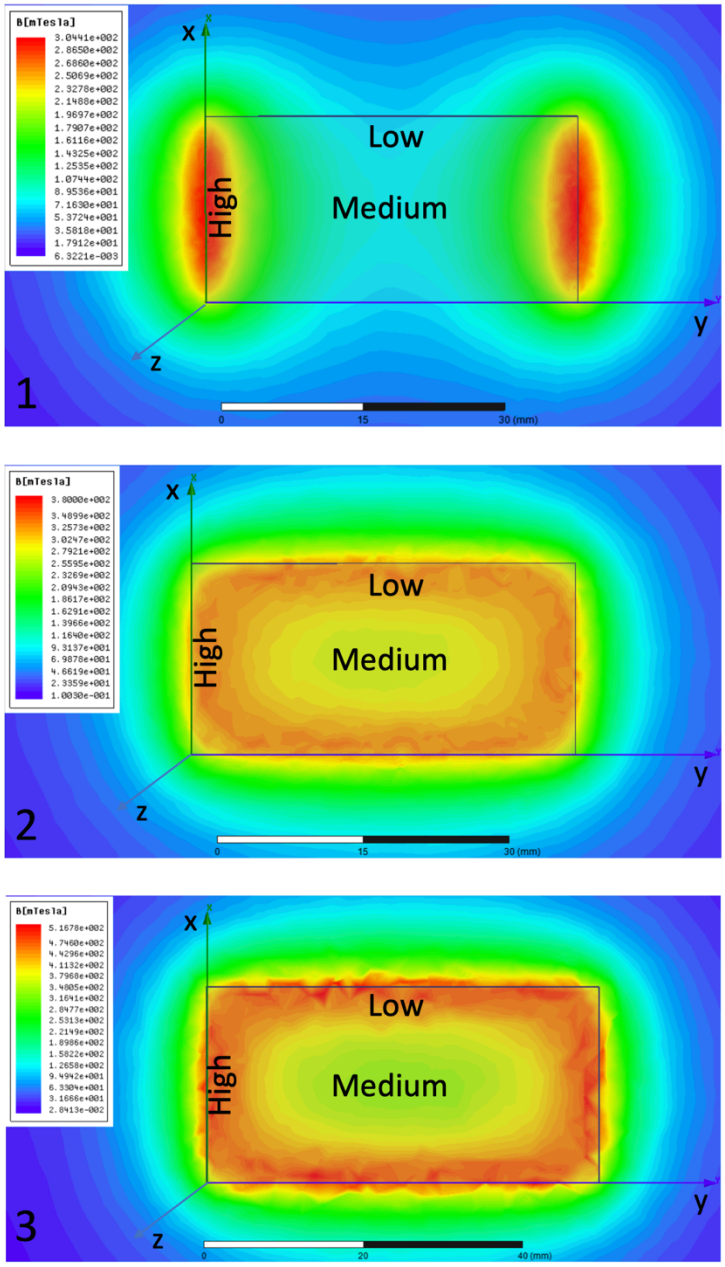

B

Magnetic Flux Density Module (mT)			
Magnets	Low	Medium	High
1 (11.2 kg)	67±0.2	81±0.8 (M1)	293±7.7
2 (21.7 kg)	227±2.1 (M2)	307±2.8	312±4.2(M3)
3 (32.2 kg)	250±2.5	441±5.4	449±5.6(M4)

Figure 4-8 Magnet simulation by ANSYS MAXWELL

(A) Magnetic flux density distribution of 11.2kg (A-1), 21.7kg (A-2) and 32.2 kg (A-3) pull Neodymium magnets. The simulation planes were 2mm above the magnet surface that considered the thickness of glass slides (B) The average magnetic flux densities in the template area that placed in three regions from low to high were calculated in each magnet (n=5).

4.5 The Influence of Magnetic Fields on the Patterns of Electrospray with Different Materials

The magnetic effect on MAEA deposition was firstly explored. As expected, the distribution of non-magnetic nanoparticles-HA did not show any sign of influence by magnetic fields, the collected patterns remained in round shapes no matter with or without magnets (Figure 4-9). Without magnet, magnetic nanoparticles (IONPs and IONPs-HA mixture) produced round-shaped patterns, but their patterns clearly changed with the addition of magnets. Both IONPs and the mixture samples were restricted inside the magnets area, which formed patterns with a similar rectangular shape to the magnet (Figure 4-9).

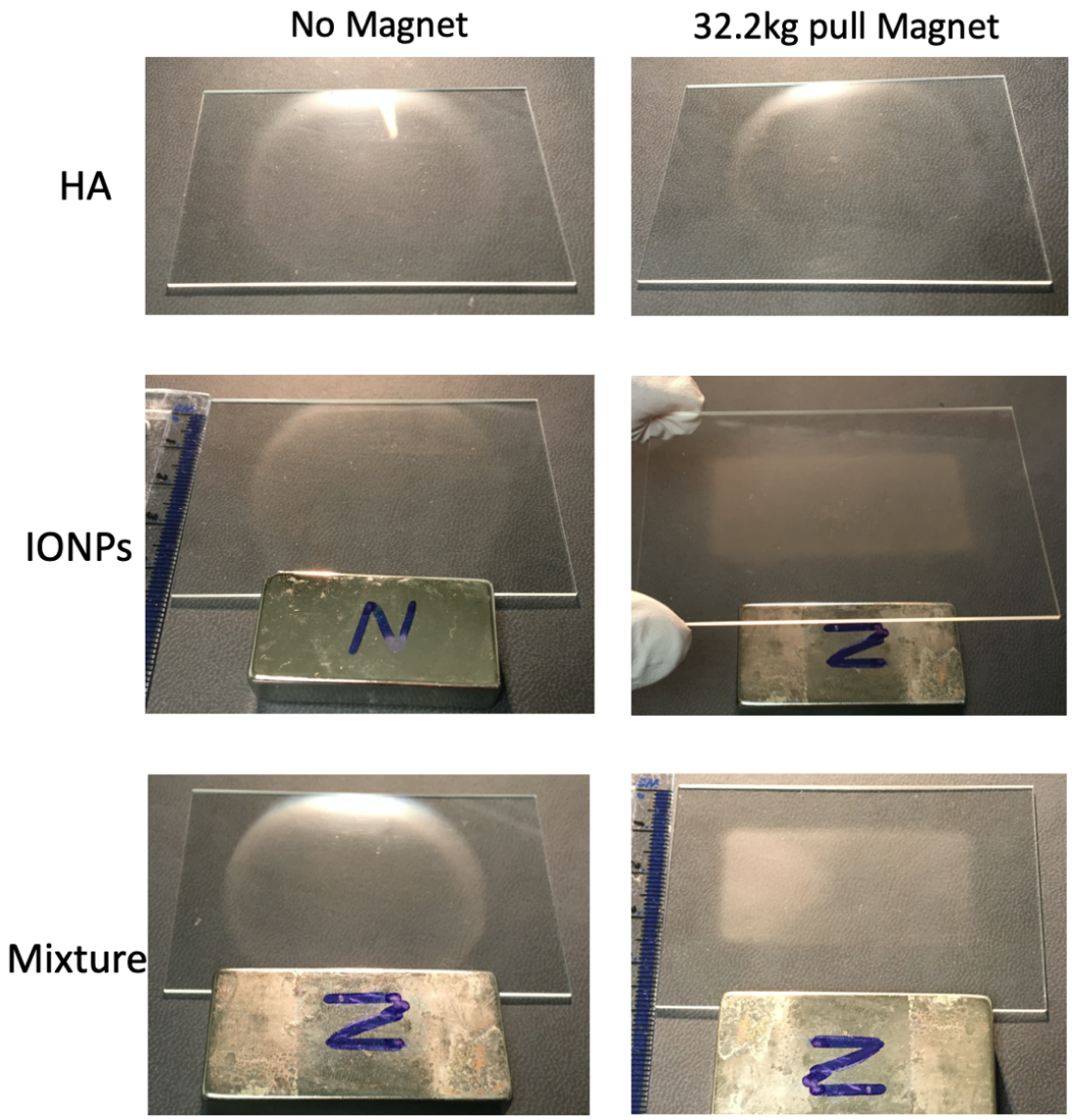

Figure 4-9 EHD coated patterns of different materials with or without the appliance of magnets.

Both HA and magnetic material (IONPs and mixture of IONPs and HA) patterns were collected by electrospray with and without magnets. Photos are collected patterns from the top view (glass slide75x50 mm).

4.6 The Influence of Magnetic Field on the TAEA Patterns

To investigate whether the magnetic field can control the patterns in a MTAEA process, magnetic nanoparticles including three magnetic MHA nanoparticles (Fe-MnHA, FeHA and MnHA) and HA, IONPs and IONPs-HA mixture as a control group were employed in TAEA and MTAEA processes to validate the influence of different magnetic fields. To mark the influence of magnetic fields, the width of lines in the coated patterns were chosen as an important parameter to indicate the fineness of the generated patterns. The gap between each template grid was measured as 280 μm. The MTAEA patterns of 50MHA, HA, IONPs and IONPs-HA mixture samples collected under the selected gradient of magnetic fields were first analyzed. Figure 4-10 has shown the increase of magnetic field flux density reduced the width of lines of all samples. A detailed measured width of lines was summarized in figure 4-11. From M0 to M4 the Fe-MnHA reduced from 260 μm to 125 μm, in FeHA the width of lines reduced from 261 μm to 116 μm and MnHA reduced from 254 μm to 144 μm. This result indicated that the influence of magnetic field was able to change the line width of MTAEA pattens composed of magnetic MHA nanoparticles. Moreover, the HA patterns did not show obvious changes according to magnetic fields. Both IONPs and IONPs-HA mixture

samples were affected by the appliance of magnetic fields that exhibited narrower width of lines after the addition of magnetic fields. IONPs were very sensitive to magnetic fields, the width of lines decreased rapidly from 192 μm to 77 μm from M0 to M4 magnetic fields. In the mixture samples, the width of lines also exhibited significant reduction according to the increase of magnetic flux density. Moreover, in the M0 control group, the three materials have shown difference in their patterns. The width of lines of IONPs (192 μm) were narrower than both HA (271 μm) and the mixture (261 μm) groups, while HA and the mixture samples did not show significant difference.

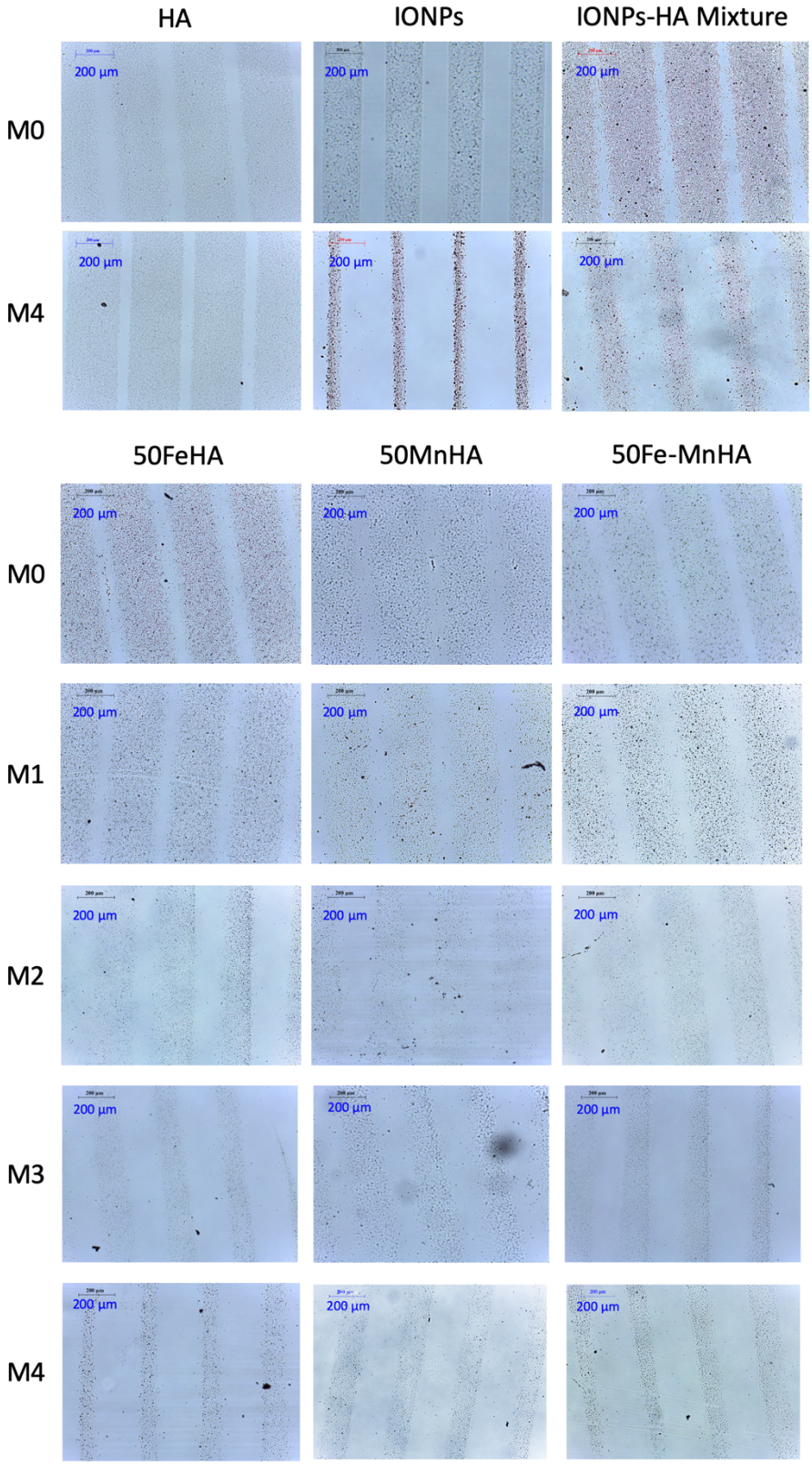

Figure 4-10 MTAEA patterns of 50 MHA, HA, IONPs and IONPs-HA mixture samples. Optical microscopy photos of MTAEA patterns with 10x magnification.

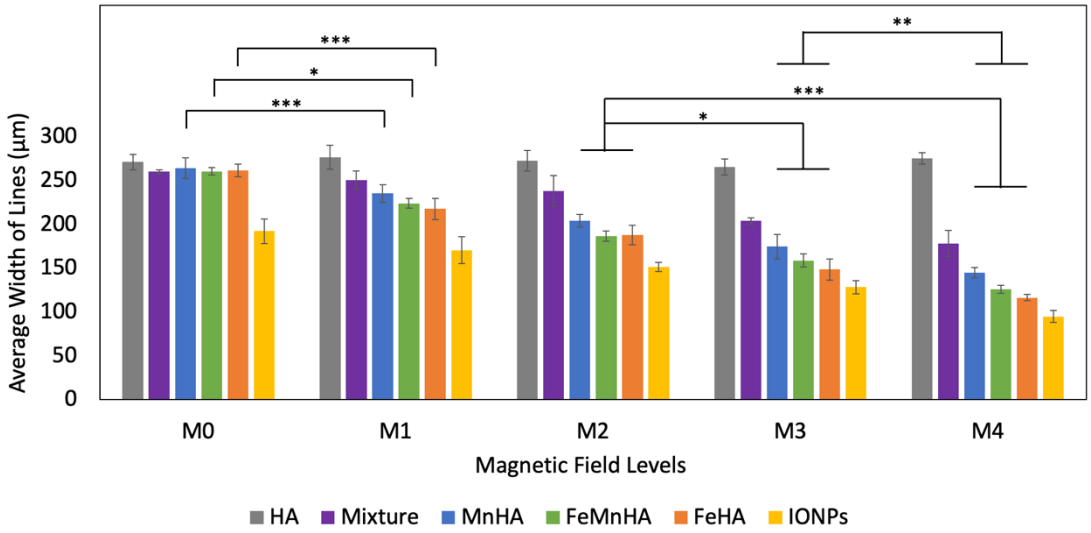

Figure 4-11 Average width of lines of 50(Fe-Mn)HA MTAEA patterns under different magnetic field.

Data contains the MTAEA results of selected gradient magnetic flux density regions. Data were acquired by Image J and are presented as mean ± SD (n=3). Student T test (n≥3): * represents P≤0.05; **P≤0.01; *** represents P≤0.001. Error bar represents standard error.

Since different materials exhibited different line width without magnetic field. To validate the sensitivity of different materials against magnetic fields, the acquired results were further integrated to reveal relative line width reduction of patterns corresponding to different magnetic fields (Figure 4-12). Among all the magnetic materials, IONPs is the most sensitive one to magnetic field. It exhibited the highest pattern reduction compared with other materials under the same magnetic flux density, which contributed to a 59% reduction in the line width percentage. The width of pattern of three magnetic ions substituted HA samples were between the IONPs and IONPs-HA mixture group. Among them, the line width percentage reductions were

56% (FeHA), 43% (MnHA) and 52% (Fe-MnHA), respectively, which means the magnetic sensitivity of Fe-MnHA and FeHA is higher than MnHA. Although the FeHA has shown the narrowest average width of patterns among the analyzed materials, no significant difference between Fe-MnHA and FeHA could be found. Since the Fe-MnHA exhibited higher bioactivity than FeHA, the co-substitution of Fe and Mn into HA may be the most valuable strategy to induce the changes of MTAEA patterns in biomedical field. Moreover, HA nanoparticles covered the largest area and showed no obvious correlation to the magnetic fields, while the significant reduction in the line width percentage of IONPs-HA mixture (33%) indicated that the IONPs successfully guided the distribution of HA particles under magnetic field, even though this effect is less obvious than IONPs itself.

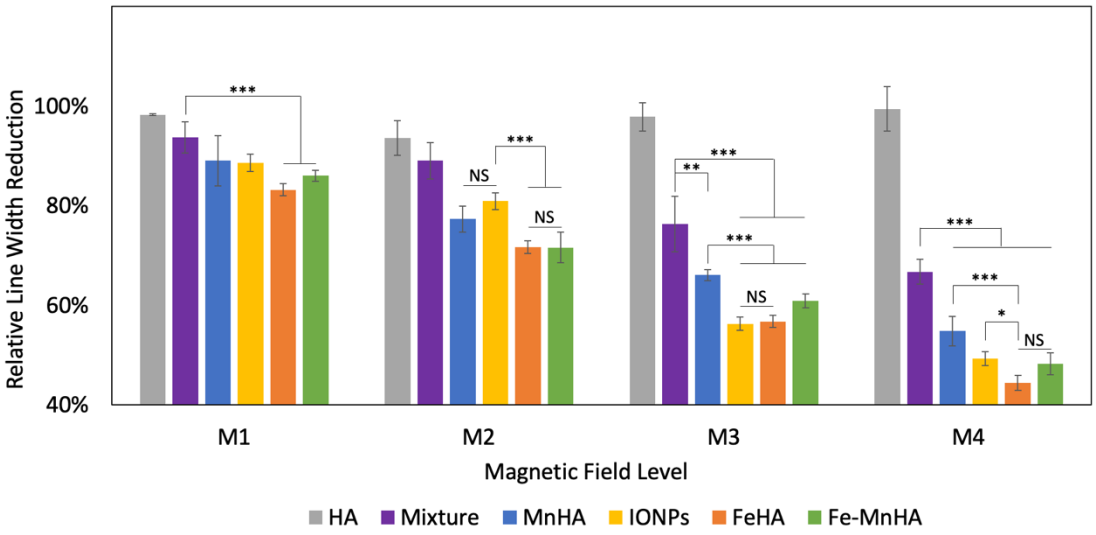

Figure 4-12 The relative line width reduction of different materials in response to different magnetic flux density

Data contains the MTAEA results of selected gradient magnetic flux density regions. Data were acquired by Image J and are presented as mean ± SD (n=3). Student T test (n≥3): * represents P≤0.05; **P≤0.01; *** represents P≤0.001. Error bar represents standard error.

4.7 The Magnetic Sensitivity of MHA with Different Metallic Content Substitution Level

The influence of different magnetic metallic ions substitution level on the sensitivity on the MTAEA process was further analyzed. Result has shown that the patterns of different MHA samples were all affected by the application of magnetic fields. When the magnetic fields were applied, all MHA samples have shown the reduction in width of lines (Figure 4-13). The influence of magnetic fields became more obvious with the increase of metallic content, the line width of 5MHA, 25MHA and 50MHA exhibited significant reduction with the increase of metallic ions substitution level ($P \leq 0.01$). All three 50MHA samples have achieved the narrowest width of lines comparing to the same MHA coated patterns, which reveals the higher magnetic susceptibility of 50MHA comparing to 5 and 25 MHA. The 5(Fe-Mn)HA and 25(Fe-Mn)HA have shown the narrowest average width of lines among three MHAs, and 50(Fe-Mn)HA has shown no significant difference comparing to the narrowest 50FeHA results. This reveals the co-substitution of Fe and Mn into HA well maintained the magnetic property.

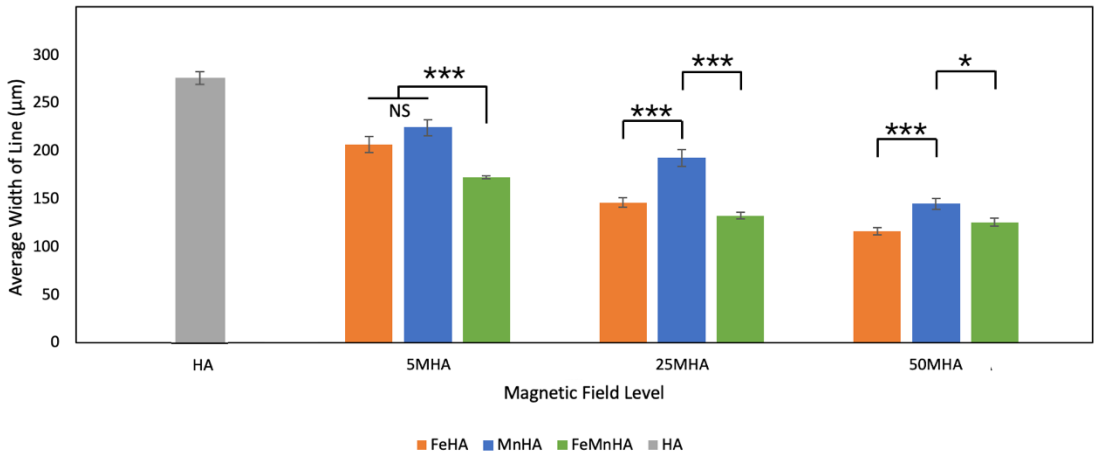

Figure 4-13 Average width of lines of different MHA MTAEA patterns in M4 region. Data contains the MTAEA results of three groups of MHA samples (5, 25, 50 MHA) collected at M4 region. Data were acquired by Image J and are presented as mean ± SD (n=3). Student T test (n≥3): * represents P≤0.05; **P≤0.01; *** represents P≤0.001. Error bar represents standard error.

4.8 Discussion

4.8.1 Fe and Mn Substituted into HA

In this chapter, HA and magnetic MHA nanoparticles, a series of Fe-MnHA, FeHA and MnHA with metallic content ranging from X_M=0.005 to X_M=0.05, were synthesized by a wet chemical method. SEM has been carried out on pure HA and MHA depositions and verified the nano structures of MHA according to the incorporation of Fe^{3+} and Mn^{2+} ions. All of the powders were characterized with XRD and FTIR, which indicated the typical structure of HA with no second phase. The chemical analysis indicates the

changes in lattice parameters were correlated to the substituent percentage. The reason of reduced lattice parameters was suggested due to the smaller ionic radius and the more electronegative character of Fe and Mn compared to Ca (Zilm et al., 2018).

4.8.2 Bioactivity of Fe-MnHA

In the in vitro bioactivity test, both Fe-MnHA and MnHA have exhibited a relatively higher CaP formation rate than FeHA, which reveals two possible explanations, first is the substitution of Fe^{3+} ions reduced the Ca^{2+} ions releasing into surrounding environment, the other possibility is the substitution of Mn^{2+} ions resulted in a higher Ca^{2+} ions releasing rate.

A study compared the substitution behavior of Fe^{2+} and Fe^{3+} and concluded that the Fe^{2+} substitution energetically prefers the sixfold-coordinated Ca(II) site (distorted octahedral) and the nonstoichiometric Fe^{3+} substitution is most stable in replacing the fourfold-coordinated Ca(I) site (Jiang et al., 2002). Due to the higher magnetic property, many studies have investigated the properties of Fe^{3+}HA. However, owing to the valence disparity of ferric ions, every two Fe^{3+} substitutions produced one calcium vacancy in order to compensate the charge imbalance, which will lead to calcium

deficient (Adamiano et al., 2019). Moreover, the substitution of Fe^{3+} ions into HA can decreased the ionic exchange rate (Christoffersen et al., 1987). The substitution of Fe^{3+} could stabilize the materials and prevent the ionic exchange in spite of the structure breaking effect caused by the substitution (Adamiano et al., 2019). Since, the SBF was supersaturated with respect to apatite the relatively lower apatite formation rate in the Fe^{3+}HA samples in this in vitro bioactivity test reveals a relatively lower Ca^{2+} ion concentration in solutions, which indicate the Fe^{3+} ions restricted the Ca^{2+} ions releasing into surrounding environment.

Meanwhile, many previous studies based on Mn co-substituted with other ions such as Ag^{+} and Sr^{2+} have indicated Mn^{2+} has a relatively higher ions exchange rate than the others (around 4 to 5 times higher than Sr^{2+} and 50 times more than Ag^{+}) (Huang et al., 2016b, Huang et al., 2018). Such a dramatically enhanced ions exchange rate directly contributes to the high bioactivities of materials, which reflected in the higher bioactivities of MnHA and Fe-MnHA in SBF soaking test.

4.8.3 Magnetic Properties of Fe-MnHA

Fe-MnHA, FeHA and MnHA were able to response to magnetic fields, the deposited patterns were similar to those from magnetic IONPs, thus demonstrating the magnetic

properties of substituted HAs. Fe-MnHA has exhibited higher line width reduction than MnHA and has no significant difference to FeHA, which represents the co-substitution of Fe and Mn is effective in introducing magnetic property into HA. Result has also indicated the magnetic susceptibility of Fe-MnHA increased with the increase of Fe and Mn content, which is consistent to previous studies (Li et al., 2009b, Li et al., 2012, Zilm et al., 2018).

Until now, there was no direct comparison of magnetic susceptibilities between Fe^{3+}HA and MnHA, but many studies have measured their magnetic moments. The value of magnetic susceptibility can be obtained by Curie-Weiss form: (Eq. *(4-1)*):

$$\chi = \frac{C}{T-\Theta} + \chi_0 \qquad (4\text{-}1)$$

Where C is the Curie-Weiss constant, Θ is the Curie-Weiss temperature and χ_0 represent the diamagnetic contribution of the HA. The Curie-Weiss constant C is directly related to the effective paramagnetic moment μ_{eff} of substituted metallic ions and can be obtained by (Eq. *(4-2)*): (Zilm et al., 2018)

$$\mathrm{C} = \mathrm{n}\boldsymbol{\mu}_{eff}{}^2/3k_B \qquad (4\text{-}2)$$

Where n is the number of metallic ions per unit mass and k_B is the Boltzmann constant

(Zilm et al., 2018). By comparing the observed Curie-Weiss constant (C) it is possible to compare the magnetic susceptibilities of different studies. The MnHA with X_M=0.004, 0.039, 0.062 and 0.121 have shown a C value as $0.18x10^{-6}$, $1.59x10^{-6}$, $2.32x10^{-6}$ and $4.94x10^{-6}$ (emu/g) respectively (Zilm et al., 2018). The Fe^{3+}HA with X_M=0.052, 0.105, 0.162 and 0.223 have shown a C value as $0.925x10^{-6}$, $4.4x10^{-6}$, $7.5x10^{-6}$ and $10x10^{-6}$ (emu/g) respectively (Li et al., 2009b, Li et al., 2012). According to these results, a magnetic susceptibility comparison between Fe^{3+}HA and Mn^{2+}HA can be plot out as below (Figure 4-14). It is consistent to the results in this project that the Fe-MnHA and FeHA are more sensitive to magnetic field than MnHA.

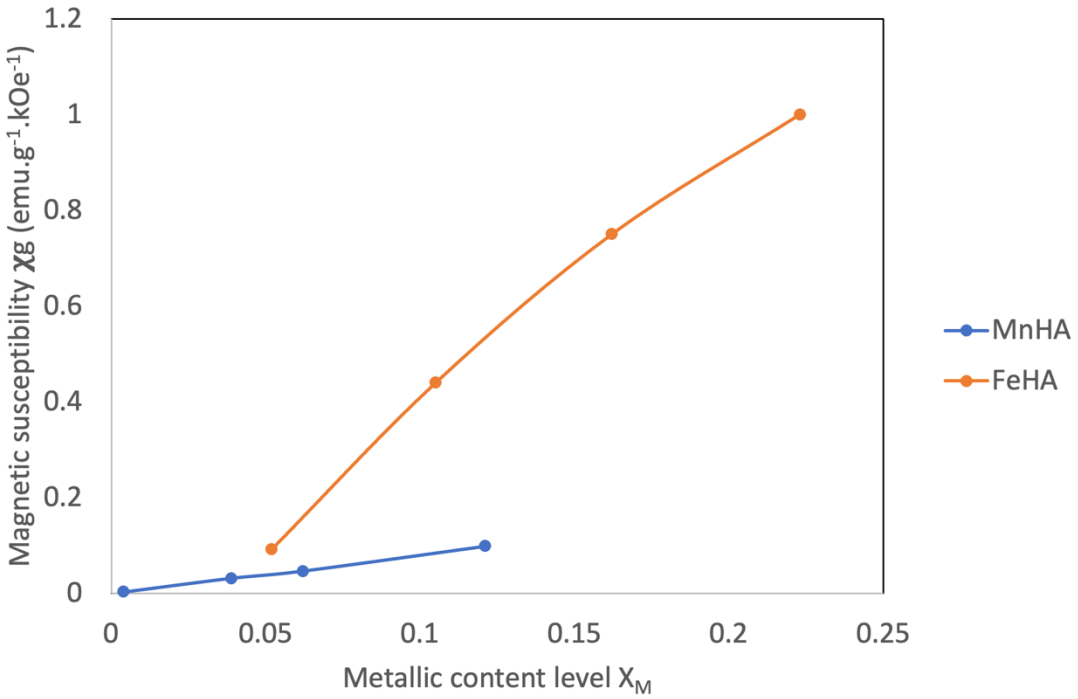

Figure 4-14 Magnetic susceptibility of Fe^{3+}HA and MnHA
(Li et al., 2009b, Zilm et al., 2018)

Since Fe^{3+} and Mn^{2+} has no significant differences in their magnetic moment, a highly possible explanation to the different magnetic susceptibility of FeHA and MnHA may be due to the different substitution levels. A previous study has indicated the achieved substitution content of Mn into HA has shown a serious restriction comparing to the designed level. For example, a group of FeHA and MnHA designed from X_M= 0.010 to 0.100 has achieved X_M=0.010 to 0.053 and X_M=0.010 to 0.117 for MnHA and FeHA respectively, which reveals Fe^{3+} has around twice substitution level than Mn^{2+}, which supported the higher magnetic sensitivity of FeHA than MnHA (Li et al., 2009b).

4.8.4 Magnetic Field Affects the Distribution of Magnetic Nanoparticles

In this study, all the magnetic materials used have shown that their patterns can be modified by magnetic field and exhibited patterns that restricted inside the magnet area and narrower lined patterns in the MTAEA process. Moreover, IONPs have been revealed to be able to guide the non-magnetic HA particles in magnetic fields to improve pattern resolution of IONP-HA mixture samples. Another finding in this chapter is that magnetic ions substituted-HA (Fe-MnHA, FeHA and MnHA) showed a higher magnetic susceptibility than the IONPs-HA mixture samples (Figure 4-18). This reveals that the substitution of magnetic ions into HA is more effective in controlling

the distribution of HA nanoparticles in a MTAEA processing than simply mixing the magnetic and non-magnetic nanoparticles.

4.8.5 The Spontaneously Reduced Width of IONPs and MHA TAEA Patterns

This chapter demonstrated that the patterns width of magnetic nanoparticles generated via MTAEA can be affected by the appliance of magnets, but surprisingly, even without magnet the width of IONPs lines (192 μm) was also narrower than other samples, which reveals forces besides other than magnetic field restricted the distribution of IONPs in smaller area.

A possible mechanism is during the process of electrospray, IONPs with high electric permittivity were positively charged and accelerated to the surface of collection plate, which can be considered as the building up of current between the high voltage spray nozzle and the collection plate connected to a ground lead (Figure 4-15 A). In this system, the movement of IONPs consuming electric potential energy leads to the formation of a resistance (R). Meanwhile, the copper grid and the aluminum alloy holding plate are separated by a non-conducting glass, which can be considered as a simple capacitance (C). Therefore, the whole system mimics a RC circuit (Figure 4-15

B). In this RC circuit, the movement of IONPs is labile, depend on the different charging state at copper templates (C). To clarify this dynamic process, it can be divided into four steps (Figure 4-16). When electrospray starts, the positive charged IONPs tend to aggregate on the top of copper grid due to its negative charged surface affected by the electric field (Figure 4-16 (1)); When the IONPs are accumulated on the surface of copper grid, it starts to charge the copper grid (C) to an electropositive state, which tends to form repulsion against other positive carriers (Figure 4-16 (2)). When more IONPs are supplied to this system (Figure 4-16 (3)), the excessive IONPs tend to aggregate in the center of copper grid gaps due to the resultant force (Figure 4-16 (4)). Therefore, it is reasonable to attract more IONPs at region ‘a’ comparing to region ‘b’ in figure 4-15 A.

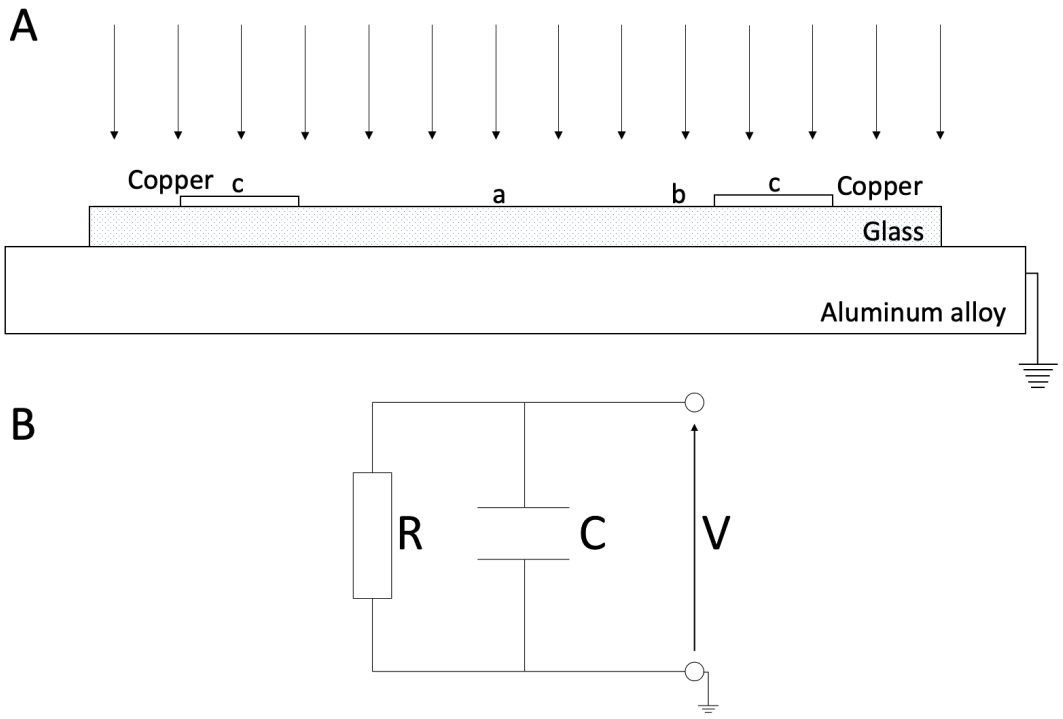

Figure 4-15 Schematic diagram of TAEA setting up

(A) Front view of a simplified model of TAEA. It is composed of a copper grid, a glass slide and an aluminum alloy holding plate connected to ground lead. There is a considerable distance between the charging nozzle and the collection plate, so the electric field can be considered as a uniform vertical electric field. 'a' marks the center region of gap between template; 'b' represents the gap area that close to template and 'c' indicate the copper template.

(B) Schematic diagram of a RC circuit . The R represent resistance, which is formed during the movement of IONPs; the C represent capacitance, which indicate the capacitance composed of the copper grid and aluminum alloy holding plate.

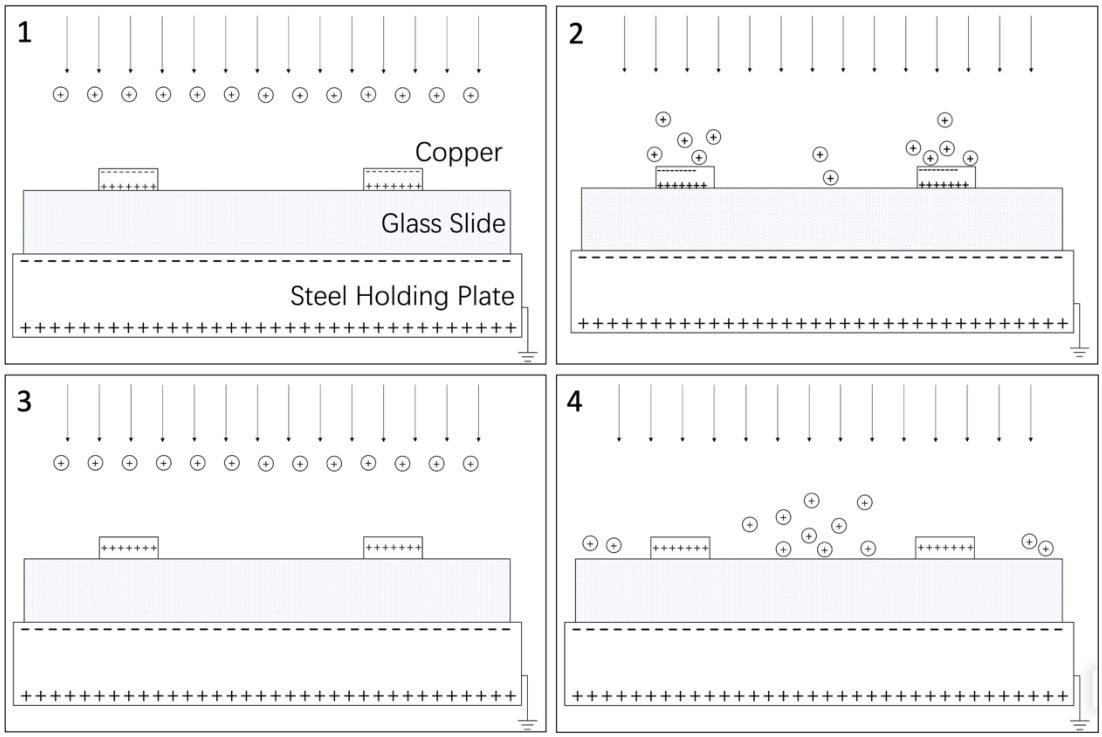

Figure 4-16 Schematic diagram of hypothetical mechanism that may lead to the accumulation of IONPs in a TAEA system.
(1) Electrostatic induction of copper grid, (2) attraction of positive IONPs to negative surface of copper grid, (3) further supplement IONPs, (4) aggregation of IONPs due to resultant force.

4.9 Conclusions

HA substituted with Fe^{3+} and Mn^{2+} was successfully synthesized by wet chemical method. All samples were single phased within the limit of characterization sensitivity. In the in vitro bioactive test, the bioactivity of all the as-formed nanoparticles has shown the apatite formation rate is related to the chemical composition with the observed apatite cover percent as (HA, Fe-MnHA, MnHA) > (FeHA, HA-IONPs mixture) >

IONPs. These results have approved the potential of using Fe-MnHA as a bioactive magnetic material in the future.

The systematic experimental investigation in this chapter have successfully demonstrated that the spatial distribution of magnetic nanoparticles can be affected by the appliance of magnets. With the influence of magnetic field during MTAEA process, the width of patterns of magnetic nanoparticles (Fe-MnHA, FeHA, MnHA, IONPs, and IONPs-HA mixture) are narrower compared to that without magnetic field, and the stronger magnetic field applied, the slenderer the pattern would be. Furthermore, comparing those different types of magnetic nanoparticles, all the magnetic ions substituted HA showed a higher sensitivity to magnetic fields than the simple mixture of IONPs and HA, and Fe-MnHA and FeHA exhibited a higher magnetic susceptibility than MnHA. This indicates Fe-MnHA has great potential to be manipulated by MTAEA coating process to produce biocompatibility fine patterns.

Chapter V

5 Multi-functional Cu and Zn Co-substitution of HA for Implant Coating

5.1 Introduction

Multifunctional implant coatings have been introduced in orthopedic applications to treat various bone diseases and maintain the bone functions. A big challenge in implant surgery is the infection at insertion sites affects the clinical functions of implants (Goodman et al., 2013). Therefore, developing biocompatible implant coatings with antibacterial ability is the key to solve this problem. The substitution of antibacterial metal ions into HA lattice structures has the potential to combine the biocompatibility and antibacterial ability at the same time (Li et al., 2011). In the recent researches, metal ions such as Ag^{+}, Cu^{2+} and Zn^{2+} have been introduced as very effective elements in introducing antibacterial ability into HA. However, AgHA has drawbacks like nanotoxicity (Panyala, 2008, Prabhu and Poulose, 2012). To solve this problem Cu^{2+} and Zn^{2+} have risen in importance in medical field.

Cu^{2+} substituted HA has a strong antimicrobial ability and low cytotoxicity at low

substitution level (Shanmugam and Gopal, 2014). However, the antimicrobial ability of CuHA recede very distinctly with the reduce of substitution level due to the restricted releasing rate (Huang et al., 2015). The dramatic reduced releasing rate can further decrease the contact rate between Cu^{2+} and bacteria, hence inhibit their bacterial killing ability. ZnHA has good antibacterial ability and higher ions releasing rate than CuHA ions (Huang et al., 2015, Anwar, 2016). Zn^{2+} is also able to increase the releasing rate of metallic ions when it co-substituted with other ions into HA (Tamm and Peld, 2006). Moreover, the co-substitution of metallic ions into HA was known to be able to enhance the phase purity that reserve more metal ions in HA, which can be further released into environment. The released metallic ions were suggested to be the main reason contributed to the antimicrobial activities (Ren et al., 2009b, Akhavan and Ghaderi, 2010, Pasquet et al., 2014, Vincent et al., 2016).

Therefore, in this study, a low level (up to X_M=0.005) co-substitution Zn^{2+} and Cu^{2+} in HA has been investigated, from synthesis, characterization to antibacterial (gram positive and negative bacterial) potential, antibiofilm formation and biocompatibility to human osteoblast cells. This chapter is going to focus on the following detailed objectives:

i. Synthesizing and characterizing Cu-ZnHA, CuHA and ZnHA with variety metallic

contents.

ii. Investigating the influence of metallic contents in different MHA (MHA represents Cu-ZnHA, CuHA and ZnHA in this chapter) on their anti-infection abilities.

iii. Analysis on the biocompatibility of MHA with different metallic content levels.

5.2 Characterization of HA, CuHA, ZnHA and Cu-ZnHA

Cu and/or Zn (co-)substituted HA, with the substitution levels varied from X_M=0.0005 to X_M=0.005 and a pure HA as control group were characterized by XRD, FTIR, EDS and SEM.

5.2.1 XRD Characterization

The XRD patterns of Cu-ZnHA, CuHA, ZnHA and HA are shown in figure 5-1 and figure 5-2 and compared to several ICDD (International Centre for Diffraction Data) database to identify the material compositions.

In the as-synthesized Cu-ZnHA group, the major HA peaks (002, 211, 112, 300, 202,

300) are matched well with HA (ICDD 00-009-0432) standard, which reveals a single-phase structure and the undesirable secondary phases, such as tricalcium phosphate, tetracalcium phosphate or calcium oxide, are not detected. With the increase of metal ions in HA lattice structure, the peak intensity decreased and no shift of peak position was detected. In the as-synthesized CuHA group the peaks were clear and matched well with CuHA (ICDD 01-078-3830) standard for CuHA (X_{Cu}=0.02), while the peaks in the as-synthesized ZnHA group were obscure and comparing to ZnHA (ICDD 01-080-6195) standard for ZnHA (X_{Zn}=0.012), no peak shift can be detected. Moreover, with the increase of both Cu and Zn content from X_M=0.0005 to X_M=0.005, both peak intensities were decreased.

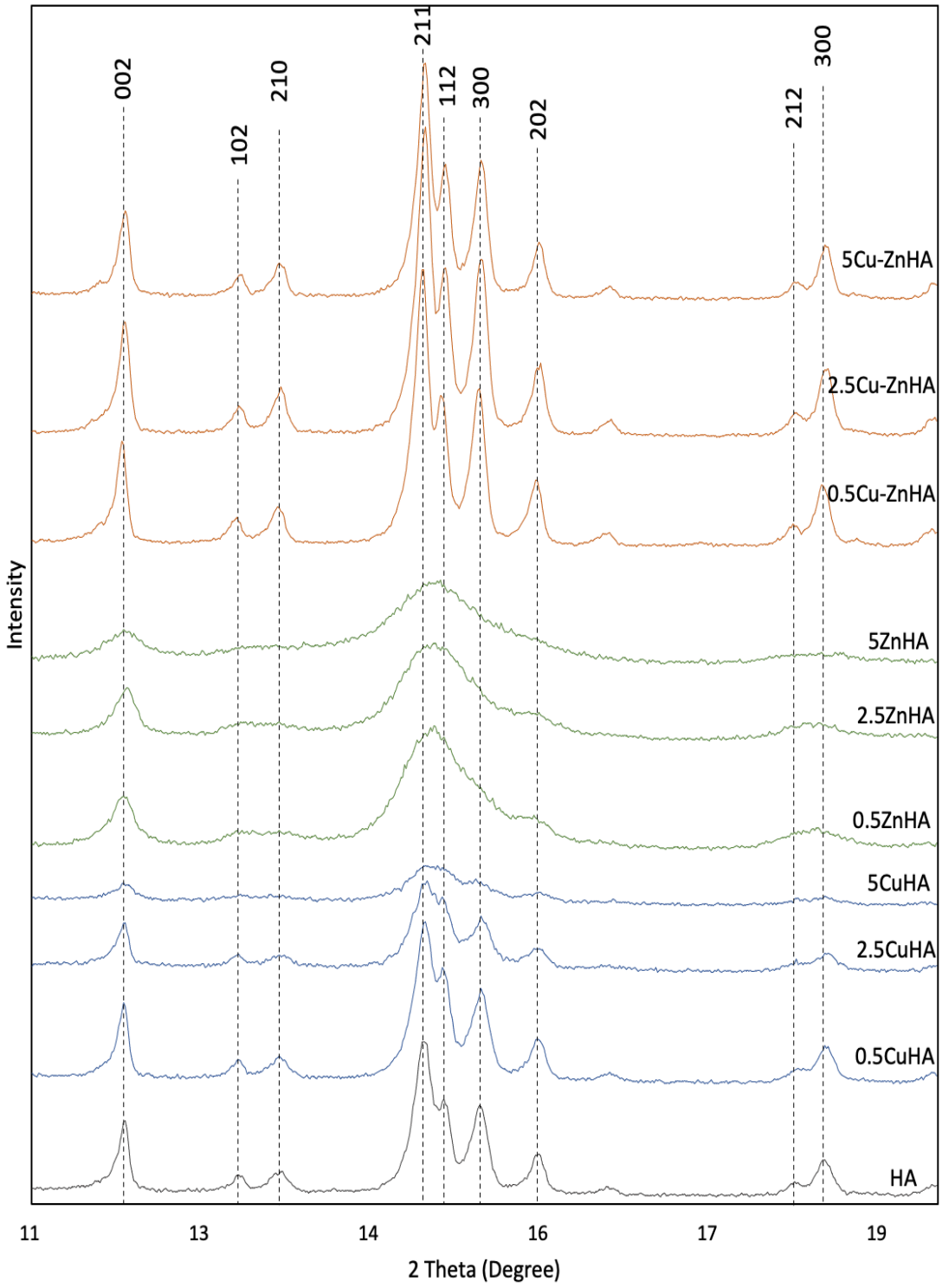

Figure 5-1 XRD patterns of as-synthesized Cu-ZnHA, ZnHA, CuHA and HA powders. Peaks were compared with HA (ICDD 00-009-0432) standard

After heat-treated the as-synthesized samples, the peak positions of Cu-ZnHA samples also match the major HA peaks in ICDD standard HA and the peak intensity of Cu-ZnHA samples was increased (Figure 5-2). The sharp peaks in XRD patterns indicated that the samples are well crystalized. In the heat-treated CuHA group, the 0.5CuHA and 2.5CuHA exhibits similar patterns and matched well with ICDD standard CuHA (X_{Cu}=0.02). However, the peak 102 and 202 in 5CuHA sample has exhibited a clear increase, and both peak 210 and 202 have shifted to the right, which represents the existence calcium copper phosphate ($Ca_{20}Cu(PO_4)_{14}$ ICDD 00-048-1126) (Figure 5-2 triangle points). In the heat treated ZnHA groups, the 0.5ZnHA and 2.5ZnHA matched well with ICDD standard ZnHA (X_{Cu}=0.012), but the 5ZnHA exhibited an unexpected peak on the right of peak 202 appeared (Figure 5-2 triangle point). According to the ICDD database, it could be due to the appearance of ZnO.

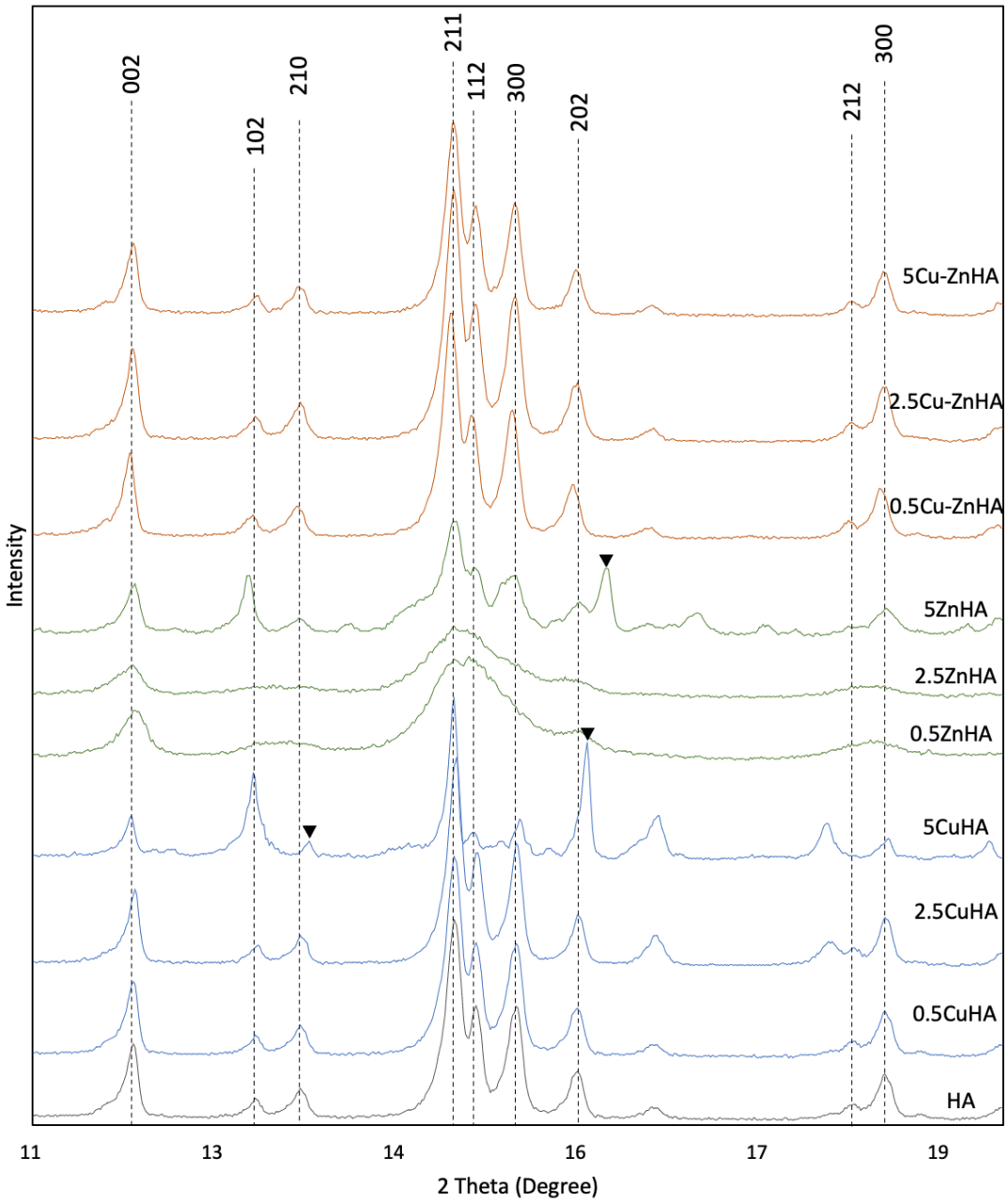

Figure 5-2 XRD patterns of heat-treated Cu-ZnHA, ZnHA, CuHA and HA powders. Peaks were compared with HA (ICDD 00-009-0432) standard

The crystallinity (X_C) of heat-treated MHA results indicated the increase of Cu and/or Zn content leaded to the decrease of crystallinity gradually (Table 5-1 and figure 5-4). In Cu-ZnHA and CuHA, the crystal sizes were increased as the amount of Cu-Zn and Cu increased. It may be due to the substitution of Cu into HA inhibited its growth. This result is consistent to a previous study that confirmed the decrease in crystal size of CuHA associated to the increase of Cu substitution level (Othmani et al., 2018). The crystal size of ZnHA from 0.5ZnHA to 2.5ZnHA first exhibited a decrease, which indicates the substitution of Zn into HA can cause the decrease of crystal size. It is consistent with Xiao et al. results that the Zn content has a negative effect on the crystal size (Xiao et al., 2008). However, as the Zn content increased to 5ZnHA, a higher crystal size was observed, which represents the appearance of ZnO reduced the Zn content in HA. In summary, Cu and Zn were proved to be successfully substituted into Cu-ZnHA. With the increase of metallic contents, MHA samples tend to show decreased crystallinity and crystal size (Figure 5-4). Results indicated the heat treatment has not affected the phase purity of Cu-ZnHA.

Table 5-1 Lattice parameters, crystal size and degree of crystallinity (X_C) of MHA with different metallic content.

Sample	Unit cell parameters			Crystal Size (nm)	Crystallinity (X_C)
	a(Å)	c(Å)	V (Å^3)		
HA	9.421	6.869	528.00	319.9	83.45±5.71%
0.5CuHA	9.414	6.882	528.22	319.9	83.73±5.46%
2.5CuHA	9.409	6.876	527.15	284.4	82.90±2.53%
5CuHA	9.356	6.880	521.57	255.9	80.81±4.41%
0.5ZnHA	9.454	6.909	534.74	182.8	82.17±3.78%
2.5ZnHA	9.419	6.928	532.32	170.6	80.97±4.17%
5ZnHA	9.433	6.886	530.56	319.9	76.74±8.20%
0.5(Cu-Zn)HA	9.417	6.887	528.93	365.6	80.70±4.18%
2.5(Cu-Zn)HA	9.433	6.889	530.91	284.4	80.55±4.41%
5(Cu-Zn)HA	9.422	6.883	529.12	255.9	79.59±6.32%

HA has hexagonal crystal structures, so the unit cell parameter a and b constants are equal, here only unit cell parameter a (Å) and unit cell parameter c (Å) constants are displayed.

5.2.2 FTIR Characterization

FTIR spectra analysis was performed to determine the functional groups existed in the heat-treated HA and MHA samples. The FTIR spectra of all samples showed the characteristic transmittance bands of HA (Figure 5-3) (Rehman, 1997). The weak band around 470 cm^{-1} was assigned to the phosphate bending vibration and the band between 560 and 602 cm^{-1} appearing as a doublet corresponds to the PO_4^{3-} bending mode. In addition, the bands with shoulder at 961–1096 cm^{-1} represent the P–O

stretching vibration of the phosphate groups (PO_4^{3-}). Hydroxyl peaks around 632 cm^{-1} are OH^- vibrational mode. Moreover, carbonate bands were also founded between 1520 and 1360 cm^{-1}. There are also small peaks around 1417 cm^{-1} ascribed as CO_3^{2-} ions. The existence of CO_3^{2-}may be due to the binding of carbon dioxide from the air by the Ca^{2+}, Cu^{2+} and Zn^{2+} ions during samples synthesis.

As an ATR measurement, the reductions of PI are related to the decrease of crystallinity. The PI of the main P–O stretching bands at 1027 cm^{-1} were plotted in figure 5-4. In the results of Cu-ZnHA and ZnHA samples, with increased metallic fraction, the peak intensity decreased. It can be observed from the FTIR spectra, the three PO_4^{3-} stretching peaks at 962, 1027 and 1091 cm^{-1} become obscure and separated from each other with the increase of Cu-Zn and Zn content and the OH bending peaks at 613 cm^{-1} became broaden (Figure 5-3). Meanwhile, the PI reduction of CuHA FTIR spectra was not obvious, which suggests the decrease of apatite crystallinity was more dependent on the increase of Zn fraction (Figure 5-4). This result suggests that the substitution of Zn^{2+} is more effective in reducing the crystallinity than Cu^{2+} ions, which matches well the crystallinity results measured in XRD patterns (Figure 5-4).

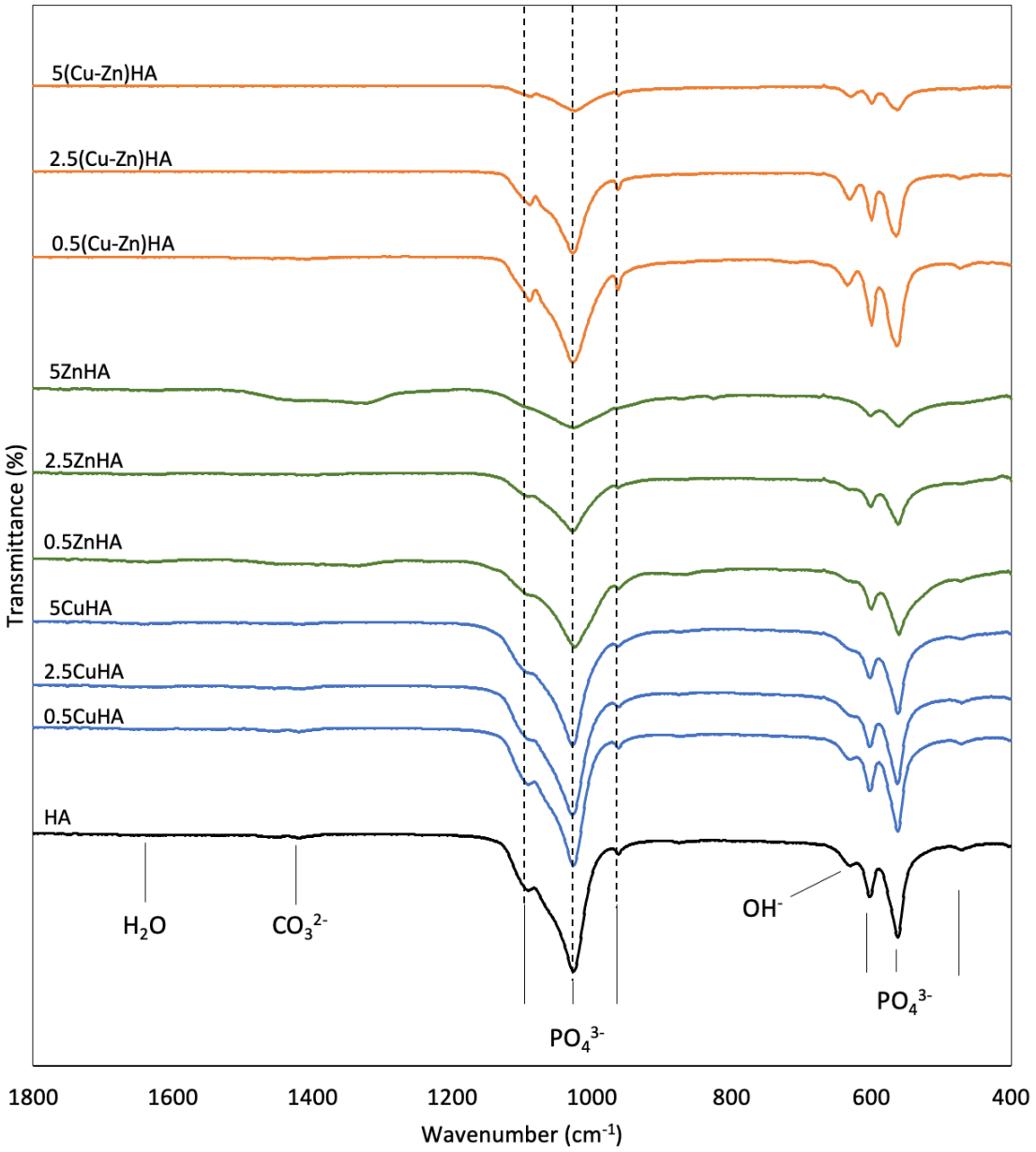

Figure 5-3 FTIR spectra of mono- and multi-ionic substituted HA with variety Cu and Zn content.

The chemical groups of the main peaks are labeled in this figure and the peaks' positions of three phosphate peaks around 961-1096 cm^{-1} are marked.

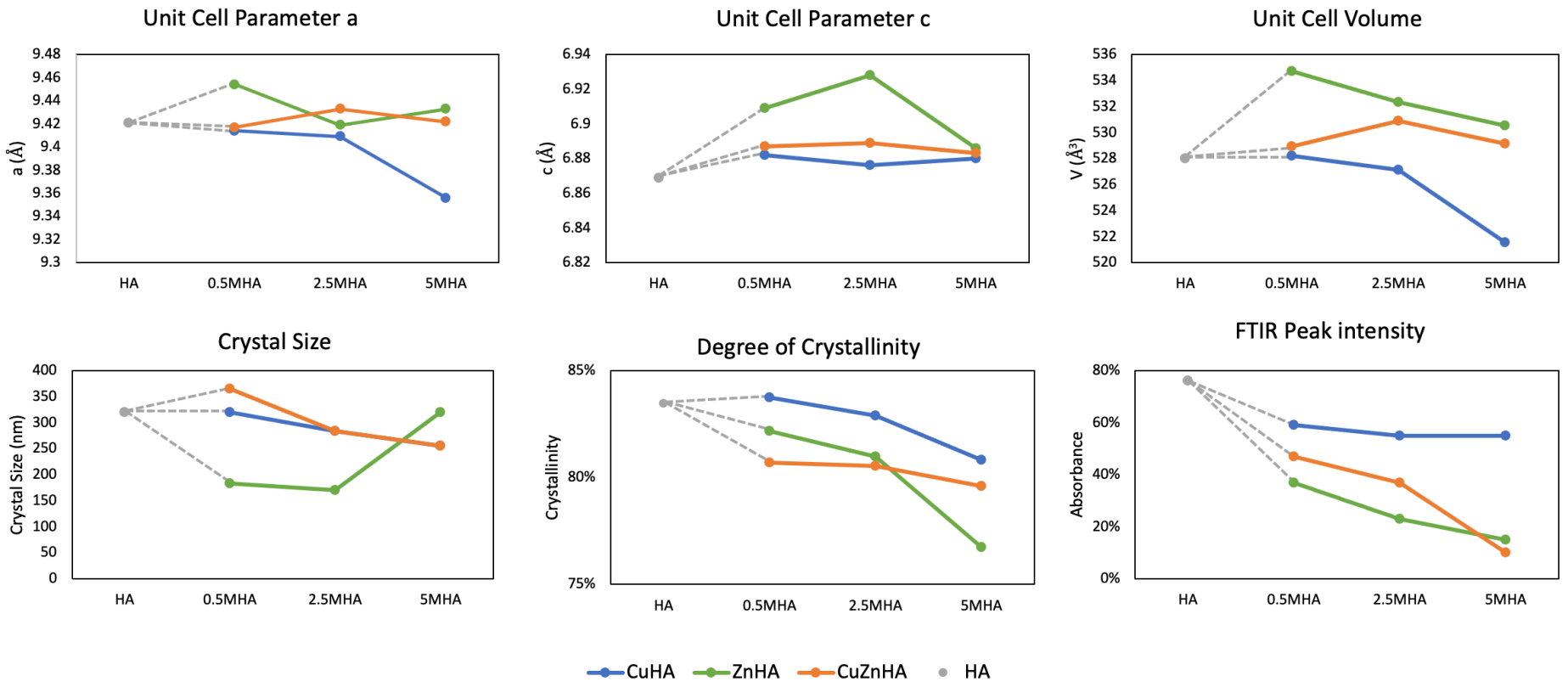

Figure 5-4 Unit cell parameters, crystal size, crystallinity measured in XRD results and Peak intensity (PI) of PO_4^{3-} stretching peak at 1027cm^{-1}.

5.2.3 EDS Analysis

The elemental composition of the heat-treated MHA nanoparticles was identified using SEM equipped with energy-dispersive X-ray analysis spectroscopy (EDS).

The EDS results can indicate the types and content of different elements contained in the samples. With the increase of designed metallic content in substituted HA samples, EDS results in the measured $X_{(Cu+Zn)}$ revealed both Cu^{2+} and Zn^{2+} were substituted into the HA crystal lattice (Figure 5-5). Among the three MHA, Cu-ZnHA has a steeper $X_{(Cu+Zn)}$ gradient and higher X_M than the expected value, which represent co-substitution of Cu^{2+} and Zn^{2+} is easier to substitute into HA than mono-substituted HA. Both 5CuHA and 5ZnHA samples have lower X_{Cu} and X_{Zn} than the expected value, which means the mono-substitution of Cu^{2+} or Zn^{2+} inhibited the metallic contents that can doped into HA lattice structure (Figure 5-5).

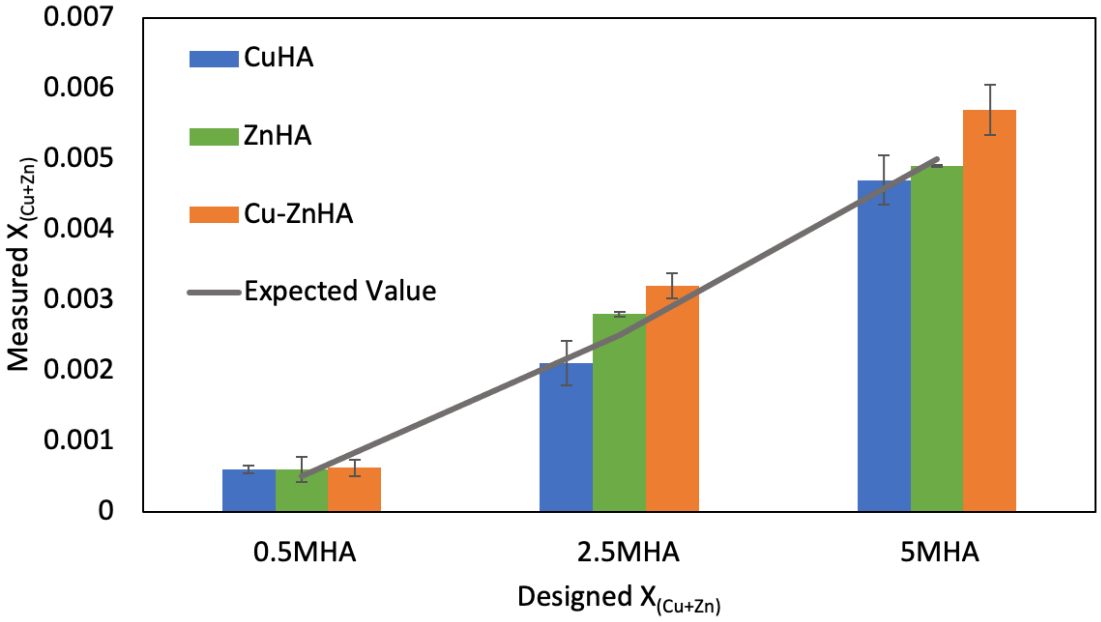

Figure 5-5 Measured XC based on EDS results of both mono-ionic and multi- ionic substituted HA.

Three different designed metallic content were labeled in x axis, and the measured $X_{(Cu+Zn)}$ were marked above each column. Data are presented as mean ± SE (n=3).

5.2.4 Investigating the Morphologies of Nanoparticles via SEM

The morphology of heat-treated HA and MHA nanoparticles was investigated. It was observed that both the shapes and sizes of the synthesized nanoparticles were associated to the amount of metallic content in MHA.

HA exhibited spherical structure (Figure 5-6 A), while Cu-ZnHA had shown an elongation according to increase in metallic content. In the 0.5(Cu-Zn)HA image, both spherical structure and rod-like structure can be detected, while in the images of higher metallic content samples, only rod-like structure was observed (Figure 5-6 D). ZnHA nanoparticles have nearly spherical structure without sharp face angles and they are highly agglomerated in coating layers (Figure 5-6 B). With the increase Cu content, CuHA were also elongated and formed needle-like structures and were less agglomerated than ZnHA (Figure 5-6 C).

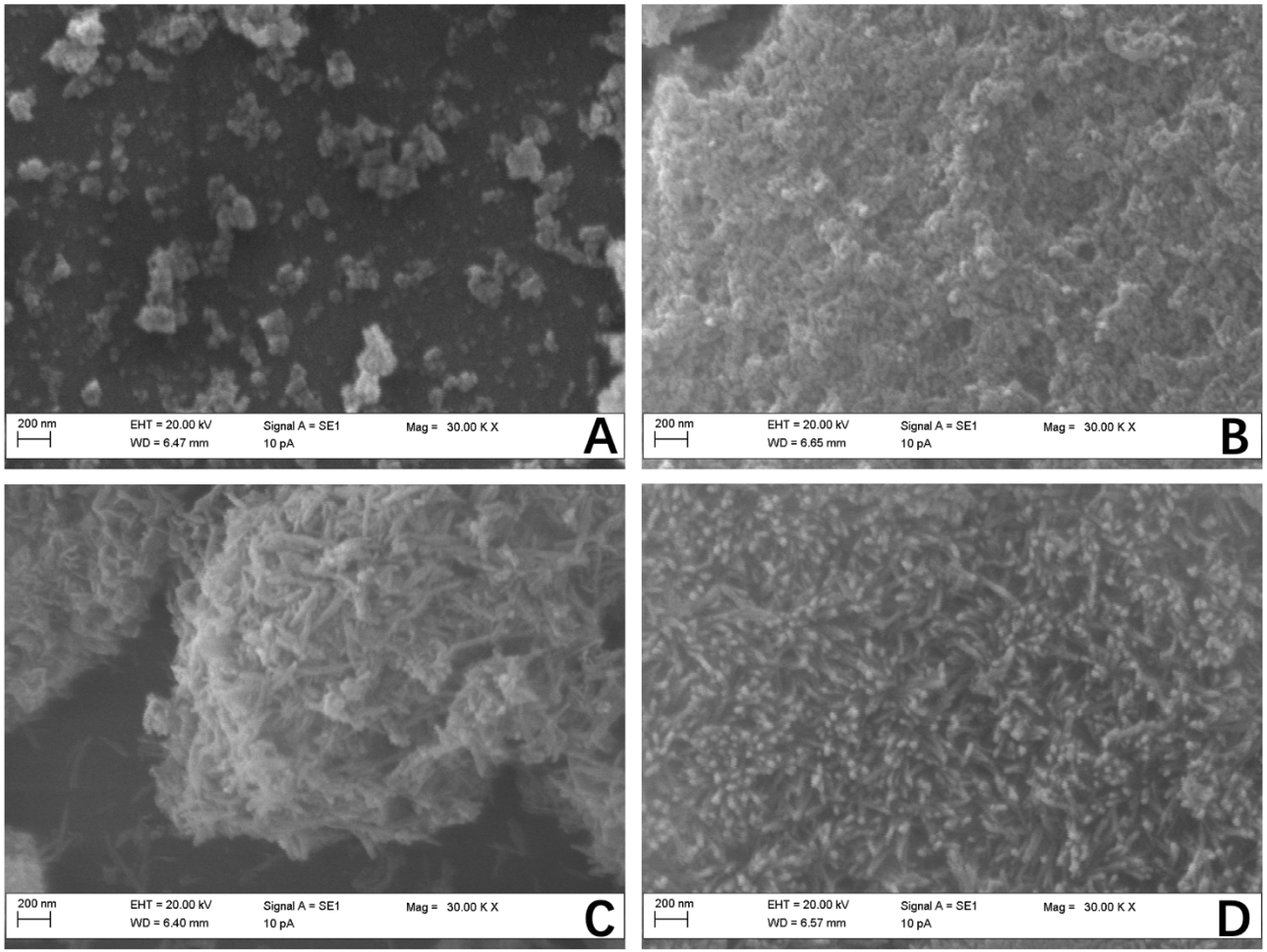

Figure 5-6 The morphologies of ZnHA, CuHA and (Cu-Zn)HA with variety metallic content.

SEM images showing the morphologies of MHA and HA. (A) HA, (B) 5ZnHA, (C) 5CuHA, (D) 5(Cu-Zn)HA.

5.3 Antibacterial Test of HA, CuHA, ZnHA and Cu-ZnHA

Two bacterial strains that commonly used in antibacterial tests, including *E. coli* and *S. aureus*, were employed to evaluate the antibacterial abilities of heat-treated Cu-ZnHA, CuHA and ZnHA nanoparticles in solutions. A group of live/dead gating analysis of flow cytometry patterns with Cu-ZnHA result was shown in Figure 5-7. The detailed results of all samples were plot in Figure 5-8. In general, with the increase of metallic content in MHA, enhanced antibacterial abilities on both *E. coli* and *S. aureus* were observed. 0.5(Cu-Zn)HA exhibits the strongest antibacterial ability against *E. coli* in the 0.5MHA group (~ 30%), while in the 2.5MHA and 5MHA groups, there was no significant difference of antibacterial ability between Cu-ZnHA and CuHA. Both Cu-ZnHA and CuHA show high bacteria killing rate, which reveals the Cu-ZnHA maintained the antibacterial ability comparing to CuHA. In terms of the *S. aureus* group, both 0.5(Cu-Zn)HA and 2.5(Cu-Zn)HA showed the strongest killing rate among three different MHA materials with the same metallic content, which was 40% and 45% respectively. In the 5MHA group, the antibacterial ability of Cu-ZnHA was similar to CuHA ($P>0.05$), both of them showed very strong antibacterial ability. It is worth to note that at the low metallic content, Cu-ZnHA produced the strongest antibacterial ability compared with the other two materials.

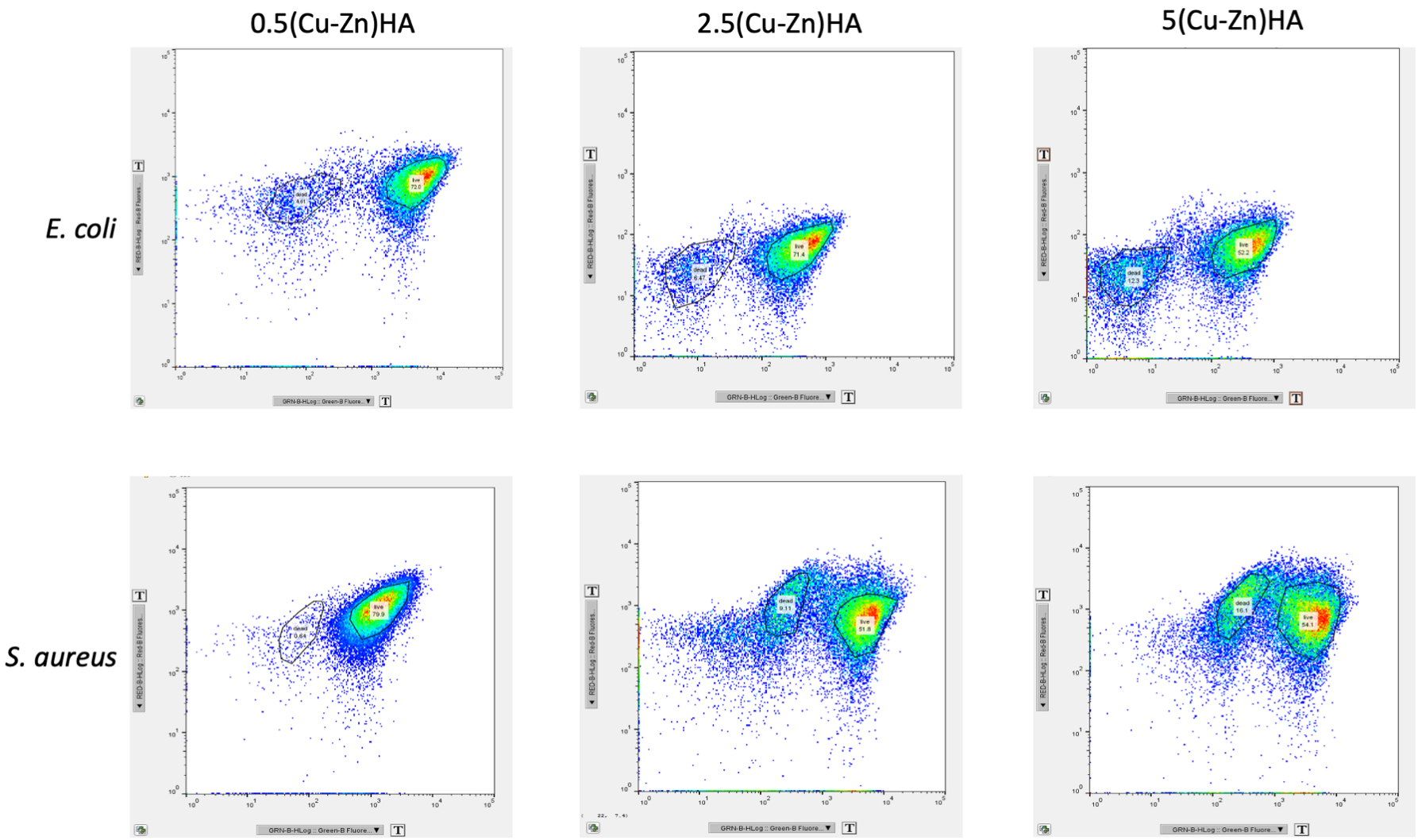

Figure 5-7 The live/dead gating analysis of flow cytometry patterns of Cu-ZnHA samples.

Figure shows a group of analysis contains Cu-ZnHA samples with three substitution levels and two bacteria strains.

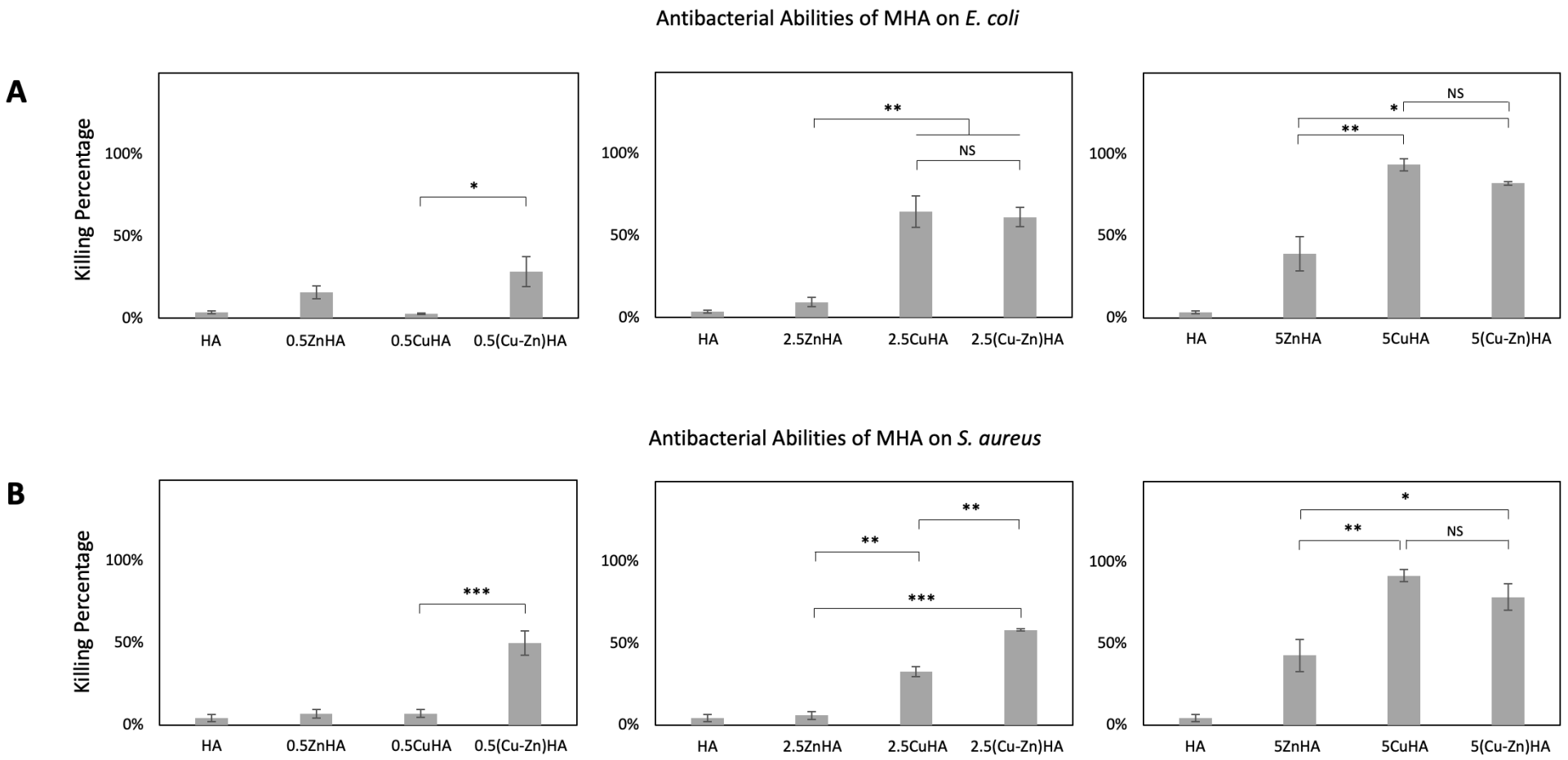

Figure 5-8 Antibacterial abilities of CuHA, ZnHA and Cu-ZnHA against E. coli and S. aureus.

Killing ratio of MHA against E. coli (A) and S. aureus (B). Student T test (n=3): * represents P≤0.05; **P≤0.01; *** represents P≤0.001. Error bar represents standard error.

5.4 Antibiofilm Formation Abilities of HA, CuHA, ZnHA and Cu-ZnHA

Both *E. coli* and *S. aureus* are biofilm-forming pathogens, they were further employed to evaluate the anti-bacterial adhesion and anti-biofilm formation properties of MHA deposited on titanium plates. Results indicated that with the increase of metallic content in Cu-ZnHA, CuHA and ZnHA, their anti-biofilm formation abilities all gradually increased. In *E. coli* test group, all ZnHA samples exhibited the highest OD among three different MHA with the same metallic content, which represents the lowest anti-biofilm formation abilities. Noticeably, the anti-biofilm ability of Cu-ZnHA showed a significant increase compare to CuHA at 0.5MHA and 2.5MHA, while both CuHA and Cu-ZnHA showed a similar inhibition ability at 5MHA (Figure 5-9 A). This finding is consistent to the hypothesis that the co-substitution of Cu and Zn ions can enhance the anti-biofilm formation ability at low metallic content. Similar findings were also observed in *S. aureus* test group. With the same metallic content, the highest anti-biofilm formation abilities were appeared in both 0.5(Cu-Zn)HA and 2.5(Cu-Zn)HA and there was no significant difference between CuHA and Cu-ZnHA in 5MHA group. In 0.5MHA groups, ZnHA has a higher antibiofilm ability than CuHA, but CuHA has achieved stronger biofilm inhibitory rates than ZnHA in 2.5 and 5MHA groups (Figure 5-9 B).

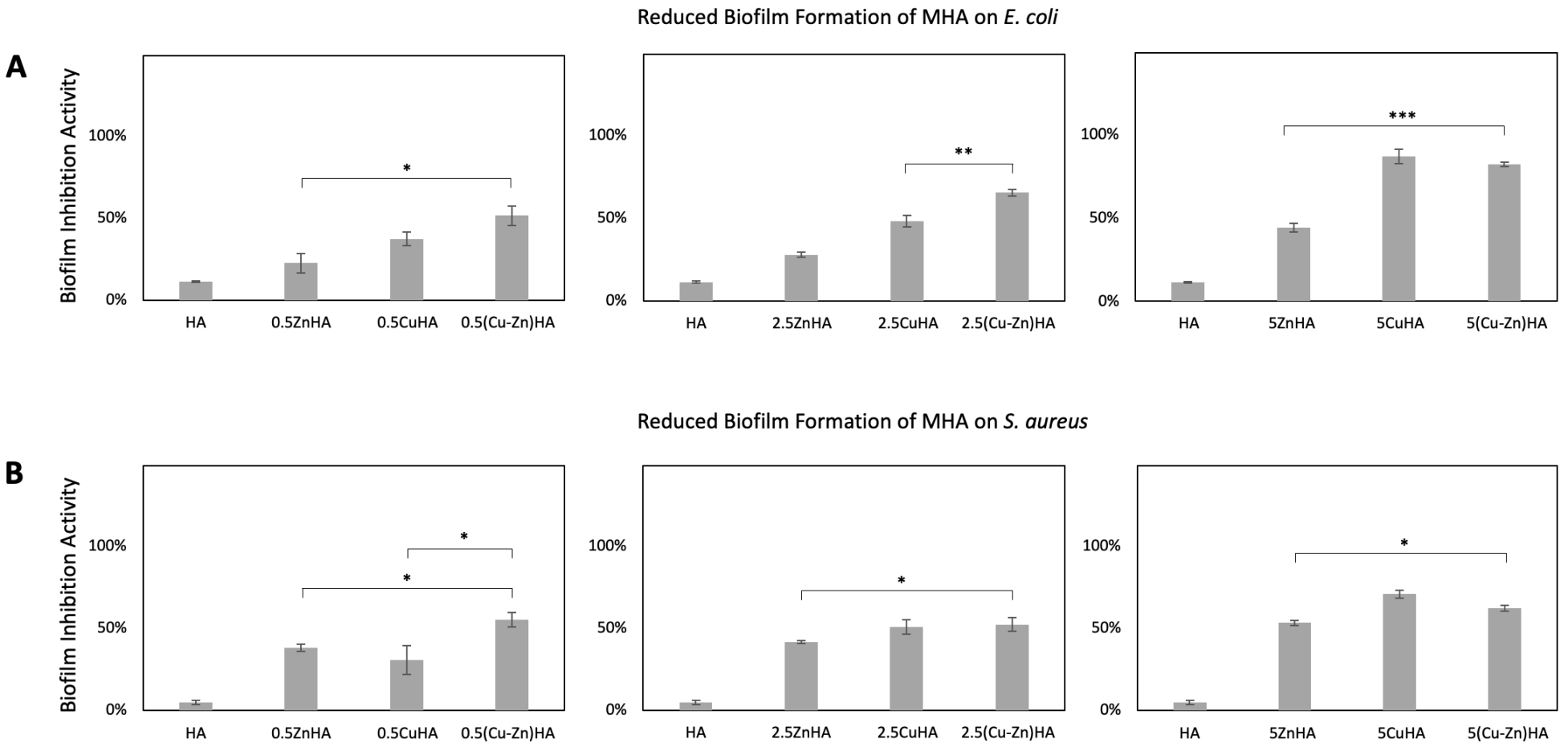

Figure 5-9 Anti-biofilm formation abilities of CuHA, ZnHA and Cu-ZnHA relative to that of HA.

Biofilm inhibition abilities of MHA against E. coli (A)and S. aureus (B).

Student T test (n=3): * represents P≤0.05; **P≤0.01; *** represents P≤0.001. Error bar represents standard error.

5.5 *In vitro* Biocompatibility Studies with MG63 Cells

The biocompatibilities of the synthesized MHA were investigated via alamarBlue cell proliferation assay using osteoblast-like cells MG63. Cells were cultured on the surface of heat-treated MHA deposited on titanium plates. The results indicated that the Cu-ZnHA showed an enhanced MG63 proliferation than ZnHA and CuHA at low metallic content and exhibited no significant difference compared to the MG63 proliferation in HA samples, which indicate the Cu-ZnHA has high biocompatibility (Figure 5-10). In the low metallic content group (0.5MHA), after one day culture, Cu-ZnHA and CuHA exhibited similar biocompatibilities that higher than ZnHA. After 5- and 10-day incubation, the cellular proliferation on Cu-ZnHA were significantly higher than those on CuHA and ZnHA, revealing that the Cu-ZnHA had higher biocompatibility than CuHA and ZnHA (Figure 5-10 A). In the medium metallic content group (2.5 MHA), there was no significant difference in the cellular proliferation on three MHA samples was observed (Figure 5-10 B). In the high metallic content group (5 MHA), after 1-day and 5-days culture CuHA has the highest biocompatibility but after 10 days' culture, there was no significant difference comparing these three MHA samples (Figure 5-10 C).

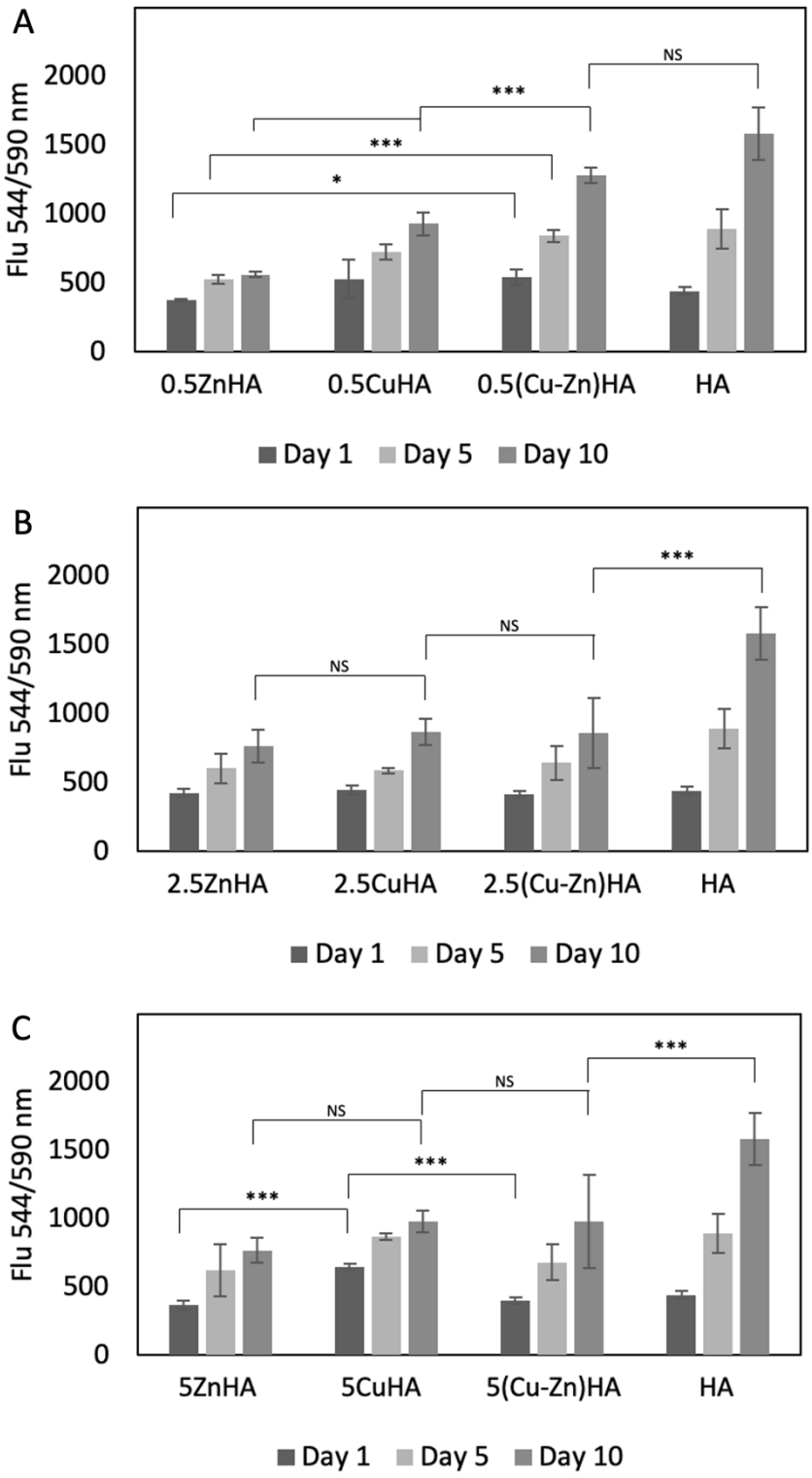

Figure 5-10 In vitro biocompatibility test based on alamarBlue cell proliferation assay. Osteoblast-like cells MG63 were cultured on the surface of different MHA samples for 1, 5 and 10 days. Cell proliferation on low metallic content MHA (A), medium metallic content MHA (B) and on high metallic content MHA (C).

The SEM images indicated the cell density and spreading patterns of MG63 cells cultured on the MHA and HA coated titanium plates after 10 days (Figure 5-11). The cell adhesion results were in agreement with the cell proliferation results that the Cu-ZnHA samples have acquired an enhanced biocompatibility with low metallic content. The images showed that the MG63 cells spread well on the surface of Cu-ZnHA and HA samples and exhibited active cytoskeletal extension. With the increase of metallic content, MG63 cells became thinner and the coverage area decreased consequently.

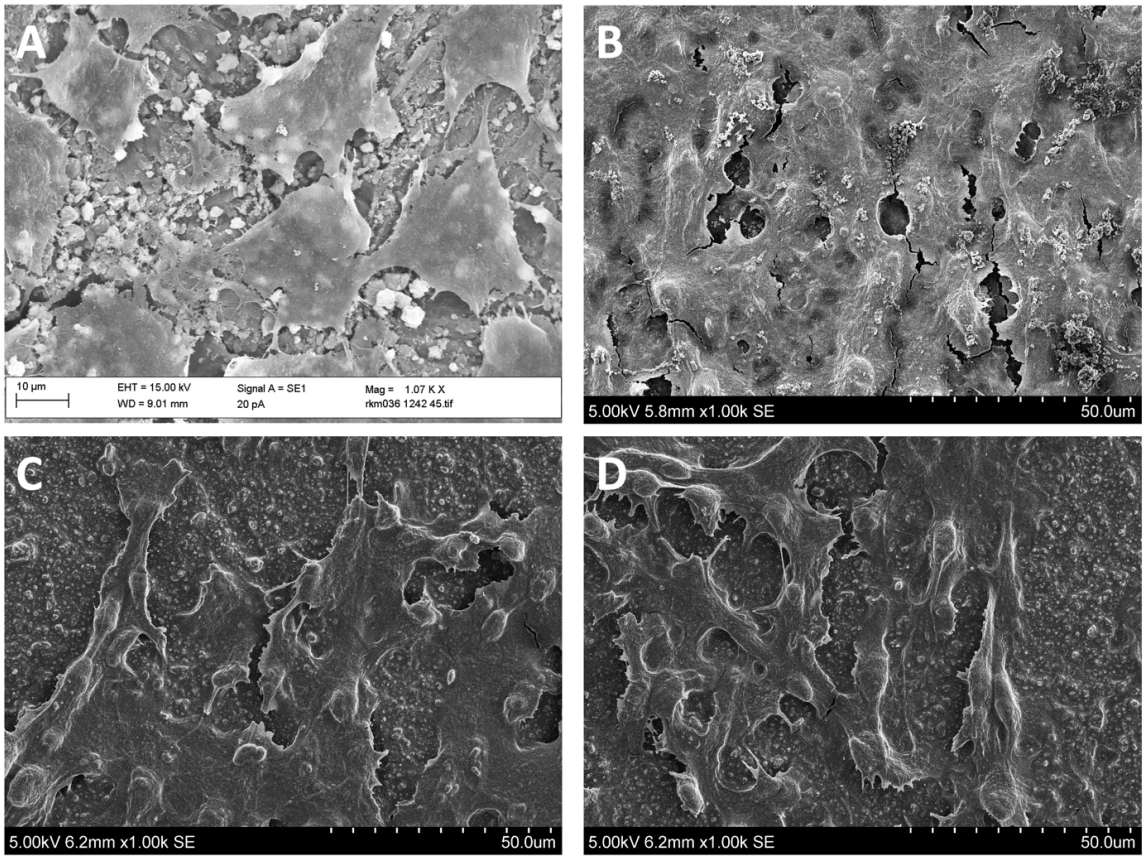

Figure 5-11 SEM images of Osteoblast-like cell MG63 cultured on HA and Cu-ZnHA surface
MG63 cell cultured on HA (A), 0.5(Cu-Zn)HA (B), 2.5(Cu-Zn)HA (C) and 5(Cu-Zn)HA (D) for 10 days.

5.6 Discussion

5.6.1 Metallic Content Affected the Crystallinity and Unit Cell Parameter of MHA

The XRD results have shown the substitution of Cu and Zn in MHA decreased the crystallinity (X_c) and unit cell parameters. This finding is consistent with many other studies (Miyaji et al., 2005, Ren et al., 2009a). The decrease of crystallinity may be due to the relative smaller sizes of substituted ions (Zn (0.074 nm), Cu (0.074 nm)) comparing to Ca (0.099 nm) (Stanić et al., 2010, Shepherd and Best, 2013). Several research groups have indicated the smaller ionic size may distort the crystal structure of HA and hinder HA crystal growth (Ren et al., 2009a). Moreover, changes of the peak intensity were found in both Cu-ZnHA and ZnHA FTIR spectra, which also supported the changes of crystallinities by the increase of Zn fractions. Another finding in XRD patterns is both lattice parameter a and c were decreased gradually. This also due to the smaller ionic radius of Zn and Cu compared with Ca and many other studies have also indicated the incorporation of Cu and Zn into HA can decrease the crystal size due to the smaller effective ionic radius of Cu^{2+} and Zn^{2+} compared with the Ca^{2+} ions (Ren et al., 2009a, Stanić et al., 2010, Shepherd and Best, 2013, Shanmugam and Gopal, 2014).

5.6.2 Co-substitution of Cu and Zn into HA May Result in High Releasing Rate and Enhance Antibacterial Ability

To achieve a better antibacterial effect with less cytotoxicity, Zn has been considered as a good candidate to be co-substituted into HA together with Cu, to avoid the potential adverse effects of Cu^{2+} (Huang et al., 2014, Huang et al., 2015). In the antibacterial tests, Cu-ZnHA samples have shown the highest antibacterial abilities, particularly at low metallic content. Generally speaking, this benefit may be caused by two factors, which may act together to further increases the antibacterial ability of Cu-ZnHA. The first is that the co-substitution may enhance the total metallic content composited into HA, and the second is that the co-substitution may increase the total releasing rate of metallic ions.

According to the XRD results, all metallic contents have been substituted into the HA lattice structure in the Cu-ZnHA, while in the mono-MHA groups, both 5CuHA and 5ZnHA has exhibited secondary phases when they were heat treated. This may be due to the attenuated substitution of metallic ions. Similar results were also observed in many previous studies. For example, secondary phases in CuHA such as CuO was detected in with X_{Cu}=0.1 (Li et al., 2010b) and β-tricalcium phosphate (β-TCP) was observed with the increase in Cu content from X_{Cu}=0.5 to 2.0 (Shanmugam and Gopal,

2014). In ZnHA, similar substitution byproduct has also been indicated, secondary phase-TCP was appeared in X_{Zn}=0.012 (Shepherd and Best, 2013) and X_{Zn}=0.1 (Sergi et al., 2018) ZnHA samples that synthesized by different research groups. The high phase purity of Cu-ZnHA measured in XRD results and high Cu-Zn content measured in the EDS results indicated the co-substitution can enhance the total amount of metallic content integrated into Cu-ZnHA, which could have more metallic ions further released to achieve a stronger antibacterial ability. This is consistent to a previous study, which demonstrated the Cu^{2+} released from the different surface is correlated with their antibacterial efficacy and was highest for pure copper, followed by Cu_2O and CuO (Hans et al., 2013).

Apart from the enhanced metallic content composited into HA, high releasing rate of metallic ions may be another major reason for better antibacterial ability of Cu-ZnHA. This may be due to the special lattice structure of HA, which has two kinds of Ca^{2+} sites (I and II) that can be replaced by cations (Kaygili and Keser, 2015, Geng et al., 2016). Many experimental and computational studies have investigated the potential substitution sites of different cations, such as Cd^{2+}, Cu^{2+}, Pb^{2+}, Sr^{2+} and Zn^{2+}, and they have indicated that a high dopant concentration is energetically favorable to substitute Ca^{2+} in the Ca(II) site, which could facilitate the uptake and release rate of metallic ions such as Cu^{2+} and Zn^{2+} without disrupting the framework of HA (Badraoui et al., 2002,

Terra et al., 2002, Ellis et al., 2006, Tamm and Peld, 2006, Bigi et al., 2007, Tang et al., 2009). The same preference also appeared when Zn^{2+} co-substituted with other cations in HA. For example, in Cd-ZnHA, both Ca(I) and Ca(II) can be replaced by Cd^{2+} and Zn^{2+}in mono-ionic substitution, but only Ca(II) sites can be replaced in Cd/Zn co-substituted HA. This is because the occupation of Cd^{2+} in a Ca(I) site would create an area that requires much higher energy for Zn^{2+} to replace Ca(I) (Tamm and Peld, 2006). In CuHA, the Ca(II) site is favorable to substitute by Cu^{2+} at high dopant concentration (Qu et al., 2014). However, with a lower concentration of dopant, many evidence indicated the substitution in the Ca(I) site was more preferred by Cu^{2+} (Huang et al., 2014, Radovanović et al., 2014). Therefore, the releasing rate of Cu^{2+} in low metallic content CuHA is much lower than the other MHA, which dramatically decrease the contact rate between Cu^{2+} and bacteria, hence inhibit the bacterial killing ability (Radovanović et al., 2014, Huang et al., 2015).

Therefore, it can be deduced that the combination of Zn^{2+} and Cu^{2+} ions in Cu-ZnHA enhanced the phase purity of MHA and increased the releasing rate of metal ions, which may further enhance the antibacterial ability of Cu-ZnHA at low metal content. A previously study has indicated the antibacterial ability of Cu-ZnHA at X_M=0.074 (Huang et al., 2015). However, the tested concentration has been confirmed to be cytotoxic (Li et al., 2010b, Hahn et al., 2011). This chapter showed a distinctive way of

thinking that balance the high antibacterial ability and biocompatibility of Cu-ZnHA with very low metallic content.

5.6.3 The Enhanced Antibiofilm Formation Ability of Cu-ZnHA

Antimicrobial materials are required in different fields, such as public hygiene, medical fields. Due to the antibacterial and biocompatibilities of Cu-ZnHA, the application of this material are not only in implant coating field but also can be made into antibacterial drugs or served as antimicrobial coatings for medical devices. The good anti-biofilm formation ability of Cu-ZnHA make it an ideal material for treating invasive medical devices to prevent infectious or chronic diseases such as pulmonary infections, osteomyelitis, otitis media and dental caries such as periodontitis (Miquel et al., 2016).

The antibiofilm formation mechanisms of Cu and Zn ions were widely investigated. For example, it was indicated that when bacteria were exposed to high copper condition, bacterial stress reaction can inhibit the expression of transporters and global regulatory locus, such as accessory gene regulator (Agr) and two-component signaling system coded by Sae, which are known to be able to regulate the expression of biofilm formation required proteins (extracellular adherence protein (Eap) and extracellular matrix protein (Emp)), which could further prevent the biofilm formation (Baker et al.,

2010). The anti-biofilm formation ability of Zn ions has not been fully investigated. It was indicated that although many pathogenic bacterial biofilms are sensitive to Zn, the anti-biofilm formation ability of Zn ions was more bacterial strains dependent (Hancock et al., 2010, Pereira, 2010, Gu et al., 2012). For example, Wu et al. has demonstrated that Zn ions at low concentrations strongly inhibited the biofilm formation of *A. pleuropneumoniae*, but biofilm formation of *E. coli*, *S. aureus* and *S. suis* was only slightly inhibited (Wu et al., 2013). It has been recently reported that Zn ions could inhibit the Polyglucosamine subunit B (PgaB) activity, which was involved in de-N-acetylation of poly-N-acetylglucosamine (PGA) in the biofilm matrix (Little et al., 2012). However, the inhibitory effect is not only dependent on PGA, but also extracellular DNA (eDNA). eDNA can interact with Zn and further affect biofilm stability (Mulcahy et al., 2008). Zn may also affect cell signaling, gene regulation, toxin-antitoxin system and cyclic diguanylate phosphodiesterases activity, which may have impact on biofilm formation (Tamayo, 2005, Klemm et al., 2010, Papadopoulos et al., 2012).

5.6.4 The High Biocompatibility of Cu-ZnHA

In many previous studies, Zn^{2+} was known to have a better biocompatibility than Cu^{2+}, but in this project, results showed MG63 had a better cellular proliferation in CuHA

than ZnHA, which may also relate to the low releasing rate of Cu^{2+} at low metallic substitution level. Although the combination of Zn^{2+} and Cu^{2+} in Cu-ZnHA are expected to have an enhanced ions-releasing rate than mono-metallic HA samples, the results have confirmed their good biocompatibilities.

To explain this, the ions concentration in solutions were displayed in Table 5-2. The metallic ion concentration in solutions were around 3×10^{-6} to 3×10^{-5} g/mL. A recent study has investigated the antibacterial ability and cytotoxicity of Cu ions with different concentrations ranges from 9×10^{-12} to 9×10^{-3} g/mL in order to find a suitable concentration of Cu ion with high antibacterial ability and no cytotoxicity on mammalian cells. They have claimed that the most suitable Cu^{2+} concentration that can inhibit the viability of *S. epidermidis* while avoid the mammalian cell toxicity on MC3T3 cells should within the range of 9×10^{-6} to 9×10^{-5} g/mL. In this project, the concentration of metallic ions of 2.5MHA and 5MHA solutions were around 1.6×10^{-5} to 3×10^{-5} g/mL, which is between the 9×10^{-6} to 9×10^{-5} g/mL. Therefore, the synthesized 2.5 and 5(Cu-Zn)HA are the optimal materials with suitable metallic ions concentrations for prokaryote death and eukaryote survival.

Table 5-2 MHA concentration and metallic ions concentrations in vitro tests

	MHA concentrations	Metallic ions molar concentration (ion/MHA)	Metallic ions concentration (g/ml)
0.5CuHA	0.01g/mL *	0.005	$3.162x10^{-6}$
2.5CuHA		0.025	$1.580x10^{-5}$
5CuHA		0.05	$3.159x10^{-5}$
0.5ZnHA		0.005	$3.257x10^{-6}$
2.5ZnHA		0.025	$1.627x10^{-5}$
5ZnHA		0.05	$3.253x10^{-5}$
0.5(Cu-Zn)HA		0.0025	$3.209x10^{-6}$
2.5(Cu-Zn)HA		0.0125	$1.604x10^{-5}$
5(Cu-Zn)HA		0.025	$3.206x10^{-5}$

*The MHA concentration in antibacterial test was 0.1 g in 10 mL and in antibiofilm formation test and biocompatibility tests was 0.002 g in 0.2 mL.

5.7 Conclusions

The analysis of FTIR, XRD, SEM confirmed that all synthesized MHA are nanoparticles and have apatite structures. Both Cu and Zn ions were successfully incorporated into HA lattice structures by wet chemical method. Cu-ZnHA, CuHA and ZnHA all exhibited good anti-infection properties against both gram-negative and gram-positive bacteria. Remarkably, Cu-ZnHA exhibited the strongest anti-infection ability against both strains at the low metallic content compared with CuHA and ZnHA. The biocompatibility assay also showed that MG63 had a better proliferation on Cu-ZnHA than ZnHA and CuHA, at low metallic content, which means Cu-ZnHA has good biocompatibility, presented

no cytotoxicity towards osteoblast cells. All these results indicate that Cu-ZnHA has advantages in enhance the antibacterial ability and reduce the required metallic content in MHA, which attenuated the cytotoxicity of Cu and promote the osteoconductivity. Therefore, Cu-ZnHA can be considered as good antibacterial materials for various purpose such as the bone defects and orthopedic implant coatings.

Chapter VI

6 General Discussion and Further Studies

6.1 General Findings of This Study

HA is a well-known biocompatible material. HA substituted with different metal ions provides add-on functions for different biomedical applications. This study combined different metallic ions in HA to introduce different physicochemical or biological functions and achieved high-resolution patterning coatings with improved bioactivity (e.g. Fe-MnHA) and biocompatible antibacterial depositions (e.g. Cu-ZnHA).

Stability of electrospray cone-jet is important in producing consistent fine droplets, which could be affected by nozzle geometry. This study first introduced different-sized ball-tip nozzles in EHDA to generate a stable cone-jet, which avoided the frequent spray mode switch observed in straight nozzles. Ball-tip nozzles were shown to be able to form cone-jet with 10-fold increased throughput and can sustain the cone-jet with solvent up to 4:1 water-ethanol ratio, which enables the usage of materials that cannot form suspensions in non-aqueous solvents.

Osteoconductivity is a key factor that determines the biological response and long-

term success of implants. An ideal implant-tissue interaction could benefit the biological fixation through inducing the cell adhesion and accelerating the cell movement to minimize the fixation time so that it can extend the functional life of inserted implants or medical devices (Wang et al., 2011). In order to improve the biocompatibility of the designed materials, all synthesized materials involved in this study were based on HA. Owing to its similar chemical composition to mineral phase of bone tissues, HA has been used in various applications, such as synthetic bone substitutes (Fihri et al., 2017) and bioimaging applications (Wagner et al., 2013). In this study, different metallic ions substituted HAs have exhibited high biocompatibility, which indicated the HA is an ideal platform for versatile biomedical applications.

Fe-MnHA has been synthesized to combine magnetic property with bioactivity. Under the influence of MTAEA, Fe-MnHA has shown a relatively higher magnetic susceptibility compared with mono-substituted HAs, magnetic IONPs and IONPs-HA mixture. The in vitro bioactivity of Fe-MnHA is similar to HA and higher than mono-substituted HA, IONPs and IONPs-HA mixture in simulated body fluid tests. Therefore, Fe-MnHA well-balanced the magnetic property and bioactivity and offers great potential in biomedical applications. In order to achieve high anti-infection ability as well as low cytotoxicity, Cu-ZnHA with low metallic content (<0.05mol%) was studied. Flow cytometry and crystal violet assay indicated their effective antibacterial and

antibiofilm ability against *E. coli* and *S. aureus*. Compared to CuHA and ZnHA, Cu-ZnHA produced the strongest anti-infection ability and biocompatibility at the lowest metallic content (0.005mol%).

6.1.1 Ball-tip Nozzle Assisted MTAEA Process Achieved Stable and Flexible Patterning Process

EHDA is a well-studied coating technology with a ambient temperature, high efficiency, lower cost and lower material consumption compared with other conventional deposition techniques such as dip coating, so-gel, thermal spray, electrochemical deposition and plasma spraying (Yang et al., 2005). This study has shown ball-tip nozzles can enhance the stability of electrospray cone-jet process. Thus, they were applied to all the deposition process of nanoparticles in this study. Comparing to electrospray cone-jet with straight nozzle, the ball-tip nozzles have enhanced coating uniformity, coating efficiency and reduced the manipulation difficulty, which are the key factors to the successful development of MTAEA.

The MTAEA was designed to fabricate patterned implant surfaces with bioactive materials thereby affecting the cell adhesion, orientation and growth (Munir et al., 2011b). Conventional TAEA has shown advantages such as the relatively lower cost,

easy manipulation, high efficiency, and low material consumption compared with other methods like chemical etching and photolithography. Furthermore, the incorporation of magnetic field and magnetic nanoparticles in MTAEA process has successfully enhanced the precision of nanoparticle distribution. Since both the resolution of template and the intensity of magnetic fields are flexible, the further increase in the resolution of fabricated patterns is foreseeable. Hence, this technology is competent for the demand of cell guidance (Ahmad et al., 2006). Apart from the increase in the patterning resolution, another advantage of MTAEA is that the strength of magnetic fields can be amended, which is able to alter the size of patterns during the patterning process, thereby controlling the structure of patterned coatings such as modifying the depth of grooves and size of ridges so that can provide more functions in implant or medical device coatings. For example, a previous study indicated the depth of grooves and size of ridges directly determines the orientation of cells. Patterns that well matches the HOB cell dimension can lead the cells and allow the attachment and grow of cells along the HA sites (Li et al., 2010a).

6.1.2 Metallic Ions Substituted HA has Multi-functions

Although HA has achieved great success in variable applications, there are more challenges in the 21st century healthcare industry in the medical field or material science. A widely accepted strategy to incorporate different functions into HA is the substitution of different functional ions into HA lattice structure. The development of substituted HA has been focused on promoting osteogenesis, inhibiting osteoclast activity and incorporating ions with antibacterial properties, as well as other medical applications (e.g. delivery carriers and imaging contrast agents). However, due to the nature of HA lattice structure, the amount of certain ion that can be substituted into HA is limited, which restricts the performance of designed functions. In order to enhance the effectiveness of certain functions or achieve add-on biological functions, the tailoring of the types and amount multiple functional substitutions in HA have been widely studied (Šupová, 2015). For example, in this study, both the co-substitution of Cu-Zn ions and Fe-Mn have promoted the substitution level of both ions and they have provided both benefits of two types of metallic ions and remedied defects in each mono-ion substituted HAs.

6.1.3 Fe-MnHA Well Matched the Designed Magnetic Property and Maintained a Good Bioactivity

Fe-MnHA has enhanced the performance in both designed properties, including the magnetic property and bioactivity. The addition of Fe ions provided strong magnetic property, and the addition of Mn ions serves as the key factor in enhancing both magnetic property and bioactivity due to the higher uptake and releasing rate of metallic ions. The substitution of magnetic ions into HA is a better strategy than other alternative strategies such as direct coating HA on the surface of magnetic nanoparticles (e.g. IONPs, $MnFe_2O_4$ NPs) (Pon-On et al., 2008, Mondal et al., 2017). Although HA coated magnetic nanoparticles has been confirmed has no cytotoxicity, but the potential in peeling or spalling of HA shell and exposing the IONPs core beneath can still affect the biocompatibility (Pon-On et al., 2008, Mondal et al., 2017).

Apart from the Fe-Mn combination, the substitution of other magnetic ions into HA such as FeHA, Fe-PtHA, CoHA and Co-ferrite-doped HA, have shown good magnetic properties, but none of them well balanced the magnetic property with biocompatibility (Petchsang et al., 2009, Ignjatović et al., 2013, Tseng et al., 2014, Syamchand and Sony, 2015). The FeHA or iron oxide HA have shown good magnetic hyperthermia but their application was restricted due to the very low thermal stability

and biocompatibility (Trandafir et al., 2014, Chiriac et al., 2018). The Fe-PtHA has a relatively high stability but limited by the toxicity (Tseng et al., 2014). Many studies based on Co substituted HA have indicated their metal toxicity to biometabolism (Petchsang et al., 2009, Ignjatović et al., 2013, Syamchand and Sony, 2015). Hence, the Fe-MnHA can be considered as a more advantageous combination of magnetic ions substituted HA for medical applications that requires relatively high biocompatibility. Apart from the implant coating application, Fe-MnHA may also be ideal to serve as insertable magnetic material for medical applications that require precise localization, such as heat media for hyperthermia in cancer treatment or contrast agent in medical imaging applications.

6.1.4 Co-substitution of Cu and Zn Achieved the Antibacterial and Anti-biofilm Formation Abilities

The co-substitution of Cu-ZnHA successfully induced the anti-infection ability into HA and maintained a good biocompatibility. Comparing to many other conventional antibacterial materials, the main advantage of Cu-ZnHA is the conservation on their biocompatibility. Similar strategy has been investigated by many previous studies, which incorporated different ions into HA to achieve antibacterial ability. For instance, Ag^{+} ion has been co-substituted with many other biocompatible ions such as Mg^{2+} and

Si^{4+} in order to reduce the cytotoxicity of Ag (Gopi et al., 2014b, Lim et al., 2014). However, overexposure to silver can lead to heavy metal toxicity which makes them unsuitable for long-term insertion in human body. Previous studies on CuHA have not figure out a suitable strategy to balance the cytotoxicity and biocompatibility. A commonly used method to enhance the antibacterial ability of CuHA was focused on employing relatively higher Cu^{2+} ions substitution levels, which always exceeded the cytotoxicity level of Cu^{2+} ions that can cause harm to host cells and seriously restricted their biocompatibilities (Huang et al., 2015, Huang et al., 2016a). On the contrary, this study indicated the co-effect of Cu and Zn ions in a very low substitution level has successfully promoted the antibacterial ability and well maintained a good biocompatibility.

6.2 Further Studies

6.2.1 Ball-tip Nozzle can Serve as a Liquid Fuel Injector in a Microcombustor

The application of ball-tip nozzles is not restricted to the coating process, but many other applications. For example, the EHDA can be used in the fuel supply process of a micro-power generator system, due to the stability of the cone-jet is crucial for

combustion of liquid fuels in a small scale (Yuliati et al., 2012). A portable high energy density micro-power generator is an alternative strategy in replacing batteries (Kyritsis et al., 2002, Li et al., 2009a, Gan et al., 2015). Many previous studies have analyzed the burning conditions of liquid fuel in an electrospray, but they found it was difficult to maintain a stable flame inside the microcombustor (Yuliati et al., 2012, Gan et al., 2015). Hence, a potential further study of ball-tip nozzles is to facilitate a fuel supply port of microcombustor owing to its sturdy stable cone-jet mode. It is necessary to select and test the performance of high temperature resistant materials to constitute the cap of ball-tip nozzles. The burning conditions of different liquid fuel ejected via different sized ball-tip nozzles and the stability of the generated flame can be tested.

6.2.2 Using MTAEA in Fabricating Biomimicking Antibacterial Nanostructures

The MTAEA has successfully localized magnetic nanoparticles into a restricted area. In the future, a more flexible MTAEA process is necessary to be designed in order to achieve complex coating patterns and even 3D structures. In the further study, it would be interesting to construct complex nanostructures via changing the magnetic fields or templates during spray process. Ideally, a gradual increase of magnetic field during spray process is possible to produce many complex structures in order to meet all kinds

of requirements, such as pyramidal structures with squared templates, a conical/dome structure with round templates, or arch/pitched line structures in lined templates.

Currently, combination of different killing mechanisms is the best solution to the treatment of biofilm infections. Via modifying the topography of coating surface, it can achieve complex antibacterial surface via contact killing. In order to achieve bio-mimic antibacterial nanostructures such as the surface of cicada wings, the MTAEA process should be modified in order to fabricate nano-cone structures. Afterwards, the contact-killing ability of fabricated bio-mimic surface can be tested via in vitro and in vivo tests.

6.2.3 Evaluation of the potential application of Fe-MnHA in Hyperthermia Treatment

Besides the application in fabricating complex nanostructures, the biocompatible magnetic nanoparticles can be applied in areas such as, lab-on-a-chip, theranostic, tissue engineering, drug release and hyperthermia. Fe-MnHA has well-balanced the biocompatibility and magnetic property. It exhibited great potential in application as heat media for hyperthermia therapy. Therefore, in the further study the cytotoxicity of Fe-MnHA can be further studied in vitro and in vivo. Moreover, it is worth to further

investigate the maximum temperature that can be raised by Fe-MnHA nanoparticles under heating in an alternating magnetic field and their magnetic properties at a high temperature. More clinically, it is also important to further investigate the direct tumor cell killing ability of Fe-MnHA or whether it can make the cells more susceptible to concomitant radio or chemotherapy in such hyperthermia treatment. In the meantime, the effect of Fe-MnHA on healthy host cells during the heating process should also be studied. Meanwhile, the cytotoxicity of Fe-MnHA can be further studied in vivo.

6.2.4 Cu-ZnHA has Great Potential as Antibacterial Drugs

The Cu-ZnHA has a good balance between antibacterial and low cytotoxicity. Zn ion was proposed as the main cause triggering the releasing of Cu while avoiding the cytotoxicity. The concentration of Cu and Zn ions released in the supernatant can be determined using ICP-OES. Additionally, a more detailed investigation on the biological performance of Cu-ZnHA in vivo is worth to study via animal model tests.

As an antibacterial and biocompatible material, Cu-ZnHA has a potential in composing biodegradable drugs such as eradication of *Helicobacter pylori* infection in chronic atrophic gastritis (CAG) (Wu et al., 2020). The ion releasing and contact killing abilities of Cu-ZnHA nanoparticles make it possible to combine with other conventional drugs

to enhance the curative effect in *H. pylori* induced CAG (Wu et al., 2020). Therefore, it would be interesting to study the antibacterial effect of Cu-ZnHA in tablet form or mixed with other bactericidal drugs against *H. pylori* in vitro and in vivo.

7 Reference

Aaseth, J., Boivin, G. & Andersen, O. 2012. Osteoporosis and trace elements–an overview. *Journal of Trace Elements in Medicine and Biology,* 26(2-3), pp 149-152.

Achar, T. K., Bose, A. & Mal, P. 2017. Mechanochemical synthesis of small organic molecules. *Beilstein journal of organic chemistry,* 13(1), pp 1907-1931.

Adamiano, A., Wu, V. M., Carella, F., Lamura, G., Canepa, F., Tampieri, A., Iafisco, M. & Uskoković, V. 2019. Magnetic calcium phosphates nanocomposites for the intracellular hyperthermia of cancers of bone and brain. *Nanomedicine,* 14(10), pp 1267-1289.

Afshar, A., Ghorbani, M., Ehsani, N., Saeri, M. & Sorrell, C. 2003. Some important factors in the wet precipitation process of hydroxyapatite. *Materials & Design,* 24(3), pp 197-202.

Aggarwal, S., Stewart, P. S. & Hozalski, R. M. 2015. Biofilm Cohesive Strength as a Basis for Biofilm Recalcitrance: Are Bacterial Biofilms Overdesigned? *Microbiol Insights,* 8(Suppl 2), pp 29-32.

Ahamed, M., Alsalhi, M. S. & Siddiqui, M. 2010. Silver nanoparticle applications and human health. *Clinica chimica acta,* 411(23-24), pp 1841-1848.

Ahmad, Z., Huang, J., Edirisinghe, M., Jayasinghe, S., Best, S., Bonfield, W., Brooks, R. & Rushton, N. 2006. Electrohydrodynamic print-patterning of nano-hydroxyapatite. *Journal of Biomedical Nanotechnology,* 2(3-4), pp 201-207.

Ahmed, F., Rashid, H., Farookhi, S., Verma, V., Khalifa, M., Sheikh, Z. & Dh, D. 2015. Surface modifications of endosseous dental implants by incorporation of roughness and hydroxyapatite coatings. *JPDA,* 24(04), pp 162-171.

Akhavan, O. & Ghaderi, E. 2010. Cu and CuO nanoparticles immobilized by silica thin films as antibacterial materials and photocatalysts. *Surface and Coatings Technology,* 205(1), pp 219-223.

Al-Amin, M., Abdul Rani, A. M., Abdu Aliyu, A. A., Bryant, M. G., Danish, M. & Ahmad, A. 2020. Bio-ceramic coatings adhesion and roughness of biomaterials through PM-EDM: a comprehensive review. *Materials and Manufacturing Processes,* 35(11), pp 1157-1180.

Albrektsson, T., Dahlin, C., Jemt, T., Sennerby, L., Turri, A. & Wennerberg, A. 2014. Is marginal bone loss around oral implants the result of a provoked foreign body reaction? *Clinical implant dentistry and*

related research, 16(2), pp 155-165.

Albrektsson, T. & Wennerberg, A. 2019. On osseointegration in relation to implant surfaces. *Clinical implant dentistry and related research,* 21(s1), pp 4-7.

Allahverdiyev, A. M., Abamor, E. S., Bagirova, M., & Rafailovich, M. 2011. Antimicrobial effects of TiO2 and Ag2O nanoparticles against drug-resistant bacteria and leishmania parasites. *Future microbiology,* 6(8), pp 933-940.

Altun, E., Aydogdu, M. O., Crabbe‐Mann, M., Ahmed, J., Brako, F., Karademir, B., Aksu, B., Sennaroglu, M., Eroglu, M. S. & Ren, G. 2019. Co‐Culture of Keratinocyte‐Staphylococcus aureus on Cu‐Ag‐Zn/CuO and Cu‐Ag‐W Nanoparticle Loaded Bacterial Cellulose: PMMA Bandages. *Macromolecular Materials and Engineering,* 304(1), pp 1800537 (1-14).

Anand, P. & Stahel, V. P. 2021. Review the safety of Covid-19 mRNA vaccines: a review. *Patient Safety in Surgery,* 15(1), pp 1-9.

Anselme, K., Noel, B., Flautre, B., Blary, M.-C., Delecourt, C., Descamps, M. & Hardouin, P. 1999. Association of porous hydroxyapatite and bone marrow cells for bone regeneration. *Bone,* 25(2), pp 51S-54S.

Anwar, A., Akbar, S., Sadiqa, A., & Kazmi, M. 2016. Novel continuous flow synthesis, characterization and antibacterial studies of nanoscale zinc substituted hydroxyapatite bioceramics. *Inorganica Chimica Acta,* 453pp 16-22.

Arcos, D., Del Real, R. & Vallet‐Regí, M. 2003. Biphasic materials for bone grafting and hyperthermia treatment of cancer. *Journal of Biomedical Materials Research Part A: An Official Journal of The Society for Biomaterials, The Japanese Society for Biomaterials, and The Australian Society for Biomaterials and the Korean Society for Biomaterials,* 65(1), pp 71-78.

Arumuganathar, S. & Jayasinghe, S. 2008. A versatile pressure assisted jet-fabrication by coating approach for forming biocompatible constructs for tissue engineering. *Materials Letters,* 62(17-18), pp 2574-2577.

Arumuganathar, S., Suter, N. & Jayasinghe, S. N. 2008. Aerodynamically assisted jets: a paradigm for directly microbubbling and microfoaming combinations of advanced materials. *Advanced Materials,* 20(23), pp 4419-4422.

Attik, G., Villat, C., Hallay, F., Pradelle‐Plasse, N., Bonnet, H., Moreau, K., Colon, P. & Grosgogeat, B. 2014. In vitro biocompatibility of a dentine substitute cement on human MG 63 osteoblasts cells: B iodentine™ versus MTA®. *International endodontic journal,* 47(12), pp 1133-1141.

Badraoui, B., Bigi, A., Debbabi, M., Gazzano, M., Roveri, N. & Thouvenot, R. 2002. Physicochemical Properties and Structural Refinement of Strontium‐Lead Hydroxyapatites. . *European Journal of Inorganic Chemistry,* 2002(7), pp 1864-1870.

Baker, J., Sitthisak, S., Sengupta, M., Johnson, M., Jayaswal, R. K. & Morrissey, J. A. 2010. Copper stress induces a global stress response in Staphylococcus aureus and represses sae and agr expression and biofilm formation. *Appl Environ Microbiol,* 76(1), pp 150-160.

Barbucci, R., Magnani, A., Lamponi, S., Pasqui, D. & Bryan, S. 2003. The use of hyaluronan and its sulphated derivative patterned with micrometric scale on glass substrate in melanocyte cell behaviour. *Biomaterials,* 24(6), pp 915-926.

Basirun, W. J., Nasiri-Tabrizi, B. & Baradaran, S. 2018. Overview of hydroxyapatite–graphene nanoplatelets composite as bone graft substitute: mechanical behavior and in-vitro biofunctionality. *Critical reviews in solid state and materials sciences,* 43(3), pp 177-212.

Bayraktar, D. & Tas, A. C. 1999. Chemical preparation of carbonated calcium hydroxyapatite powders at 37 C in urea-containing synthetic body fluids. *Journal of the European Ceramic Society,* 19(13-14), pp 2573-2579.

Bellof, G., Most, E. & Pallauf, J. 2007. Concentration of copper, iron, manganese and zinc in muscle, fat and bone tissue of lambs of the breed German Merino Landsheep in the course of the growing period and different feeding intensities. *Journal of animal physiology and animal nutrition,* 91(3-4), pp 100-108.

Berlanga, M., Domenech, O. & Guerrero, R. 2014. Biofilm formation on polystyrene in detached vs. planktonic cells of polyhydroxyalkanoate-accumulating Halomonas venusta. *Int Microbiol,* 17(4), pp 205-212.

Bigi, A., Boanini, E., Capuccini, C. & Gazzano, M. 2007. Strontium-substituted hydroxyapatite nanocrystals. *Inorganica Chimica Acta,* 360(3), pp 1009-1016.

Bishop, J. A., Palanca, A. A., Bellino, M. J. & Lowenberg, D. W. 2012. Assessment of compromised fracture healing. *JAAOS-Journal of the American Academy of Orthopaedic Surgeons,* 20(5), pp 273-282.

Blanco, E., Kessinger, C. W., Sumer, B. D. & Gao, J. 2009. Multifunctional micellar nanomedicine for cancer therapy. *Experimental biology and medicine,* 234(2), pp 123-131.

Boanini, E., Gazzano, M. & Bigi, A. 2010. Ionic substitutions in calcium phosphates synthesized at low temperature. *Acta biomaterialia,* 6(6), pp 1882-1894.

Bohner, M. & Lemaitre, J. 2009. Can bioactivity be tested in vitro with SBF solution? *Biomaterials,* 30(12), pp 2175-2179.

Bondarenko, O., Ivask, A., Kakinen, A. & Kahru, A. 2012. Sub-toxic effects of CuO nanoparticles on bacteria: kinetics, role of Cu ions and possible mechanisms of action. *Environmental Pollution (1987),* 169pp 81-89.

Bosco, R., Van Den Beucken, J., Leeuwenburgh, S. & Jansen, J. 2012. Surface engineering for bone implants: a trend from passive to active surfaces. *Coatings,* 2(3), pp 95-119.

Botelho, C. M., Lopes, M. A., Gibson, I. R., Best, S. M., & Santos, J. D. 2002. Structural analysis of Si-substituted hydroxyapatite: zeta potential and X-ray photoelectron spectroscopy. *Journal of Materials Science: Materials in Medicine,* 13(12), pp 1123-1127.

Bouyer, E., Gitzhofer, F. & Boulos, M. 2000. Morphological study of hydroxyapatite nanocrystal suspension. *Journal of Materials Science: Materials in Medicine,* 11(8), pp 523-531.

Brånemark, P. I., Hansson, B. O., Adell, R., Breine, U., Lindström, J., Hallén, O. & Ohman, A. 1977. Osseointegrated implants in the treatment of the edentulous jaw. Experience from a 10-year period. *Scand J Plast Reconstr Surg Suppl,* 16pp 1-132.

Buffet-Bataillon, S., Tattevin, P., Bonnaure-Mallet, M. & Jolivet-Gougeon, A. 2012. Emergence of resistance to antibacterial agents: the role of quaternary ammonium compounds--a critical review. *Int J Antimicrob Agents,* 39(5), pp 381-389.

Buga, C., Hunyadi, M., Gácsi, Z., Hegedűs, C., Hakl, J., Schmidt, U., Ding, S.-J. & Csík, A. 2019. Calcium silicate layer on titanium fabricated by electrospray deposition. *Materials Science and Engineering: C,* 98pp 401-408.

Cai, Y. L., Zhang, J. J., Zhang, S., Venkatraman, S. S., Zeng, X. T., Du, H. J., & Mondal, D. 2010. Osteoblastic cell response on fluoridated hydroxyapatite coatings: the effect of magnesium incorporation. *Biomedical Materials,* 5(5), pp 054114.

Carlin, R. L. 2012. Magnetochemistry. *Springer Science & Business Media,* pp 1-10.

Chen, D.-R., Pui, D. Y. & Kaufman, S. L. 1995. Electrospraying of conducting liquids for monodisperse aerosol generation in the 4 nm to 1.8 μm diameter range. *Journal of Aerosol Science,* 26(6), pp 963-977.

Chen, F., Huang, P., Zhu, Y.-J., Wu, J., Zhang, C.-L. & Cui, D.-X. 2011a. The photoluminescence, drug delivery and imaging properties of multifunctional Eu3+/Gd3+ dual-doped hydroxyapatite

nanorods. *Biomaterials,* 32(34), pp 9031-9039.

Chen, P.-Y., Toroian, D., Price, P. A. & Mckittrick, J. 2011b. Minerals form a continuum phase in mature cancellous bone. *Calcified tissue international,* 88(5), pp 351-361.

Chen, Q. & Thouas, G. A. 2015. Metallic implant biomaterials. *Materials Science and Engineering: R: Reports,* 87pp 1-57.

Chen, Y. W., Hsu, T. T., Wang, K. & Shie, M. Y. 2016. Preparation of the fast setting and degrading Ca-Si-Mg cement with both odontogenesis and angiogenesis differentiation of human periodontal ligament cells. *Mater Sci Eng C Mater Biol Appl,* 100(60), pp 374-383.

Chen, Z., Yi, D., Zheng, X., Chang, J., Wu, C. & Xiao, Y. 2014. Nutrient element-based bioceramic coatings on titanium alloy stimulating osteogenesis by inducing beneficial osteoimmmunomodulation. *Journal of Materials Chemistry B,* 2(36), pp 6030-6043.

Cheong, Y.-K., Calvo-Castro, J., Ciric, L., Edirisinghe, M., Cloutman-Green, E., Illangakoon, U. E., Kang, Q., Mahalingam, S., Matharu, R. K. & Wilson, R. M. 2017. Characterisation of the chemical composition and structural features of novel antimicrobial nanoparticles. *Nanomaterials,* 7(7), pp 152.

Chiriac, L., Todea, M., Vulpoi, A., Muresan-Pop, M., Turcu, R. & Simon, S. 2018. Freeze-drying assisted sol–gel-derived silica-based particles embedding iron: synthesis and characterization. *Journal of Sol-Gel Science and Technology,* 87(1), pp 195-203.

Choudhury, P. & Agrawal, D. 2012. Hydroxyapatite (HA) coatings for biomaterials. *Nanomedicine, Woodhead Publishing,* pp 84-127.

Christoffersen, M., Thyregod, H. & Christoffersen, J. 1987. Effects of aluminum (III), chromium (III), and iron (III) on the rate of dissolution of calcium hydroxyapatite crystals in the absence and presence of the chelating agent desferrioxamine. *Calcified tissue international,* 41(1), pp 27-30.

Chung, R. J., Hsieh, M. F., Huang, C. W., Perng, L. H., Wen, H. W. & Chin, T. S. 2006. Antimicrobial effects and human gingival biocompatibility of hydroxyapatite sol-gel coatings. *J Biomed Mater Res B Appl Biomater,* 76(1), pp 169-78.

Cloupeau, M. & Prunet-Foch, B. 1989. Electrostatic spraying of liquids in cone-jet mode. *Journal of electrostatics,* 22(2), pp 135-159.

Cloupeau, M. & Prunet-Foch, B. 1990. Electrostatic spraying of liquids: Main functioning modes. *Journal of electrostatics,* 25(2), pp 165-184.

Costerton, J. W., Montanaro, L., & Arciola, C. R. 2005. Biofilm in implant infections: its production and regulation. . *The International journal of artificial organs,* 28(11), pp 1062-1068.

Cox, S. C., Walton, R. I. & Mallick, K. K. 2015. Comparison of techniques for the synthesis of hydroxyapatite. *Bioinspired, Biomimetic and Nanobiomaterials,* 4(1), pp 37-47.

Culotta, V. C., Yang, M. & O'halloran, T. V. 2006. Activation of superoxide dismutases: putting the metal to the pedal. *Biochimica et Biophysica Acta (BBA)-Molecular Cell Research,* 1763(7), pp 747-758.

Cunha, F. R., Abade, G. C., Sousa, A. J. & Hinch, E. J. 2002. Modeling and Direct Simulation of Velocity Fluctuations and Particle-Velocity Correlations in Sedimentation. *Journal of Fluids Engineering,* 124(4), pp 957-968.

Curtis, A. & Wilkinson, C. 1997. Topographical control of cells. *Biomaterials,* 18(24), pp 1573-1583.

Dastourani, H., Jahannama, M. & Eslami-Majd, A. 2018. A physical insight into electrospray process in cone-jet mode: Role of operating parameters. *International Journal of Heat and Fluid Flow,* 70pp 315-335.

Del Barrio, J. & Sánchez‐Somolinos, C. 2019. Light to shape the future: from photolithography to 4D printing. *Advanced Optical Materials,* 7(16), pp 1900598 (1-33).

Deligianni, D. D., Katsala, N. D., Koutsoukos, P. G. & Missirlis, Y. F. 2000. Effect of surface roughness of hydroxyapatite on human bone marrow cell adhesion, proliferation, differentiation and detachment strength. *Biomaterials,* 22(1), pp 87-96.

Dizaj, S. M., Lotfipour, F., Barzegar-Jalali, M., Zarrintan, M. H. & Adibkia, K. 2014. Antimicrobial activity of the metals and metal oxide nanoparticles. *Mater Sci Eng C Mater Biol Appl,* 44pp 278-84.

Donath, K., Laaß, M. & Günzl, H.-J. 1992. The histopathology of different foreign-body reactions in oral soft tissue and bone tissue. *Virchows Archiv A,* 420(2), pp 131-137.

Donlan, R. M. & Costerton, J. W. 2002. Biofilms: Survival Mechanisms of Clinically Relevant Microorganisms. *Clinical Microbiology Reviews,* 15(2), pp 167-193.

Dorozhkin, S. V. 2009. Calcium orthophosphates in nature, biology and medicine. *Materials,* 2(2), pp 399-498.

Dorozhkin, S. V. & Epple, M. 2002. Biological and medical significance of calcium phosphates. *Angewandte Chemie International Edition,* 41(17), pp 3130-3146.

Edmiston, C. E., Seabrook, G. R., Goheen, M. P., Krepel, C. J., Johnson, C. P., Lewis, B. D., Brown, K. R. & Towne, J. B. 2006. Bacterial adherence to surgical sutures: can antibacterial-coated sutures reduce the risk of microbial contamination? *J Am Coll Surg,* 203(4), pp 481-489.

El-Sherif, A. A. & Eldebss, T. M. 2011. Synthesis, spectral characterization, solution equilibria, in vitro antibacterial and cytotoxic activities of Cu(II), Ni(II), Mn(II), Co(II) and Zn(II) complexes with Schiff base derived from 5-bromosalicylaldehyde and 2-aminomethylthiophene. *Spectrochim Acta A Mol Biomol Spectrosc,* 79(5), pp 1803-1814.

Eliaz, N. & Metoki, N. 2017. Calcium phosphate bioceramics: a review of their history, structure, properties, coating technologies and biomedical applications. *Materials,* 10(4), pp 334-438.

Ellis, D. E., Terra, J., Warschkow, O., Jiang, M., Gonzalez, G. B., Okasinski, J. S., Bedzyk, M. J., Rossi, A. M. & Eon, J. G. 2006. A theoretical and experimental study of lead substitution in calcium hydroxyapatite. *Phys Chem Chem Phys,* 8(8), pp 967-976.

Epinette, J.-A. & Manley, M. T. 2003. *The early biological history of calcium phosphates. In Fifteen years of clinical experience with hydroxyapatite coatings in joint arthroplasty*, Springer Science & Business Media, pp 3-8.

Eshtiagh-Hosseini, H., Housaindokht, M. R. & Chahkandi, M. 2007. Effects of parameters of sol–gel process on the phase evolution of sol–gel-derived hydroxyapatite. *Materials Chemistry and Physics,* 106(2-3), pp 310-316.

Farahmandjou, M. & Soflaee, F. 2015. Synthesis and characterization of α-Fe2O3 nanoparticles by simple co-precipitation method. *Physical Chemistry Research,* 3(3), pp 191-196.

Farokhi, M., Mottaghitalab, F., Samani, S., Shokrgozar, M. A., Kundu, S. C., Reis, R. L., Fatahi, Y. & Kaplan, D. L. 2018. Silk fibroin/hydroxyapatite composites for bone tissue engineering. *Biotechnology advances,* 36(1), pp 68-91.

Fathi, M., Hanifi, A. & Mortazavi, V. 2008. Preparation and bioactivity evaluation of bone-like hydroxyapatite nanopowder. *Journal of materials processing technology,* 202(1-3), pp 536-542.

Fernandez De Grado, G., Keller, L., Idoux-Gillet, Y., Wagner, Q., Musset, A.-M., Benkirane-Jessel, N., Bornert, F. & Offner, D. 2018. Bone substitutes: a review of their characteristics, clinical use, and perspectives for large bone defects management. *Journal of tissue engineering,* 9pp 2041731418776819-2041731418776819.

Fernández De La Mora, J. 2007. The fluid dynamics of Taylor cones. *Annu. Rev. Fluid Mech.,* 39pp 217-243.

Figgis, B. & Lewis, J., Lewis, J.; Wilkins, R.G. (Eds.). 1960. The magnetochemistry of complex compounds. *Modern Coordination Chemistry,* New York: Wiley Interscience. pp 400-454.

Fihri, A., Len, C., Varma, R. S. & Solhy, A. 2017. Hydroxyapatite: A review of syntheses, structure and applications in heterogeneous catalysis. *Coordination Chemistry Reviews,* 347pp 48-76.

Gamero-Castaño, M. 2008. The structure of electrospray beams in vacuum. *Journal of Fluid Mechanics,* 604pp 339-368.

Gan, Y., Luo, Z., Cheng, Y. & Xu, J. 2015. The electro-spraying characteristics of ethanol for application in a small-scale combustor under combined electric field. *Applied Thermal Engineering,* 87pp 595-604.

Ganan-Calvo, A., Davila, J. & Barrero, A. 1997. Current and droplet size in the electrospraying of liquids. Scaling laws. *Journal of aerosol science,* 28(2), pp 249-275.

Gañán-Calvo, A., Lasheras, J., Dávila, J. & Barrero, A. 1994. The electrostatic spray emitted from an electrified conical meniscus. *Journal of aerosol science,* 25(6), pp 1121-1142.

Gañan-Calvo, A. M., Pantano-Rubino, C. A. & Barrero, A. 1996. The equilibrium shapes of liquid menisci emitting liquid and charges in steady cone-jet mode. *Journal of Aerosol Science,* 27(SUPPL. 1), pp S187-S188.

Geetha, M., Singh, A. K., Asokamani, R. & Gogia, A. K. 2009. Ti based biomaterials, the ultimate choice for orthopaedic implants–a review. *Progress in materials science,* 54(3), pp 397-425.

Geng, Z., Wang, R., Li, Z., Cui, Z., Zhu, S., Liang, Y., Liu, Y., Huijing, B., Li, X., Huo, Q., Liu, Z. & Yang, X. 2016. Synthesis, characterization and biological evaluation of strontium/magnesium-co-substituted hydroxyapatite. *J Biomater Appl,* 31(1), pp 140-151.

Getzlaf, M. A., Lewallen, E. A., Kremers, H. M., Jones, D. L., Bonin, C. A., Dudakovic, A., Thaler, R., Cohen, R. C., Lewallen, D. G. & Van Wijnen, A. J. 2016. Multi-disciplinary antimicrobial strategies for improving orthopaedic implants to prevent prosthetic joint infections in hip and knee. *J Orthop Res,* 34(2), pp 177-186.

Gohil, J. M. & Choudhury, R. R. 2019. Introduction to Nanostructured and Nano-enhanced Polymeric Membranes: Preparation, Function, and Application for Water Purification. *Nanoscale Materials in Water Purification.* Elsevier, pp 25-57.

Goodman, S. B., Yao, Z., Keeney, M. & Yang, F. 2013. The future of biologic coatings for orthopaedic implants. *Biomaterials,* 34(13), pp 3174-3183.

Gopi, D., Ramya, S., Rajeswari, D., Karthikeyan, P. & Kavitha, L. 2014a. Strontium, cerium co-substituted hydroxyapatite nanoparticles: Synthesis, characterization, antibacterial activity towards prokaryotic strains and in vitro studies. *Colloids and Surfaces A: Physicochemical and Engineering Aspects,* 451pp 172-180.

Gopi, D., Shinyjoy, E. & Kavitha, L. 2014b. Synthesis and spectral characterization of silver/magnesium co-substituted hydroxyapatite for biomedical applications. *Spectrochim Acta A Mol Biomol Spectrosc,* 127pp 286-291.

Green, F., Salter, T., Gilmore, I., Stokes, P. & O'connor, G. 2010. The effect of electrospray solvent composition on desorption electrospray ionisation (DESI) efficiency and spatial resolution. *Analyst,* 135(4), pp 731-737.

Gu, H., Fan, D., Gao, J., Zou, W., Peng, Z., Zhao, Z., Ling, J. & Legeros, R. Z. 2012. Effect of ZnCl2 on plaque growth and biofilm vitality. *Arch Oral Biol,* 57(4), pp 369-375.

Gu, X., Li, N., Zhou, W., Zheng, Y., Zhao, X., Cai, Q. & Ruan, L. 2011. Corrosion resistance and surface biocompatibility of a microarc oxidation coating on a Mg–Ca alloy. *Acta Biomaterialia,* 7(4), pp 1880-1889.

Guglielmotti, M. B., Olmedo, D. G. & Cabrini, R. L. 2019. Research on implants and osseointegration. *Periodontology 2000,* 79(1), pp 178-189.

Gupta, A. K. & Gupta, M. 2005. Synthesis and surface engineering of iron oxide nanoparticles for biomedical applications. *biomaterials,* 26(18), pp 3995-4021.

Gür, A., Çolpan, L., Nas, K., Çevik, R., Saraç, J., Erdoğan, F. & Düz, M. Z. 2002. The role of trace minerals in the pathogenesis of postmenopausal osteoporosis and a new effect of calcitonin. *Journal of bone and mineral metabolism,* 20(1), pp 39-43.

Hahn, B.-D., Lee, J.-M., Park, D.-S., Choi, J.-J., Ryu, J., Yoon, W.-H., Choi, J.-H., Lee, B.-K., Kim, J.-W., Kim, H.-E. & Kim, S.-G. 2011. Enhanced bioactivity and biocompatibility of nanostructured hydroxyapatite coating by hydrothermal annealing. *Thin Solid Films,* 519(22), pp 8085-8090.

Hajikarimi, Z., Khoei, S., Khoee, S. & Mahdavi, S. R. 2014. Evaluation of the cytotoxic effects of PLGA coated iron oxide nanoparticles as a carrier of 5-fluorouracil and mega-voltage X-ray radiation in DU145 prostate cancer cell line. *IEEE transactions on nanobioscience,* 13(4), pp 403-408.

Hamed, E. & Jasiuk, I. 2013. Multiscale damage and strength of lamellar bone modeled by cohesive finite elements. *journal of the mechanical behavior of biomedical materials,* 28pp 94-110.

Hamed, E., Lee, Y. & Jasiuk, I. 2010. Multiscale modeling of elastic properties of cortical bone. *Acta mechanica,* 213(1), pp 131-154.

Han, Y., Wang, X. & Li, S. 2009. A simple route to prepare stable hydroxyapatite nanoparticles suspension. *Journal of Nanoparticle Research,* 11(5), pp 1235-1240.

Hancock, V., Dahl, M. & Klemm, P. 2010. Abolition of biofilm formation in urinary tract Escherichia coli and Klebsiella isolates by metal interference through competition for fur. *Appl Environ Microbiol,* 76(12), pp 3836-3841.

Hans, M., Erbe, A., Mathews, S., Chen, Y., Solioz, M. & MüCklich, F. 2013. Role of copper oxides in contact killing of bacteria. *Langmuir,* 29(52), pp 16160-16166.

Hartman, R., Borra, J.-P., Brunner, D., Marijnissen, J. & Scarlett, B. 1999a. The evolution of electrohydrodynamic sprays produced in the cone-jet mode, a physical model. *Journal of electrostatics,* 47(3), pp 143-170.

Hartman, R., Brunner, D., Camelot, D., Marijnissen, J. & Scarlett, B. 1999b. Electrohydrodynamic atomization in the cone–jet mode physical modeling of the liquid cone and jet. *Journal of Aerosol science,* 30(7), pp 823-849.

Hartman, R., Brunner, D., Camelot, D., Marijnissen, J. & Scarlett, B. 2000. Jet break-up in electrohydrodynamic atomization in the cone-jet mode. *Journal of aerosol science,* 31(1), pp 65-95.

Heinlaan, M., Ivask, A., Blinova, I., Dubourguier, H. C. & Kahru, A. 2008. Toxicity of nanosized and bulk ZnO, CuO and TiO2 to bacteria Vibrio fischeri and crustaceans Daphnia magna and Thamnocephalus platyurus. *Chemosphere,* 71(7), pp 1308-1316.

Henstock, J. R., Canham, L. T. & Anderson, S. I. 2015. Silicon: the evolution of its use in biomaterials. *Acta Biomater,* 11pp 17-26.

Hickok, N. J. & Shapiro, I. M. 2012. Immobilized antibiotics to prevent orthopaedic implant infections. *Adv Drug Deliv Rev,* 64(12), pp 1165-1176.

Hidalgo-Robatto, B. M., López-Álvarez, M., Azevedo, A. S., Dorado, J., Serra, J., Azevedo, N. F., & González, P. 2018. Pulsed laser deposition of copper and zinc doped hydroxyapatite coatings for biomedical applications. *Surface and Coatings Technology,* 333pp 168-177.

Hijano, A., Loscertales, I., Ibáñez, S. & Higuera, F. 2015. Periodic emission of droplets from an oscillating electrified meniscus of a low-viscosity, highly conductive liquid. *Physical Review E,* 91(1), pp

013011(1-12).

Hirota, K., Murakami, K., Nemoto, K. & Miyake, Y. 2005. Coating of a surface with 2-methacryloyloxyethyl phosphorylcholine (MPC) co-polymer significantly reduces retention of human pathogenic microorganisms. *FEMS microbiology letters,* 248(1), pp 37-45.

Hogan, C. J., Yun, K. M., Chen, D.-R., Lenggoro, I. W., Biswas, P. & Okuyama, K. 2007. Controlled size polymer particle production via electrohydrodynamic atomization. *Colloids and Surfaces A: Physicochemical and Engineering Aspects,* 311(1), pp 67-76.

Hogan Jr, C. J., Yun, K. M., Chen, D.-R., Lenggoro, I. W., Biswas, P. & Okuyama, K. 2007. Controlled size polymer particle production via electrohydrodynamic atomization. *Colloids and Surfaces A: Physicochemical and Engineering Aspects,* 311(1-3), pp 67-76.

Hou, C.-H., Hou, S.-M., Hsueh, Y.-S., Lin, J., Wu, H.-C. & Lin, F.-H. 2009. The in vivo performance of biomagnetic hydroxyapatite nanoparticles in cancer hyperthermia therapy. *Biomaterials,* 30(23-24), pp 3956-3960.

Huang, J., Best, S., Bonfield, W., Brooks, R., Rushton, N., Jayasinghe, S. & Edirisinghe, M. 2004. In vitro assessment of the biological response to nano-sized hydroxyapatite. *Journal of Materials Science: Materials in Medicine,* 15(4), pp 441-445.

Huang, Y., Bu, N., Duan, Y., Pan, Y., Liu, H., Yin, Z. & Xiong, Y. 2013a. Electrohydrodynamic direct-writing. *Nanoscale,* 5(24), pp 12007-12017.

Huang, Y., Ding, Q., Pang, X., Han, S. & Yan, Y. 2013b. Corrosion behavior and biocompatibility of strontium and fluorine co-doped electrodeposited hydroxyapatite coatings. *Applied Surface Science,* 282pp 456-462.

Huang, Y., Hao, M., Nian, X., Qiao, H., Zhang, X., Zhang, X., Song, G., Guo, J., Pang, X. & Zhang, H. 2016a. Strontium and copper co-substituted hydroxyapatite-based coatings with improved antibacterial activity and cytocompatibility fabricated by electrodeposition. *Ceramics International,* 42(10), pp 11876-11888.

Huang, Y., Qiao, H., Nian, X., Zhang, X., Zhang, X., Song, G., Xu, Z., Zhang, H. & Han, S. 2016b. Improving the bioactivity and corrosion resistance properties of electrodeposited hydroxyapatite coating by dual doping of bivalent strontium and manganese ion. *Surface and Coatings Technology,* 100(291), pp 205-215.

Huang, Y., Wang, W., Zhang, X., Liu, X., Xu, Z., Han, S., Su, Z., Liu, H., Gao, Y. & Yang, H. 2018. A prospective material for orthopedic applications: Ti substrates coated with a composite coating of a titania-

nanotubes layer and a silver-manganese-doped hydroxyapatite layer. *Ceramics International,* 44(5), pp 5528-5542.

Huang, Y., Zhang, X., Mao, H., Li, T., Zhao, R., Yan, Y. & Pang, X. 2015. Osteoblastic cell responses and antibacterial efficacy of Cu/Zn co-substituted hydroxyapatite coatings on pure titanium using electrodeposition method. *RSC Advances,* 5(22), pp 17076-17086.

Huang, Y., Zhang, X., Zhao, R., Mao, H., Yan, Y. & Pang, X. 2014. Antibacterial efficacy, corrosion resistance, and cytotoxicity studies of copper-substituted carbonated hydroxyapatite coating on titanium substrate. *Journal of Materials Science,* 50(4), pp 1688-1700.

Hussain, S. M., Javorina, A. K., Schrand, A. M., Duhart, H. M., Ali, S. F. & Schlager, J. J. 2006. The interaction of manganese nanoparticles with PC-12 cells induces dopamine depletion. *Toxicological sciences,* 92(2), pp 456-463.

Ignjatović, N., Ajduković, Z., Savić, V., Najman, S., Mihailović, D., Vasiljević, P., Stojanović, Z., Uskoković, V. & Uskoković, D. 2013. Nanoparticles of cobalt-substituted hydroxyapatite in regeneration of mandibular osteoporotic bones. *Journal of Materials Science: Materials in Medicine,* 24(2), pp 343-354.

Itatani, K., Tsugawa, T., Umeda, T., Musha, Y., Davies, I. J. & Koda, S. 2010. Preparation of submicrometer-sized porous spherical hydroxyapatite agglomerates by ultrasonic spray pyrolysis technique. *Journal of the Ceramic Society of Japan,* 118(1378), pp 462-466.

Ito, A., Honda, H. & Kobayashi, T. 2006. Cancer immunotherapy based on intracellular hyperthermia using magnetite nanoparticles: a novel concept of “heat-controlled necrosis” with heat shock protein expression. *Cancer Immunology, Immunotherapy,* 55(3), pp 320-328.

Ito, A., Ojima, K., Naito, H., Ichinose, N., & Tateishi, T. 2000. Preparation, solubility, and cytocompatibility of zinc‐releasing calcium phosphate ceramics. *Journal of Biomedical Materials Research: An Official Journal of The Society for Biomaterials, The Japanese Society for Biomaterials, and The Australian Society for Biomaterials and the Korean Society for Biomaterials,,* 50(2), pp 178-183.

Jacobsson, M., Albrektsson, T., Chrcanovic, B. & Wennerberg, A. 2017. Osseointegration of implants: a biological and clinical overview. *JSM Dental Surgery,* 2(3), pp 1022-1027.

Jalota, S., Bhaduri, S. & Tas, A. 2006. Effect of carbonate content and buffer type on calcium phosphate formation in SBF solutions. *Journal of Materials Science: Materials in Medicine,* 17(8), pp 697-707.

Jaworek, A. & Krupa, A. 1999a. Classification of the modes of EHD spraying. *Journal of Aerosol Science,* 30(7), pp 873-893.

Jaworek, A. & Krupa, A. 1999b. Jet and drops formation in electrohydrodynamic spraying of liquids. A systematic approach. *Experiments in fluids,* 27(1), pp 43-52.

Jaworek, A., Sobczyk, A. & Krupa, A. 2018. Electrospray application to powder production and surface coating. *Journal of Aerosol Science,* 125pp 57-92.

Jaworek, A. & Sobczyk, A. T. 2008. Electrospraying route to nanotechnology: An overview. *Journal of electrostatics,* 66(3-4), pp 197-219.

Jayasinghe, S. & Edirisinghe, M. 2002. Effect of viscosity on the size of relics produced by electrostatic atomization. *Journal of Aerosol Science,* 33(10), pp 1379-1388.

Jayasinghe, S. N. 2017. Thoughts on scaffolds. *Advanced Biosystems,* 1(7), pp 1700067 (1-16).

Jaye, D. L., Bray, R. A., Gebel, H. M., Harris, W. A. & Waller, E. K. 2012. Translational applications of flow cytometry in clinical practice. *The Journal of Immunology,* 188(10), pp 4715-4719.

Jevtic, M., Mitric, M., Skapin, S., Jancar, B., Ignjatovic, N. & Uskokovic, D. 2008. Crystal structure of hydroxyapatite nanorods synthesized by sonochemical homogeneous precipitation. *Crystal Growth and Design,* 8(7), pp 2217-2222.

Ji, H., Sun, H. & Qu, X. 2016. Antibacterial applications of graphene-based nanomaterials: Recent achievements and challenges. *Adv Drug Deliv Rev,* 105(Pt B), pp 176-189.

Jiang, M., Terra, J., Rossi, A., Morales, M., Saitovitch, E. B. & Ellis, D. E. 2002. Fe 2+/F e 3+ substitution in hydroxyapatite: Theory and experiment. *Physical Review B,* 66(22), pp 224107.

Jiang, Y., Yuan, Z. & Huang, J. 2020. Substituted hydroxyapatite: a recent development. *Materials Technology,* 35(11-12), pp 785-796.

Johnson, D. W., Dobson, B. P. & Coleman, K. S. 2015. A manufacturing perspective on graphene dispersions. *Current Opinion in Colloid & Interface Science,* 20(5-6), pp 367-382.

Jordan, A., Scholz, R., Maier-Hauff, K., Johannsen, M., Wust, P., Nadobny, J., Schirra, H., Schmidt, H., Deger, S. & Loening, S. 2001. Presentation of a new magnetic field therapy system for the treatment of human solid tumors with magnetic fluid hyperthermia. *Journal of magnetism and magnetic materials,* 225(1-2), pp 118-126.

Kadiyala, U., Kotov, N. A., & Vanepps, J. S. 2018. Antibacterial Metal Oxide Nanoparticles: Challenges in Interpreting the Literature. *Current pharmaceutical design,* 24(8), pp 896-903.

Kalishwaralal, K., Barathmanikanth, S., Pandian, S. R., Deepak, V. & Gurunathan, S. 2010. Silver nanoparticles impede the biofilm formation by Pseudomonas aeruginosa and Staphylococcus epidermidis. *Colloids Surf B Biointerfaces,* 79(2), pp 340-344.

Karas, M., Bahr, U. & Dülcks, T. 2000. Nano-electrospray ionization mass spectrometry: addressing analytical problems beyond routine. *Fresenius' journal of analytical chemistry,* 366(6), pp 669-676.

Kaygili, O. & Keser, S. 2015. Sol–gel synthesis and characterization of Sr/Mg, Mg/Zn and Sr/Zn co-doped hydroxyapatites. *Materials Letters,* 141pp 161-164.

Kebiroglu, M. H., Orek, C., Bulut, N., Kaygili, O., Keser, S. & Ates, T. 2017. Temperature dependent structural and vibrational properties of hydroxyapatite: A theoretical and experimental study. *Ceramics International,* 43(17), pp 15899-15904.

Kern, P., Veh, J. & Michler, J. 2007. New developments in through-mask electrochemical micromachining of titanium. *Journal of Micromechanics and Microengineering,* 17(6), pp 1168-1177.

Kien Nguyen, T., Nguyen, V. D., Seong, B., Hoang, N., Park, J. & Byun, D. 2014. Control and improvement of jet stability by monitoring liquid meniscus in electrospray and electrohydrodynamic jet. *Journal of Aerosol Science,* 71pp 29-39.

Kim, H.-S., Lee, D.-Y., Park, J.-H., Kim, J.-H., Hwang, J.-H. & Jung, H.-I. 2007. Optimization of electrohydrodynamic writing technique to print collagen. *Experimental techniques,* 31(4), pp 15-19.

Kim, N.-S. & Han, K. N. 2010. Future direction of direct writing. *Journal of Applied Physics,* 108(10), pp 102801 (1-6).

Kim, T. N., Feng, Q. L., Kim, J. O., Wu, J., Wang, H., Chen, G. C., & Cui, F. Z. 1998. Antimicrobial effects of metal ions (Ag+, Cu2+, Zn2+) in hydroxyapatite. *Journal of materials science: Materials in Medicine,* 9(3), pp 129-134.

Kingshott, P., Wei, J., Bagge-Ravn, D., Gadegaard, N. & Gram, L. 2003. Covalent attachment of poly (ethylene glycol) to surfaces, critical for reducing bacterial adhesion. *Langmuir,* 19(17), pp 6912-6921.

Klemm, P., Vejborg, R. M. & Hancock, V. 2010. Prevention of bacterial adhesion. *Appl Microbiol Biotechnol,* 88(2), pp 451-459.

Kokubo, T. 1990. Surface chemistry of bioactive glass-ceramics. *Journal of Non-Crystalline Solids,* 120(1-3), pp 138-151.

Kokubo, T. & Takadama, H. 2006. How useful is SBF in predicting in vivo bone bioactivity? *Biomaterials,* 27(15), pp 2907-2915.

Krella, A. K., Krupa, A., Gazda, M., Sobczyk, A. T. & Jaworek, A. 2017. Protective properties of Al2O3+ TiO2 coating produced by the electrostatic spray deposition method. *Ceramics International,* 43(15), pp 12126-12137.

Kuznetsov, A., Fomin, A., Veresov, A., Putlyaev, V., Fadeeva, I. & Barinov, S. 2008. Hydroxyapatite of platelet morphology synthesized by ultrasonic precipitation from solution. *Russian Journal of Inorganic Chemistry,* 53(1), pp 1-5.

Kyritsis, D. C., Guerrero-Arias, I., Roychoudhury, S. & Gomez, A. 2002. Mesoscale power generation by a catalytic combustor using electrosprayed liquid hydrocarbons. *Proceedings of the Combustion Institute,* 29(1), pp 965-972.

Landi, E., Tampieri, A., Mattioli-Belmonte, M., Celotti, G., Sandri, M., Gigante, A., Fava, P. & Biagini, G. 2006. Biomimetic Mg- and Mg,CO3-substituted hydroxyapatites: synthesis characterization and in vitro behaviour. *Journal of the European Ceramic Society,* 26(13), pp 2593-2601.

Lastow, O. & Balachandran, W. 2007. Novel low voltage EHD spray nozzle for atomization of water in the cone jet mode. *Journal of electrostatics,* 65(8), pp 490-499.

Lazić, S., Zec, S., Miljević, N. & Milonjić, S. 2001. The effect of temperature on the properties of hydroxyapatite precipitated from calcium hydroxide and phosphoric acid. *Thermochimica Acta,* 374(1), pp 13-22.

Le Guéhennec, L., Soueidan, A., Layrolle, P. & Amouriq, Y. 2007. Surface treatments of titanium dental implants for rapid osseointegration. *Dental materials,* 23(7), pp 844-854.

Leventouri, T., Kis, A., Thompson, J. & Anderson, I. 2005. Structure, microstructure, and magnetism in ferrimagnetic bioceramics. *Biomaterials,* 26(24), pp 4924-4931.

Li, C., Yu, D.-G., Williams, G. R. & Wang, Z.-H. 2014. Fast-dissolving core-shell composite microparticles of quercetin fabricated using a coaxial electrospray process. *PLoS One,* 9(3), pp e92106 (1-9).

Li, J., Chou, S., Huang, G., Yang, W. & Li, Z. 2009a. Study on premixed combustion in cylindrical micro combustors: transient flame behavior and wall heat flux. *Experimental Thermal and Fluid Science,* 33(4), pp 764-773.

Li, W. R., Xie, X. B., Shi, Q. S., Duan, S. S., Ouyang, Y. S. & Chen, Y. B. 2011. Antibacterial effect of silver nanoparticles on Staphylococcus aureus. *Biometals,* 24(1), pp 135-141.

Li, X., Huang, J. & Edirisinghe, M. 2008. Novel patterning of nano-bioceramics: template-assisted electrohydrodynamic atomization spraying. *Journal of the Royal Society Interface,* 5(19), pp 253-257.

Li, X., Koller, G., Huang, J., Di Silvio, L., Renton, T., Esat, M., Bonfield, W. & Edirisinghe, M. 2010a. A novel jet-based nano-hydroxyapatite patterning technique for osteoblast guidance. *Journal of the Royal Society Interface,* 7(42), pp 189-197.

Li, Y., Ho, J. & Ooi, C. P. 2010b. Antibacterial efficacy and cytotoxicity studies of copper (II) and titanium (IV) substituted hydroxyapatite nanoparticles. *Materials Science and Engineering: C,* 30(8), pp 1137-1144.

Li, Y., Nam, C. T. & Ooi, C. P. 2009b. Iron (III) and manganese (II) substituted hydroxyapatite nanoparticles: characterization and cytotoxicity analysis. *Journal of Physics: Conference Series,* 187(012024), pp 1-8.

Li, Y., Widodo, J., Lim, S. & Ooi, C. P. 2012. Synthesis and cytocompatibility of manganese (II) and iron (III) substituted hydroxyapatite nanoparticles. *Journal of Materials Science,* 47(2), pp 754-763.

Lim, P. N., Shi, Z., Neoh, K. G., Ho, B., Tay, B. Y. & San Thian, E. 2014. The effects of silver, silicon-containing apatite towards bacteria and cell responses. *Biomedical Materials,* 9(1), pp 015010 (1-9).

Lim, P. N., Tay, B. Y., Chan, C. M. & Thian, E. S. 2012. Synthesis and characterization of silver/silicon-cosubstituted nanohydroxyapatite. *J Biomed Mater Res B Appl Biomater,* 100(1), pp 285-291.

Lim, P. N., Teo, E. Y., Ho, B., Tay, B. Y. & Thian, E. S. 2013. Effect of silver content on the antibacterial and bioactive properties of silver‐substituted hydroxyapatite. *Journal of Biomedical Materials Research Part A,* 101(9), pp 2456-2464.

Lin, K., Liu, P., Wei, L., Zou, Z., Zhang, W., Qian, Y. & Chang, J. 2013. Strontium substituted hydroxyapatite porous microspheres: surfactant-free hydrothermal synthesis, enhanced biological response and sustained drug release. . *Chemical engineering journal,* 222pp 49-59.

Lin, W.-C., Chuang, C.-C., Chang, C.-J., Chiu, Y.-H., Yan, M. & Tang, C.-M. 2019. The effect of electrode topography on the magnetic properties and MRI application of electrochemically-deposited, synthesized, cobalt-substituted hydroxyapatite. *Nanomaterials,* 9(2), pp 200 (1-14).

Little, D. J., Poloczek, J., Whitney, J. C., Robinson, H., Nitz, M. & Howell, P. L. 2012. The structure- and metal-dependent activity of Escherichia coli PgaB provides insight into the partial de-N-acetylation of poly-beta-1,6-N-acetyl-D-glucosamine. *J Biol Chem,* 287(37), pp 31126-31137.

Little, N., Rogers, B. & Flannery, M. 2011. Bone formation, remodelling and healing. *Surgery (Oxford),* 29(4), pp 141-145.

Liu, M. A. 2011. DNA vaccines: an historical perspective and view to the future. *Immunological reviews,* 239(1), pp 62-84.

Liu, S., Zeng, T. H., Hofmann, M., Burcombe, E., Wei, J., Jiang, R., Kong, J. & Chen, Y. 2011. Antibacterial activity of graphite, graphite oxide, graphene oxide, and reduced graphene oxide: membrane and oxidative stress. *ACS nano,* 5(9), pp 6971-6980.

López-Herrera, J., Riesco-Chueca, P. & Gañán-Calvo, A. 2005. Linear stability analysis of axisymmetric perturbations in imperfectly conducting liquid jets. *Physics of Fluids,* 17(3), pp 034106-034106.

Mah, T. F. C., & O'toole, G. A. 2001. Mechanisms of biofilm resistance to antimicrobial agents. *Trends in microbiology,* 9(1), pp 34-39.

Mahajan, A. & Sidhu, S. 2018. Surface modification of metallic biomaterials for enhanced functionality: a review. *Materials technology,* 33(2), pp 93-105.

Manam, N., Harun, W., Shri, D., Ghani, S., Kurniawan, T., Ismail, M. H. & Ibrahim, M. 2017. Study of corrosion in biocompatible metals for implants: A review. *Journal of Alloys and Compounds,* 701pp 698-715.

Marinho, A. R., Martins, P. D., Ditmer, E. M., D'azevedo, P. A., Frazzon, J., Van Der Sand, S. T. & Frazzon, A. P. G. 2013. Biofilm formation on polystyrene under different temperatures by antibiotic resistant Enterococcus faecalis and Enterococcus faecium isolated from food. *Brazilian Journal of Microbiology,* 44(2), pp 423-426.

Martín‐Hernández, F. & Ferré, E. C. 2007. Separation of paramagnetic and ferrimagnetic anisotropies: A review. *Journal of Geophysical Research: Solid Earth,* 112(B3), pp B03105 (1-16).

Mayer, I., Jacobsohn, O., Niazov, T., Werckmann, J., Iliescu, M., Richard‐Plouet, M., Burghaus, O. & Reinen, D. 2003. Manganese in precipitated hydroxyapatites. *European Journal of Inorganic Chemistry,* 2003(7), pp 1445-1451.

Mechay, A., Feki, H. E., Schoenstein, F. & Jouini, N. 2012. Nanocrystalline hydroxyapatite ceramics prepared by hydrolysis in polyol medium. *Chemical Physics Letters,* 541pp 75-80.

Miquel, S., Lagrafeuille, R., Souweine, B. & Forestier, C. 2016. Anti-biofilm activity as a health issue. *Frontiers in microbiology,* 7pp 592 (1-14).

Miyaji, F., Kono, Y. & Suyama, Y. 2005. Formation and structure of zinc-substituted calcium hydroxyapatite. *Materials Research Bulletin,* 40(2), pp 209-220.

Mo, Z., Hu, R., Wang, Y. & He, J. 2014. Review of antibacterial materials and their mechanisms. *Mater Rev,* 28(1), pp 50-52.

Mobasherpour, I., Heshajin, M. S., Kazemzadeh, A. & Zakeri, M. 2007. Synthesis of nanocrystalline hydroxyapatite by using precipitation method. *Journal of Alloys and Compounds,* 430(1-2), pp 330-333.

Mocanu, A., Furtos, G., Rapuntean, S., Horovitz, O., Flore, C., Garbo, C., Danisteanu, A., Rapuntean, G., Prejmerean, C. & Tomoaia-Cotisel, M. 2014. Synthesis; characterization and antimicrobial effects of composites based on multi-substituted hydroxyapatite and silver nanoparticles. *Applied Surface Science,* 298pp 225-235.

Mohseni, E., Zalnezhad, E. & Bushroa, A. R. 2014. Comparative investigation on the adhesion of hydroxyapatite coating on Ti–6Al–4V implant: A review paper. *International Journal of Adhesion and Adhesives,* 48pp 238-257.

Mondal, S., Dorozhkin, S. V. & Pal, U. 2018. Recent progress on fabrication and drug delivery applications of nanostructured hydroxyapatite. *Wiley Interdisciplinary Reviews: Nanomedicine and Nanobiotechnology,* 10(4), pp e1504-e1536.

Mondal, S., Manivasagan, P., Bharathiraja, S., Santha Moorthy, M., Nguyen, V. T., Kim, H. H., Nam, S. Y., Lee, K. D. & Oh, J. 2017. Hydroxyapatite coated iron oxide nanoparticles: a promising nanomaterial for magnetic hyperthermia cancer treatment. *Nanomaterials,* 7(12), pp 426 (1-15).

Monsees, T. K., Barth, K., Tippelt, S., Heidel, K., Gorbunov, A., Pompe, W. & Funk, R. H. 2005. Effects of different titanium alloys and nanosize surface patterning on adhesion, differentiation, and orientation of osteoblast-like cells. *Cells Tissues Organs,* 180(2), pp 81-95.

Morad, M. R., Rajabi, A., Razavi, M. & Sereshkeh, S. P. 2016. A very stable high throughput Taylor cone-jet in electrohydrodynamics. *Scientific reports,* 6(1), pp 1-10.

Morais, A. Í., Vieira, E. G., Afewerki, S., Sousa, R. B., Honorio, L., Cambrussi, A. N., Santos, J. A., Bezerra, R. D., Furtini, J. A. & Silva-Filho, E. C. 2020. Fabrication of polymeric microparticles by electrospray: the impact of experimental parameters. *Journal of functional biomaterials,* 11(1), pp 4 (1-26).

Morris, T., Malardier-Jugroot, C. & Jugroot, M. 2013. Characterization of electrospray beams for micro-spacecraft electric propulsion applications. *Journal of Electrostatics,* 71(5), pp 931-938.

Moura, C. C., Souza, M. A., Dechichi, P., Zanetta-Barbosa, D., Teixeira, C. C. & Coelho, P. G. 2010. The effect of a nanothickness coating on rough titanium substrate in the osteogenic properties of human bone cells. *J Biomed Mater Res A,* 94(1), pp 103-111.

Mulcahy, H., Charron-Mazenod, L. & Lewenza, S. 2008. Extracellular DNA chelates cations and induces antibiotic resistance in Pseudomonas aeruginosa biofilms. *PLoS Pathog,* 4(11), pp e1000213 (1-12).

Munir, G., Di Silvio, L., Edirisinghe, M., Bonfield, W. & Huang, J. 2011a. A novel surface topographical concept for bone implant. *MRS Online Proceedings Library,* 1301(1), pp 67-72.

Munir, G., Koller, G., Di Silvio, L., Edirisinghe, M., Bonfield, W. & Huang, J. 2011b. The pathway to intelligent implants: osteoblast response to nano silicon-doped hydroxyapatite patterning. *Journal of the Royal Society Interface,* 8(58), pp 678-688.

Nagata, F., Yamauchi, Y., Tomita, M. & Kato, K. 2013. Hydrothermal synthesis of hydroxyapatite nanoparticles and their protein adsorption behavior. *Journal of the Ceramic Society of Japan,* 121(1417), pp 797-801.

Nakahira, A., Sakamoto, K., Yamaguchi, S., Kaneno, M., Takeda, S. & Okazaki, M. 1999. Novel Synthesis Method of Hydroxyapatite Whiskers by Hydrolysis of alpha‐Tricalcium Phosphate in Mixtures of Water and Organic Solvent. *Journal of the American Ceramic Society,* 82(8), pp 2029-2032.

Nan, L., Ren, G., Wang, D. & Yang, K. 2016. Antibacterial performance of Cu-bearing stainless steel against Staphylococcus aureus and Pseudomonas aeruginosa in whole milk. *Journal of Materials Science & Technology,* 32(5), pp 445-451.

Naseem, T. & Durrani, T. 2021. The role of some important metal oxide nanoparticles for wastewater and antibacterial applications: a review. *Environmental Chemistry and Ecotoxicology,* 3(3), pp 59-75.

Navarro, M., Michiardi, A., Castano, O. & Planell, J. 2008. Biomaterials in orthopaedics. *Journal of the royal society interface,* 5(27), pp 1137-1158.

Nayak, A. K. 2010. Hydroxyapatite synthesis methodologies: an overview. *International Journal of ChemTech Research,* 2(2), pp 903-907.

Nguyen, T. K., Nguyen, V. D., Seong, B., Hoang, N., Park, J. & Byun, D. 2014. Control and improvement of jet stability by monitoring liquid meniscus in electrospray and electrohydrodynamic jet. *Journal of Aerosol Science,* 71pp 29-39.

Nguyen, V. D. & Byun, D. 2009. Mechanism of electrohydrodynamic printing based on ac voltage without

a nozzle electrode. *Applied Physics Letters,* 94(17), pp 173509 (1-3).

Nicolau Korres, A. M., Aquije, G. M., Buss, D. S., Ventura, J. A., Fernandes, P. M. & Fernandes, A. A. 2013. Comparison of biofilm and attachment mechanisms of a phytopathological and clinical isolate of Klebsiella pneumoniae Subsp. pneumoniae. *ScientificWorldJournal,* 2013pp 925375-925375.

Nithyanandan, A., Mahalingam, S., Huang, J., Rehman, S., Draper, E. & Edirisinghe, M. 2013. Template-assisted electrohydrodynamic atomization of polycaprolactone for orthopedic patterning applications. *Materials Science and Engineering: C,* 33(8), pp 4608-4615.

Nudelman, F. & Sommerdijk, N. A. 2012. Biomineralization as an inspiration for materials chemistry. *Angewandte Chemie International Edition,* 51(27), pp 6582-6596.

O'brien, J., Wilson, I., Orton, T., & Pognan, F. 2000. Investigation of the Alamar Blue (resazurin) fluorescent dye for the assessment of mammalian cell cytotoxicity. *European journal of biochemistry,* 267(17), pp 5421-5426.

Oka, T., Muraya, T., Kawasaki, N., Fukui, S., Ogawa, J., Sato, T. & Terasawa, T. 2012. Magnetizing of permanent magnets using HTS bulk magnets. *Cryogenics,* 52(1), pp 27-31.

Olszta, M. J., Cheng, X., Jee, S. S., Kumar, R., Kim, Y.-Y., Kaufman, M. J., Douglas, E. P. & Gower, L. B. 2007. Bone structure and formation: A new perspective. *Materials Science and Engineering: R: Reports,* 58(3-5), pp 77-116.

Or, D. & Ghezzehei, T. A. 2000. Dripping into subterranean cavities from unsaturated fractures under evaporative conditions. *Water resources research,* 36(2), pp 381-393.

Othman, R., Mustafa, Z., Loon, C. W. & Noor, A. F. M. 2016. Effect of calcium precursors and pH on the precipitation of carbonated hydroxyapatite. *Procedia Chemistry,* 19pp 539-545.

Othmani, M., Bachoua, H., Ghandour, Y., Aissa, A. & Debbabi, M. 2018. Synthesis, characterization and catalytic properties of copper-substituted hydroxyapatite nanocrystals. *Materials Research Bulletin,* 97pp 560-566.

Oyane, A., Onuma, K., Ito, A., Kim, H. M., Kokubo, T. & Nakamura, T. 2003. Formation and growth of clusters in conventional and new kinds of simulated body fluids. *Journal of Biomedical Materials Research Part A: An Official Journal of The Society for Biomaterials, The Japanese Society for Biomaterials, and The Australian Society for Biomaterials and the Korean Society for Biomaterials,* 64(2), pp 339-348.

Oyane, A., Wang, X., Sogo, Y., Ito, A. & Tsurushima, H. 2012. Calcium phosphate composite layers for

surface-mediated gene transfer. *Acta biomaterialia,* 8(6), pp 2034-2046.

Page, K., Wilson, M. & Parkin, I. P. 2009. Antimicrobial surfaces and their potential in reducing the role of the inanimate environment in the incidence of hospital-acquired infections. *Journal of Materials Chemistry,* 19(23), pp 3819-3831.

Pan, Y. & Zeng, L. 2019. Simulation and validation of droplet generation process for revealing three design constraints in electrohydrodynamic jet printing. *Micromachines,* 10(2), pp 94 (1-12).

Panyala, N. R., Peña-Méndez, E. M., & Havel, J 2008. Silver or silver nanoparticles: a hazardous threat to the environment and human health? *Journal of Applied Biomedicine,* 6(3), pp 117-129.

Papadopoulos, E., Collet, J.-F., Vukojević, V., Billeter, M., Holmgren, A., Gräslund, A. & Vlamis-Gardikas, A. 2012. Solution structure and biophysical properties of MqsA, a Zn-containing antitoxin from Escherichia coli. *Biochimica et Biophysica Acta (BBA) - Proteins and Proteomics,* 1824(12), pp 1401-1408.

Park, H., Kim, K. & Kim, S. 2004. Effects of a guard plate on the characteristics of an electrospray in the cone-jet mode. *Journal of aerosol science,* 35(11), pp 1295-1312.

Park, J.-U., Hardy, M., Kang, S. J., Barton, K., Adair, K., Kishore Mukhopadhyay, D., Lee, C. Y., Strano, M. S., Alleyne, A. G. & Georgiadis, J. G. 2007. High-resolution electrohydrodynamic jet printing. *Nature materials,* 6(10), pp 782-789.

Parker-Esquivel, B., Flores, K. J., Louiselle, D., Craig, M., Dong, L., Garrad, R., Ghosh, K., Wanekaya, A., Glaspell, G. & Delong, R. K. 2012. Association of poly I: C RNA and plasmid DNA onto MnO nanorods mediated by PAMAM. *Langmuir,* 28(8), pp 3860-3870.

Pasandideh, Z., Tajabadi, M., Javadpour, J. & Mirkazemi, S. M. 2020. The effects of Fe3+ and Co2+ substitution in Ca10-x-yFexCoy (PO4) 6 (OH) 2 hydroxyapatite nanoparticles: magnetic, antibacterial, and improved drug release behavior. *Ceramics International,* 46(10), pp 16104-16118.

Pasquet, J., Chevalier, Y., Pelletier, J., Couval, E., Bouvier, D. & Bolzinger, M.-A. 2014. The contribution of zinc ions to the antimicrobial activity of zinc oxide. *Colloids and Surfaces A: Physicochemical and Engineering Aspects,* 457pp 263-274.

Patel, N., Best, S. M., Bonfield, W., Gibson, I. R., Hing, K. A., Damien, E., & Revell, P. A. 2002. A comparative study on the in vivo behavior of hydroxyapatite and silicon substituted hydroxyapatite granules. *Journal of Materials Science: Materials in Medicine,* 13(12), pp 1199-1206.

Patel, N., Brooks, R. A., Clarke, M. T., Lee, P. M. T., Rushton, N., Gibson, I. R., & Bonfield, W. 2005. In

vivo assessment of hydroxyapatite and silicate-substituted hydroxyapatite granules using an ovine defect model. *Journal of materials science: materials in medicine,* 16(5), pp 429-440.

Patel, N. R. & Gohil, P. P. 2012. A review on biomaterials: scope, applications & human anatomy significance. *International Journal of Emerging Technology and Advanced Engineering,* 2(4), pp 91-101.

Peltier, L. F., Bickel, E. Y., Lillo, R. & Thein, M. S. 1957. The use of plaster of Paris to fill defects in bone. *Annals of surgery,* 146(1), pp 61-69.

Peng, H., Wang, J., Lv, S., Wen, J. & Chen, J.-F. 2015. Synthesis and characterization of hydroxyapatite nanoparticles prepared by a high-gravity precipitation method. *Ceramics International,* 41(10), pp 14340-14349.

Pereira, A. L., Silva, T. N., Gomes, A. C., Araújo, A. C., & Giugliano, L. G. 2010. Diarrhea-associated biofilm formed by enteroaggregative Escherichia coli and aggregative Citrobacter freundii: a consortium mediated by putative F pili. . *BMC microbiology,* 10(1), pp 57 (1-18).

Peruzzi, M., Pedarnig, J., Sturm, H., Huber, N. & Bäuerle, D. 2004. F2-laser ablation and micro-patterning of GaPO4. *EPL (Europhysics Letters),* 65(5), pp 652-657.

Petchsang, N., Pon-On, W., Hodak, J. & Tang, I. 2009. Magnetic properties of Co-ferrite-doped hydroxyapatite nanoparticles having a core/shell structure. *Journal of magnetism and magnetic materials,* 321(13), pp 1990-1995.

Pogodin, S., Hasan, J., Baulin, V. A., Webb, H. K., Truong, V. K., Nguyen, T. H. P., Boshkovikj, V., Fluke, C. J., Watson, G. S. & Watson, J. A. 2013. Biophysical model of bacterial cell interactions with nanopatterned cicada wing surfaces. *Biophysical journal,* 104(4), pp 835-840.

Pon-On, W., Meejoo, S. & Tang, I.-M. 2008. Substitution of manganese and iron into hydroxyapatite: Core/shell nanoparticles. *Materials Research Bulletin,* 43(8-9), pp 2137-2144.

Posner, A. S. 1969. Crystal chemistry of bone mineral. *Physiological reviews,* 49(4), pp 760-792.

Prabhu, S. & Poulose, E. K. 2012. Silver nanoparticles: mechanism of antimicrobial action, synthesis, medical applications, and toxicity effects. *International nano letters,* 2(1), pp 1-10.

Pryor, L. S., Gage, E., Langevin, C.-J., Herrera, F., Breithaupt, A. D., Gordon, C. R., Afifi, A. M., Zins, J. E., Meltzer, H. & Gosman, A. 2009. Review of bone substitutes. *Craniomaxillofacial trauma & reconstruction,* 2(3-4), pp 151-160.

Pu'ad, N. M., Haq, R. A., Noh, H. M., Abdullah, H., Idris, M. & Lee, T. 2020. Synthesis method of hydroxyapatite: A review. *Materials Today: Proceedings,* 29pp 233-239.

Puckett, S., Pareta, R. & Webster, T. J. 2008. Nano rough micron patterned titanium for directing osteoblast morphology and adhesion. *International journal of nanomedicine,* 3(2), pp 229-241.

Qu, Z., Sun, Y., Chen, D. & Wang, Y. 2014. Possible sites of copper located on hydroxyapatite structure and the identification of active sites for formaldehyde oxidation. *Journal of Molecular Catalysis A: Chemical,* 393pp 182-190.

Radovanović, Ž., Jokić, B., Veljović, D., Dimitrijević, S., Kojić, V., Petrović, R. & Janaćković, D. 2014. Antimicrobial activity and biocompatibility of Ag+- and Cu2+-doped biphasic hydroxyapatite/α-tricalcium phosphate obtained from hydrothermally synthesized Ag+- and Cu2+-doped hydroxyapatite. *Applied Surface Science,* 307pp 513-519.

Raghavendra, S. S., Jadhav, G. R., Gathani, K. M. & Kotadia, P. 2017. Bioceramics in endodontics - a review. *J Istanb Univ Fac Dent,* 51(3 Suppl 1), pp S128-S137.

Rahmany, M. B. & Van Dyke, M. 2013. Biomimetic approaches to modulate cellular adhesion in biomaterials: A review. *Acta Biomater,* 9(3), pp 5431-5437.

Ratnayake, J. T., Mucalo, M. & Dias, G. J. 2017. Substituted hydroxyapatites for bone regeneration: A review of current trends. *Journal of Biomedical Materials Research Part B: Applied Biomaterials,* 105(5), pp 1285-1299.

Rehman, I., & Bonfield, W. 1997. Characterization of hydroxyapatite and carbonated apatite by photo acoustic FTIR spectroscopy. *Journal of Materials Science: Materials in Medicine,* 8(1), pp 1-4.

Ren, F., Xin, R., Ge, X. & Leng, Y. 2009a. Characterization and structural analysis of zinc-substituted hydroxyapatites. *Acta Biomaterialia,* 5(8), pp 3141-3149.

Ren, G., Hu, D., Cheng, E. W., Vargas-Reus, M. A., Reip, P. & Allaker, R. P. 2009b. Characterisation of copper oxide nanoparticles for antimicrobial applications. *International journal of antimicrobial agents,* 33(6), pp 587-590.

Reneker, D. H. & Yarin, A. L. 2008. Electrospinning jets and polymer nanofibers. *Polymer,* 49(10), pp 2387-2425.

Reyes, C. D., Petrie, T. A., Burns, K. L., Schwartz, Z. & Garcia, A. J. 2007. Biomolecular surface coating to enhance orthopaedic tissue healing and integration. *Biomaterials,* 28(21), pp 3228-3235.

Rho, J.-Y., Kuhn-Spearing, L. & Zioupos, P. 1998. Mechanical properties and the hierarchical structure of bone. *Medical engineering & physics,* 20(2), pp 92-102.

Ribeiro, T. P., Monteiro, F. J. & Laranjeira, M. S. 2020. Duality of iron (III) doped nano hydroxyapatite in triple negative breast cancer monitoring and as a drug-free therapeutic agent. *Ceramics International,* 46(10), pp 16590-16597.

Roosjen, A., Kaper, H. J., Van Der Mei, H. C., Norde, W. & Busscher, H. J. 2003. Inhibition of adhesion of yeasts and bacteria by poly (ethylene oxide)-brushes on glass in a parallel plate flow chamber. *Microbiology,* 149(11), pp 3239-3246.

Rosell-Llompart, J. & De La Mora, J. F. 1994. Generation of monodisperse droplets 0.3 to 4 μm in diameter from electrified cone-jets of highly conducting and viscous liquids. *Journal of Aerosol Science,* 25(6), pp 1093-1119.

Rosell-Llompart, J., Grifoll, J. & Loscertales, I. G. 2018. Electrosprays in the cone-jet mode: from Taylor cone formation to spray development. *Journal of Aerosol Science,* 125pp 2-31.

Rouhani, P., Taghavinia, N. & Rouhani, S. 2010. Rapid growth of hydroxyapatite nanoparticles using ultrasonic irradiation. *Ultrasonics sonochemistry,* 17(5), pp 853-856.

Rulison, A. J. & Flagan, R. C. 1994. Electrospray atomization of electrolytic solutions. *Journal of colloid and interface science,* 167(1), pp 135-145.

Sachse, A., Wagner, A., Keller, M., Wagner, O., Wetzel, W.-D., Layher, F., Venbrocks, R.-A., Hortschansky, P., Pietraszczyk, M. & Wiederanders, B. 2005. Osteointegration of hydroxyapatite-titanium implants coated with nonglycosylated recombinant human bone morphogenetic protein-2 (BMP-2) in aged sheep. *Bone,* 37(5), pp 699-710.

Sadat-Shojai, M., Khorasani, M.-T., Dinpanah-Khoshdargi, E. & Jamshidi, A. 2013. Synthesis methods for nanosized hydroxyapatite with diverse structures. *Acta biomaterialia,* 9(8), pp 7591-7621.

Saez, A. E. & Carbonell, R. 1987. The equilibrium shape and stability of menisci formed between two touching cylinders. *Journal of fluid mechanics,* 176pp 357-378.

Saif, T. A. 2002. On the capillary interaction between solid plates forming menisci on the surface of a liquid. *Journal of Fluid Mechanics,* 473pp 321-347.

Salwiczek, M., Qu, Y., Gardiner, J., Strugnell, R. A., Lithgow, T., Mclean, K. M. & Thissen, H. 2014. Emerging rules for effective antimicrobial coatings. *Trends Biotechnol,* 32(2), pp 82-90.

Santos, M. H., Oliveira, M. D., Souza, L. P. D. F., Mansur, H. S. & Vasconcelos, W. L. 2004. Synthesis control and characterization of hydroxyapatite prepared by wet precipitation process. *Materials Research,* 7(4), pp 625-630.

Schmidt-Wolf, G. D. & Schmidt-Wolf, I. G. 2003. Non-viral and hybrid vectors in human gene therapy: an update. *Trends Mol Med,* 9(2), pp 67-72.

Sergi, R., Bellucci, D., Candidato, R. T., Lusvarghi, L., Bolelli, G., Pawlowski, L., Candiani, G., Altomare, L., De Nardo, L. & Cannillo, V. 2018. Bioactive Zn-doped hydroxyapatite coatings and their antibacterial efficacy against Escherichia coli and Staphylococcus aureus. *Surface and Coatings Technology,* 352pp 84-91.

Shanmugam, S. & Gopal, B. 2014. Copper substituted hydroxyapatite and fluorapatite: Synthesis, characterization and antimicrobial properties. *Ceramics International,* 40(10), pp 15655-15662.

Shannon, R. D. 1976. Revised effective ionic radii and systematic studies of interatomic distances in halides and chalcogenides. *Acta crystallographica section A: crystal physics, diffraction, theoretical and general crystallography,* 32(5), pp 751-767.

Shepherd, D. & Best, S. M. 2013. Production of zinc substituted hydroxyapatite using various precipitation routes. *Biomed Mater,* 8(2), pp 025003 (1-12).

Sima, L. E., Stan, G. E., Morosanu, C. O., Melinescu, A., Ianculescu, A., Melinte, R., Neamtu, J. & Petrescu, S. M. 2010. Differentiation of mesenchymal stem cells onto highly adherent radio frequency-sputtered carbonated hydroxylapatite thin films. *J Biomed Mater Res A,* 95(4), pp 1203-1214.

Singh, A. & Van Den Mooter, G. 2016. Spray drying formulation of amorphous solid dispersions. *Advanced drug delivery reviews,* 100pp 27-50.

Slavin, Y. N., Asnis, J., Häfeli, U. O. & Bach, H. 2017. Metal nanoparticles: understanding the mechanisms behind antibacterial activity. *Journal of nanobiotechnology,* 15(1), pp 1-20.

Smaniotto, D., D'agostino, G., Luzi, S., Valentini, V., Macchia, G., Mantini, G., Margariti, P. A., Ferrandina, G. & Scambia, G. 2005. Concurrent 5-fluorouracil, mitomycin C and radiation with or without brachytherapy in recurrent cervical cancer: a scoring system to predict clinical response and outcome. *Tumori Journal,* 91(4), pp 295-301.

Song, W., Zhang, J., Guo, J., Zhang, J., Ding, F., Li, L. & Sun, Z. 2010. Role of the dissolved zinc ion and reactive oxygen species in cytotoxicity of ZnO nanoparticles. *Toxicology letters,* 199(3), pp 389-397.

Souza, E. L. D., Meira, Q. G. S., Barbosa, I. D. M., Athayde, A. J. A. A., Conceição, M. L. D., & Siqueira

Júnior, J. P. D. 2014. Biofilm formation by Staphylococcus aureus from food contact surfaces in a meat-based broth and sensitivity to sanitizers. *Brazilian Journal of Microbiology,* 45(1), pp 67-75.

Spence, G., Patel, N., Brooks, R. & Rushton, N. 2009. Carbonate substituted hydroxyapatite: resorption by osteoclasts modifies the osteoblastic response. *J Biomed Mater Res A,* 90(1), pp 217-224.

Stanić, V., Dimitrijević, S., Antić-Stanković, J., Mitrić, M., Jokić, B., Plećaš, I. B. & Raičević, S. 2010. Synthesis, characterization and antimicrobial activity of copper and zinc-doped hydroxyapatite nanopowders. *Applied Surface Science,* 256(20), pp 6083-6089.

Stanić, V., Janaćković, D., Dimitrijević, S., Tanasković, S. B., Mitrić, M., Pavlović, M. S., Krstić, A., Jovanović, D. & Raičević, S. 2011. Synthesis of antimicrobial monophase silver-doped hydroxyapatite nanopowders for bone tissue engineering. *Applied Surface Science,* 257(9), pp 4510-4518.

Suh, J., Han, B., Okuyama, K. & Choi, M. 2005. Highly charging of nanoparticles through electrospray of nanoparticle suspension. *Journal of colloid and interface science,* 287(1), pp 135-140.

Šupová, M. 2015. Substituted hydroxyapatites for biomedical applications: A review. *Ceramics International,* 41(8), pp 9203-9231.

Syamchand, S. S. & Sony, G. 2015. Multifunctional hydroxyapatite nanoparticles for drug delivery and multimodal molecular imaging. *Microchimica Acta,* 182(9), pp 1567-1589.

Szcześ, A., Hołysz, L. & Chibowski, E. 2017. Synthesis of hydroxyapatite for biomedical applications. *Advances in colloid and interface science,* 249pp 321-330.

Szuster-Ciesielska, A., Stachura, A., Słotwińska, M., Kamińska, T., Śnieżko, R., Paduch, R., Abramczyk, D., Filar, J. & Kandefer-Szerszeń, M. 2000. The inhibitory effect of zinc on cadmium-induced cell apoptosis and reactive oxygen species (ROS) production in cell cultures. *Toxicology,* 145(2-3), pp 159-171.

Tadano, S. & Giri, B. 2012. X-ray diffraction as a promising tool to characterize bone nanocomposites. *Science and technology of advanced materials,* 12(12), pp 064708 (1-11).

Takegami, K., Sano, T., Wakabayashi, H., Sonoda, J., Yamazaki, T., Morita, S., Shibuya, T. & Uchida, A. 1998. New ferromagnetic bone cement for local hyperthermia. *Journal of biomedical materials research,* 43(2), pp 210-214.

Tamayo, R., Tischler, A. D., & Camilli, A. 2005. The EAL domain protein VieA is a cyclic diguanylate phosphodiesterase. *Journal of Biological Chemistry,* 280(39), pp 33324-33330.

Tamm, T. & Peld, M. 2006. Computational study of cation substitutions in apatites. *Journal of Solid State Chemistry,* 179(5), pp 1581-1587.

Tampieri, A., D'alessandro, T., Sandri, M., Sprio, S., Landi, E., Bertinetti, L., Panseri, S., Pepponi, G., Goettlicher, J. & Bañobre-López, M. 2012. Intrinsic magnetism and hyperthermia in bioactive Fe-doped hydroxyapatite. *Acta biomaterialia,* 8(2), pp 843-851.

Tang, K. & Gomez, A. 1995. Generation of monodisperse water droplets from electrosprays in a corona-assisted cone-jet mode. *Journal of Colloid and Interface Science,* 175(2), pp 326-332.

Tang, Y., Chappell, H. F., Dove, M. T., Reeder, R. J. & Lee, Y. J. 2009. Zinc incorporation into hydroxylapatite. . *Biomaterials,* 30(15), pp 2864-2872.

Tank, K. P., Chudasama, K. S., Thaker, V. S. & Joshi, M. J. 2013. Cobalt-doped nanohydroxyapatite: synthesis, characterization, antimicrobial and hemolytic studies. *Journal of Nanoparticle Research,* 15(5), pp 1-11.

Tathe, A., Ghodke, M. & Nikalje, A. P. 2010. A brief review: biomaterials and their application. *International Journal of Pharmacy and Pharmaceutical Sciences,* 2(4), pp 19-23.

Taylor, G. I. 1964. Disintegration of water drops in an electric field. *Proceedings of the Royal Society of London. Series A. Mathematical and Physical Sciences,* 280(1382), pp 383-397.

Terra, J., Jiang, M. & Ellis, D. E. 2002. Characterization of electronic structure and bonding in hydroxyapatite: Zn substitution for Ca. *Philosophical Magazine A,* 82(11), pp 2357-2377.

Thian, E. S., Konishi, T., Kawanobe, Y., Lim, P. N., Choong, C., Ho, B. & Aizawa, M. 2013. Zinc-substituted hydroxyapatite: a biomaterial with enhanced bioactivity and antibacterial properties. *J Mater Sci Mater Med,* 24(2), pp 437-445.

Thorek, D. L., Chen, A. K., Czupryna, J. & Tsourkas, A. 2006. Superparamagnetic iron oxide nanoparticle probes for molecular imaging. *Annals of biomedical engineering,* 34(1), pp 23-38.

Townsend-Nicholson, A. & Jayasinghe, S. 2018. Cell Electrospinning and Technology Transfer from Lab to Market Scale. *Electrospinning,* pp 79-94.

Tram Do, T. N., Lee, W.-H., Loo, C.-Y., Zavgorodniy, A. V. & Rohanizadeh, R. 2012. Hydroxyapatite nanoparticles as vectors for gene delivery. *Therapeutic delivery,* 3(5), pp 623-632.

Trandafir, D.-L., Mirestean, C., Turcu, R., Frentiu, B., Eniu, D. & Simon, S. 2014. Structural characterization of nanostructured hydroxyapatite–iron oxide composites. *Ceramics International,* 40(7), pp 11071-

11078.

Tseng, C.-L., Chang, K.-C., Yeh, M.-C., Yang, K.-C., Tang, T.-P. & Lin, F.-H. 2014. Development of a dual-functional Pt–Fe-HAP magnetic nanoparticles application for chemo-hyperthermia treatment of cancer. *Ceramics International,* 40(4), pp 5117-5127.

Ullah, I., Li, W., Lei, S., Zhang, Y., Zhang, W., Farooq, U., Ullah, S., Ullah, M. W. & Zhang, X. 2018. Simultaneous co-substitution of Sr2+/Fe3+ in hydroxyapatite nanoparticles for potential biomedical applications. *Ceramics International,* 44(17), pp 21338-21348.

Uskoković, V. & Uskoković, D. P. 2011. Nanosized hydroxyapatite and other calcium phosphates: chemistry of formation and application as drug and gene delivery agents. *Journal of biomedical materials research Part B: Applied biomaterials,* 96(1), pp 152-191.

Valiense, H., Barreto, M., Resende, R. F., Alves, A. T., Rossi, A. M., Mavropoulos, E., Granjeiro, J. M. & Calasans-Maia, M. D. 2016. In vitro and in vivo evaluation of strontium-containing nanostructured carbonated hydroxyapatite/sodium alginate for sinus lift in rabbits. *J Biomed Mater Res B Appl Biomater,* 104(2), pp 274-82.

Vargas-Reus, M. A., Memarzadeh, K., Huang, J., Ren, G. G. & Allaker, R. P. 2012. Antimicrobial activity of nanoparticulate metal oxides against peri-implantitis pathogens. *International journal of antimicrobial agents,* 40(2), pp 135-139.

Verdoold, S., Agostinho, L., Yurteri, C. & Marijnissen, J. 2014. A generic electrospray classification. *Journal of Aerosol Science,* 67pp 87-103.

Vincent, M., Hartemann, P. & Engels-Deutsch, M. 2016. Antimicrobial applications of copper. *International journal of hygiene and environmental health,* 219(7), pp 585-591.

Von Der Mark, K. & Park, J. 2013. Engineering biocompatible implant surfaces. *Progress in Materials Science,* 58(3), pp 327-381.

Wagner, D. E., Eisenmann, K. M., Nestor-Kalinoski, A. L. & Bhaduri, S. B. 2013. A microwave-assisted solution combustion synthesis to produce europium-doped calcium phosphate nanowhiskers for bioimaging applications. *Acta biomaterialia,* 9(9), pp 8422-8432.

Wang, M.-C., Chen, H.-T., Shih, W.-J., Chang, H.-F., Hon, M.-H. & Hung, I.-M. 2015. Crystalline size, microstructure and biocompatibility of hydroxyapatite nanopowders by hydrolysis of calcium hydrogen phosphate dehydrate (DCPD). *Ceramics International,* 41(2), pp 2999-3008.

Wang, W., Ouyang, Y. & Poh, C. K. 2011. Orthopaedic implant technology: biomaterials from past to

future. *Annals of the Academy of Medicine-Singapore,* 40(5), pp 237.

Wang, Y., Zhang, S., Wei, K., Zhao, N., Chen, J. & Wang, X. 2006. Hydrothermal synthesis of hydroxyapatite nanopowders using cationic surfactant as a template. *Materials Letters,* 60(12), pp 1484-1487.

Webster, T. J., Patel, A. A., Rahaman, M. & Bal, B. S. 2012. Anti-infective and osteointegration properties of silicon nitride, poly (ether ether ketone), and titanium implants. *Acta biomaterialia,* 8(12), pp 4447-4454.

Wilking, J. N., Zaburdaev, V., De Volder, M., Losick, R., Brenner, M. P. & Weitz, D. A. 2013. Liquid transport facilitated by channels in Bacillus subtilis biofilms. *Proceedings of the National Academy of Sciences,* 110(3), pp 848-852.

Winkler, T., Sass, F., Duda, G. & Schmidt-Bleek, K. 2018. A review of biomaterials in bone defect healing, remaining shortcomings and future opportunities for bone tissue engineering: The unsolved challenge. *Bone & joint research,* 7(3), pp 232-243.

Wu, C., Labrie, J., Tremblay, Y. D., Haine, D., Mourez, M. & Jacques, M. 2013. Zinc as an agent for the prevention of biofilm formation by pathogenic bacteria. *J Appl Microbiol,* 115(1), pp 30-40.

Wu, H.-C., Wang, T.-W., Sun, J.-S., Wang, W.-H. & Lin, F.-H. 2007a. A novel biomagnetic nanoparticle based on hydroxyapatite. *Nanotechnology,* 18(16), pp 165601 (1-9).

Wu, H.-C., Wang, T.-W., Sun, J.-S., Wang, W.-H. & Lin, F.-H. 2007b. A novel biomagnetic nanoparticle based on hydroxyapatite. *Nanotechnology,* 18(16), pp 165601.

Wu, S., Bao, C., Wang, R., Zhang, X., Gao, S., Qin, W., Zhang, J., Zhang, J., Li, R. & Chen, X. 2020. Therapeutic effect of Zuojin Pill on chronic atrophic gastritis induced by Helicobacter pylori through JMJD2B/COX-2/VEGF. *Reaearch square,* PREPRINT (3), pp 1-27.

Wu, W., Dey, D., Memis, O. G., Katsnelson, A. & Mohseni, H. 2008. Fabrication of large area periodic nanostructures using nanosphere photolithography. *Nanoscale research letters,* 3(10), pp 351-354.

Wu, Y. & Clark, R. L. 2008. Electrohydrodynamic atomization: a versatile process for preparing materials for biomedical applications. *Journal of Biomaterials Science, Polymer Edition,* 19(5), pp 573-601.

Xiao, X., Liu, R., Chen, C. & Huang, L. 2008. Structural characterization of zinc-substituted hydroxyapatite prepared by hydrothermal method. *Journal of materials science: Materials in medicine,* 19(2), pp 797-803.

Xie, J., Jiang, J., Davoodi, P., Srinivasan, M. P. & Wang, C. H. 2015. Electrohydrodynamic atomization: A two-decade effort to produce and process micro-/nanoparticulate materials. *Chem Eng Sci,* 125pp 32-57.

Xu, Y., Ma, G., Wang, X. & Wang, M. 2012. Solution–air interface synthesis and growth mechanism of tooth enamel-like hydroxyapatite/chondroitin sulfate films. *Crystal Growth & Design,* 12(7), pp 3362-3368.

Yadav, H. M., Kim, J.-S. & Pawar, S. H. 2016. Developments in photocatalytic antibacterial activity of nano TiO 2: A review. *Korean Journal of Chemical Engineering,* 33(7), pp 1989-1998.

Yang, Y., Kim, K. H. & Ong, J. L. 2005. A review on calcium phosphate coatings produced using a sputtering process--an alternative to plasma spraying. *Biomaterials,* 26(3), pp 327-37.

Yang, Y. C., Chen, C. C., Wang, J. B., Wang, Y. C. & Lin, F. H. 2017. Flame sprayed zinc doped hydroxyapatite coating with antibacterial and biocompatible properties. *Ceramics International,* 43pp S829-S835.

Yang, Z., Liu, Z., Allaker, R., Reip, P., Oxford, J., Ahmad, Z. & Ren, G. 2010. A review of nanoparticle functionality and toxicity on the central nervous system. *Journal of the Royal Society Interface,* 7(suppl_4), pp S411-S422.

Yanhua, W., Hao, H., Li, Y. & Zhang, S. 2016. Selenium-substituted hydroxyapatite nanoparticles and their in vivo antitumor effect on hepatocellular carcinoma. *Colloids and Surfaces B: Biointerfaces,* 140pp 297-306.

Yao, J., Tjandra, W., Chen, Y. Z., Tam, K. C., Ma, J. & Soh, B. 2003. Hydroxyapatite nanostructure material derived using cationic surfactant as a template. *Journal of materials chemistry,* 13(12), pp 3053-3057.

Yelten-Yilmaz, A. & Yilmaz, S. 2018. Wet chemical precipitation synthesis of hydroxyapatite (HA) powders. *Ceramics International,* 44(8), pp 9703-9710.

Yeong, K., Wang, J. & Ng, S. 2001. Mechanochemical synthesis of nanocrystalline hydroxyapatite from CaO and CaHPO4. *Biomaterials,* 22(20), pp 2705-2712.

Yoshikawa, T., Ohgushi, H. & Tamai, S. 1996. Immediate bone forming capability of prefabricated osteogenic hydroxyapatite. *Journal of Biomedical Materials Research: An Official Journal of The Society for Biomaterials and The Japanese Society for Biomaterials,* 32(3), pp 481-492.

Yuliati, L., Seo, T. & Mikami, M. 2012. Liquid-fuel combustion in a narrow tube using an electrospray technique. *Combustion and Flame,* 159(1), pp 462-464.

Zaidi, S., Patel, A., Mehta, N., Patel, K., Takiar, R. & Saiyed, H. 2005. Early biochemical alterations in manganese toxicity: ameliorating effects of magnesium nitrate and vitamins. *Industrial health,* 43(4), pp 663-668.

Zameer, F., Rukmangada, M. S., Chauhan, J. B., Khanum, S. A., Kumar, P., Devi, A. T., & Dhananjaya, B. L. 2016. Evaluation of adhesive and anti-adhesive properties of Pseudomonas aeruginosa biofilms and their inhibition by herbal plants. *Iranian journal of microbiology,* 8(2), pp 108-119.

Zhakin, A. I. 2012. Electrohydrodynamics. *Physics-Uspekhi,* 55(5), pp 465-488.

Zhang, G., Chen, J., Yang, S., Yu, Q., Wang, Z. & Zhang, Q. 2011. Preparation of amino-acid-regulated hydroxyapatite particles by hydrothermal method. *Materials letters,* 65(3), pp 572-574.

Zhang, N., Zhai, D., Chen, L., Zou, Z., Lin, K. & Chang, J. 2014a. Hydrothermal synthesis and characterization of Si and Sr co-substituted hydroxyapatite nanowires using strontium containing calcium silicate as precursors. *Mater Sci Eng C Mater Biol Appl,* 37pp 286-291.

Zhang, W., Chai, Y., Cao, N. & Wang, Y. 2014b. Synthesis and characterization of selenium substituted hydroxyapatite via a hydrothermal procedure. *Materials Letters,* 134pp 123-125.

Zhao, J. M., Tsuru, K., Hayakawa, S. & Osaka, A. 2008. Modification of Ti implant surface for cell proliferation and cell alignment. *Journal of Biomedical Materials Research Part A: An Official Journal of The Society for Biomaterials, The Japanese Society for Biomaterials, and The Australian Society for Biomaterials and the Korean Society for Biomaterials,* 84(4), pp 988-993.

Zhao, L., Chu, P. K., Zhang, Y. & Wu, Z. 2009. Antibacterial coatings on titanium implants. *J Biomed Mater Res B Appl Biomater,* 91(1), pp 470-480.

Zhao, S. F., Jiang, Q. H., Peel, S., Wang, X. X. & He, F. M. 2013. Effects of magnesium-substituted nanohydroxyapatite coating on implant osseointegration. *Clin Oral Implants Res,* 24 Suppl A100pp 34-41.

Zhu, B., Lu, Q., Yin, J., Hu, J. & Wang, Z. 2005. Alignment of osteoblast-like cells and cell-produced collagen matrix induced by nanogrooves. *Tissue engineering,* 11(5-6), pp 825-834.

Zhu, B., Zhang, Q., Lu, Q., Xu, Y., Yin, J., Hu, J. & Wang, Z. 2004a. Nanotopographical guidance of C6 glioma cell alignment and oriented growth. *Biomaterials,* 25(18), pp 4215-4223.

Zhu, M., Ye, H., Fang, J., Zhong, C., Yao, J., Park, J., Lu, X. & Ren, F. 2019. Engineering high-resolution micropatterns directly onto titanium with optimized contact guidance to promote osteogenic differentiation and bone regeneration. *ACS Applied Materials & Interfaces,* 11(47), pp 43888-43901.

Zhu, X., Chen, J., Scheideler, L., Altebaeumer, T., Geis-Gerstorfer, J. & Kern, D. 2004b. Cellular reactions of osteoblasts to micron-and submicron-scale porous structures of titanium surfaces. *Cells Tissues Organs,* 178(1), pp 13-22.

Zilm, M. E., Yu, L., Hines, W. A. & Wei, M. 2018. Magnetic properties and cytocompatibility of transition-metal-incorporated hydroxyapatite. *Materials Science and Engineering: C,* 87pp 112-119.